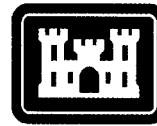


ERDC/GL TR-00-3

Geotechnical Laboratory



**US Army Corps  
of Engineers.**

Engineer Research and  
Development Center

## **Response of Granular Layers in Flexible Pavements Subjected to Aircraft Loadings**

Donald Mark Smith

May 2000

20000630 070

The contents of this report are not to be used for advertising, publication, or promotional purposes. Citation of trade names does not constitute an official endorsement or approval of the use of such commercial products.

The findings of this report are not to be construed as an official Department of the Army position, unless so designated by other authorized documents.



PRINTED ON RECYCLED PAPER

#### **Engineer Research and Development Center Cataloging-in-Publication Data**

Smith, Donald M.

Response of granular layers in flexible pavements subjected to aircraft loadings / by Donald Mark Smith ; prepared for U.S. Army Corps of Engineers.

266 p. : ill. ; 28 cm. — (ERDC/GL ; TR-00-3)

Includes bibliographic references.

1. Pavements, Flexible — Foundations — Mathematical models. 2. Pavements, Concrete — Foundations — Mathematical models. 3. Granular materials — Plastic properties. 4. Runways (Aeronautics) — Foundations — Mathematical models. I. United States. Army. Corps of Engineers. II. Engineer Research and Development Center (U.S.) III. Geotechnical Laboratory (U.S.) IV. Title. V. Series: ERDC/GL TR ; 00-3.

TA7 E8 no.ERDC/GL TR-00-3

## TABLE OF CONTENTS

LIST OF TABLES .....	iv
LIST OF FIGURES.....	v
PREFACE .....	x
CHAPTER	
1 INTRODUCTION .....	1
Background.....	1
Objective.....	1
Originality.....	2
Scope of Work .....	2
2 PROBLEM STATEMENT .....	4
3 LITERATURE REVIEW.....	7
Model Requirements.....	7
Elasticity Models .....	7
Plasticity Models.....	14
Yield Functions .....	16
Flow Rules .....	22
Hardening Rules .....	23
Recent Developments .....	27
Summary of Literature Review .....	28
4 SELECTION AND IMPLEMENTATION OF CANDIDATE MODELS .....	33
Candidate Constitutive Models.....	33
Description of ABAQUS .....	35
ABAQUS Drucker-Prager Cap Model.....	35
Yield Surface .....	36
Failure Surface.....	37
Cap Yield Surface.....	37
Defining Yield and Hardening Parameters .....	37
Plastic Flow .....	38
Calibration .....	38
WES Multimechanical Constitutive Model .....	38
Background .....	38
General Description.....	39
Stiffness Parameters.....	40
Yield Parameters.....	41
Shear-Volume Coupling .....	42
Details of Calculations.....	42
Coding Details .....	43
ABAQUS Features .....	43
Material Properties .....	44
Associated Parameters – Global Parameters.....	44
Associated Parameters – Mechanism Parameters .....	45



Flow Scheme .....	45
Solution – Dependent Variables (SDV's).....	45
UMAT Main Subroutine .....	46
Subroutine Sand_driver.....	46
Subroutine Ammos.....	47
Subroutine Hydros.....	47
Subroutine RadialReturn .....	48
Summary of Calling Schedule .....	48
Model Operation.....	48
 5 MODEL CALIBRATION .....	 68
General.....	68
ABAQUS Drucker-Prager Model .....	68
Failure Surface.....	68
Cap Yield Surface.....	68
Calibration .....	70
WES Multimechanical Constitutive Model .....	70
Calibrating the Model – General Approach.....	70
Laboratory Tests .....	72
Material .....	72
Specimen Preparation .....	73
Description of Test Device .....	78
Results of Laboratory Tests .....	81
Unconfined Compression Tests .....	81
Conventional Triaxial Compression Tests .....	83
Uniaxial Strain Tests .....	86
Hydrostatic Compression Tests .....	89
Determination of ABAQUS Drucker-Prager Model Parameters .....	91
Determination of WES Multimechanical Model Parameters .....	93
Strength Parameters.....	93
Stiffness Parameters.....	93
Other Parameters .....	94
Mechanism Parameters.....	96
Application of MVIEWER .....	97
 6 MODEL VERIFICATION.....	 103
Verification Analyses.....	103
ABAQUS Issues .....	103
Simulation of Laboratory Tests.....	105
Conventional Triaxial Compression Tests .....	105
Uniaxial Strain Tests .....	111
Hydrostatic Compression Tests .....	114
Unconfined Compression Tests .....	114
Cyclic Triaxial Compression Tests .....	115
Field Test Sections.....	119
General Test Section Description .....	119
As-Constructed Properties .....	120
Instrumentation .....	120
Traffic .....	122
ABAQUS FEM Analysis of Test Sections .....	123

Material Properties .....	123
FEM Mesh .....	124
Results of FEM Analyses of Test Sections .....	129
Model Sensitivity.....	143
7 CONCLUSIONS AND RECOMMENDATIONS.....	145
Conclusions .....	145
Recommendations.....	147
REFERENCES.....	149
APPENDIXES	
A WES MM MODEL UMAT SOURCE CODE .....	153
B SAMPLE ABAQUS INPUT FILE.....	181
C RESULTS OF CONVENTIONAL TRIAXIAL COMPRESSION TESTS .....	188
D RESULTS OF HYDROSTATIC COMPRESSION TESTS .....	215
E RESULTS OF UNCONFINED COMPRESSION TESTS .....	221
F RESULTS OF UNIAXIAL STRAIN TESTS .....	232
G OPERATION OF THE WES MULTIMECHANICAL MODEL VIEWER.....	239
H DETERMINATION OF STRENGTH PARAMETERS.....	245
I THREE DIMENSIONAL VERIFICATION.....	249

## LIST OF TABLES

3.1. Parameters Used in Yield Functions.....	16
3.2. Cap Models with Isotropic Hardening Rules.....	25
4.1. Critical Features of Selected Models for Unbound Pavement Materials .....	34
4.2. Global Properties.....	51
4.3. Mechanism Properties .....	51
4.4. Frequency of Calls.....	51
5.1. Granular Limestone Specimen Properties .....	73
5.2. Summary of Results at Maximum Axial Stress from UCC Tests .....	81
5.3. Summary of Results at Maximum Axial Stress from CTC Tests .....	84
5.4. Summary of Peak Stress Results from Uniaxial Strain Tests .....	88
5.5. Summary of Peak Stress Results from HC Tests.....	89
5.6. Global Properties for Granular Limestone.....	95
5.7. Strength Parameters by Confining Stress for Granular Limestone .....	96
5.8. Mechanism Properties for Granular Limestone .....	96
6.1. Global Properties for Modified Calibration.....	116
6.2. Mechanism Properties for Modified Calibration .....	116
6.3. As-constructed Properties for Subgrade and Base Course.....	120
6.4. Material Properties Used for Asphalt and Subgrade Layers .....	124
6.5. Layer Thickness Values.....	124
6.6. Predicted Base Course Deformation in Lane 1-1 with Changes in $\phi$ and G .....	144

## LIST OF FIGURES

2.1. Typical flexible pavement configuration .....	6
2.2. Comparison of aircraft and truck (18K-ESAL) loadings.....	6
3.1. Coulomb yield function and surface.....	17
3.2. Tresca yield function and surface.....	18
3.3. Drucker-Prager yield function and surface.....	19
3.4. Von Mises yield function and surface .....	20
3.5. Lade Duncan yield function and surface .....	21
3.6. Flow diagram summarizing the evolution of plastic constitutive models for soils .....	32
4.1. ABAQUS Drucker-Prager model yield surface.....	36
4.2. Idealized representation of WES Multimechanical model.....	40
4.3. Flow chart for WES MM ABAQUS UMAT.....	52
4.4. Flow chart for Subroutine Sand_driver (Part1) .....	53
4.5. Flow chart for Subroutine Sand _driver (Part 2) .....	54
4.6. Flow chart for Subroutine Ammos .....	55
4.7. Idealized representation of the WES MM model.....	56
4.8. Stress versus strain for a cyclic test .....	56
4.9. WES MM stress path at Point 1 (initial yield of Mechanism 1) .....	57
4.10. WES MM stress path at Point 2 (initial yield of Mechanism 2) .....	58
4.11. WES MM stress path at Point 3 (initial yield of Mechanism 3) .....	59
4.12. WES MM stress path at Point 4 (unload).....	60
4.13. WES MM stress path at Point 5 (extension yield of Mechanism 1) .....	61
4.14. WES MM stress path at Point 6 (extension yield of Mechanism 2) .....	62
4.15. WES MM stress path at Point 7 (reload).....	63

4.16. WES MM stress path at Point 8 (reload yield of Mechanism 1).....	64
4.17. WES MM stress path at Point 9 (reload yield of Mechanism 2).....	65
4.18. WES MM stress path at Point 10 (reload yield of Mechanism 3).....	66
4.19. WES MM stress path at Point 11 (continued loading) .....	67
5.1. ABAQUS Drucker-Prager model with stress regime of interest shown in gray .....	69
5.2. Void ratio versus log normal stress plot used to determine NCL for WES MM model.....	71
5.3. Well-graded crushed limestone used in laboratory tests .....	74
5.4. Grain-size analysis of well-graded crushed limestone used in laboratory tests.....	74
5.5. Schematic of the gyratory testing machine .....	76
5.6. Gyratory testing machine used for specimen preparation .....	77
5.7. Instron servo-controlled testing machine.....	79
5.8. Granular limestone specimen with instrumentation attached.....	80
5.9. Axial stress versus axial strain for unconfined compression tests of granular limestone.....	82
5.10. Mean normal stress versus volumetric strain for unconfined compression tests of granular limestone .....	82
5.11. Principal stress difference versus principal strain difference for conventional triaxial compression tests of granular limestone .....	85
5.12. Principal stress difference versus mean normal stress for conventional triaxial compression tests of granular limestone .....	85
5.13. Mean normal stress versus volumetric strain for conventional triaxial compression tests of granular limestone .....	86
5.14. Mean normal stress versus principal stress difference for uniaxial strain tests.....	87
5.15. Principal stress difference versus principal strain differences for uniaxial strain tests .....	87

5.16. Principal stress difference versus mean normal stress for uniaxial strain tests .....	88
5.17. Mean normal stress versus volumetric strain for hydrostatic compression tests of granular limestone.....	90
5.18. Failure surface for crushed limestone base course material .....	92
5.19. Composite plot of initial portion of principal stress difference versus principal strain difference showing shear modulus .....	92
5.20. Plot used to determine NCL relationship for granular limestone material .....	95
5.21. Stress strain response with $G=30,000$ psi (206.8 MPa) (lower line) and $G=60,000$ psi (413.6 MPa) (upper line).....	99
5.22. Stress strain response with $G=30,000$ psi (206.8 MPa) (upper line) and 15,000 psi (103.4 MPa) (lower line) .....	99
5.23. Stress strain response with $K=20,000$ psi (137.9 MPa) (upper line), 10,000 psi (68.9 MPa) (middle line), and 5,000 psi (34.3 MPa) (lower line).....	100
5.24. Stress strain response with $\phi=48^\circ$ (lower line) and $\phi=52.6^\circ$ (upper line) .....	101
5.25. Stress strain response with $C = 0.25$ (lower line) and $C = 2.5$ (upper line) .....	101
5.26. Stress strain response with PHIRATIO=0.5 (lower line) and PHIRATIO=0.75 (upper line).....	102
5.27. Stress strain response with DECAY=3.6 (lower line) and DECAY=1.8 (upper line) .....	102
6.1. Composite plot of principal stress difference versus principal strain difference for 15 psi (103.4 kPa) test.....	107
6.2. Composite plot of principal stress difference versus principal strain difference for 30 psi (206.8 kPa) test.....	108
6.3. Composite plot of principal stress difference versus principal strain difference for 50 psi (344.7 kPa) test.....	108
6.4. Composite plot of principal stress difference versus principal strain difference for 80 psi (551.6 kPa) test .....	109
6.5. Predicted failure surface for Drucker-Prager model compared with test results.....	109

6.6. Composite plot of mean normal stress versus volumetric strain for DP predictions of CTC tests.....	110
6.7. Predicted failure surface for WES MM model compared with test results .....	110
6.8. Composite plot of mean normal stress versus volumetric strain for WES MM predictions of CTC tests .....	111
6.9. Composite plot of principal stress difference versus mean normal stress for uniaxial strain tests .....	112
6.10. Composite plot of principal stress difference versus principal strain difference for uniaxial strain tests.....	113
6.11. Composite plot of mean normal stress versus volumetric strain for uniaxial strain tests.....	113
6.12. Composite plot of mean normal stress versus volumetric strain for hydrostatic compression tests .....	117
6.13. Composite plot of axial stress versus axial strain for unconfined compression tests .....	117
6.14. Composite plot of mean normal stress versus volumetric strain for unconfined compression tests.....	118
6.15. Comparison of FEM prediction of cyclic response with test data.....	118
6.16. Typical cross-section of MDD after installation .....	121
6.17. Loaded single wheel test cart with C-130 tire.....	122
6.18. Typical axisymmetric FEM model of a pavement .....	127
6.19. Finite element mesh for Lane 1-1 .....	128
6.20. Finite element mesh for Lane 2-1 .....	128
6.21. Deformed shape (100 X) under 5 <sup>th</sup> load application for Lane 1-1 .....	130
6.22. Deformed shape (100 X) after 5 <sup>th</sup> load application for Lane 1-1 .....	131
6.23. Deformed shape (100 X) under 5 <sup>th</sup> load application for Lane 2-1 .....	131
6.24. Deformed shape (100 X) after 5 <sup>th</sup> load application for Lane 2-1 .....	132
6.25. Vertical deformation versus load cycles from FEM simulation of Lane 1-1 .....	133
6.26. Vertical deformation versus load cycles from FEM simulation of Lane 2-1 .....	133

6.27. Principal strain difference in Lane 1-1 (i.e. shear strain) under load cycle 1 .....	135
6.28. Principal strain difference in Lane 1-1 (i.e. shear strain) after load cycle 1 .....	136
6.29. Principal strain difference in Lane 1-1 (i.e. shear strain) under load cycle 5 .....	137
6.30. Principal strain difference in Lane 1-1 (i.e. shear strain) after load cycle 5 .....	138
6.31. Principal strain difference in Lane 2-1 (i.e. shear strain) under load cycle 1 .....	139
6.32. Principal strain difference in Lane 2-1 (i.e. shear strain) after load cycle 1 .....	140
6.33. Principal strain difference in Lane 2-1 (i.e. shear strain) under load cycle 5 .....	141
6.34. Principal strain difference in Lane 2-1 (i.e. shear strain) after load cycle 5 .....	142



## PREFACE

The research reported herein was sponsored by the U.S. Army Corps of Engineers through the Research, Development, Testing, and Evaluation (RDT&E) Program, Pavements Research Work Package, AT22. This research was conducted by the U.S. Army Engineer Research and Development Center (ERDC), Geotechnical Laboratory (GL), Airfields and Pavements Division (APD), Vicksburg, MS.

The study was conducted under the general supervision of Dr. Michael J. O'Connor, Acting Director, GL, Dr. W.F. Marcuson III, former Director, GL, and Dr. David W. Pittman, Chief, APD. Technical direction was provided by Dr. Raymond S. Rollings, Team Leader, APD Analytical Modeling Team. Dr. John B. Metcalf, Louisiana State University, provided much insight and technical advise during the testing, analysis, and publication phases of this research. Dr. John F. Peters, GL, provided essential technical guidance throughout all aspects of this project. Dr. Donald M. Smith, APD, was the project principal investigator and author of this report. Messrs. Tommy Carr, Robert Walker, and David Stinson, ERDC, provided assistance during the testing, programming, and analysis phases of this research. This report was submitted by Dr. Smith to and accepted by the Graduate School, Louisiana State University, in partial fulfillment of the requirements for the degree of Doctor of Philosophy.

At the time of publication of this report, Acting Director of ERDC was Dr. Lewis E. Link, and Commander was COL Robin R. Cababa, EN.

*The contents of this report are not to be used for advertising, publication, or promotional purposes. Citation of trade names does not constitute and official endorsement of the use of such commercial products*

# **CHAPTER 1: INTRODUCTION**

## **BACKGROUND**

Airfield pavement design is a complex blend of relatively simple linear elastic theory, fatigue concepts, correlations with small and full-scale tests, and pragmatic adjustments to reflect observations of in-service pavements. This philosophy served the design community well for many years as it allowed total thickness, asphalt concrete pavement thickness, and material requirements for constituent layers in the pavement to be determined to avoid a pre-selected level of distress in the pavement. For airfields, this level of distress at “design” failure was selected to be one inch of shear rutting in the subgrade or fatigue cracking of the asphalt concrete.

However, today’s designers are being asked to predict pavement performance. This is a far more complex task than simply providing safe thickness and specifications for the material. To deal with this new challenge, the design community must have material models that predict cumulative deformations under repetitive aircraft loads. With heavy loading, such as may be encountered with many airfields, the nonlinear response of base course materials must be considered when predicting pavement performance. The advances made in computational mechanics have created new tools of application for this type of problem. Theoretically rigorous material models may be implemented within many of the general-purpose finite element computer programs available today. In order to apply these material models, mechanical response data is required to calibrate the necessary model parameters (Barker and Gonzalez, 1991).

## **OBJECTIVE**

The objective of this research was to provide an analytical method for modeling the response of unbound granular layers in flexible pavements subjected to aircraft loads. The

essential features of pavement response that are required from a constitutive model include non-linear elastic response, permanent or plastic deformation after yield, cyclic loading, strain softening/hardening, and shear dilatancy. A pavement model should be simple in operation, implementation and calibration. The model must be executable within a proven general purpose finite element code like ABAQUS from HKS, Inc. The model must also provide pavement analysts with the capability of predicting the performance of unbound materials under traffic loadings.

### **ORIGINALITY**

The contribution or originality of the research is in the following area: The identification, implementation, and evaluation of a new constitutive model that can provide for response predictions of stresses in granular pavement layers for current and future aircraft.

### **SCOPE OF WORK**

This research was conducted as a four-phase effort.

- Phase 1: State of the Art Review and Assessment: This phase included a review of related publications, research, and test results. Candidate theories, models, test methods and historically significant field test data were identified in this review. Particular emphasis was placed on a model that was relatively simple to calibrate with the capability to capture the critical response features of granular material behavior.
- Phase 2: Model Integration: In this phase, a candidate constitutive model was implemented as a user defined material model in the ABAQUS General Purpose Finite Element Code.
- Phase 3: Model Calibration: In this phase, the granular material response model was calibrated with laboratory test data. The testing requirements were a function of the type of model selected in Phase 1. Historical test data was acquired and new tests were conducted where necessary to define material properties for unbound granular pavement materials.

- Phase 4: Model Verification, Evaluation and Documentation: In this phase, the newly calibrated model was exercised against laboratory test data and selected historical field pavement system response data to assess the predictive suitability of the model (Webster, 1993). The ABAQUS finite element code was used to make these predictions. The strengths and weaknesses of the response model and calibration parameter relationships were evaluated and documented.

## CHAPTER 2: PROBLEM STATEMENT

Classically, the flexible pavement used in military airfields consists of a thin asphalt concrete (AC) surface to provide a high-quality waterproof surface, and relatively thick layers of granular base and subbase down to the subgrade. These thick granular layers are used to reduce the stresses applied by aircraft traffic on the pavement surface. A typical pavement of this type is shown in Figure 2.1.

The magnitude and frequency of loading in airfield pavements are very different from typical highway pavements. The magnitudes of aircraft loadings are much greater than the loads seen in highways as shown in Figure 2.2. The amount of load repetitions applied to airfield pavement is several orders of magnitude less than that seen in highways. A high-volume highway may experience 60 million equivalent single axle loads (ESAL), while a high volume airfield may only experience 250,000 aircraft coverages in a 20-year period. These differences led to a divergence in the research focus between the airfield and highway pavement communities. The major focus of research into highway flexible pavement design has been in the area of viscous fatigue modeling of asphalt concrete. The airfield pavement community has been required to broaden the focus of analytical research to include the AC and all supporting layers (Ahlvin, 1991).

The granular base and subbase have always posed the most difficult analytical problem in traditional airfield pavement design methodologies. For this reason, the granular layers have never been treated explicitly in design as have the AC layer and subgrade layer, which have used predictive models for cracking in the AC and rutting in the subgrade as a function of linear-elastic strain and material properties. Instead these granular layers were carefully specified in terms of gradation, plasticity, and in-situ density to minimize deformation under traffic. However, in order to eventually develop theoretical methods to

predict performance of the pavement, sound methodologies must be developed that will predict plastic deformation within these granular layers.

The structural components of flexible pavements are highly nonlinear-elastic plastic materials. With heavy loading, such as may be encountered with many roads and airfields, the nonlinear response of pavement materials should be considered when predicting pavement performance. The advances made in computational mechanics have created new tools, such as the newer generation finite element codes, for this type of problem. The beauty of the finite element method is that it can incorporate both features and handle arbitrary geometries. Theoretically rigorous material models may be implemented within many of the general-purpose finite element computer programs available today. In order to apply these material models, mechanical response data is required to calibrate the necessary model parameters.

The essential features of pavement response that are required from any constitutive model include non-linear elastic response, permanent or plastic deformations after yield, cyclic loading, strain softening/hardening, and shear dilatancy. This research addresses the inadequacies of present design and analysis procedures as related to prediction of the response of granular pavement layers subjected to aircraft loads.

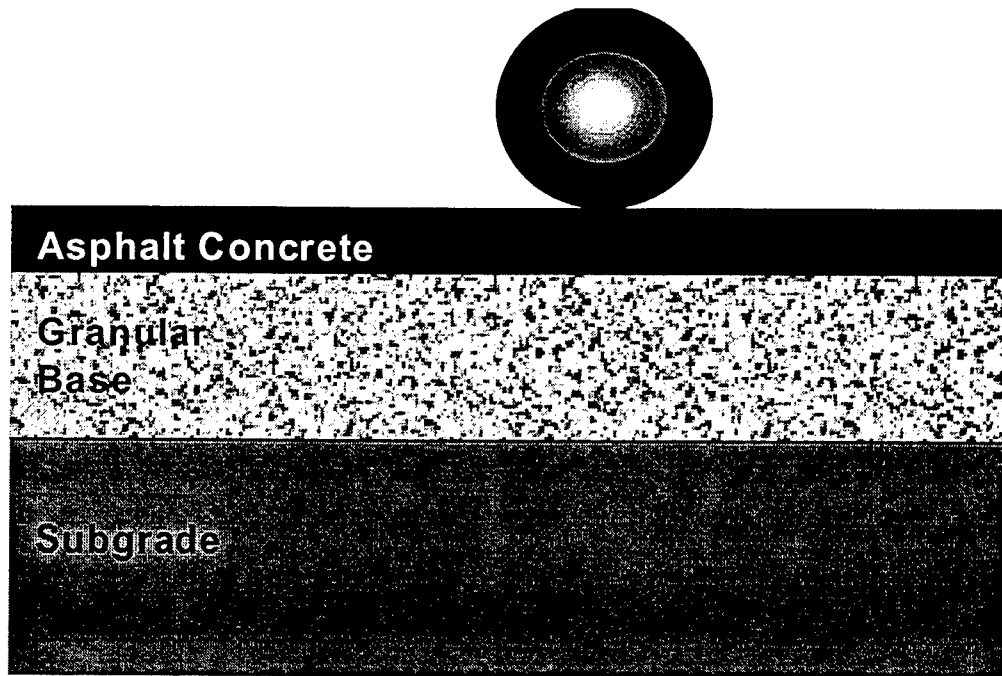


Figure 2.1. Typical flexible pavement configuration

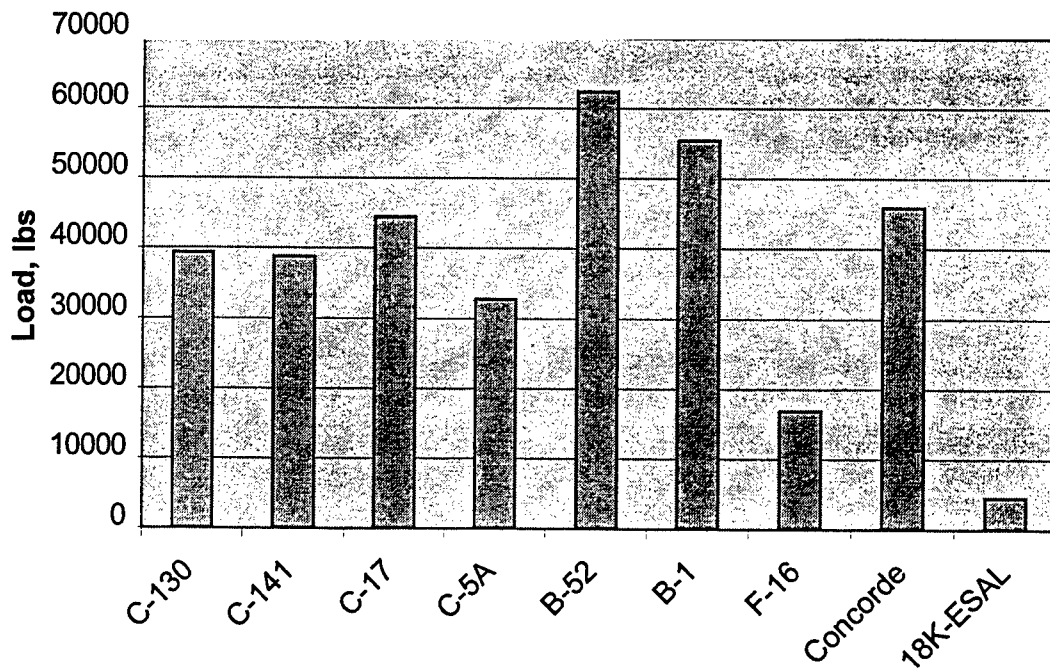


Figure 2.2. Comparison of aircraft and truck (18K-ESAL) loadings

## **CHAPTER 3: LITERATURE REVIEW**

### **MODEL REQUIREMENTS**

Typical rational design procedures couple theoretical response models that predict traffic induced stresses, strains, and deflections with damage models for fatigue cracking and pavement rutting. The various layers in a pavement system are characterized by their engineering properties and the structural design is subsequently based upon limiting stresses, strains, or deflections computed at certain critical locations in the pavement structure. The procedures use an iterative process, which involves theoretical response analysis, material characterization, distress prediction, and adjustment factors. Several rational (mechanistic) pavement design procedures have been introduced into design over the past years. The development of the procedures is summarized in the Proceedings of the International Conferences on the Structural Design of Asphalt Pavements (University of Michigan, 1962, 1967, 1972, 1977, 1982, 1987, and International Society for Asphalt Pavements, 1992).

### **ELASTICITY MODELS**

Elasticity models can be divided into three distinct classes: (1) Cauchy elasticity, (2) hyperelasticity, and (3) hypoelasticity. Cauchy elasticity is based on total stress, and the current stress depends only on the current strain. Cauchy elasticity models are also reversible. Hyperelasticity is a total stress model where the current stress depends only on the current strain. In addition, hyperelasticity models are based on the principle of virtual work to insure compliance with the first law of thermodynamics. Hypoelastic models are incremental stress models that are incrementally reversible. The current state of stress is independent on the stress and strain path followed. Each of these three classes of models are addressed in the following sections.



Many theoretical response models treat a pavement system as a layered, linear elastic system. For these type analyses, load associated responses are governed by the magnitude and geometry of the applied loads, and the thickness, elastic modulus, and Poisson's ratio of the individual layers. In these analyses, each layer is completely characterized by the elastic modulus and the Poisson's ratio. Previous research, however, has shown that both the resilient (elastic) and permanent deformation behavior of granular paving materials are extremely complex, depending on material characteristics, drainage, and loading conditions. The inability of layered elastic theory to account for stress dependent material properties has become an area of serious concern.

The stress dependency of the resilient modulus and Poisson's ratio of granular materials have been examined and evaluated by a number of researchers (Seed, et al., 1967, Hicks and Finn, 1970, Hicks and Monismith, 1971, and Rada and Witczak, 1981). The research indicates that the deformation response of granular materials is highly stress dependent, and that the resilient modulus increases with increasing confining stresses. The constitutive relationship developed in these studies, called the bulk stress model, expresses the resilient modulus as a function of the bulk stress, using Equation 3.1.

$$E_r = k_1 \theta^{k_2} \quad (3.1)$$

where  $E_r$  = resilient modulus

$\theta$  = bulk stress ( $\Phi_1 + 2\Phi_3$ )

$k_1, k_2$  = regression coefficients

Also, in some of the same research, Poisson's ratio was determined to increase with increasing values of the principal stress ratio. Historically, the bulk stress model, above, has been combined with a "constant" Poisson's ratio and used widely as the constitutive model of granular materials for pavement design.

In continued research with granular materials, May and Witczak (1981) and Uzan (1985), concluded that measured and predicted responses using the bulk stress model did not sufficiently agree, and that not only the stress state, but also the magnitude of the induced shear strains influenced the resilient modulus. As a result, Witczak and Uzan (1988) improved on previous relationships and introduced the octahedral shear stress term to the determination of the resilient modulus. In addition to the octahedral shear stress, which is an invariant shear stress term for three-dimensional analysis, they also made the equation dimensionally correct by normalizing the bulk and shear stress terms using atmospheric pressure. Equation 3.2 presents the modified equation, called the universal model because it is applicable to both granular and cohesive soils.

$$E_r = k_1 P_A \left( \frac{\theta}{P_A} \right)^{k_2} \left( \frac{\tau_{oct}}{P_A} \right)^{k_3} \quad (3.2)$$

where  $E_r$  = resilient modulus

$\theta$  = bulk stress

$\tau_{oct}$  = octahedral shear stress

$P_A$  = atmospheric pressure

$k_1, k_2, k_3$  = regression coefficients

The use of Equations 3.2 and 3.3 above have been recommended as the constitutive model for unbound pavement material layers in highway performance models developed at Texas A&M (Lytton, et al., 1993). The five material parameters in these models are determined using nonlinear regression analysis of data from repeated load triaxial tests.

The above nonlinear Cauchy elastic models are modifications, or a simple extension, of the generalized form of Hooke's law, and use secant moduli determined from the stress or strain invariants; thereby accounting for confinement effects. These Cauchy elastic models

are total stress models in which the current stress depends only on the current strain and the state of stress is path independent. An essential advantage in the use of these models is that the model parameters have physical significance. These models were evaluated by Bonaquist (1996) who concluded two limitations. First, the Cauchy elastic models can not account for the volume changes which result from the application of shear stresses, because they are based upon Hooke's law and, therefore, can not model either plastic responses or dilation. Second, nonlinear elastic models may violate the first law of thermodynamics and generate energy along certain cyclic stress paths (Chen and Saleeb, 1982), because the secant moduli are arbitrarily selected.

To mitigate the problems associated with violating the first law of thermodynamics, hyperelastic constitutive relationships have been developed based upon the principle of conservation of energy during the loading and unloading of an elastic body (Lade and Nelson, 1987, Chen and Mizuno, 1990, and Uzan et al., 1992). Like the previously mentioned elastic models, these relationships are also not dependent upon the stress or strain history, and the stress-strain behavior is both reversible and path independent. Hyperelastic models, however, are typically higher order equations with a large number of regression coefficients, or fitting parameters. As the order increases, the number of parameters increases, and subsequently the difficulty in performing suitable laboratory tests to evaluate the parameters.

One of the more straightforward hyperelastic models is that proposed by Uzan et al. (1992), as a part of the Strategic Highway Research Program. They assumed both the resilient modulus and Poisson's ratio to be stress dependent and developed the following stress dependent relationship for Poisson's ratio using the principle of conservation of energy and the universal model presented in Equation 3.2. The basic form of this non-linear hyperelastic model for a variable Poisson's ration is given in Equation 3.3.

$$\begin{aligned}
\nu_s = I_1^{k_2} J_2^{k_3} & \left[ \frac{3^{k_3}}{2(I_1^2 - 3J_2)^{\frac{k_2+k_3}{2}}} \left( -k_2 B_v \left( \frac{k_2}{2} + k_3, -k_3 + 1 \right) \right. \right. \\
& \left. \left. + k_3 B_v \left( \frac{k_2}{2} + k_3, -k_3 \right) \right) + k_4 (3J_2 - I_1^2)^{k_5} \right]
\end{aligned} \tag{3.3}$$

where

$\nu_s$  = secant Poisson's ratio

$I_1$  = 1<sup>st</sup> stress invariant =  $\sigma_1 + \sigma_2 + \sigma_3$

$J_2$  = 2<sup>nd</sup> deviatoric stress invariant

=  $1/6 [(\sigma_1 - \sigma_2)^2 + (\sigma_2 - \sigma_3)^2 + (\sigma_3 - \sigma_1)^2]$

$\sigma_1, \sigma_2, \sigma_3$  = principal stress

$B_v(i,j)$  = Incomplete Beta function

$k_2, k_3, k_4, k_5$  = regression coefficients

Hyperelastic models are total stress models, which satisfy the first law of thermodynamics, account for nonlinearity, confinement, dilation, and can be used to model cyclic loading. Cyclic loading and unloading, however, must follow the same path, since the current stress depends on the current strain. The primary disadvantage to most high order hyperelastic models is that they do not include plastic response and that many of the fitting parameters have no physical significance, and consequently testing to evaluate these parameters is frequently complicated.

A third type elasticity model is the hypoelastic constitutive model, which addresses the fact that in many materials, including granular materials, the stress-strain behavior is path dependent and the response is not necessarily reversible. The hypoelastic formulation is an incremental constitutive relationship, with the behavior determined in small increments of stress, rather than for the entire applied stress. The current state of stress of a material

depends upon the current state of strain, as well as, the stress path followed to reach the current state. Like the hyperelastic models, the true hypoelastic models account for nonlinearity, confinement effects, and dilation. Unfortunately, also like the hyperelastic models, many of the true hypoelastic models are higher order formulations which result in greater numerical complexity and a large number of material fitting parameters which have no physical significance, or interpretation.

There are, however, some simpler hypoelastic models, which have been developed from an incremental form of the generalized Hooke's law. For these models, the resilient modulus is replaced with variable, or incremental, tangent moduli, which are functions of the stress or strain invariants. The models are path dependent and a large variety of nonlinear material behavior can be modeled. While these models lack rigorous theory and can not include dilation, they are relatively simple and the model parameters do have physical significance. Three of these simplified hypoelastic models are presented below. Duncan and Chang (1970) presented the following model shown in Equation 3.4.

$$E_t = \left[ 1 - \frac{R_f(1 - \sin \Phi)(\sigma_1 - \sigma_3)}{2(c \cos \Phi + \sigma_3 \sin \Phi)} \right]^2 k p_a \left( \frac{\sigma_3}{p_a} \right)^n \quad (3.4 \text{ a})$$

$$\nu_t = \frac{G - F \log \left( \frac{\sigma_3}{p_a} \right)}{\left[ 1 - \frac{d(\sigma_1 - \sigma_3)}{k p_a \left( \frac{\sigma_3}{p_a} \right)^n \left( 1 - \frac{R_f(\sigma_1 - \sigma_3)(1 - \sin \Phi)}{2(c \cos \Phi + a_3 \sin \Phi)} \right)} \right]^2} \quad (3.4 \text{ b})$$

where:

$E_t$  = tangent Young's Modulus

$\nu_t$  = tangent Poisson's ratio

$\sigma_1, \sigma_3$  = principal stresses

$p_a$  = atmospheric pressure

$c$  = cohesion

$\phi$  = angle of internal friction

$k, n, G, F, d$  = material constants

Duncan et al., 1978, presented the following as in Equation 3.5 where the elastic constants are functions of the current stress state and the Mohr Coulomb yield surface location.

$$E_t = \left[ 1 - \frac{R_f (1 - \sin \Phi)(\sigma_1 - \sigma_3)}{2(c \cos \Phi + \sigma_3 \sin \Phi)} \right]^2 k p_a \left( \frac{\sigma_3}{p_a} \right)^n \quad (3.5 a)$$

$$K_t = k_b P_a \left( \frac{\sigma_3}{P_a} \right)^m \quad (3.5 b)$$

where:

$E_t$  = tangent Young's Modulus

$K_s$  = tangent bulk modulus

$\sigma_1, \sigma_3$  = principal stresses

$p_a$  = atmospheric pressure

$c$  = cohesion

$\phi$  = angle of internal friction

$k, n, k_b, m$  = material constants

$R_f$  = failure ratio

Domaschuk and Wade (1969) presented the following relationship shown in Equation 3.6, where the bulk and shear modulus constants are related to the current stress state. The octahedral shear and normal stresses are used to determine the elastic constants.

$$K_t = K_0 = m \sigma_m \quad (3.6 \text{ a})$$

$$G_t = G_0 (1 - b \tau_{oct})^2 \quad (3.6 \text{ b})$$

where:

$K_t$  = tangent bulk modulus

$G_t$  = tangent shear modulus

$\sigma$  = octahedral normal stress

$\tau_{oct}$  = octahedral normal stress

$K_0$  = initial bulk modulus

$G_0$  = initial shear modulus

$b, m$  = material constants

In the use of hypoelastic models, initial conditions must be specified since the stress-strain behavior of the materials will be dictated depending upon the initial starting point. With the specification of loading and unloading criteria, these models can be used to model the plastic behavior of some granular materials. These models have seen little use in pavement analysis except for limited applications in nondestructive pavement testing and pavement thickness design to resist fatigue cracking.

## PLASTICITY MODELS

Plasticity models characterize the plastic deformation behavior of soils under cyclic loading and are particularly useful in modeling earthquake responses. Since these models predict responses to cyclic loading their benefits in performing pavement rutting analyses are obvious.

The first type models considered here are the variable modulus models. These models are based upon the deformation theory of plasticity, are relatively simple formulations derived from the theory of elasticity. The incremental nonlinear elastic constitutive models presented previously in are frequently used with the variable modulus models to describe

permanent deformation under cyclic loading. With these models, different tangent moduli are selected (prescribed) for the loading, unloading, and reloading conditions. It is common practice to assume that the unloading and reloading moduli are equal to the initial tangent modulus on loading. With these assumptions, greater deformations occur on loading than unloading, and as a result, cyclic loading produces permanent deformations.

Since the incremental nonlinear constitutive models presented are based upon the generalized Hooke's law, the stress invariants for octahedral normal stress and octahedral shear stress are normally used to define volumetric and shear loading conditions. If more complex constitutive models like the hyperelastic or hypoelastic models are selected for use, the distinction between loading and unloading must be accomplished with the use of an energy density function. For these models, loading represents positive work, while unloading represents negative work.

The primary advantage to variable modulus models are that they are a conceptually and computationally simple formulation and a logical extension to the elasticity models based upon incremental forms of Hooke's law, presented previously. In addition, the model parameters used in the models have physical significance and interpretation. A disadvantage to the use of these models is that since they are based on incremental forms of Hooke's law, they can not account for shear dilation. Another disadvantage is that these models violate continuity for the neutral loading condition; when the loading function is equal to zero. For this condition, either loading or unloading behavior (and moduli) can be assumed.

A theoretically rigorous formulation for plasticity has been developed based upon flow theory. Constitutive models based upon the flow theory of plasticity are incremental and extend the elastic stress-strain relationships into the plastic range. The total strain is the summation of the reversible elastic strains and the irreversible plastic strains. Here again, an incremental form of Hooke's law using elastic moduli (Young's modulus, Lamé's constants,



etc.), that are functions of the stress or strain invariants determines the elastic strains. The plastic strains are functions of the current states of stress and strain, and the incremental stress gradient. Yield functions are introduced in flow theory to differentiate between the elastic and plastic states (Chen and Mizuno, 1990) (Salami, 1994).

### Yield Functions

A yield function in flow theory differentiates between elastic and plastic behavior. Yield functions mathematically describe a surface, within which purely elastic recoverable deformations or strains occur and along which purely plastic deformations occur. Intersections of the stress path with the yield surface result in both elastic and plastic deformations. Yield functions have been commonly used in many civil and geotechnical engineering applications to describe plastic behavior of soils and other construction materials. Much of the response requirements in traditional geotechnical applications require monotonic loading capabilities only (Chen and Mizuno, 1990), while pavements applications are strongly tied to cyclic response. Five of the more commonly applied yield functions for geotechnical materials are presented below. The yield functions are generally expressed in terms of stress invariants in a principal stress space to simplify the comparison of one surface to another. The basic parameters used in the formulations of these yield functions are given in Table 3.1. Although only five yield functions are presented, these are typical the large number of theories that have been proposed over the last 40 years of geotechnical engineering history.

Table 3.1. Parameters Used in Yield Functions

$\theta$ = Lode angle
$I_1$ = first invariant of the stress tensor
$J_2$ = second invariant of the stress deviator tensor
$I_3$ = third invariant of the stress tensor
$J_3$ = third invariant of the stress deviator tensor
$c$ = cohesion
$M$ = angle of internal friction
$k, a$ = material constants

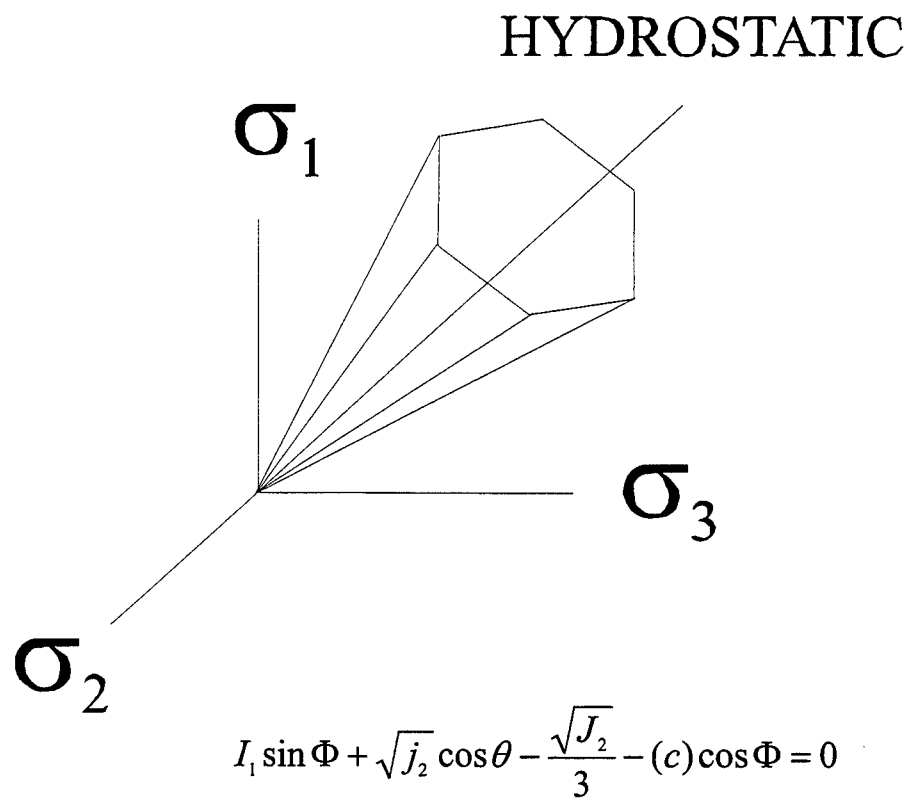
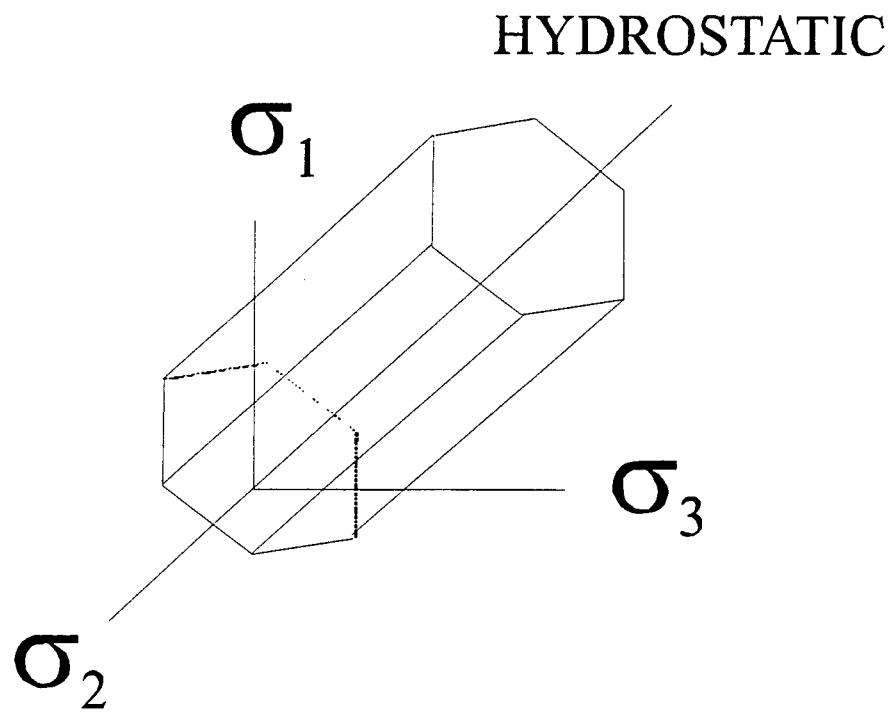


Figure 3.1. Coulomb yield function and surface



$$4J_2^3 - 27J_3^2 - 36k^2J_2^2 + 96k^4J_2 - 64k^6 = 0$$

Figure 3.2. Tresca yield function and surface

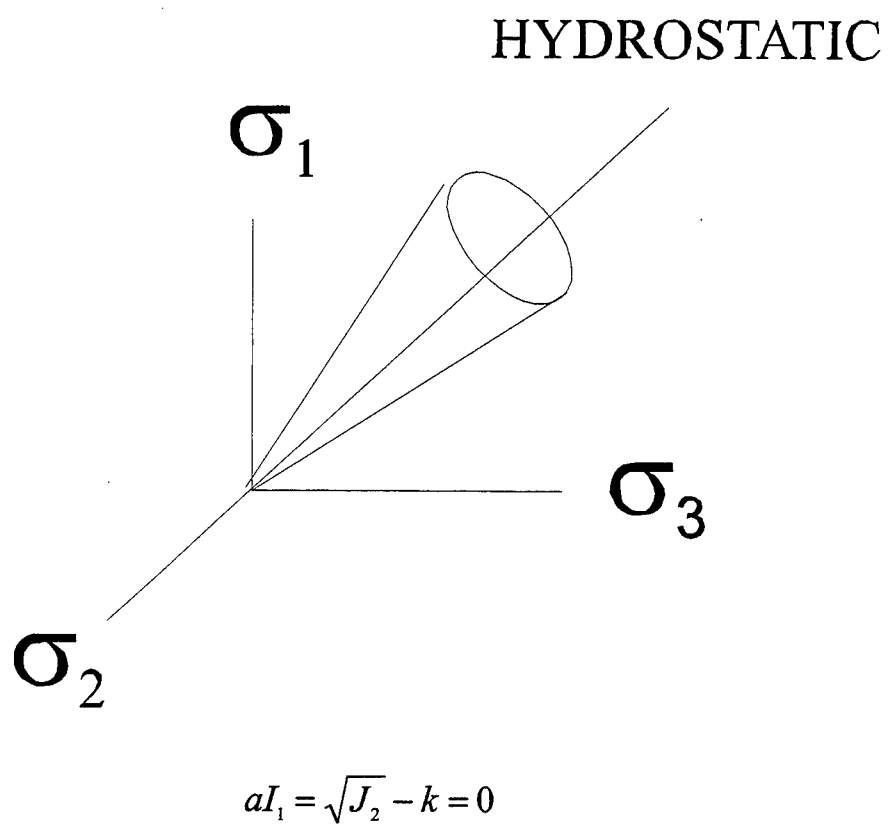


Figure 3.3. Drucker-Prager yield function and surface

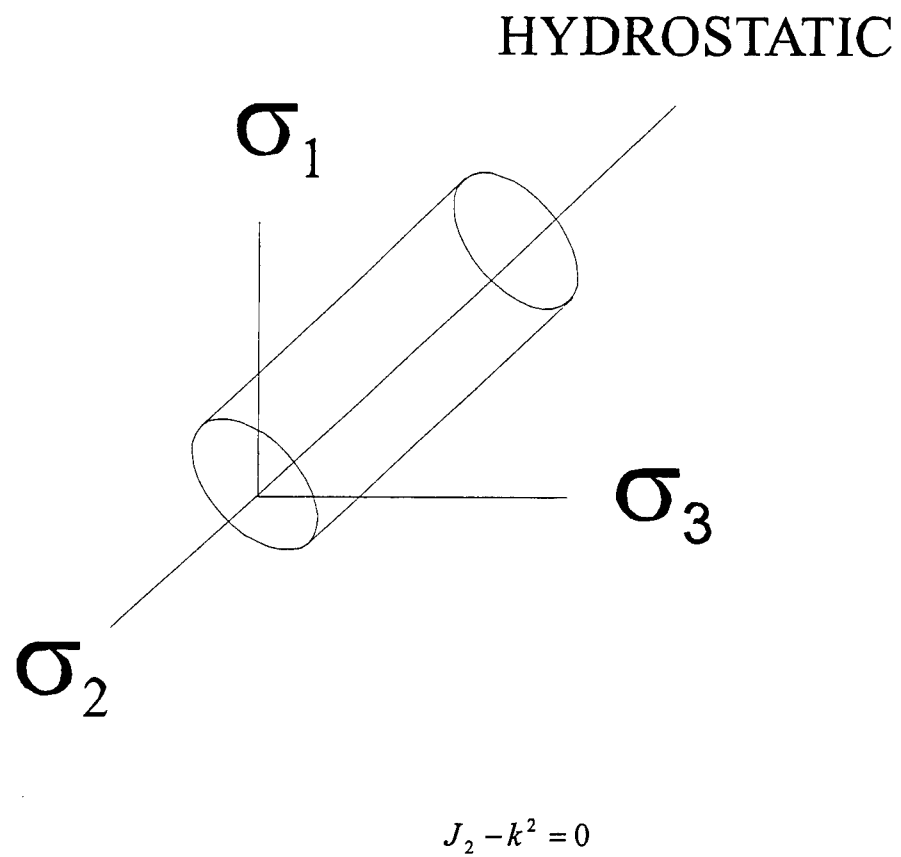


Figure 3.4. Von Mises yield function and surface

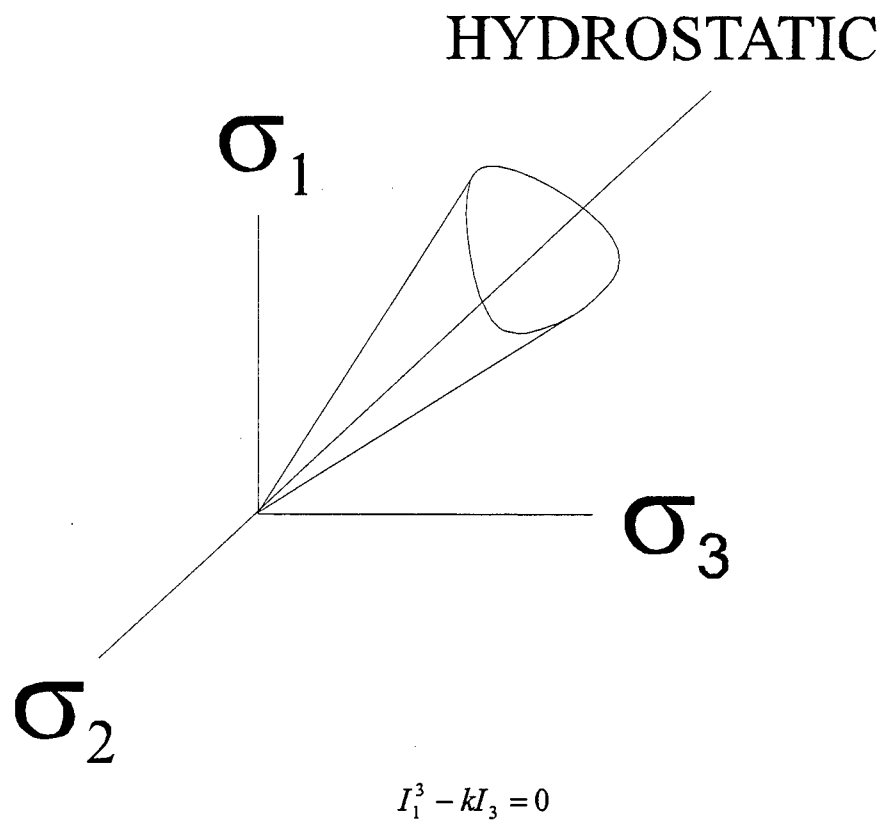


Figure 3.5. Lade Duncan yield function and surface

The Coulomb yield function shown in Figure 3.1 is a three dimensional generalization of the well-known Coulomb failure criterion from soil mechanics. This yield function reduces to the Tresca yield function for the case of frictionless materials, i.e.,  $\phi = 0$ . While both of these criteria are conceptually simple, they both have singularities at the corners of the hexagonal shapes, as illustrated in Figures 3.1 and 3.2.

These singularities are avoided, however, with use of the Drucker-Prager and Lade-Duncan yield functions, which are approximations that use a smooth function shown in Figures 3.3 and 3.5. In addition, the Von Mises yield function (Figure 3.4) is a smooth approximation of the Tresca yield function for saturated cohesive soils (frictionless soils). While both the Von Mises and Drucker-Prager smooth yield functions neglect the effect of the third stress invariant, the Lade-Duncan yield function includes this effect in the approximation of the Coulomb yield function. The only disadvantage to the Lade-Duncan approximation is that it requires multiaxial testing to determine the material coefficients; otherwise, it is excellent for general three-dimensional analyses.

### Flow Rules

Once a yield function is selected to differentiate between elastic and plastic behavior of granular materials analyzed using flow theory, a flow rule is needed to specify the incremental stress-strain relationships in the plastic region. The flow rule specifies the relationship between the incremental plastic strains and the current state of stress for yielded materials subjected to additional loading. The flow rule states that the direction of the plastic strain increment is normal to the plastic potential function at the current state of stress (Bonaquist, 1996). Equation 3.7 presents the general mathematical form for a plasticity flow rule.

$$d\varepsilon_{ij}^p = d\lambda \frac{\partial g}{\partial \sigma_{ij}} \quad (3.7)$$

where:

$d\epsilon_{ij}^p$  = plastic strain increment

$d\lambda$  = proportionality constant which is a function of stress

$g$  = plastic potential function

$\sigma_{ij}$  = current state of stress

If the plastic potential function is coincident with the yield function, the rule is said to be an associated flow rule. On the other hand, if the plastic potential function is different from the yield function, the rule is called a non-associated flow rule.

With only a yield function and flow rule, the behavior of elastic - perfectly plastic materials can be modeled. In a perfectly plastic material, continued loading results in an increase in strain with no increase in stress. Soils and granular materials, however, are known to exhibit strain hardening or strain softening with continued loading in the plastic region.

### **Hardening Rules**

Hardening rules have, therefore, been developed to model the strain hardening and strain softening behaviors of soils analyzed using flow theory. A hardening rule permits, and specifies, a movement of the yield function in stress space for various stress increments. An initial yield surface (function) is specified, and once the stress path reaches the yield surface subsequent stress increments can, and normally do, result in the generation of a new yield surface. If the yield surface is expanding, hardening behavior is said to be occurring, and if the yield surface contracts, strain softening is being exhibited. Stresses within the yield surface generate elastic responses, while stresses that intersect the yield surface result in a plastic response.

A variety of hardening rules has been developed to model the behavior of geotechnical materials. Most plasticity models use an isotropic hardening rule, which assumes that the yield surface either expands or contracts uniformly as plastic strains occur.



If a yield surface translates in stress space as a rigid body and retains its original size and shape, a kinematic hardening rule is applicable. Complex mixed hardening rules are possible which allow both translation and expansion or contraction of the yield surface as plastic strains occur. One of the better known applications of hardening rules is the cap model, shown schematically in Figure 1, which was developed specifically for geotechnical materials.

Cap models specify a failure envelope, above which plastic behavior occurs, and a strain-hardening cap. The failure envelope is typically based upon one of the yield functions presented earlier, such as the Drucker-Prager or the Lade-Duncan functions, while the strain hardening cap can be modeled with a variety of assumptions - an ellipsoid, a sphere, or a straight line. With this type model, elastic behavior is expected when the stress path is within the “yield surfaces,” plastic behavior occurs when the stress path intersects the failure envelope, and strain hardening occurs when the stress path intersects the cap. Bonaquist (1996) considered some of the attributes of several cap models, which use isotropic hardening rules as shown in Table 3.2.

The Hierarchical Single Surface (HiSS) model by Desai, et al. (1986) was investigated in depth by Bonaquist. The HiSS model is not a true cap model since it approximates a cap model using a single continuous function to provide yield surfaces similar to the cap models. This model represents a significant simplification of the cap models because the single continuous function that includes both the yield and ultimate failure surfaces eliminates singularities and the numerical difficulties associated with the two functions used in conventional cap models. This model has since been extended to include strain softening. Bonaquist concluded that the HiSS model should be pursued as a constitutive model for granular pavement materials. The HiSS model was calibrated for a base course material and verified with a stand-alone driver code. It was not implemented in a finite element code at that time.

Table 3.2. Cap Models with Isotropic Hardening Rules

Model	Yield Surface	Flow Rule	Hardening Rule	Elastic Response
Drucker et al., 1957	Drucker-Prager with spherical cap	Associated	Isotropic hardening of both cone and cap	Linear
Di Maggio and Sandler, 1971	Modified Drucker-Prager with elliptical cap	Associated	Isotropic hardening and softening of cap	Linear
Sandler, et al., 1976	Modified Drucker-Prager with elliptical cap	Associated	Isotropic hardening of cap	General, incremental nonlinear
Lade, 1975	Modified Lade-Duncan with spherical cap	Two component: non-associated cone, associated cap	Isotropic hardening and softening of cone and cap	Duncan and Chang (1970) incremental nonlinear
Baladi and Rohani, 1979	Drucker-Prager with elliptical cap	Associated	Isotropic hardening of cap	General, incremental nonlinear
(HiSS) Desai et al., 1986	Similar to Lade-Duncan with curved cap	Associated or non-associated	Isotropic or anisotropic hardening of cap and cone	General, incremental nonlinear

Isotropic hardening rules, such as those employed in the plasticity models based upon flow theory above were originally developed for monotonic loading conditions. Under cyclic loading conditions these models are inadequate. While they extend the yield surfaces during elastic-plastic behavior, they behave elastically during unloading and reloading, as long as the stress path remains within the yield surface. As a consequence, cyclic loading at the same stress state result in no additional permanent deformations. To account for the hysteresis and incremental permanent deformations that occur during cyclic loading, several cyclic load hardening rules have been developed as modifications to isotropic hardening models (Desai et

al., 1986). These models typically consist of a series of nested yield surfaces, which translate during loading, sequentially intercepting and providing different yield functions, depending upon the stress path and the state of stress. If the translating yield surfaces are allowed to expand and contract, depending upon the state of stress, complex anisotropic hardening models can be generated which are capable of modeling a wide range of cyclic behavior and hysteresis in soils.

Constitutive models based upon the flow theory of plasticity provide theoretically rigorous solutions and numerical stability is guaranteed for many conditions. These models account for shear dilation and the model parameters, which can be determined from conventional laboratory triaxial tests, have physical significance. The primary disadvantage to flow theory models is that the numerical analyses, even though stable, are relatively complex due to the nature of the yield functions in stress space (Salami, 1994).

On the other end of the spectrum from the variable modulus models, and the flow plasticity models are the theoretically rigorous formulations for plasticity based upon endochronic theory. Endochronic theory uses incremental constitutive equations and extends the elastic stress strain relationships into the plastic range. In fact, inelastic behavior is assumed to occur from the onset of loading. The constitutive relationships divide the material responses into deviatoric and volumetric components. The plastic responses are subsequently characterized by scalar variables (intrinsic time) which are measures of the rearrangement of grain configurations during plastic deformation, and either strain hardening or strain softening of the material. For rate independent materials, the scalar variables (sometimes referred to as internal variables) are functions of the strain history and related to the length of the plastic strain path.

Using endochronic theory Valanis (1971) and Valanis and Read (1987) developed constitutive laws for the inelastic behavior of concrete sand, and clay. The strain hardening

and strain softening functions within these constitutive models are determined by curve fitting experimental data using functional forms, which represent the effects of structural changes within a material. Typically, extensive laboratory testing is required in the fitting of model parameters.

A wide range of material behavior, including cyclic loading, can be modeled through the appropriate selection of elastic constants and strain hardening/softening functions (Bonaquist, 1996). These strain hardening/softening functions can become quite complex when a large range of material behavior is modeled.

The complexity of formulation and extensive laboratory testing required for plasticity models has been a traditional source of reluctance on the part of pavement designers to use these models in pavement analysis and design procedures. Most pavement design and construction agencies are limited to traditional geotechnical and materials testing capabilities (Ulidtz, 1998).

## **RECENT DEVELOPMENTS**

Recent studies have explored the applicability of a simpler class of constitutive models for soils based on micromechanics. These models are constructed by superposing or integrating the response of smaller units, either micromechanical or simply mechanisms of yielding in particular stress sub-spaces. Often, concepts of plasticity are stated at the level of the postulated micromechanism in order to characterize its kinetics. The numerical implementation of such models is rather delicate (Peters, 1983)(Peters, 1997) (Horner, 1997) (Prevost and Popescu, 1996).

More truly micromechanically- based models have also been proposed. In these models, soil is viewed as an assemblage of particles, and the unit micro-mechanism response is defined at the truly micromechanical level of contact forces with rolling and sliding

kinematics among the particles, and given macroscopic counter parts by proper definitions and averaging procedures (Ulidtz, 1998) (Prevost and Popescu, 1996).

Recent studies at WES have identified a relatively simple constitutive model formulation for soils that is a non-linear elastic-plastic formulation for a continuum based on response laws that come from micromechanics. The model recently developed at WES (Peters, 1983, 1997, 1998) has been used successfully in vehicle mobility and earthquake analysis efforts and shows great promise for implementation and application to the pavements problem

The elastic-plastic model produces the essential features of soil behavior under complex loading histories without the difficult analytical and numerical procedures required for calibration and implementation of existing models with similar capabilities. The central concept is a multi-mechanical model that produces the behavior of an internal variable model; particularly those derived from endochronic plasticity theory. As for an endochronic model, the material is idealized by mechanisms acting in parallel. The simplicity comes from making each mechanism an elastic-perfectly-plastic element that approximates the response of an endochronic element (Valanis, 1971). The coupling among the elements is mathematically simpler than for the endochronic model, a feature designed to simplify both calibration and numerical integration. The details captured best by the model are initial stiffness, yield/failure stress, shear-induced volume changes, and hysteresis produced by cyclic loading.

## **SUMMARY OF LITERATURE REVIEW**

This review of potential constitutive models for granular materials in pavements has considered a number of different model formulations. This is not intended to be a comprehensive presentation of constitutive models for soils but a review of those models that have received attention for the pavements industry to date. The elastic models evaluated consisted of Cauchy elastic, hyperelastic, and hypoelastic models. Within the Cauchy elastic

models, the bulk stress and universal models were considered in detail. These two models are nonlinear extensions of the generalized form of Hooke's law, which use the secant moduli, determined from the stress or strain invariants. The hyperelastic models considered are total stress models, which satisfy the first law of thermodynamics, and do not generate energy along certain cyclic stress paths. The hypoelastic models likewise satisfy the first law of thermodynamics, but address the fact that in granular materials the stress-strain behavior is path dependent, and the response is not necessarily reversible.

The plastic models considered in this review addressed formulations based upon plasticity theory, endochronic theory, micromechanical theory, and the WES Multimechanical elastic-plastic model. A flow diagram summarizing the evolution of these plastic models is shown in Figure 3. 6. Models based upon the deformation theory of plasticity represent extensions of incremental, nonlinear elastic models, and extend such models to cover both loading and unloading behavior. The models based upon endochronic theory use no loading criteria, or yield surfaces, and elastic-plastic response is assumed from the beginning of loading. With these models, a scalar internal variable called intrinsic time is used to account for loading history and the stress path. Finally, models based upon flow theory of plasticity were considered. These models extend the elastic stress-strain relationships into the plastic region with the use of a yield function which differentiates between elastic and elastic-plastic material behavior. The yield function defines a surface in stress space, inside of which elastic behavior occurs, and on and outside of which plastic responses can be expected. A flow rule is used to specify the incremental stress-strain relationships that occur in the plastic region, i.e., outside the yield surface. Strain hardening and strain softening behaviors are modeled by specifying hardening rules, which permit movement of the yield surface in stress space for various stress increments.

The use of elastic models for pavement systems has been generally restricted to nondestructive pavement testing and pavement thickness design to resist fatigue cracking and subgrade rutting, due to their inability to adequately model cyclic loading. On the other hand, plasticity models, with their ability to model cyclic loading and plastic deformations, are obviously beneficial in modeling rutting behavior and permanent deformations in pavement systems. However, each plasticity theory has certain advantages and disadvantages when it comes to implementation in pavement systems modeling.

Models based upon deformation theory of plasticity are direct extensions of the incremental forms of Hooke's law, and as a result are conceptually straightforward and computationally simple. In addition, the model parameters used in deformation models have physical and engineering significance. On the other hand, these models can not account for shear dilation and violate continuity conditions for neutral loading conditions.

Endochronic models use relatively straightforward constitutive relationships and use a scalar internal variable to govern inelastic responses and account for strain history. Unlike deformation theory models, endochronic models can model and account for shear dilation. The theory is relatively new, however, and currently only limited applications have been developed. When used, model parameters have physical/engineering significance, but fitting of model parameters requires extensive laboratory materials testing.

Models based upon flow theory of plasticity provide theoretically rigorous solutions, and numerical stability is guaranteed for certain conditions. These models can, also, account for shear dilation and their parameters have physical and engineering significance. Material behavior is divided into elastic and elastic-plastic responses by yield functions, which can be relatively complex shapes in stress space. Incremental, nonlinear elastic models are used inside the yield surfaces to define material behavior, while flow rules and hardening rules are used to define the response on and outside the yield surface.

To date plasticity models have not been used extensively in pavement applications. This fact is a result of several factors. First, their primary application would be in modeling rutting and permanent deformations in pavement systems, which typically result from cyclic or repeated load applications. The modeling of cyclic or repeated load applications using plasticity models is computationally intensive, requiring the dedication of significant computing resources. Next, typical values of model parameters for most common paving materials have not been established, and can not be derived from traditional empirical characterization tests used for soil and aggregate bases. In addition, the majority of geotechnical tests performed on soils and aggregates do not evaluate the effects of cyclic hardening or softening of the materials.

A constitutive model that can capture the essential behavior of pavement materials under service environments has many requirements including simplicity of calibration and operation, physical significance of the model parameters, and the ability to be readily incorporated into analysis codes. The WES Multimechanical model possesses all of these features and is yet untested in the pavement community, and its application to pavement system analysis will be the primary focus of this dissertation.



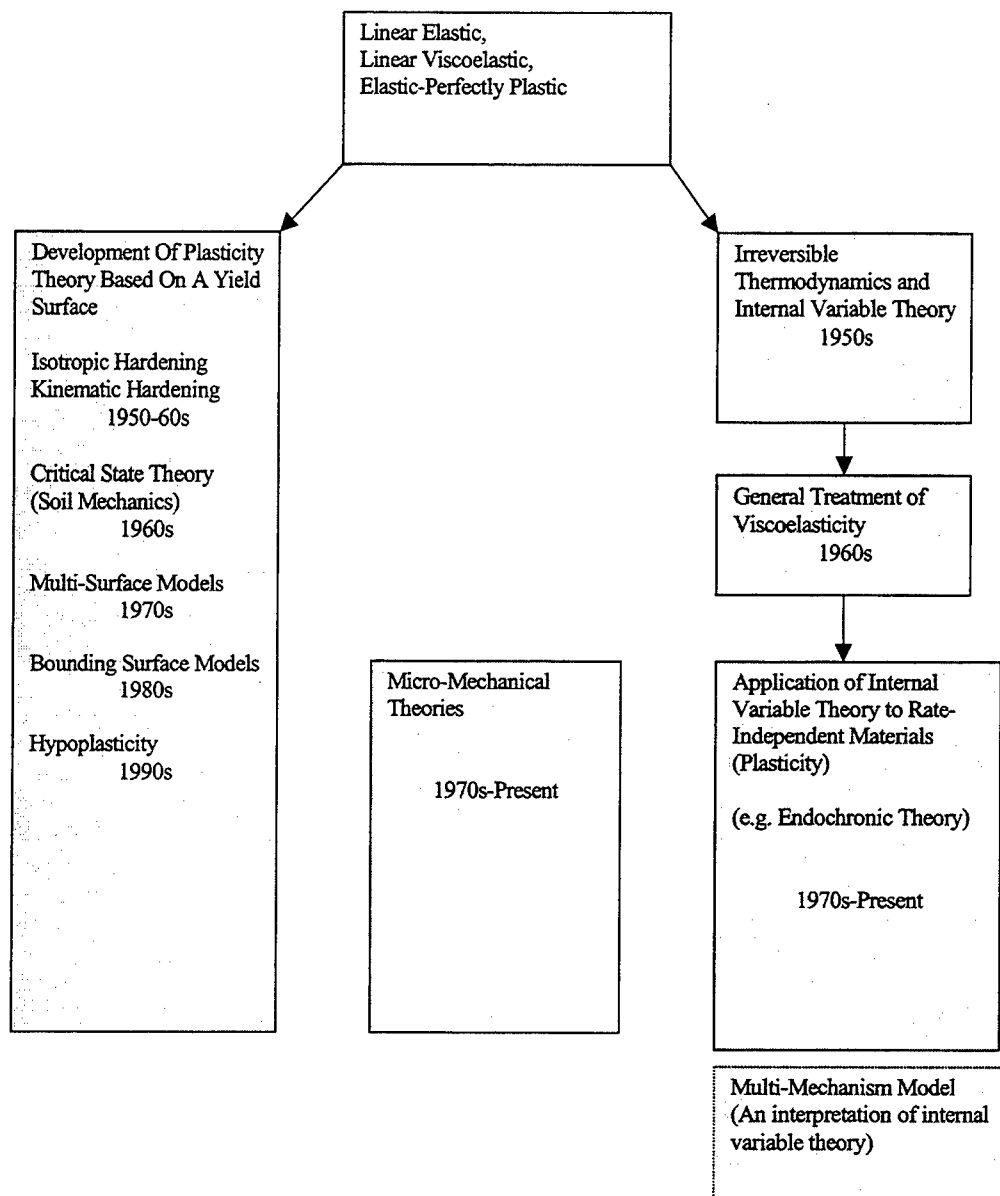


Figure 3.6. Flow diagram summarizing the evolution of plastic constitutive models for soils

## **CHAPTER 4: SELECTION AND IMPLEMENTATION OF MODEL**

### **CANDIDATE CONSTITUTIVE MODELS**

The essential features of pavement response that are required from any constitutive model include non-linear elastic response, permanent or plastic deformation after yield, cyclic loading, strain softening/hardening, and shear dilatancy. A pavement model should be simple in operation, implementation and calibration. The model must be executable within a proven general purpose Finite Element code. Of the general classes of constitutive theories studied (Linear Elastic, Non-Linear Elastic, and Plasticity), only those theories based on plasticity have the necessary features to perform adequately as a model for granular pavement materials. A summary of selected models discussed in Chapter 3 and their features is shown in Table 4.1.

The HiSS model by Desai was thoroughly investigated by Bonaquist in 1996 at the University of Maryland. Although, Bonaquist concluded that it shows promise as a potential model for granular pavement material, the HiSS model does not appear to have the simplicity of calibration and implementation desired for a pavement material model.

Many engineers in the pavement industry tasked with advanced analysis of pavement behavior will use a commercial general purpose FEM like ABAQUS as their typical analysis program since special purpose non-linear FEM programs for pavements are not readily available. The Modified Drucker-Prager (DP) is recommended by ABAQUS as the model for use in modeling granular material behavior. The DP model has been around in various forms for many years and was originally developed for soils with much lower strength than the base course materials under investigation here. It has the capability to capture ultimate failure/yield stress for a wide range of materials, however it does not have the sophistication required to adequately represent the complex multi-stage yielding seen in highly-compacted granular materials. Its usefulness for this effort is to demonstrate the inadequacies of classical constitutive models that one would find in an FEM code like ABAQUS.

The WES Multimechanical elastic-plastic model produces essential features of soil behavior without the difficult analytical and numerical procedures required for calibration and implementation of existing models with similar capabilities. The details captured best by the model are initial stiffness, yield/failure stress, shear-induced volume changes, and cyclic behavior. The WES Multimechanical model, which shows high potential in the area of granular pavement material modeling, its calibration requirements, and its application for constitutive modeling of granular pavement materials will be the primary focus of this research. A discussion of the ABAQUS Drucker-Prager Cap model and the WES Multimechanical model follows.

Table 4.1. Critical Features of Selected Models for Unbound Pavement Materials

Model	Critical Response Features					
	Linear Elastic	Non-Linear Elastic	Plastic	Shear Dilation	Cyclic Loading	Selected Reference
Linear Elasticity	x					Barker and Gonzalez, 1991
Bulk Stress (KThetaK)	x	x				Hicks and Monismith, 1971 Rada and Witczak, 1981
HiSS	x	x	x	x	x	Desai, 1986, Bonaquist, 1996
WES	x	x	x	x	x	Horner, 1997, Peters, 1998, Meade, 1997, 1998
Drucker-Prager	x		x	Limited		Baladi and Rohani, 1979, ABAQUS Theory Manual, 1998

## **DESCRIPTION OF ABAQUS**

ABAQUS is a general-purpose finite element program developed and marketed by Hibbitt, Karlsson, and Sorensen, Inc. of Pawtucket, Rhode Island. ABAQUS is written in transportable FORTRAN, although the input/output routines are optimized for specific computer systems. The source code for ABAQUS, not available to the user, contains about 300,000 executable statements.

One of the most important features of ABAQUS is its use of the library concept to create different models by combining different solution procedures, element types, and material models. The analysis module consists of an element library, a material library, a procedure library, and a loading library. Selections from each of these libraries can be mixed and matched in any reasonable way to create a finite element model.

The material library includes linear and nonlinear elasticity models as well as plasticity and viscoplasticity formulations. The analysis procedure library includes static stress analysis, steady state and transient dynamic analysis, and a number of other specialized procedures. In all of these analysis types, time is used as the index for incremental solution techniques. Time is a purely arbitrary index in the static procedures used in this study.

### **ABAQUS DRUCKER-PRAGER CAP MODEL**

The modified Drucker-Prager / Cap plasticity is intended to model cohesive geological materials that exhibit pressure-dependent yield, such as soils and rocks. It is based on the addition of a cap yield surface to the Drucker-Prager plasticity, which provides an inelastic hardening mechanism to account for plastic deformation and helps to control volume dilatancy under yielding. The ABAQUS DP model provides a reasonable response to large stress reversals in the cap region through an isotropic hardening rule; however, in the failure surface region the response is reasonable only for essentially monotonic loading (ABAQUS, 1998).

## Yield Surface

The addition of the cap yield surface to the Drucker-Prager model serves two main purposes: it bounds the yield surface in hydrostatic compression, thus providing an inelastic hardening mechanism to represent plastic compaction. The addition of the cap also helps to control volume dilatancy when the material yields in shear by providing softening as a function of the inelastic volume increase created as the material yields on the Drucker-Prager shear failure surface.

The yield surface has two principal segments: a pressure-dependent Drucker-Prager shear failure segment and a compression cap segment, as shown in Figure 4.1. The Drucker-Prager failure segment is a perfectly plastic yield surface (no hardening). Plastic flow on this segment produces inelastic volume increase (dilation) that causes the cap to soften. On the cap surface, plastic flow causes the material to compact.

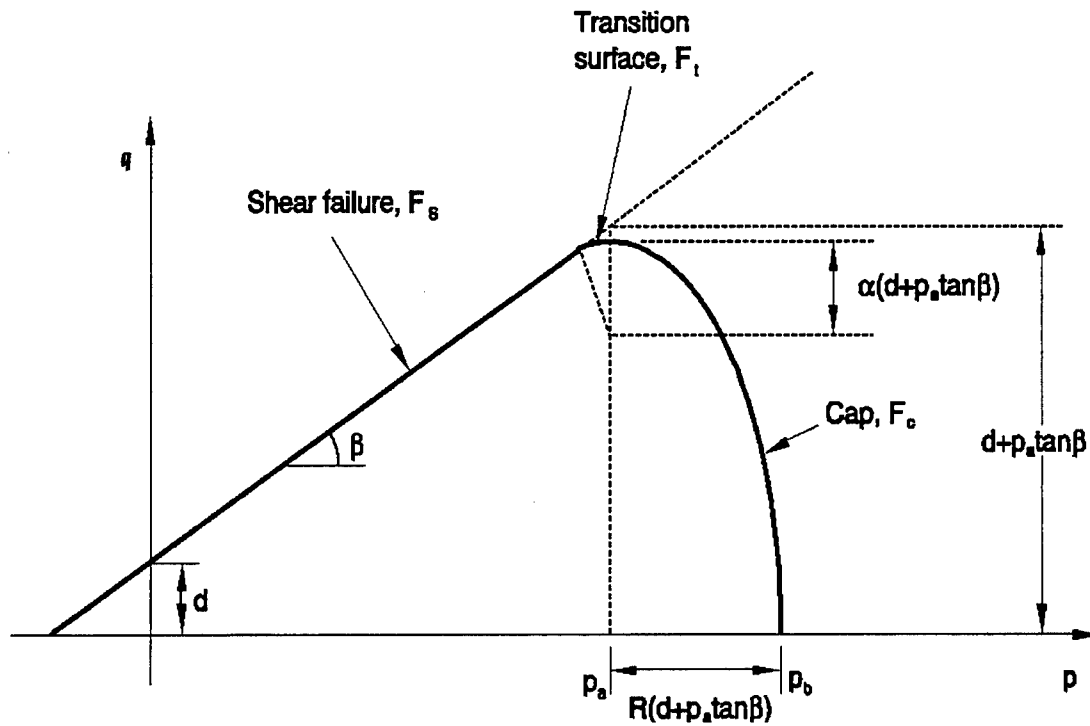


Figure 4.1. ABAQUS Drucker-Prager model yield surface

### Failure Surface

The ABAQUS Drucker-Prager failure surface is written in a  $q$  (principal stress difference,  $q = \sigma_1 - \sigma_3$ ) versus  $p$  (mean normal stress,  $p = (\sigma_1 + 2\sigma_3)/3$ ) space as:

$$F_s = q - p \tan \beta - d = 0 \quad (4.1)$$

Where,  $\sigma_1$  is the maximum principal stress,  $\sigma_3$  is the minimum principal stress,  $\beta$  represents the angle of friction in the  $q$ - $p$  plane, and  $d$  is the cohesion.

### Cap Yield Surface

The cap yield surface has an elliptical shape with constant eccentricity in  $q$ - $p$  plane and also includes dependence on the third stress invariant in the deviatoric plane. The cap surface hardens or softens as a function of the volumetric inelastic strain. The ABAQUS Drucker-Prager cap yield surface  $F_c$  and transition surface  $F_t$  is written as :

$$F_c = \sqrt{[p - p_a]^2 + \left[ \frac{Rq}{(1 + \alpha - \alpha / \cos \beta)} \right]^2} - R(d + p_a \tan \beta) = 0 \quad (4.2 a)$$

$$F_c = \sqrt{[p - p_a]^2 + \left[ t - \left( 1 - \frac{\alpha}{\cos \beta} \right) (d + p_a \tan \beta) \right]^2} - \alpha(d + p_a \tan \beta) = 0 \quad (4.2 b)$$

Where  $R$  is a parameter that controls the shape of the cap,  $\alpha$  is a cap transition factor, and  $p_a$  is an evolution parameter that represents the volumetric inelastic strain driven hardening/softening. The  $p_a$  parameter is a function of the plastic volumetric strain and volumetric yield stress  $p_b$ .

### Defining Yield and Hardening Parameters

The variables  $d$ ,  $\beta$ ,  $R$ , and  $\alpha$  are provided by the user to define the shape of the yield surface. The hardening curve specified for this model interprets yielding in the hydrostatic pressure sense: the hydrostatic pressure yield stress is defined as a tabular function of the

volumetric inelastic strain, and, if desired, a function of temperature and other predefined field variables. The range of values for which  $p_b$  is defined should be sufficient to include all values of effective pressure stress that the material will be subjected to during the analysis.

### **Plastic Flow**

Plastic flow is defined by a flow potential that is associated in the deviatoric plane, associated in the cap region in the meridional plane, and nonassociated in the failure surface and transition regions in the meridional plane. The flow potential surface is made up of an elliptical portion in the cap region that is identical to the cap yield surface, and another elliptical portion in the failure and transition regions that provides the nonassociated flow component in the model. The two elliptical portions form a continuous and smooth potential surface (ABAQUS, 1998).

### **Calibration**

At least three experiments are required to calibrate the simplest version of the DP model: a hydrostatic compression test and two triaxial compression tests (more than two tests are useful for a more accurate calibration). A more detailed discussion of the tests and procedures used for calibration is given in Chapter 5.

## **WES MULTIMECHANICAL CONSTITUTIVE MODEL**

### **Background**

The elastic-plastic model produces the essential features of soil behavior under complex loading histories without the difficult analytical and numerical procedures required for calibration and implementation of existing models with similar capabilities. The central concept is a multi-mechanical model that mimics the behavior of internal variable model, particularly those derived from endochronic plasticity theory. As for an endochronic model, the material is idealized by mechanisms acting in parallel. The WES model uses four mechanisms in its current form. The simplicity comes from making each mechanism an

elastic-perfectly-plastic element that approximates the response of an endochronic element. The coupling among the elements is mathematically simpler than for the endochronic model, a feature designed to simplify both calibration and numerical integration. The details captured best by the model are initial stiffness, yield/failure stress, shear-induced volume changes, and hysteresis produced by cyclic loading.

In order to accomplish the objectives of this research the WES model was implemented in two distinct forms. A PC-Compatible stand-alone version and an ABAQUS User Defined Material Model Subroutine, (UMAT). The stand-alone model, MVIEWER, was used to provide quick feedback during the iterative calibration process for the WES model. A discussion of the MVIEWER program is presented in Appendix G. The MVIEWER was compiled using a commercial PC compatible FORTRAN 77 compiler. Since this model had originally been developed for use on a PC it was relatively simple to take the model subroutines and add a constitutive driver program to produce outputs of stress and strain for a given stress or strain path. The UMAT was programmed in FORTRAN 77 according to the guidelines given by ABAQUS for development and implementation of a user-defined material model.

### **General Description**

The elastic-plastic-perfectly-plastic elements act in parallel by making the total strain common to all mechanisms as represented in Figure 4.2. Thus, each element is computationally independent and can be integrated using an efficient radial return procedure. The total stress is the sum of the component stresses. The shear and hydrostatic mechanisms are independent because they represent different deformation mechanisms. A coupling exists between shear and hydrostatic mechanisms in the form of a shear-dilatancy law. The coupling law imparts a plastic hydrostatic strain increment to the total volumetric strain that in proportion to the total plastic shear strain produced by the shear mechanisms. The volumetric proportionality constant depends on the shear stress to hydrostatic stress ratio in a manner



reminiscent of classical Critical State Soil Mechanics (CSSM) (Schofield, C. P., and Wroth, D. M., 1968). In contrast to the CSSM unidirectional dilatancy law, the present model senses the direction of shear loading and correctly predicts the magnitude and sign of plastic volumetric strain during unloading.

The stresses within the mechanism, and the void ratio of the soil describe the material state. The plastic strains are thermodynamic “forces” that retain the effects of the stress history of the material. The model uses three groups of parameters: stiffness parameters, strength parameters, and a shear-volume coupling parameters. (Meade, 1998) (Peters, 1998)

### Stiffness Parameters

The stiffness parameters are shear modulus for each shear mechanism and bulk modulus for each hydrostatic mechanism. The sum of the stiffness moduli defines the initial elastic stiffness of the material. By distributing the moduli among the mechanisms according to the mechanism’s yield strength, the shape of the stress-strain curve can be modeled.

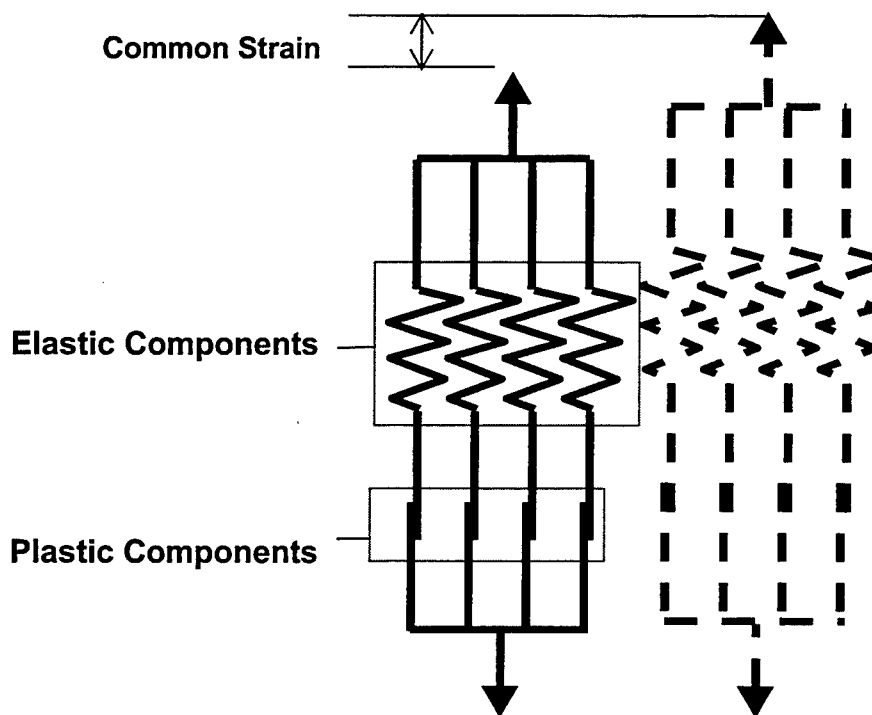


Figure 4.2. Idealized representation of WES Multimechanical model

## Yield Parameters

The strength parameters define the yield stress for each mechanism. Each mechanism acts as an elastic-plastic component whereby the response is elastic for all stress increments within the surface and plastic when the stress point lies on the surface. Stress increments that fall outside of the surface are scaled back to the surface.

A friction parameter and cohesion determine the limiting shear stress. The friction is introduced through a yield law of the form:

$$f(Q') = Y'(\phi) \quad (4.3)$$

where  $Q'$  is the total stress for mechanism  $r$  defined as:

$$Q' = Q'_s + \alpha^r (\sigma + a) \quad (4.4)$$

The shear component  $Q'_s$  is determined from the constitutive response of the mechanism.

The hydrostatic component,  $(\sigma + a)$  is distributed from the total hydrostatic stress and cohesion in proportion to the distribution factor  $\alpha^r$ . Thus the shear mechanism sees the hydrostatic stress as a parameter. The function  $f$  is chosen to represent a Mohr-Coulomb-like yield surface with  $Y'$  being the limit parameter for the mechanism that is scaled to the friction angle,  $\phi$ , of the material.

Yield of the hydrostatic mechanisms is scaled by a reference stress that depends on void ratio by the law:

$$Q'_h = H' P_e(e) \quad (4.5)$$

The scale factor  $H'$  determines the limit stress of hydrostatic mechanism,  $r$ . The reference stress,  $P_e(e)$ , lies on the virgin loading curve at the point corresponding to the prevailing void ratio,  $e$ . The effect of void ratio on shear response comes through the dependence of shear yield stress on the hydrostatic stress.

Materials possessing cohesion can withstand some tensile stresses. The tensile strength is accounted for by applying a reduction to the mean stress that is proportional to the

material cohesion. Each mechanism is allocated a portion of the tensile strength in proportion to the amount of volumetric stiffness that the mechanism contributes to the overall bulk stiffness of the material.

### **Shear-Volume Coupling**

The magnitude of the shear volume coupling is controlled by two parameters, the ratio,  $M_c$ , of shear to hydrostatic stress at which a specimen begins to dilate in a monotonic loading test and a parameter,  $\gamma$ , that scales the dilatancy rate as the stress ratio becomes greater. In the CCSM, only  $M_c$  is used because it is assumed by critical state theory  $\gamma=1$ . The hydrostatic strain “seen” by the hydrostatic mechanisms is distinct from that caused by coupling with the shear.

### **Details of Calculations**

The model computation is strain driven. Given the current internal state and strain increment, the model produces an updated stress state. The integration procedure is explicit. First the response for each shear mechanism is computed. This computation consists of (1) computing an elastic “trial” stress, (2) comparing the resulting elastic stress to the yield stress, and (3) if beyond yield, scaling back along a radial path to the yield surface. The elastic strain associated with the stress increment inside the yield surface is subtracted from the total strain increment. The plastic shear strain is computed as the difference between the elastic stress and total stress divided by the shear modulus.

Once the shear response is computed, the plastic shear strain is used to compute the volumetric strain that results from shear-volume coupling. The shear strain is the weighted sum of the shear strain for the individual mechanisms. The weighting factor for a mechanism is the ratio of its shear modulus to the total shear modulus. These factors add up to one. The dilatancy strain is removed from the total volumetric strain to produce a net hydrostatic strain that is used for the computation of the hydrostatic response.

The hydrostatic response is similar to that of the shear stress. A trial elastic stress is computed which is compared to the limit hydrostatic stress. If the stress exceeds the limit stress, it is scaled back to the limit value.

Finally, the shear stress is adjusted to account for a reduction in hydrostatic stress due to combined effects of dilatancy and hydrostatic strain. The adjustment is accomplished simply by setting the shear strain increment set to zero and using the shear computation described previously. Note that the computation for the shear strain treats the hydrostatic stress as a parameter. Thus this final step can be viewed as an adjustment to account for a change in a state dependant parameter.

The numerical procedure is efficient, without iteration, and is accurate. It does not become unstable near failure and its efficiency is virtually the same for both elastic and plastic conditions.

### **Coding Details**

The model has been implemented in the finite element program ABAQUS. The ABAQUS program permits the user to write a subroutine that contains a user-defined constitutive model or UMAT. The UMAT was written in FORTRAN 77 and consists of one main subroutine, five sub-task subroutines, and two functions. A separate subroutine, titled SDVINI, was written to initialize solution-dependent state variables, which include the full stress tensor and a void ratio. The FORTRAN source code is shown in Appendix A.

### **ABAQUS Features**

ABAQUS is a general-purpose finite element program licensed from Hibbitt, Karlsson & Sorenson, Inc. Version 5.8 of ABAQUS was used. The program permits the user to employ a constitutive model of one's choosing. The model calculations are contained in the UMAT. The UMAT author must conform to certain conventions to enable the UMAT to interface properly with the finite element solver. The user may specify material properties that

are entered on a command line in the input data set. The user may use solution-dependent state variables that may be updated within the UMAT.

The main program calling the UMAT provides stresses at the start of a loading step, total strains, and strain increments for the current step. The UMAT must determine the stress increment caused by the strain increment and update both the stress and solution-dependent state variables at end of the step. In addition, the UMAT must provide a stress gradient matrix, a Jacobian. The Jacobian is an estimate of the stiffness at the current material state, which uses the most recent stresses that were in equilibrium. A direct strain increment is applied to each direction X and Y, and a shear strain increment is applied to the X-Y plane. These strains are applied independently and the stress increment produced by each strain is calculated. The ratio of stress increment to the strain increment is used as an estimate of the Jacobian.

### **Material Properties**

Thirty material properties are required. Ten of these properties are global and the remaining twenty are associated with each of the four mechanisms. The global properties are listed in Table 4.2 and the mechanism-specific properties are listed in Table 4.3.

### **Associated Parameters – Global Parameters**

Two pairs of global parameters are associated. One pair is used to adjust the friction angle for the effects of mean stress. Then, a yield criterion is determined based on adjusted friction angle. The parameters are phi ratio (PHIRATIO) and an Over Consolidation factor (Decay). The expression used in the code for OC factor is the ratio of the reference stress,  $P_e$ , to the mean stress,  $\sigma_m$ .

The expression for the Yield limit is based on the formulation  $I_1^2 I_2 / I_3$ , where the “I” terms are the stress invariants. The stress tensor used in the calculation is given in vector form as STRESS (6). Stress 1 has the magnitude of  $(1 + \sin(\phi)) / (1 - \sin(\phi))$ . The shearing stresses

are zero (STRESS (4), STRESS (5), and STRESS (6)). The normal stresses are given as principal stresses. STRESS (2) and STRESS (3) are unity.

The other pair of associated parameters is used in the shear-volume coupling term. The volume change is proportional to the plastic strain. The volume change is the difference of two terms. The first term is the inner product of the shear stress and the total plastic strain and that quantity normalized by the mean stress. The second term is square root of inner product of the plastic strains. This quantity is a scalar that is the magnitude of the plastic strain. This term is multiplied by a dilatancy factor,  $M_c$ . In this model a scaling factor,  $\gamma$ , was introduced to reduce the effect of the shear volume coupling.  $\gamma$  is unity in traditional CSSM.

#### **Associated Parameters – Mechanism Parameters**

Each mechanism acts without consideration of the other mechanisms. That is, subroutine *Ammos* is called once per mechanism and performs its calculations without consideration of previous calls. However, selection of mechanism parameters does require some consideration of all of mechanisms acting as a unit of four. The stiffness, both shear and volumetric, must be distributed among the mechanisms such that the sum of each mechanism stiffness equals the global stiffness parameters.

#### **Flow Scheme**

The main UMAT initializes variables and calls Subroutine *Sand\_driver* seven times. The first call to *Sand\_driver* returns a solution for the stress and updated solution-dependent state variables (SDV's). The remaining calls return portions of the Jacobian. The main UMAT updates the Jacobian, stress, and SDV's.

#### **Solution Dependent Variables (SDV's)**

The constitutive model has internal variables whose purpose is similar to the internal variables of endochronic theory. The internal variables hold the stress state of each mechanism in terms of an internal force. Two types of internal forces are used.  $Q_s$  are the

shear forces, and  $Q_h$  are the hydrostatic forces. Each mechanism has six shear forces and one hydrostatic force associated with its strain history. A total of seven internal forces are needed for each mechanism. The four mechanisms require 28 internal forces to be carried through each step. The void ratio must be carried as well. Twenty-nine SDV's are used in all.

### **UMAT Main Subroutine**

The UMAT is called from the ABAQUS program, herein described as the main calling-program. The UMAT main program initializes stress to values sent from the ABAQUS main calling-program and assigns properties to values set in the UMAT control card. The internal variables (SDV's), total strain and strain increments enter the UMAT with the values passed by the main calling-program. A flow chart for the UMAT main program is shown in Figure 4.3.

Then, the UMAT main program calls subroutine Sand\_driver passing all of the stresses, strains, strain increments, and internal variables. Sand\_driver returns appropriate stress and internal variables that may have been clipped if the material yielded. The main subroutine pushes the new stresses and internal variables into the appropriate arrays and then prepares dummy strains to send to Sand\_driver for the purpose of determining the Jacobian. Sand\_driver is called again in a loop to create the data for the six Jacobian terms. Once the loop is complete, the main program returns the Jacobian, the updated stresses and updated internal variables to the ABAQUS main calling-program.

### **Subroutine Sand\_driver**

Sand\_driver is called from the UMAT main program. Sand\_driver is provided with strains, and internal variables, and stresses. Sand\_driver calculates plastic strain, volumetric strain, computes a normalizing stress from the NCL variable and the void ratio, and determines a hydrostatic parameter associated with the internal variables for hydrostatic stress. Also, the internal variables for each mechanism are updated. Flow charts for the Sand\_driver subroutine are shown in Figures 4.4 and 4.5. The yield limit is calculated for each

mechanism. The yield limit is a function of the frictional strength of each mechanism. Sand\_driver calls two other subroutines, Ammos and Hydros in order to perform these calculations. Sand\_driver returns to the UMAT main with updated stresses and internal variables.

Subroutine Sand\_driver is called again by a loop in the UMAT main to determine data for the tangent stiffness matrix or Jacobian. The UMAT main provides updated stress and internal variables and dummy strain to enable a partial derivative to be estimated for each term of the tangent stiffness matrix or Jacobian.

#### **Subroutine Ammos**

Ammos is used to set a yield limit and check the shearing stress produced by the incremental strains provided in the call from the Sand\_driver subroutine. Ammos is called from Sand\_driver one time for each of the four mechanisms. Ammos is sent incremental strains, internal variables and yield limit for the mechanism. Ammos checks for a mean tensile stress and sets the value of mean stress to a small compressive value if tension was detected. The shear strains are determined and the shear stress increment is determined assuming that the strain was elastic. The location of the yield surface is determined for the mechanism based on the values of the internal variables and compared to the yield limit. A clipping subroutine RadialReturn is called if the shear stress point is located beyond the yield limit. If clipping was required due to yielding, Ammos updates the plastic strain for each mechanism and the total plastic strain. Ammos records the plastic strain as zero if no clipping was necessary. Ammos updates and returns the values of shear stress and shear internal variables to Sand\_driver. A flow chart for the Ammos subroutine is shown in Figure 4.6.

#### **Subroutine Hydros**

Hydros is called by Sand\_driver and used to update the hydrostatic internal variables and clip the hydrostatic internal variables if either the compression limit or the tensile limit were exceeded. Since the hydrostatic stress can be described as a scalar quantity, this



subroutine is much simpler than AMMOS. Hydros returns the updated hydrostatic internal variables (hydrostatic stresses) to Sand\_driver.

### **Subroutine RadialReturn**

RadialReturn is a clipping subroutine called by Ammos. The subroutine performs radial return of stress point to yield function (Matsuoka and Nakai, 1977), given by:

$$F_y(Q) = I_1 * I_2 / I_3 \quad (4.5)$$

where,  $I_1$ ,  $I_2$ , and  $I_3$  are the stress invariants. A transformation is first performed to principal stress space, then the return is performed such that  $I_1$  and  $(Pv_2 - Pv_3)/(Pv_1 - Pv_3)$  are held constant.  $Pv_1$ ,  $Pv_2$ , and  $Pv_3$  are the principal stress values. With these constraints,  $F_y = Y_{limit}$  becomes a cubic equation. The stress tensor is computed from the eigenvectors and adjusted eigenvalues. Therefore, the adjusted stress tensor has the same principal axes, mean stress, and Lode parameter as the original stress tensor.

### **Summary of Calling Schedule**

For each time the UMAT is called. Subroutine Sand\_driver is called seven times, once for the stresses and internal variables and six times for the Jacobian or tangent stiffness matrix required by ABAQUS. Subroutine Ammos is called eight times per call to Subroutine Sand\_driver. Subroutine Hydros is called four times per call to Sand\_driver. Subroutine RadialReturn could be called a maximum of one time per call to Ammos. Subroutine RadialReturn is called only when plastic strain has occurred. Table 4.4 shows the range of potential numbers of calls to each subroutine per iteration of each load increment of each step in an ABAQUS analysis (Meade, 1998).

### **Model Operation**

In order to demonstrate the operational characteristics of the WES Multimechanical constitutive model (WES MM) the following discussion of a cyclic stress strain curve is presented. An idealized representation of the WES MM model is shown in Figure 4.6. The

major points emphasized are that the model has four mechanisms with elastic-plastic behavior. The strain experienced under load application is common to all elements, and the stiffness and yield of each element are different. Figure 4.7 shows the stress strain curve for a cyclic test with the crucial stages of the test numbered as Points 1-11.

The stress path from which the above stress-strain curve is derived is presented in Figures 4.8 through 4.18. A separate figure for each of the critical points shown in Figure 4.7 is used to describe the various stages of yielding and stress reversals. In many plasticity models, a hardening law is employed to describe the change in yield strength that accompanies the occurrence of plastic strain. From the discussion presented in Chapter 3 it is evident that these hardening rules can become very complex and difficult to implement. The WES MM model employs 4 predefined yield surfaces to capture the hardening that occurs in a material loaded beyond an initial yield stress.

At point 1 the first mechanism has yielded and begun experiencing plastic deformation. Figure 4.8 shows the stress path of each of the four mechanisms at Point 1 in a principal stress difference versus mean normal stress space ( $q$  versus  $p$ ). The stress path of each of the mechanisms is shown in a separate plot labeled M1 through M4. The yield surfaces for the mechanisms are shown as the thin lines emanating from the origin of each  $q$ - $p$  axis. The actual stress path of the elements is shown as the dark lines moving off the horizontal axis at some distance  $p$  from the origin. The stress difference or shear stress in a yielded mechanism increases after yield only as a function of the increase of normal stress,  $p$ .

At Point 2 Mechanism 2 has yielded and begun accumulating plastic strain along with Mechanism 1. The stress path at Point 2 is shown in Figure 4.9. Mechanisms 3 and 4 continue to respond elastically until Mechanism 3 yields at Point 3 (Figure 4.10).

At Point 4 (Figure 4.11) the stress is reversed and unloading begins. During the initial stage of unloading, all mechanisms are undergoing elastic strain. As the mechanisms reach yield in extension (Figures 4.12 and 4.13), the stress-strain curve breaks over to change slope

just as it does in loading. The mean stress is higher at each of the breaks points in this unload-reload cycle and therefore the shear stress at yield is higher.

Figure 4.15 depicts the stress path at the time of yielding in Mechanism 1 under reloading. In Figure 4.7 this occurs at Point 8 with a higher yield stress than that seen in the initial loading curve. The same type of behavior is seen in Mechanism 2 at Point 9 as shown in Figure 4.16.

At Point 9 in Figure 4.7, the third mechanism yields in reload as shown in Figure 4.17. Again this occurs at a higher mean and shear stress than the initial loading. The resulting hysteresis loops formed from Points 4-10 produce permanent deformation under cyclic loading conditions. Figure 4.18 shows the continued loading resulting in plastic strains for all but Mechanism 4, which remains elastic. This ratcheting effect produces a strain that increases with load repetitions.

Table 4.2. Global Properties

Name	Label in code	Comments
Phi	PHILIMIT	friction angle
Cohesion	C	cohesion
Bulk Modulus	K	
Shear Modulus	G	
phi ratio	PHIRATIO	
Hydrostatic Intercept	Fh	Intercept of Normal Consolidation Line (NCL)
Reciprocal of Cc	BETA	Reciprocal of the slope of NCL
Shear-volume factor	Mc	shear-volume coupling term
OC factor	Decay	strength reduction term
dilatancy scaling factor	GAMMA	

Table 4.3. Mechanism Properties

Name	Label in code	Comments
Strength factor	PHIFRAC	scales friction angle
Mean Stress factor	PFACT	scales mean stress
Shear Stiffness factor	SHEARRATIO	distributes shear stiffness
Compression limit	HLIMIT	absolute compression limit
Volumetric Stiffness factor	BULKRATIO	distributes volumetric stiffness

Table 4.4. Frequency of Calls

Subroutine	Relative # of calls	Total # of calls per Step
Sand_driver	7 per call to UMAT	7
Ammos	8 per call to Sand_driver	56
RadialReturn	0 or 1 per call to Ammos	0 to 56
Hydros	4 per call to Sand_driver	28

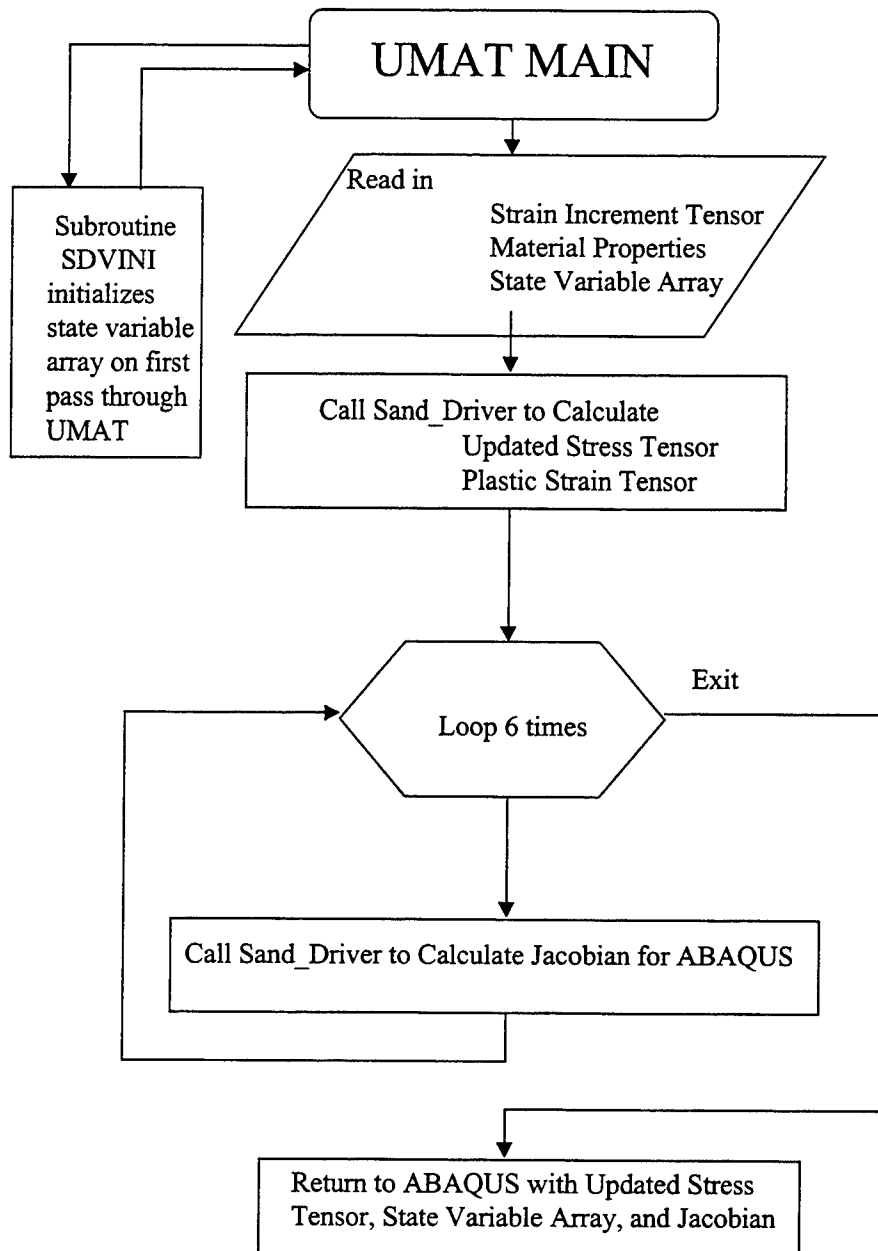


Figure 4.3. Flow chart for WES MM ABAQUS UMAT

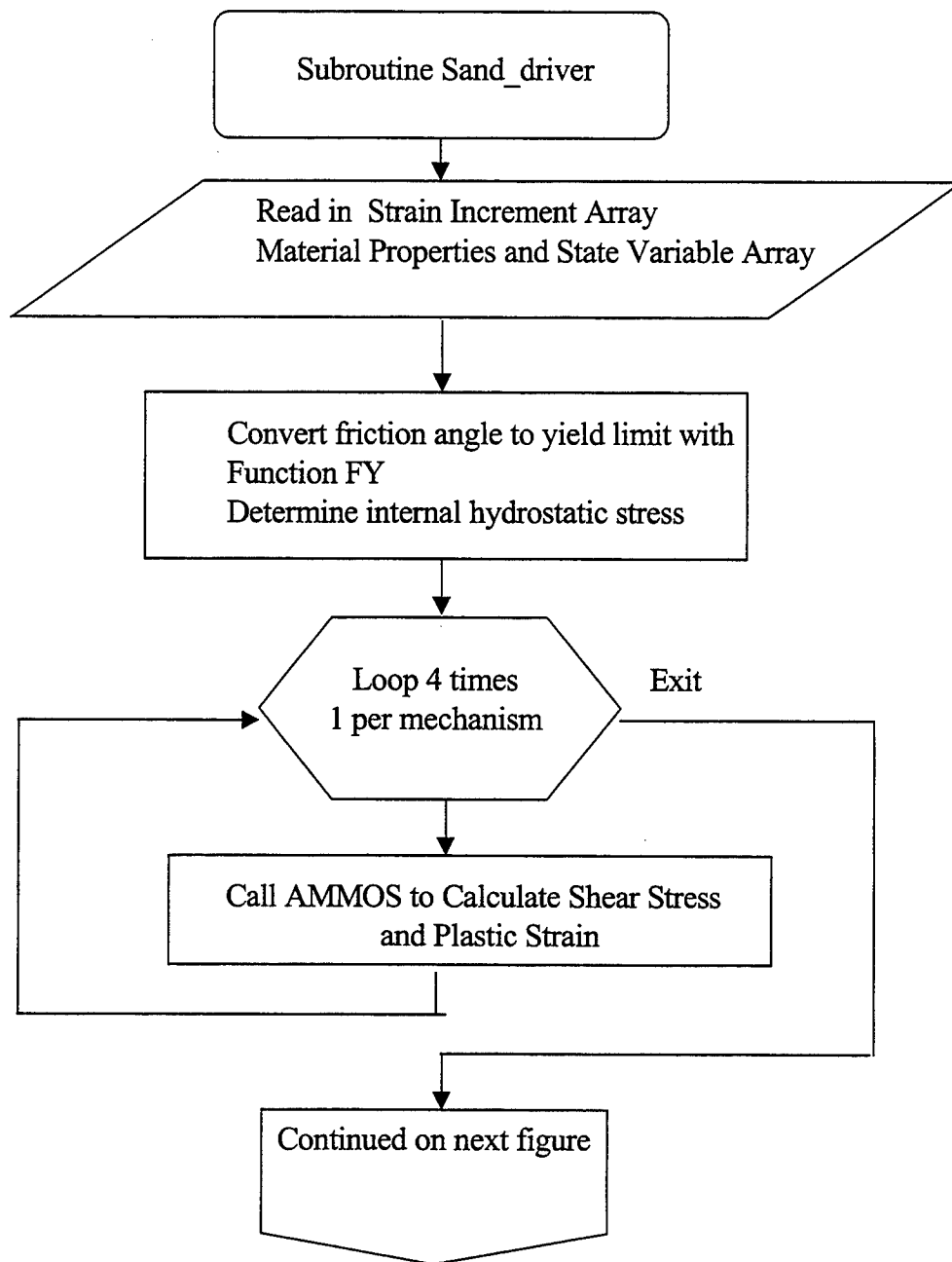


Figure 4.4. Flow chart for Subroutine Sand\_driver (Part 1)

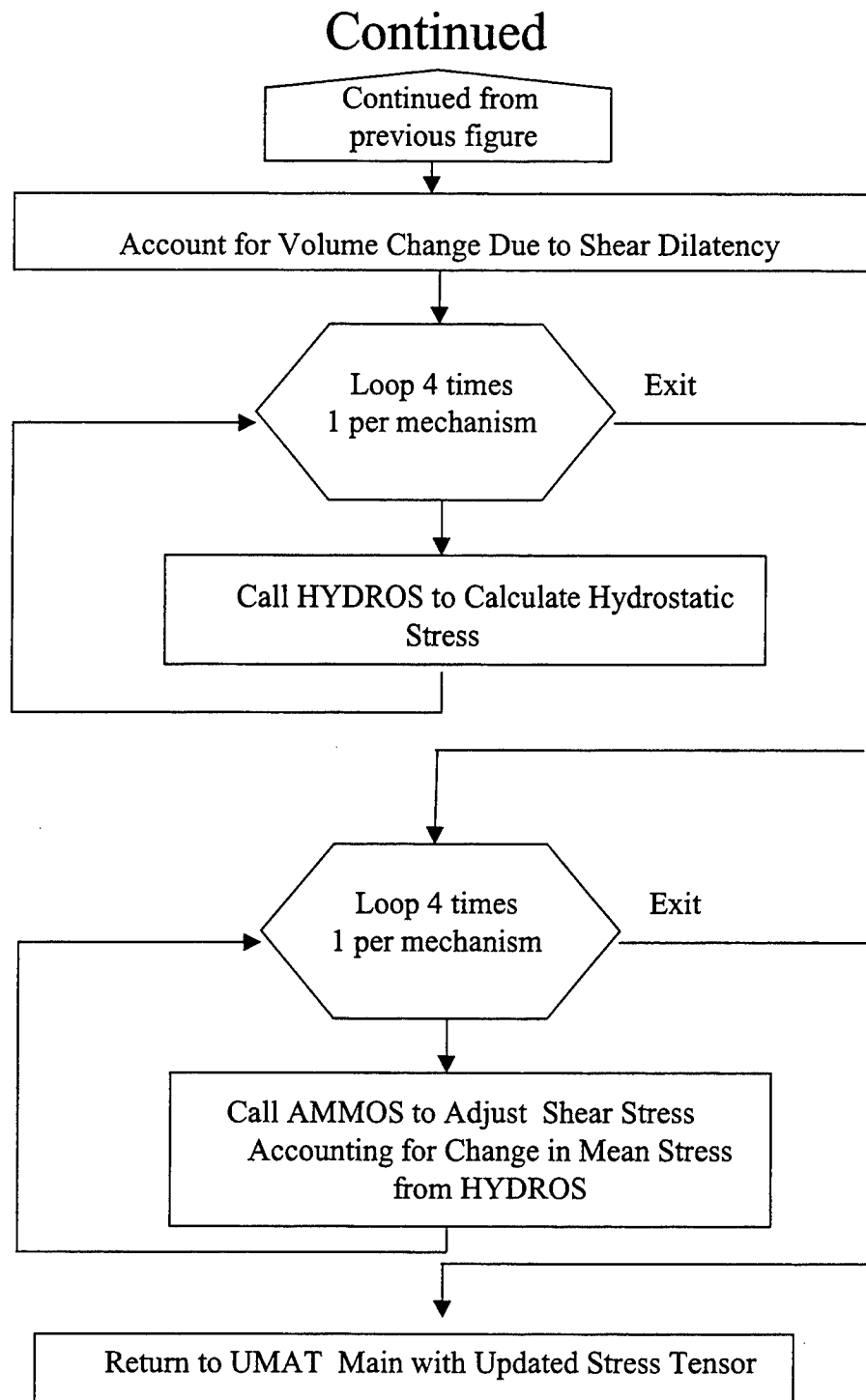


Figure 4.5. Flow chart for Subroutine Sand\_driver (Part 2)

## AMMOS Subroutine

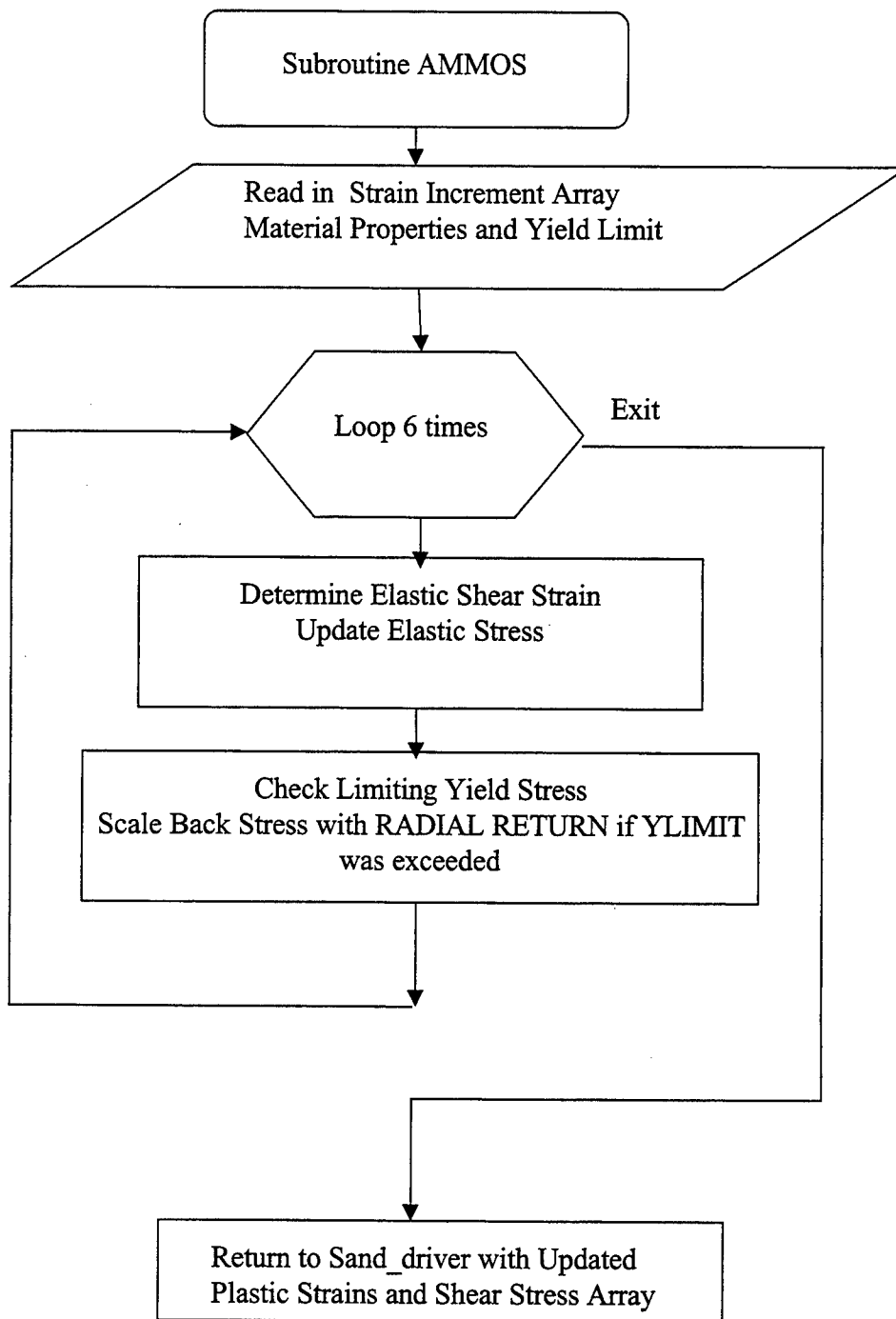


Figure 4.6. Flow chart for Subroutine Ammos



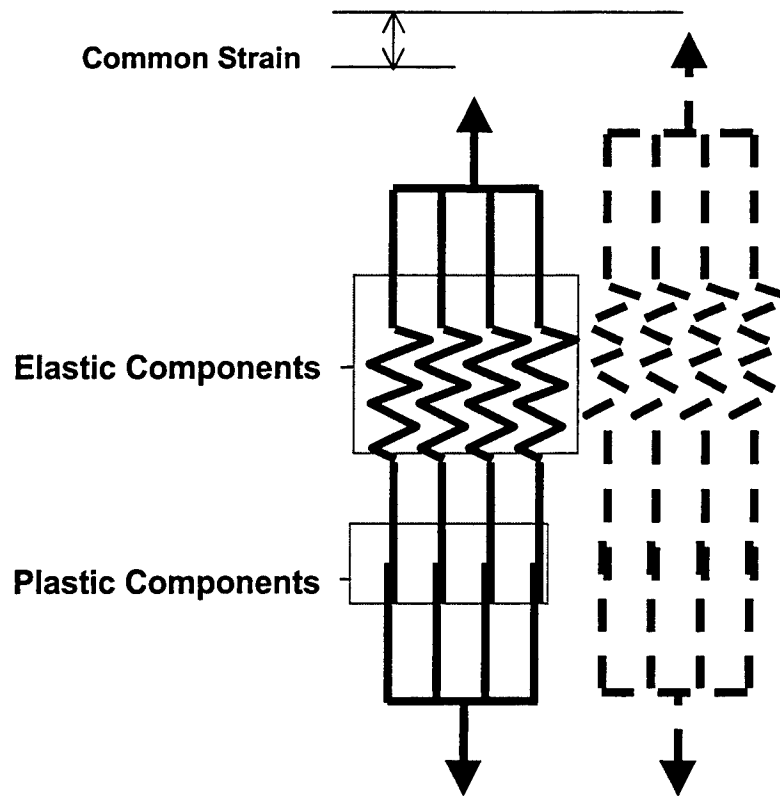


Figure 4.7. Idealized representation of the WES MM model

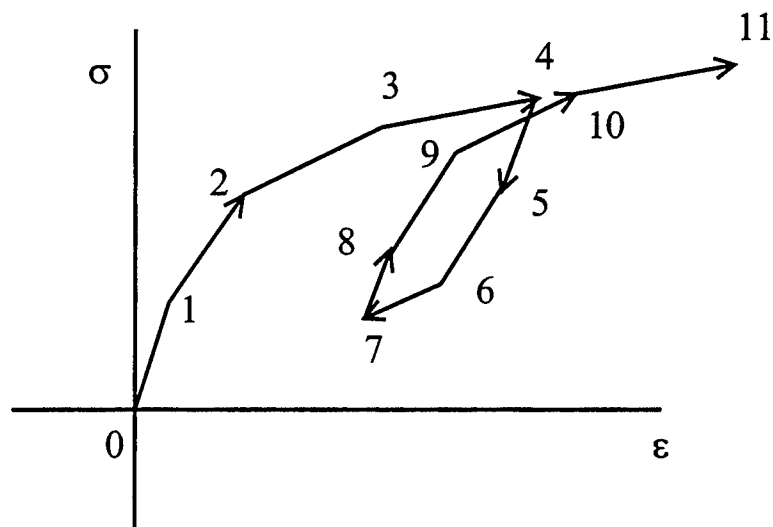


Figure 4.8. Stress versus strain for a cyclic test

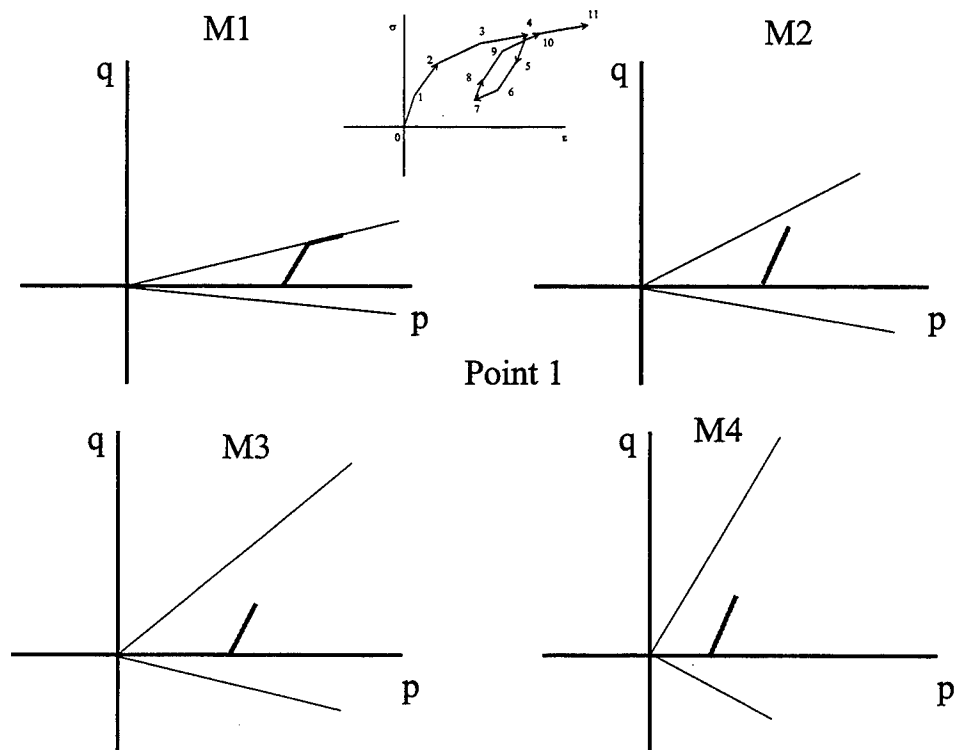


Figure 4.9. WES MM stress path at Point 1(initial yield of Mechanism 1)

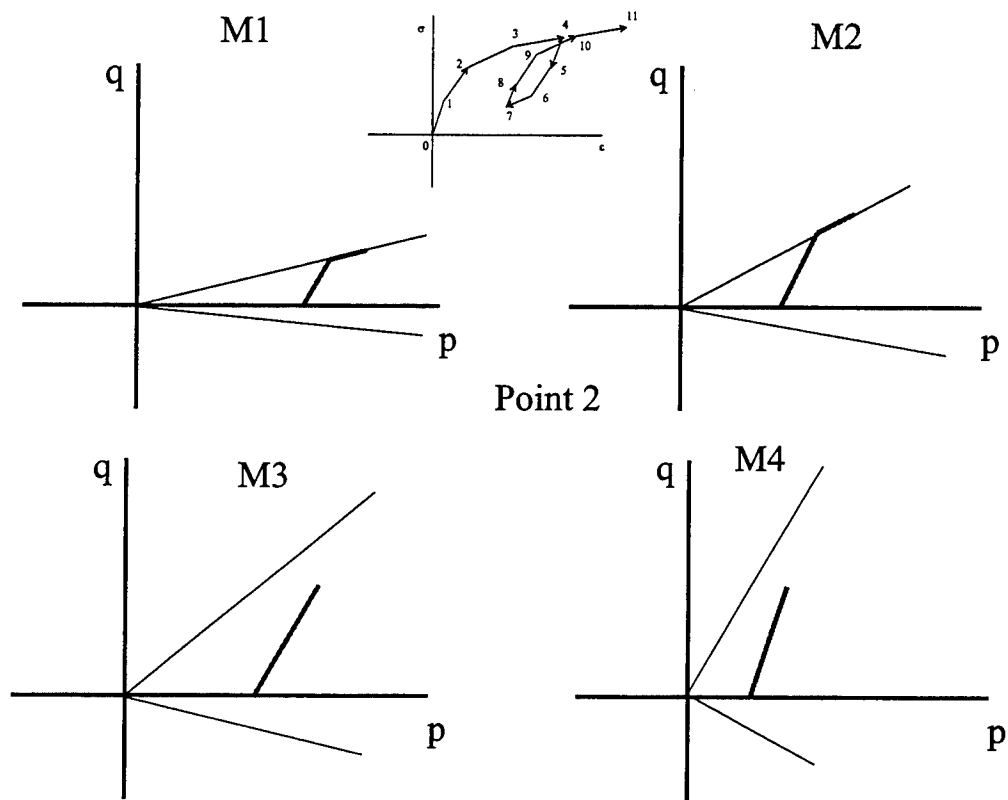


Figure 4.10. WES MM stress path at Point 2 (initial yield of Mechanism 2)

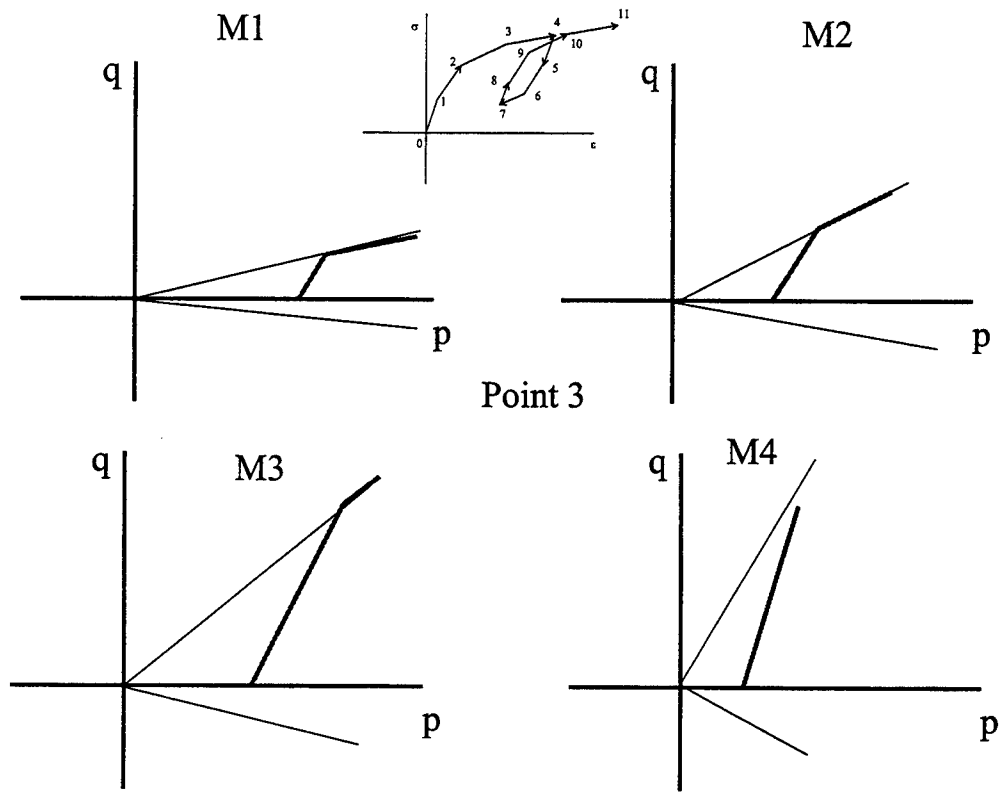


Figure 4.11. WES MM stress path at Point 3 (initial yield of Mechanism 3)

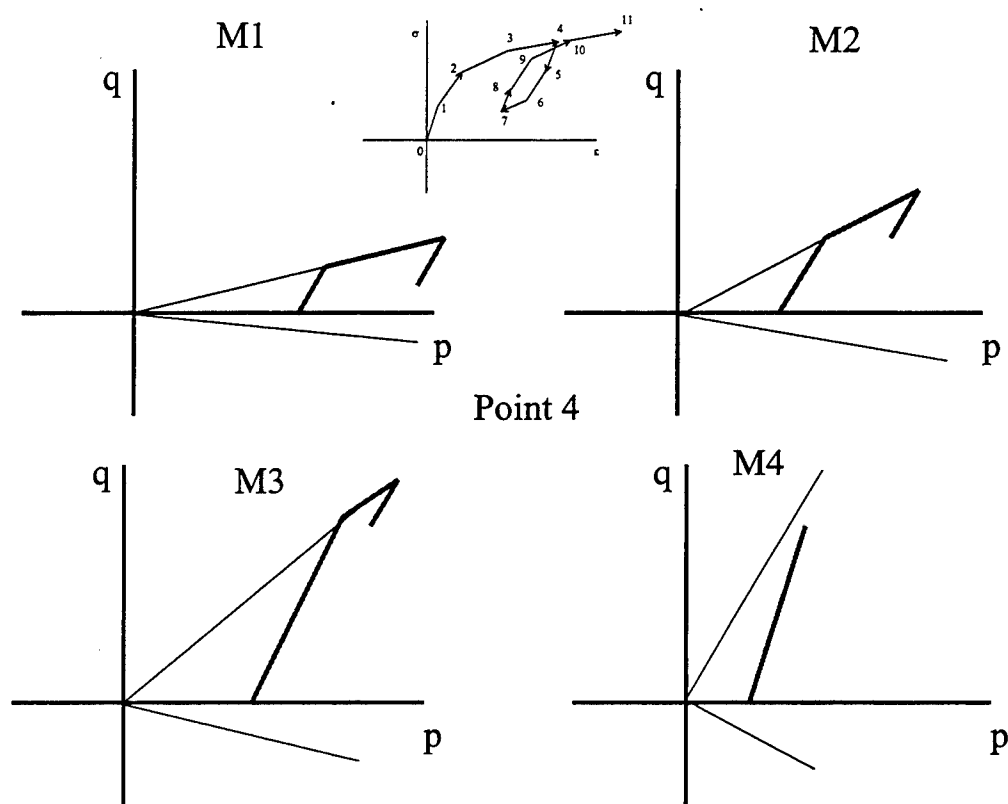


Figure 4.12. WES MM stress path at Point 4 (unload)

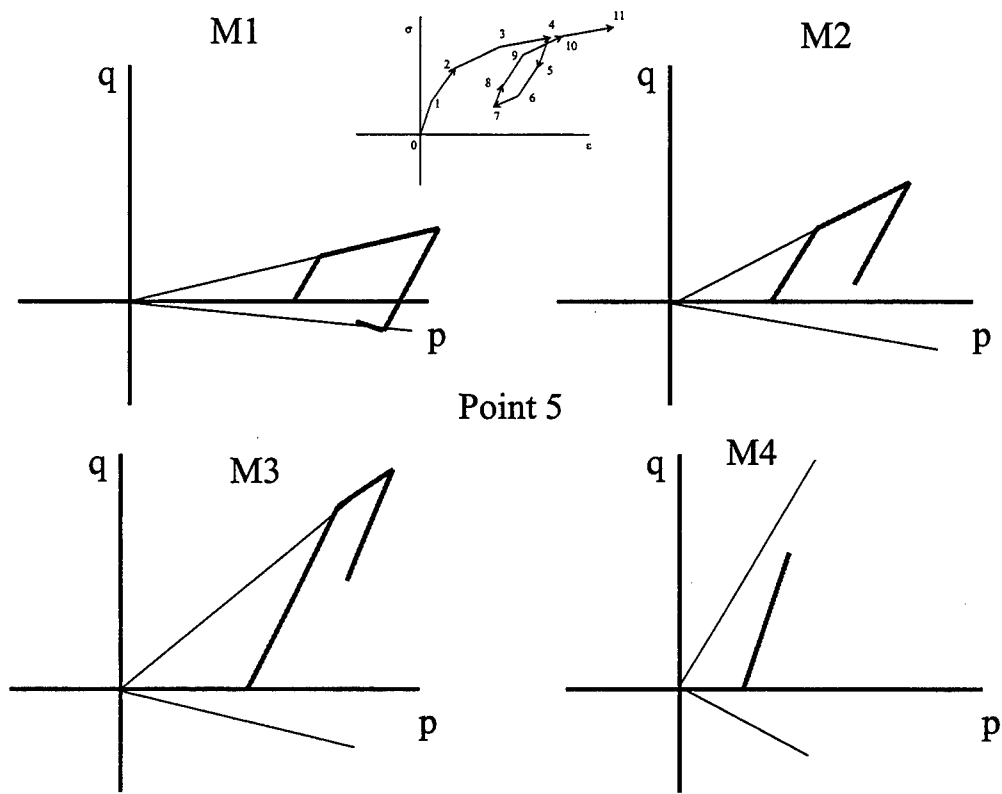


Figure 4.13. WES MM stress path at Point 5 (extension yield of Mechanism 1)

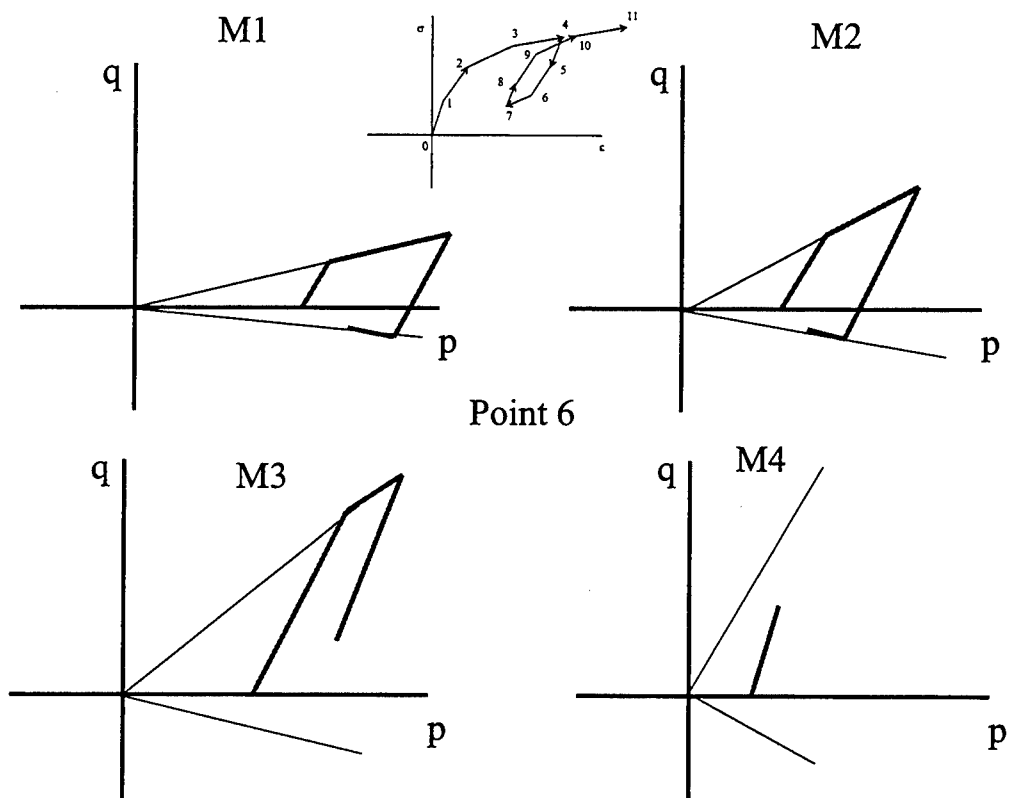


Figure 4.14. WES MM stress path at Point 6 (extension yield of Mechanism 2)

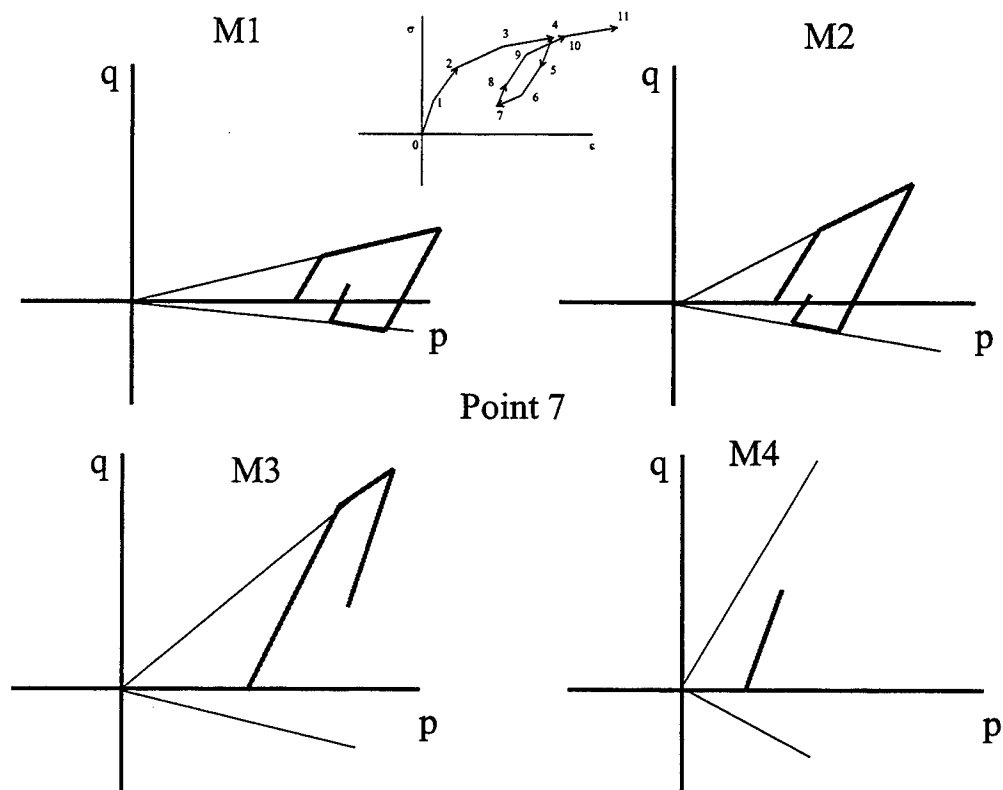


Figure 4.15. WES MM stress path at Point 7 (reload)



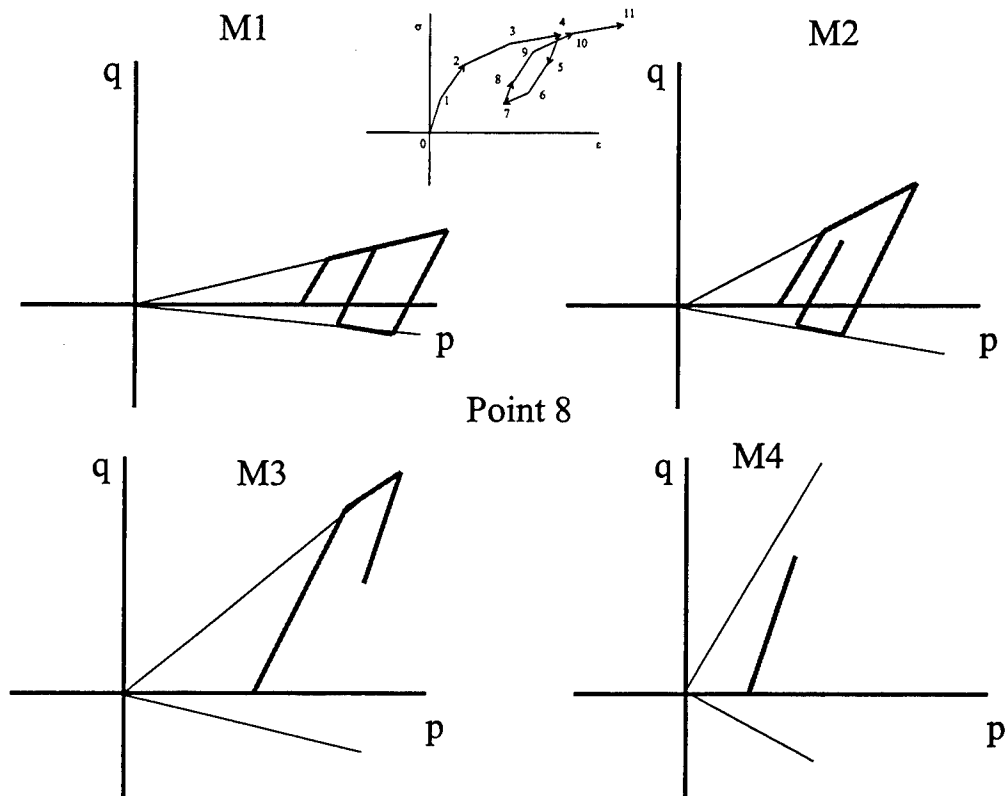


Figure 4.16. WES MM stress path at Point 8 (reload yield of Mechanism 1)

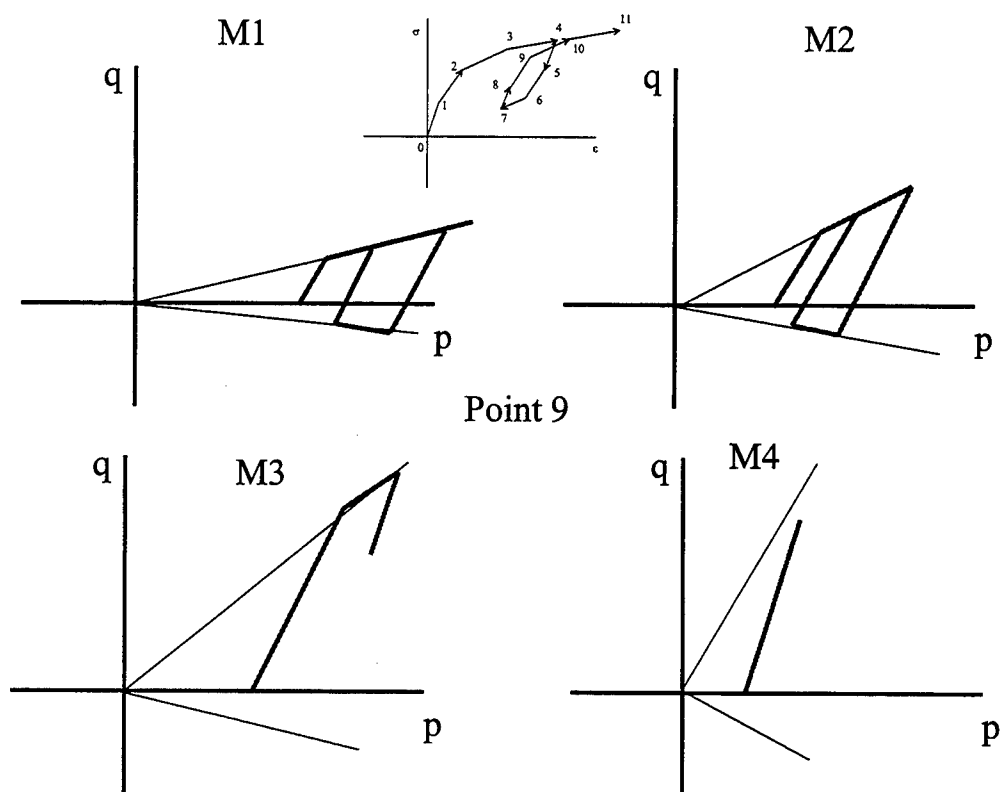


Figure 4.17. WES MM stress path at Point 9 (reload yield of Mechanism 2)

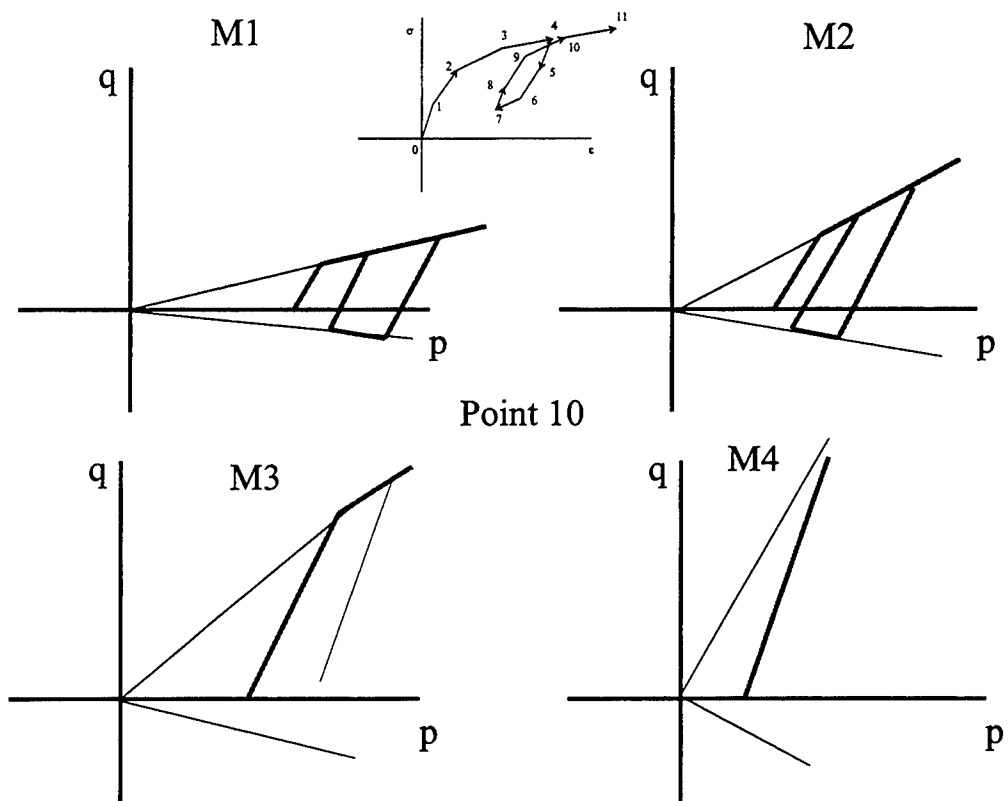


Figure 4.18. WES MM stress path at Point 10 (reload yield of Mechanism 3)

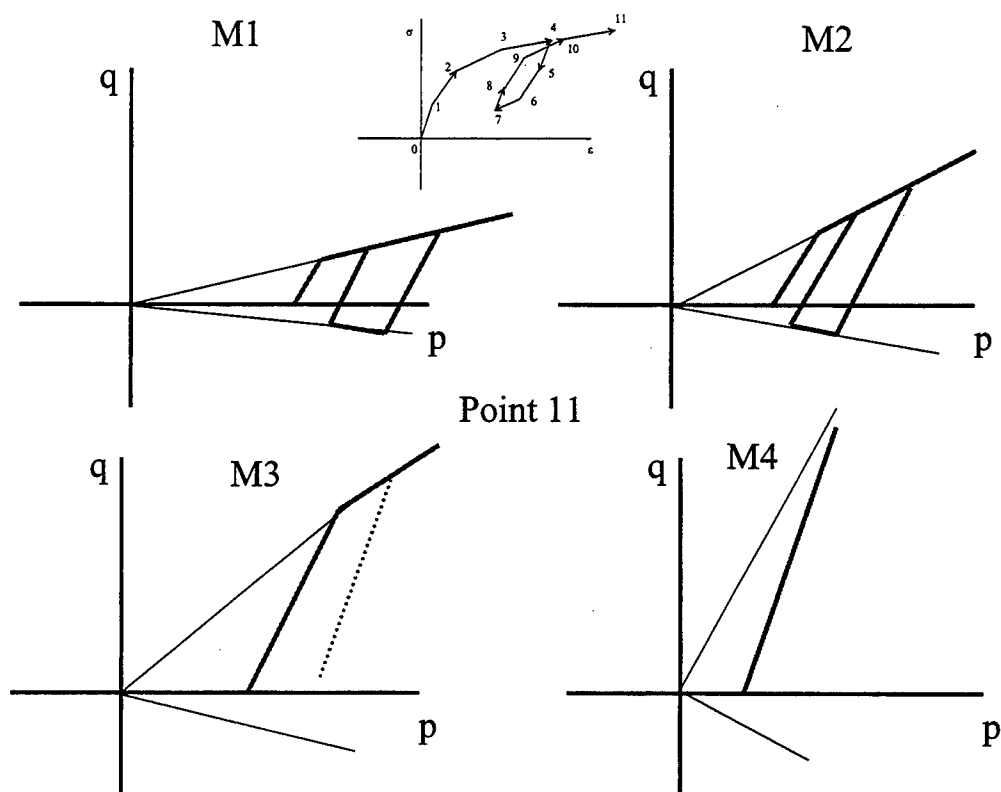


Figure 4.19. WES MM stress path at Point 11 (continued loading)

## CHAPTER 5: MODEL CALIBRATION

### GENERAL

In order to properly apply any constitutive model to predict the response of materials under load the models must be calibrated with test data. In essence the parameters used to define strength, failure, and deformation properties must be defined for any material to be modeled. This chapter describes the model requirements, laboratory tests, and analysis to achieve a proper calibration for both the ABAQUS Drucker-Prager model and the WES Multimechanical model.

### ABAQUS DRUCKER-PRAGER MODEL

The model uses three groups of parameters: stiffness parameters, failure surface parameters, and cap parameters. The general procedures used to determine these parameters from laboratory test data are presented in this section.

#### Failure Surface

As presented in Chapter 4, the ABAQUS Drucker-Prager failure surface is written in a  $q$  (principal stress difference) versus  $p$  (mean normal stress) space as:

$$F_s = q - p \tan \beta - d = 0 \quad (4.1)$$

where  $\beta$  and  $d$  represent the angle of friction of the material and its cohesion, respectively.

#### Cap Yield Surface

The cap yield surface has an elliptical shape with constant eccentricity in  $q$ - $p$  plane and also includes dependence on the third stress invariant in the deviatoric plane. The cap surface hardens or softens as a function of the volumetric inelastic strain. The ABAQUS Drucker-Prager failure surface is written in a  $q$  (principal stress difference) versus  $p$  (mean normal stress) space as Equation 4.2,

$$F_c = \sqrt{[p - p_a]^2 + \left[ \frac{Rq}{(1 + \alpha - \alpha / \cos \beta)} \right]^2} - R(d + p_a \tan \beta) = 0 \quad (4.2)$$

where  $R$  is a material parameter that controls the shape of the cap,  $\alpha$ , a cap transition factor), and  $p_a$  is an evolution parameter that represents the volumetric inelastic strain driven hardening/softening. The  $p_a$  parameter is a function of the plastic volumetric strain and volumetric yield stress. The materials typically used in granular base courses in pavements have a very high level of compaction and strength. One would only expect to intersect the cap in such materials under loads much higher than those experienced in pavements, such as blast or shock conditions. In essence this reduces the cap model's operation back to a simpler two-parameter friction model based on  $\beta$  and  $d$ . Figure 5.1 shows the simplified model parameters with the stress regime of interest in the shaded area.

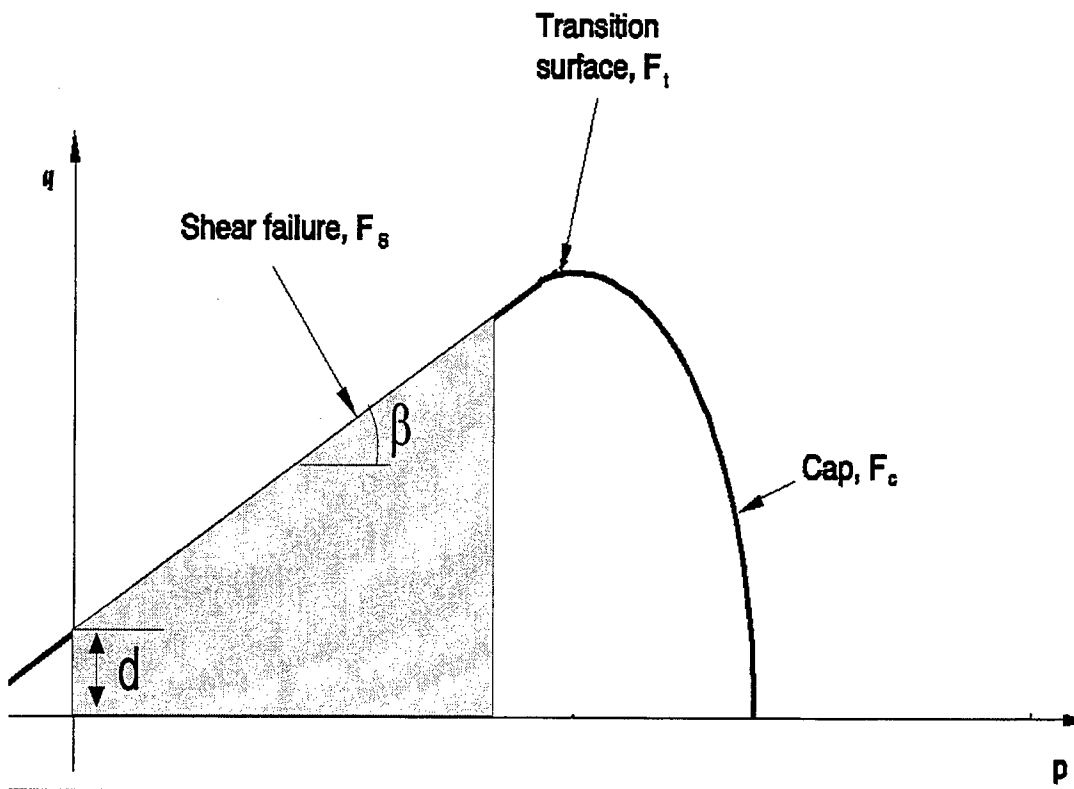


Figure 5.1. ABAQUS Drucker-Prager model with stress regime of interest shown in gray

## Calibration

At least three experiments are required to calibrate the simplest version of the Drucker-Prager model: a hydrostatic compression test and two triaxial compression tests (more than two tests are useful for a more accurate calibration).

The hydrostatic compression test is performed by pressurizing the sample equally in all directions. The applied pressure and the volume change are recorded. Triaxial compression experiments are performed using a standard triaxial machine where a fixed confining pressure is maintained while the differential stress is applied. Several tests covering the range of confining pressures of interest are usually performed. Again, the stress and strain in the direction of loading are recorded, together with the lateral strain so that the correct volume changes can be calibrated. Unloading measurements in these tests are useful in determining elastic properties, particularly in cases where the initial elastic region is not well defined.

The stress-strain curve from the hydrostatic compression test gives the evolution of the hydrostatic compression yield stress. The friction angle,  $\beta$ , and cohesion,  $d$ , which define the shear failure dependence on hydrostatic pressure, are calculated by plotting the failure stresses of any two uniaxial and/or triaxial compression experiments in  $q$  (principal stress difference) versus  $p$  (mean normal stress) space: the slope of the straight line passing through the two points gives the angle  $\beta$  and the intersection with the  $q$ -axis gives  $d$ .

## WES MULTIMECHANICAL CONSTITUTIVE MODEL

The model uses three groups of parameters: stiffness parameters, strength parameters, and a shear-volume coupling parameter. The general procedures used to determine these parameters from laboratory test data are presented in this section.

### Calibrating the Model – General Approach

The procedure for calibrating the model requires a set of several triaxial tests, either drained or undrained with pore pressure measurements. First, the relation between mean

effective stress and void ratio at the ultimate state is plotted similar to an  $e - \log p$  curve as shown in Figure 5.2. The slope  $C_c$  and intercept,  $F_h$ , are used to determine the relation between void ratio and the reference pressure,  $P_e$ . Next, the hydrostatic stress-strain curve is plotted in a normalized form in which the hydrostatic stress is divided by the reference stress. In this form the hardening effect of void ratio decrease is removed, leaving the fundamental curve. The normalized curve is then divided into regions to be represented by each mechanism. The yield stress associated with each mechanism is thus determined. The stiffness of each mechanism is determined by the change in modulus that occurs as each yield limit is crossed.

A similar procedure is carried out for the shear response. The shear yield limit is determined for each mechanism. Friction angles are selected based on the ultimate friction angle at a stress level close to that of the expected service loads. From these data, the distribution factor for hydrostatic stress can be determined for each mechanism. The calibration from the shear moduli is the same as that for the bulk moduli of the hydrostatic mechanism.

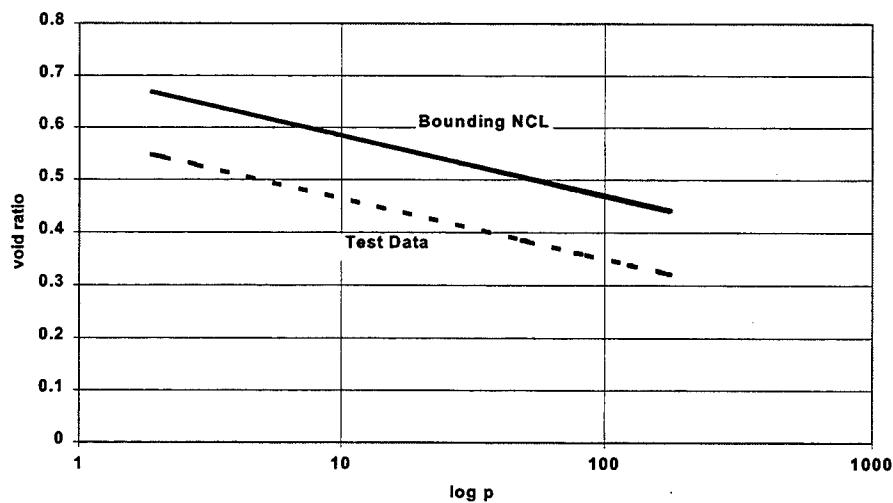


Figure 5.2. Void ratio versus log normal stress plot used to determine NCL for WES MM model



## **LABORATORY TESTS**

Tests were conducted on a well-graded limestone base course material to determine its response to loads and to define its yield surface for use with plasticity formulations such as the Mohr-Coulomb and Drucker-Prager models. Five Unconfined Compression (UCC) tests were conducted. Conventional Triaxial Compression (CTC) tests were conducted at four confining pressures up to 80 psi (551.6 kPa), with axial strains up to 5 percent. Uniaxial Strain (UXE) tests and Hydrostatic Compression (HC) tests were conducted up to confining pressure levels of 100 psi (689.5 kPa). Replicates of each test were performed to insure that variations in response could be identified and corrected.

The mechanical response of granular materials must be clearly understood to accurately predict the performance of flexible pavements. Due in large part to testing difficulties, the measurement of load-induced response of granular materials has received little attention in the geotechnical. Considerable effort expended during this research was aimed at developing equipment, procedures and skills necessary for preparing and testing unbound, highly angular, granular materials.

### **Material**

The Type 610 (MDOT, 1990) well-graded crushed limestone material, as shown in Figure 5.3, selected for this study was used as a base course in an airfield pavement test section (Webster 1993). The grain-size analysis is shown in Figure 5.4. This grain size distribution is typical for aggregate base course materials used in many airfield pavements. Webster reported the material to be an SW-SC according to the Unified Soil Classification System. However, further investigation proved that the material was actually a GW material. It had a liquid limit of 17, a plastic limit of 11, and a plasticity index of 6. Using modified proctor procedures, in accordance with ASTM D 1557, optimum moisture content for compaction was determined to be 4.5 percent. Dry unit weight at optimum moisture content was determined to be 144 lb/ft<sup>3</sup> (2306.7 kg/m<sup>3</sup>).

Prior to performing each mechanical property test, the height, diameter and weight of each remolded specimen were determined. These measurements, along with the aggregate specific gravity and water content, were used to calculate dry density and void ratio for each specimen. The variation of height, weight, and diameter of the specimens were carefully controlled to arrive at the dimensions shown in Table 5.1. All specimens were constructed using the GTM procedure to the dimensions and the weight shown. Specimens were fabricated to reproduce the field density of 137.2 lb/ft<sup>3</sup> (2199.5 kg/m<sup>3</sup>) and moisture content of 4.0 %. A digital electronic caliper with accuracy of +/- 0.001 inches (0.03 mm) was used to verify specimen dimensions prior to testing. A digital electronic scale with a maximum range of 22 lbs. (10 kg) and an accuracy of +/- 0.0002 lbs. (0.1 g) was used to verify specimen weight prior to testing. Specimens not meeting weight and dimension requirements were rejected for testing.

Table 5.1. Granular Limestone Specimen Properties

Diameter In. (mm)	Height in. (mm)	Area in <sup>2</sup> (mm <sup>2</sup> )	Dry Weight lb. (kg)	Volume ft <sup>3</sup> (m <sup>3</sup> )	Density lb/ft <sup>3</sup> (kg/m <sup>3</sup> )	Void Ratio	Moisture Content %
4.00 (101.6)	8.36 (213.4)	12.57 (8109.7)	8.38 (3.81)	0.061 (0.00173)	137.2 (2199.5)	0.21	4.0

### Specimen Preparation

Each granular specimen tested in this study was exactly 4 inches (101.6 mm) in diameter by 8.36 inches (213.4 mm) in height as seen in table 5.1. The compacted specimens were tested in a conventional triaxial compression chamber meeting ASTM D2850, which consisted of a reinforced Plexiglas pressure vessel, a stainless steel base, and a stainless steel top. All specimens were tested in the triaxial chamber immediately following completion of the compaction process to insure that no damage or moisture/strength loss occurred during extended storage periods.

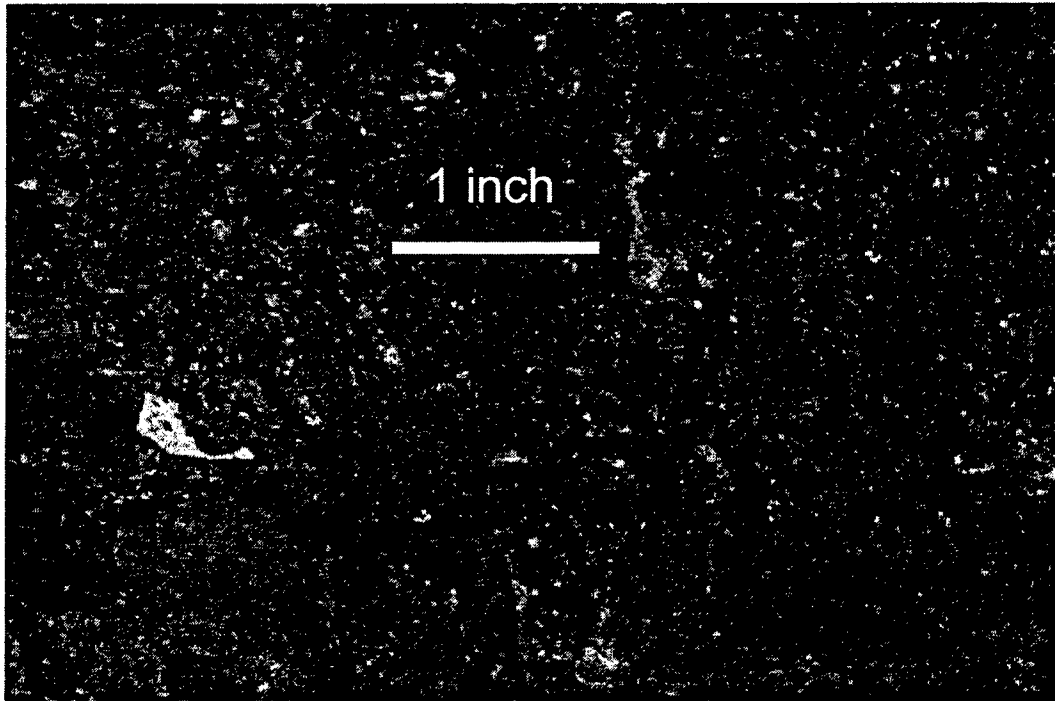


Figure 5.3. Well-graded crushed limestone used in laboratory tests

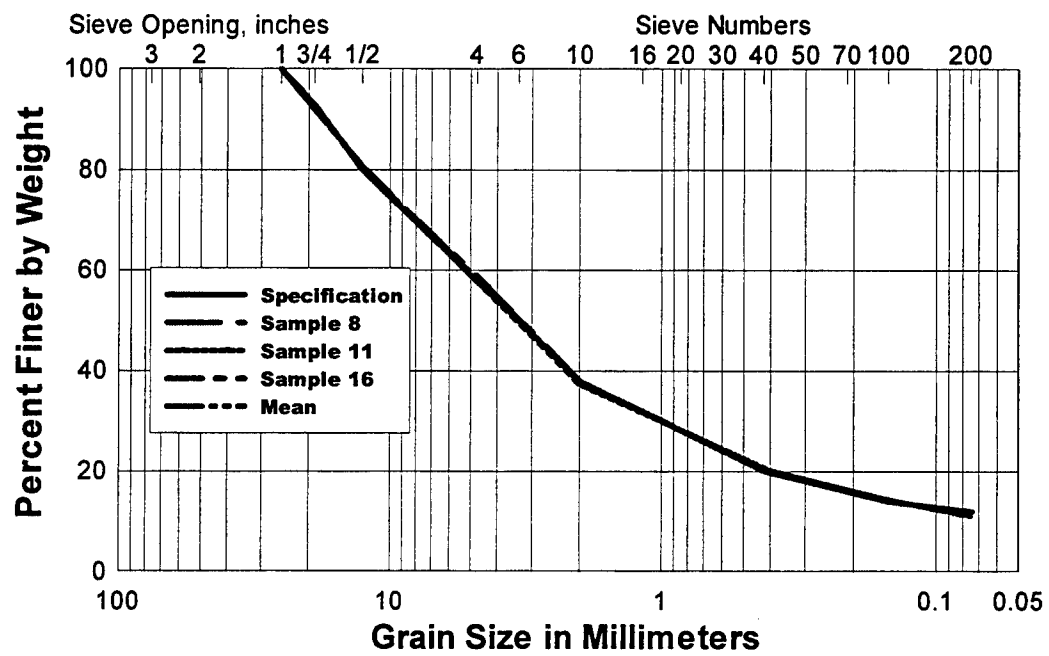


Figure 5.4. Grain-size analysis of well-graded crushed limestone used in laboratory tests

Specimens were prepared using the Corps of Engineers Gyratory Compaction Testing Machine (GTM) (ASTM D 3387). Compaction of materials using the gyratory method applies normal forces to both the top and bottom faces of the material confined in cylindrically shaped molds. Normal forces at designated pressures are supplemented with a kneading action or gyratory motion to compact the material into a denser configuration with aggregate particle orientation more consistent with in-place pavements.

The gyratory compaction method involves placing loose material into a 4-inch diameter by 10-inch length mold and loading into the GTM at a prescribed normal stress level which represents anticipated traffic contact pressure. The material and mold are then rotated through a 1-degree gyration angle for a specified number of revolutions of the roller assembly. This compaction process produces stress-strain properties that are representative of those in a field compacted material (Ahlrich, 1997). A schematic of the gyratory compaction device is shown in Figure 5.5.

The gyratory testing machine shown in Figure 5.6 was used to compact all laboratory specimens in this research. The gyratory compactive effort used in this laboratory study was a 200-psi (1378.7 kPa) normal stress level, 1-degree gyration angle and 30–50 revolutions of the roller assembly. This compaction effort produced specimens that were nominally 8 inches long and 4 inches in diameter. The specimens were sealed with 1-in. (25.4-mm) thick aluminum endcaps and double 0.025-in. (0.635-mm) latex membranes before being placed in the triaxial testing device. A target density of 137.2 lb/ft<sup>3</sup> (2199.5 kg/mm<sup>3</sup>) was used to select the compaction effort described above. The gyratory compaction process produced highly repeatable samples and contributed greatly to the success of the laboratory testing phase of this research. Experiences with other compaction methods such as vibratory and hammer compaction procedures for granular materials proved unsuitable for this investigation.

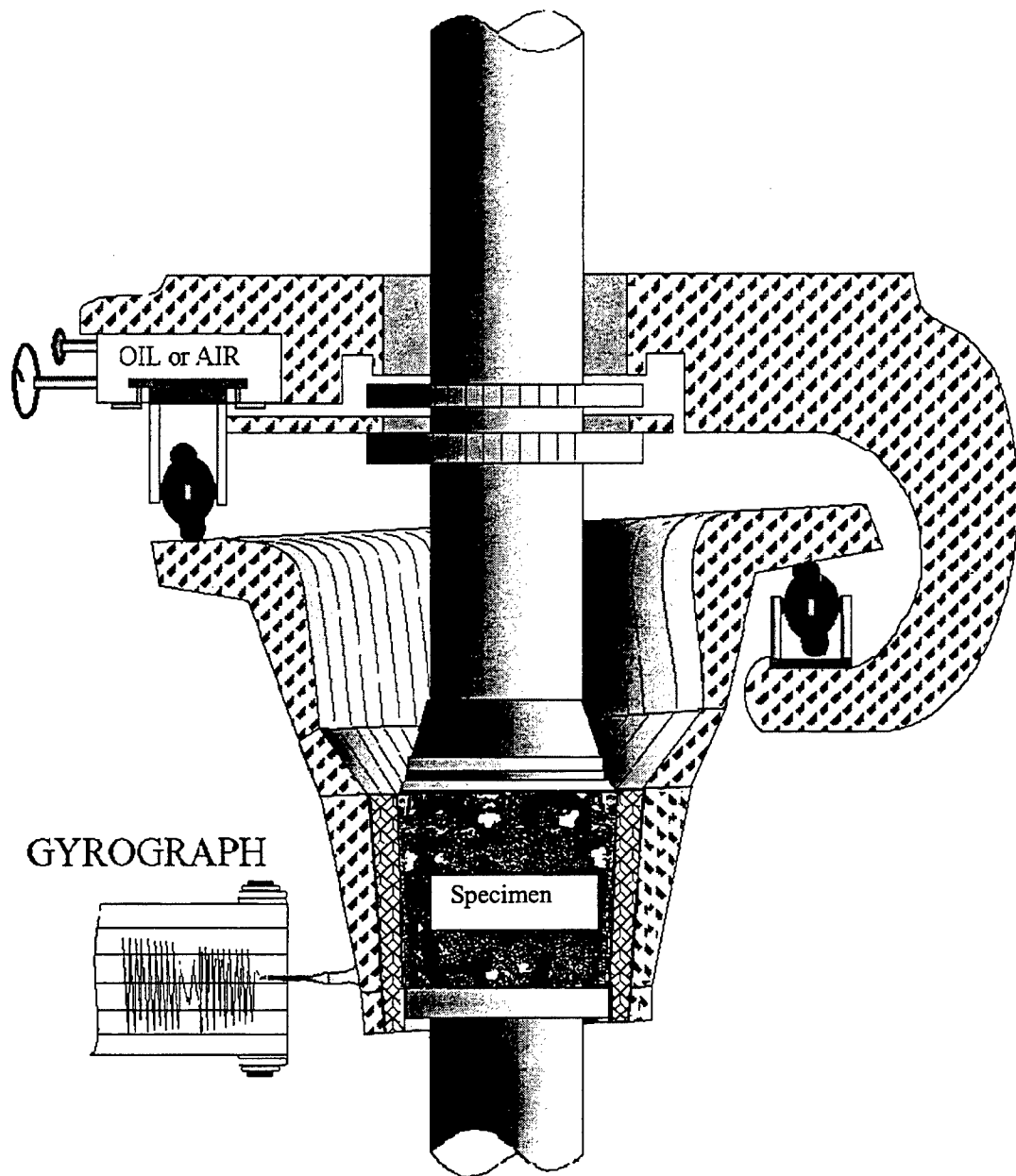


Figure 5.5. Schematic of gyratory testing machine

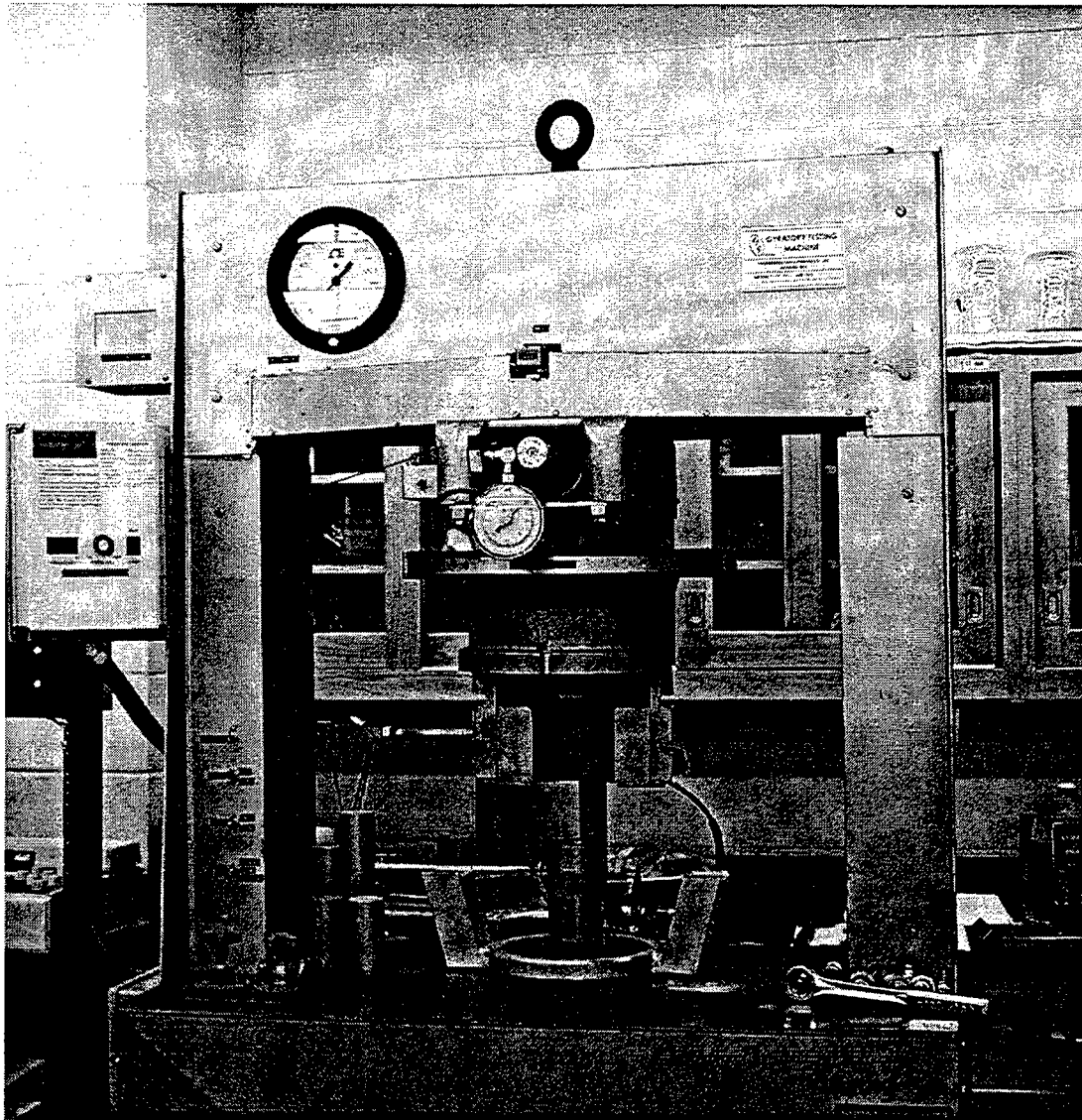


Figure 5.6. Gyratory testing machine used for specimen preparation

### **Description of Test Device**

A conventional cylindrical soils triaxial testing device conforming to ASTM D2850 was used to perform the mechanical property tests. The test device had overall nominal dimensions 18 inches (457.2 mm) in height by 12 inches (304.8 mm) in diameter with a capacity to test specimens up to 5 inches (127 mm) in diameter. The pressure vessel was reinforced Plexiglas with hardened stainless steel encaps and connecting rods.

The confining pressure was supplied by air pressure. A servo-controlled Instron testing machine, capable of applying tensile or compressive loads up to 60,000 lb. (266 kN) supplied the axial load. The Instron testing machine and triaxial chamber is shown in Figure 5.7. The loader could be controlled either manually or by computer in order to produce a desired rate of loading or displacement. The input to the servo-control unit was produced by a function generator, which could be programmed to produce large variety of load or displacement histories. A load cell measured the axial force applied to each granular specimen. The confining pressure applied to the specimens is measured with a pressure transducer, located at the air supply regulator.

Measurement of the changes in the specimen dimensions were critical considerations in the testing. Measurements of deformation under load of a remolded cohesionless material is a very difficult task. The measurement devices must provide for accurate changes in length and diameter without affecting the response of the material.

Changes in specimen length were measured with two diametrically opposed linear variable differential transducers (LVDT), mounted on the end platens on the inside of the chamber. The change in diameter of the specimen under load was measured with a device that consisted of four strain-gaged spring arms attached to a mounting ring and calibrated to provide a diameter change output in a full bridge configuration. A photo of a specimen with its deformation devices attached is shown in Figure 5.8.

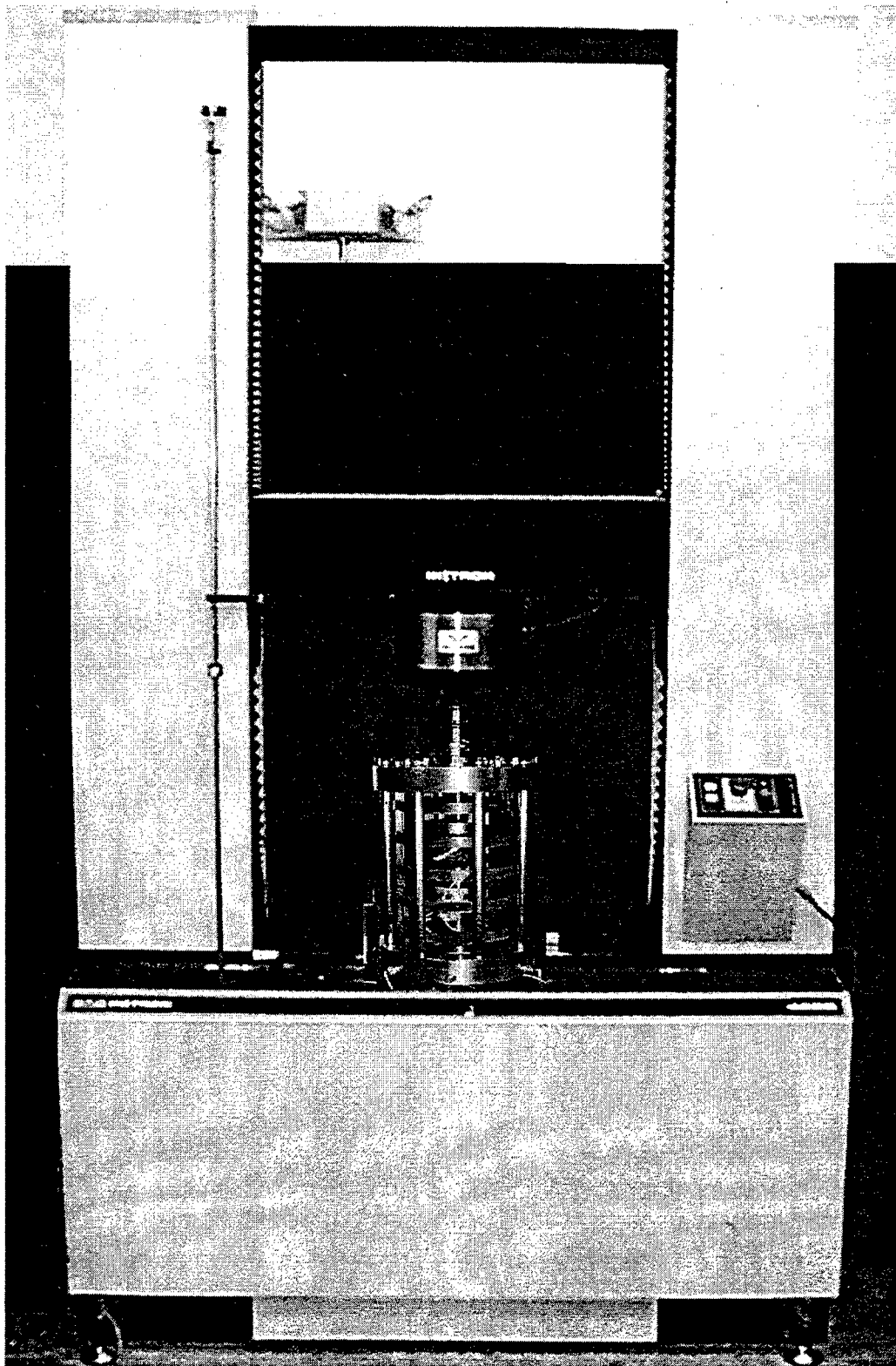


Figure 5.7. Instron servo-controlled testing machine



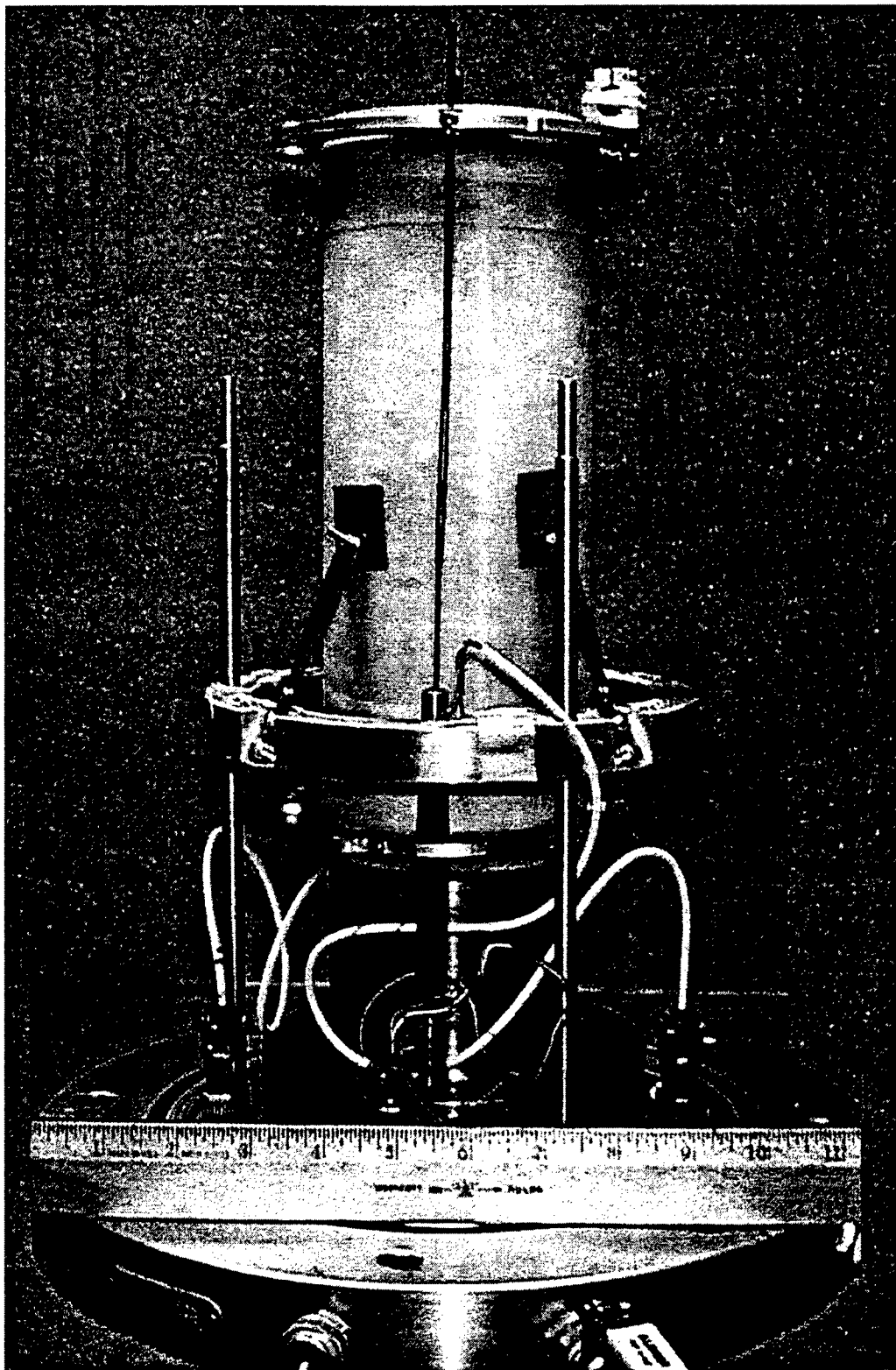


Figure 5.8. Granular limestone specimen with instrumentation attached

## RESULTS OF LABORATORY TESTS

### Unconfined Compression Tests

Five unconfined compression tests were conducted on remolded 4-in by 8-in specimens. The tests were conducted in the same chamber as the CTC tests. Each unconfined compression (UC) test was conducted by applying an axial load with a constant rate of 1% per minute. The load was applied until the granular material exhibited either a maximum axial stress (peak) or an axial strain of 5 percent. With a specimen length of 8.36 inches (212.3 mm) a strain of 5 percent equals a total change in length of 0.418 inches (10.9 mm). Controlling the test by a specified rate of strain allowed for the capture of softening response during post-yield stress application.

A summary of these tests is shown in Table 5.2. Plots of Axial stress versus axial strain are shown in Figure 5.9. Figure 5.10 shows a plot of mean normal stress versus volumetric strain for the tests. The individual plots of test data from the unconfined compression tests are shown in Appendix E.

Table 5.2. Summary of Results at Maximum Axial Stress from UCC Tests

	Axial Strain	Radial Strain	Volumetric Strain	Axial Stress		Mean Normal Stress	
	%	%	%	psi	kPa	psi	kPa
Ucc_1	1.9	-6.0	-10.1	7.6	52.7	2.5	17.6
Ucc_2	1.3	-4.2	-7.1	8.4	57.6	2.8	19.2
Ucc_3	1.3	-3.7	-6.0	11.7	80.7	3.9	26.9
Ucc_4	1.9	-5.2	-8.5	10.1	69.6	3.4	23.2
Ucc_5	2.3	-6.1	-9.8	8.8	61.0	2.9	20.3
Mean	1.7	-5.0	-8.3	9.3	64.3	3.1	21.4
$\sigma^*$	0.4	1.1	1.8	1.6	11.0	0.5	3.7

\* Standard Deviation

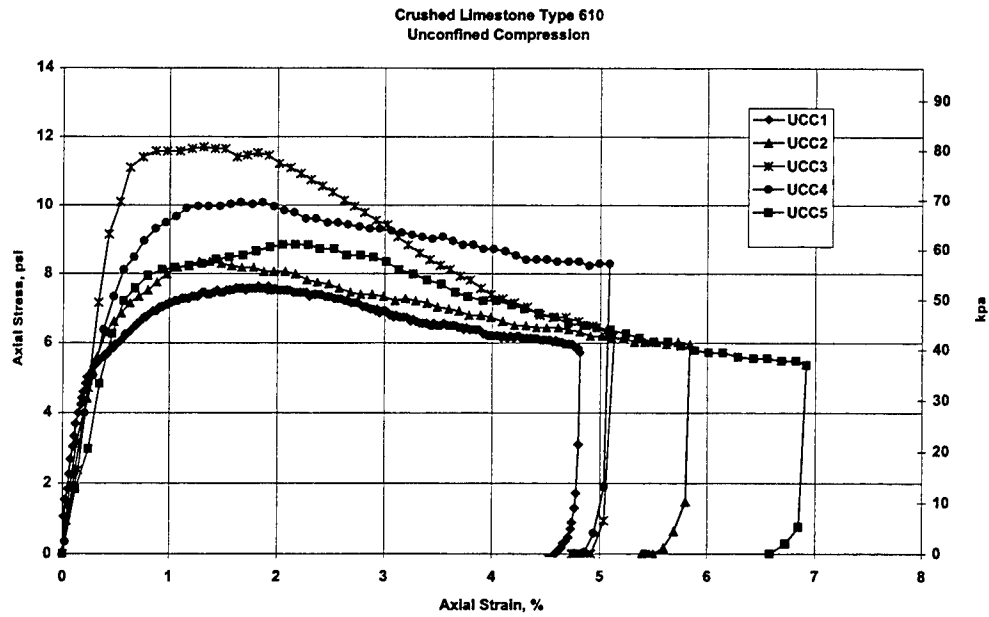


Figure 5.9. Axial stress versus strain for unconfined compression tests of granular limestone

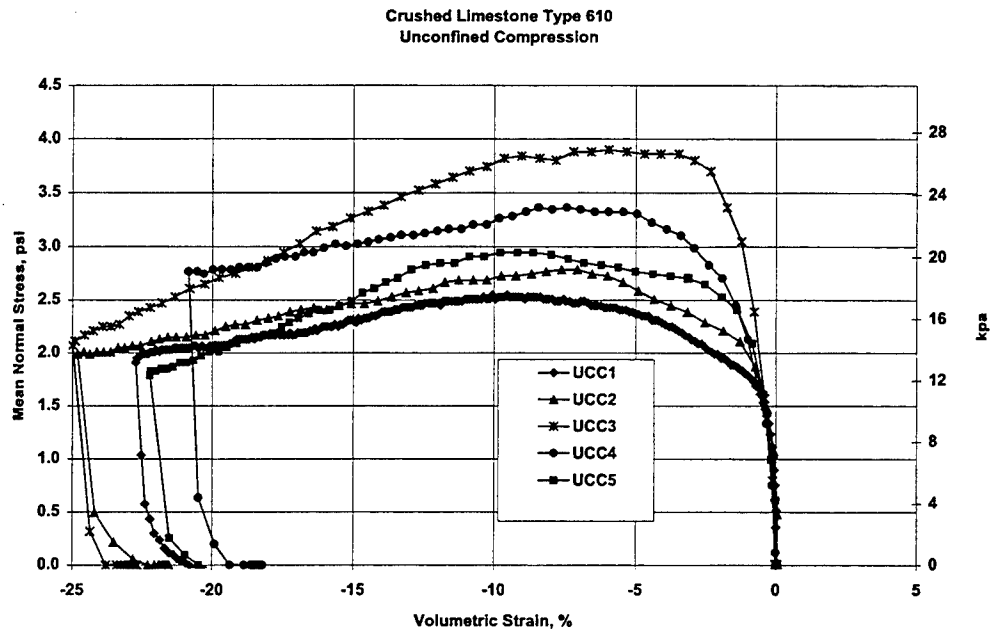


Figure 5.10. Mean normal stress versus volumetric strain for unconfined compression tests of granular limestone

### Conventional Triaxial Compression Tests

Conventional triaxial tests (CTC) were conducted according to ASTM D2850 except for the displacement measuring system and subtle differences required to prevent damage of the specimen during assembly of the device. Tests at four confining pressure levels with a at least three repetitions at each level of confining pressure were conducted. Each conventional triaxial compression (CTC) test was conducted in two phases. An isotropic compression (IC) phase was conducted by applying a confining pressure to all sides of the cylindrical specimen, while measuring its change in height and diameter. These data are often plotted as mean normal stress versus volumetric strain, the slope of which is the bulk modulus,  $K$ . After the desired confining pressure had been attained during the IC phase, the triaxial compression phase was conducted. This was accomplished by applying an axial load with a strain rate of 1% per minute, while the confining pressure was held constant. After the maximum strain of 5 percent was reached the test machine was reversed to allow measurement of unloading response. These tests were essentially undrained tests that did not generate any excess pore water pressure. The specimens had saturation levels in the range of 50% with void ratios on the order of 0.21 at the beginning of each test.

A summary of these tests is shown in Table 5.3. The data in Table 5.3 is organized according to confining pressure with a statistical summary of each level of response provided in the table. Plots of principal stress difference versus principal strain difference are shown in Figure 5.11. Plots of principal stress difference versus mean normal stress are shown in Figure 5.12. Figure 5.13 shows a composite plot of mean normal stress versus volumetric strain. The individual plots of test data from the conventional triaxial compression tests are shown in Appendix C. The tests are designated as CTCxx\_y. The coding designation xx is the confining pressure in pounds per square inch, and y is the replicate number at the confining pressure xx..

Table 5.3. Summary of Results at Maximum Axial Stress from CTC Tests

	Axial Strain	Radial Strain	Strain Difference	Confining Pressure		Volumetric Strain	Axial Stress		Mean Normal Stress		Principal Stress Difference	
	%	%	%	psi	kPa	%	psi	kPa	psi	kPa	psi	kPa
CTC15_1	5.0	-8.8	13.8	15.4	106.2	-12.6	119.4	823.1	50.1	345.2	104.0	716.9
CTC15_2	5.2	-8.5	13.7	15.8	109.0	-11.7	115.3	795.5	49.0	337.8	99.5	686.6
CTC15_3	5.4	-8.7	14.1	16.5	113.8	-11.9	120.5	831.4	51.2	353.0	104.0	717.6
Mean (CTC15)	5.2	-8.6	13.8	15.9	109.7	-12.1	118.4	816.7	50.1	345.3	102.5	707.0
$\sigma^*$ (CTC15)	0.2	0.2	0.2	0.6	3.8	0.5	2.7	18.8	1.1	7.6	2.6	17.7
CTC30_3	4.5	-6.0	10.5	31.4	216.6	-7.5	194.3	1340.1	85.7	591.1	162.9	1123.6
CTC30_4	6.0	-7.9	13.9	31.9	220.0	-9.8	171.1	1180.2	78.3	540.1	139.2	960.1
CTC30_5	5.7	-7.4	13.1	31.4	216.6	-9.1	194.2	1339.2	85.7	590.8	162.8	1122.6
Mean (CTC30)	5.4	-7.1	12.5	31.6	217.7	-8.8	186.5	1286.5	83.2	574.0	155.0	1068.8
$\sigma^*$ (CTC30)	0.8	1.0	1.8	0.3	2.0	1.2	13.4	92.1	4.3	29.4	13.6	94.1
CTC50_1r	5.1	-6.2	11.3	51.5	355.2	-7.2	274.1	1890.2	125.7	866.9	222.6	1535.0
CTC50_2r	5.4	-7.3	12.7	51.3	353.8	-9.3	286.0	1972.7	129.5	893.4	234.7	1618.9
CTC50_3r	5.6	-6.6	12.2	51.9	357.9	-7.6	268.5	1851.9	124.1	855.9	216.6	1494.0
Mean (CTC50)	5.4	-6.7	12.1	51.6	355.6	-8.0	276.2	1904.9	126.4	872.1	224.6	1549.3
$\sigma^*$ (CTC50)	0.2	0.6	0.7	0.3	2.1	1.1	8.9	61.7	2.8	19.3	9.2	63.6
CTC80_1	5.7	-5.7	11.4	76.4	526.9	-5.8	339.9	2344.3	164.2	1132.7	263.5	1817.4
CTC80_2	5.5	-5.9	11.3	81.6	562.8	-6.3	364.0	2510.6	175.7	1212.1	282.4	1947.8
CTC80_3	5.7	-5.9	11.6	80.3	553.8	-6.2	398.7	2750.0	186.4	1285.9	318.4	2196.1
Mean (CTC80)	5.6	-5.8	11.4	79.4	547.8	-6.1	367.6	2535.0	175.5	1210.2	288.1	1987.1
$\sigma^*$ (CTC80)	0.1	0.1	0.1	2.7	18.7	0.2	29.6	203.9	11.1	76.6	27.9	192.4

\* Standard Deviation

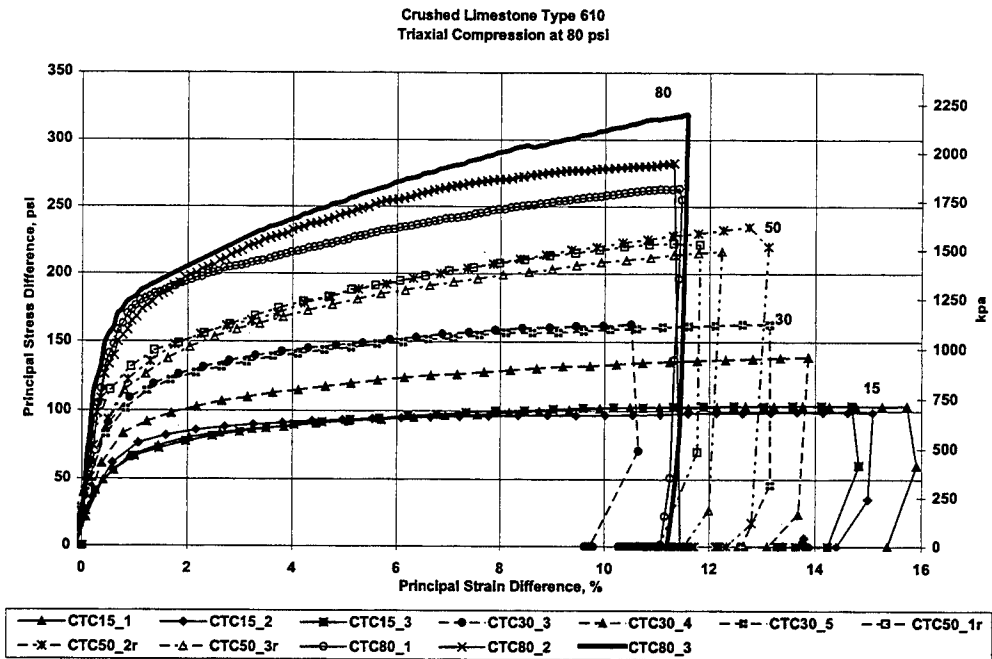


Figure 5.11. Principal stress difference versus principal strain difference for conventional triaxial compression tests of granular limestone

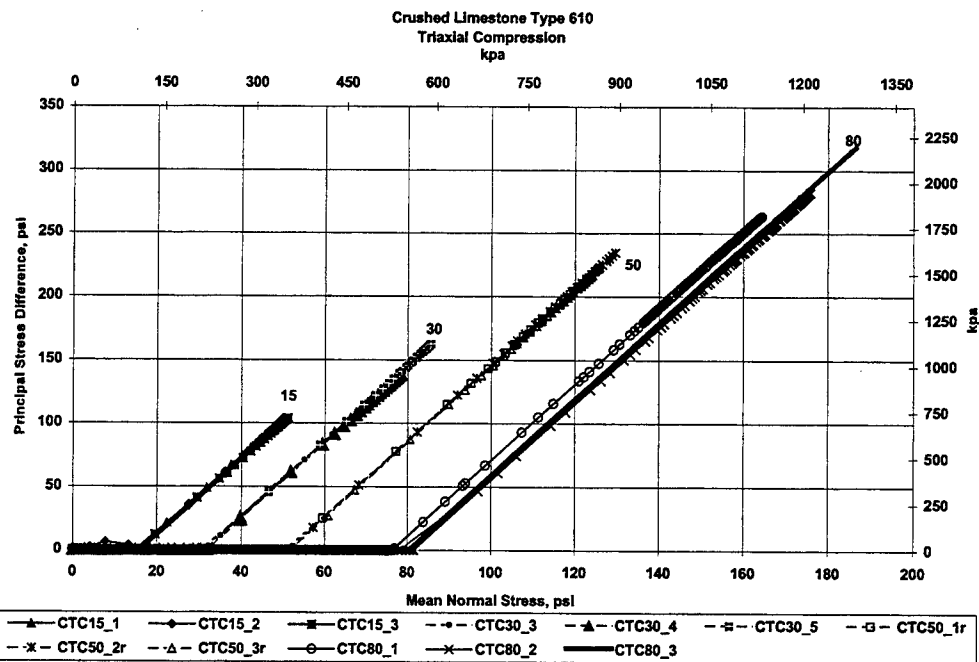


Figure 5.12. Principal stress difference versus mean normal stress for conventional triaxial compression tests of granular limestone

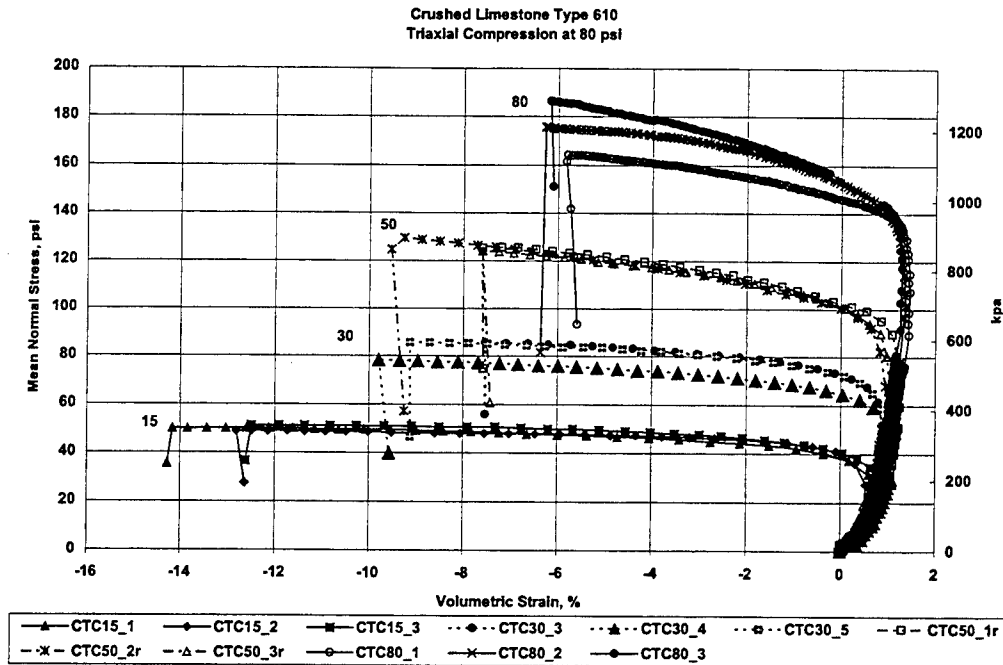


Figure 5.13. Mean normal stress versus volumetric strain for conventional triaxial compression tests of granular limestone

### Uniaxial Strain Tests

Uniaxial strain tests were conducted until confining pressures reached a maximum of 100 psi for two tests. Difficulties with membrane leakage resulted in the maximum pressure being reduced to 80 psi for the two other UXE tests. Each UXE test was conducted by applying an increment of axial load until a slight increase in specimen diameter was detected. Confining pressure was then applied until the specimen diameter returned to its original value. These processes were repeated throughout the test until the desired maximum confining pressure was reached.

A summary of these tests is shown in Table 5.4. Plots of mean normal stress versus volumetric strain are shown in Figure 5.14. Figure 5.15 shows a composite plot of principal stress difference versus principal strain difference. Plots of principal stress difference versus mean normal stress are shown in Figure 5.16. The individual plots of test data from the uniaxial strain tests are shown in Appendix F.

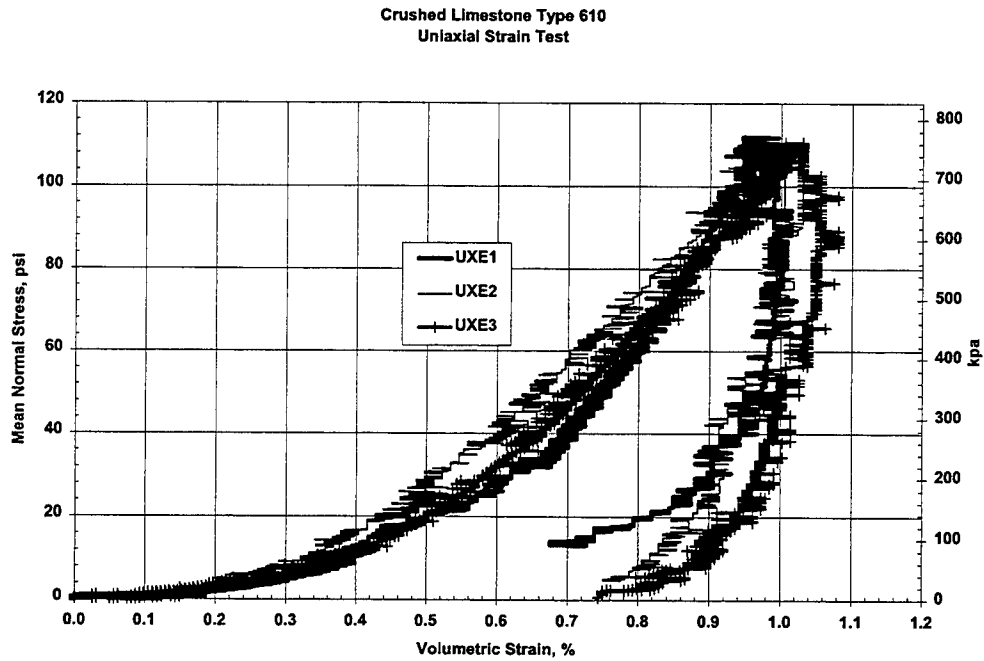


Figure 5.14. Mean normal stress versus principal stress difference for uniaxial strain tests

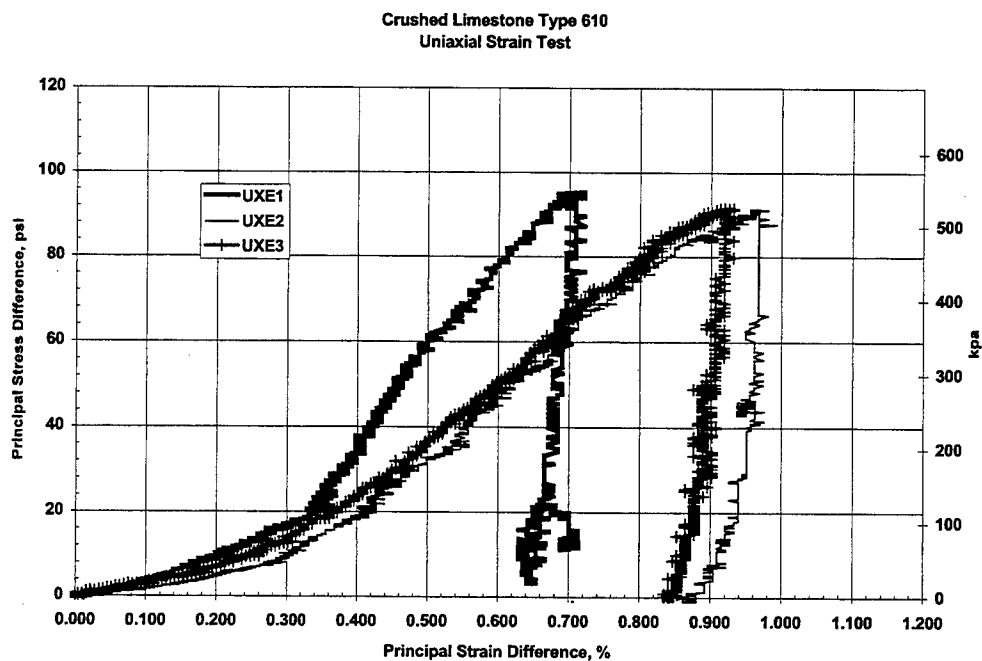


Figure 5.15. Principal stress difference versus principal strain difference for uniaxial strain tests



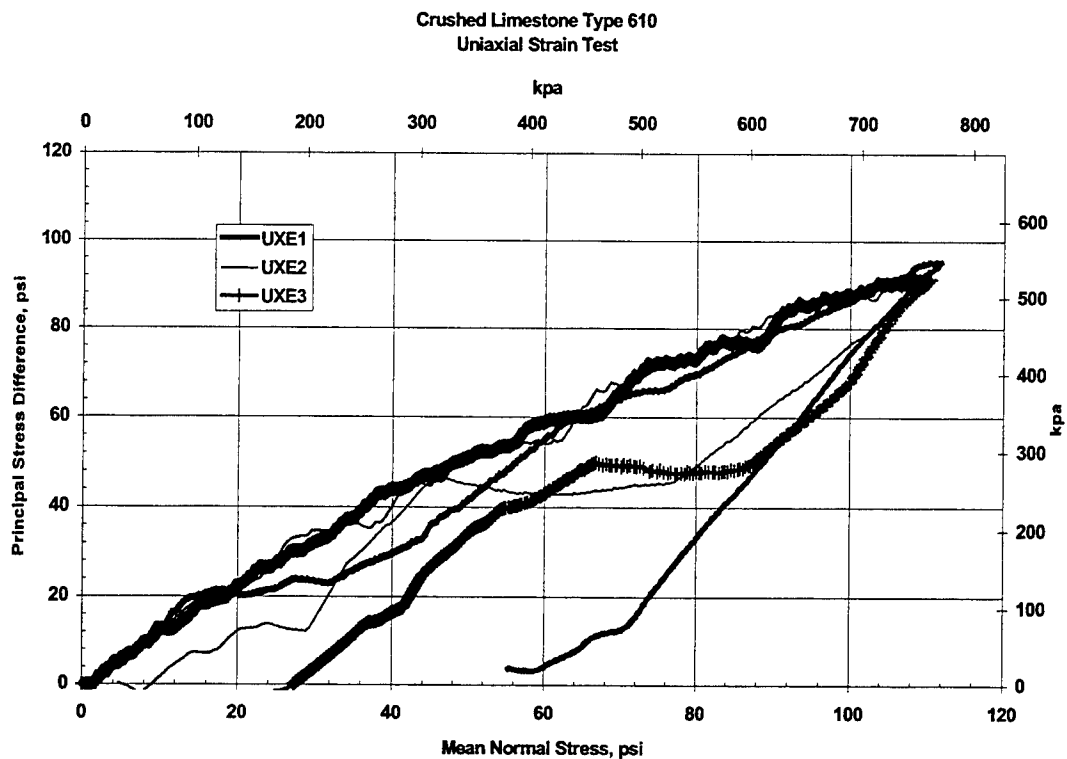


Figure 5.16. Principal stress difference versus mean normal stress for uniaxial strain tests

Table 5.4. Summary of Peak Stress Results from Uniaxial Strain Tests

	Strain			Confining Pressure		Volumetric Strain	Axial Stress		Mean Normal Stress		Principal Stress Difference	
	Axial	Radial	Difference									
	%	%	%	psi	kPa	%	psi	kPa	psi	kPa	psi	kPa
UXE1	0.8	0.1	0.7	80.1	552.4	1.0	175.3	1209.3	111.9	771.4	95.2	656.8
UXE2	1.0	0.0	1.0	80.0	551.8	1.0	171.0	1179.7	110.4	761.1	91.0	627.9
UXE3	1.0	0.0	0.9	80.0	551.8	1.0	171.5	1182.6	110.5	762.0	91.5	630.8
Mean	0.9	0.0	0.9	80.0	552.0	1.0	172.6	1190.5	110.9	764.8	92.6	638.5
$\sigma^*$	0.1	0.0	0.1	0.1	0.4	0.0	2.4	16.3	0.8	5.7	2.3	15.9

\* Standard Deviation

### Hydrostatic Compression Tests

Hydrostatic Compression Tests were conducted until confining pressures reached a maximum of 100 psi (689.5 kPa) for four tests. The primary reason for conducting this type of test is to define the response of the material in a zero shear or pure normal stress environment. This hydrostatic state of stress produces strains that are totally decoupled from any deviatoric shear. The data from this test is used to define the normal consolidation and critical state parameters for the material. This test is not necessarily representative of any condition that exists. These tests were conducted by applying an all around pressure in the CTC test device until a desired maximum pressure was reached. Difficulties with membrane leakage resulted in the maximum pressure being reduced to 80 psi (551.6 kPa) for one HC test. A summary of the peak stress results from the HC tests is shown in Table 5.5. Plots of mean normal stress versus volumetric strain are shown in Figure 5.17. The individual plots of test data from the hydrostatic compression tests are shown in Appendix D.

Table 5.5. Summary of Peak Stress Results from HC Tests

	Axial Strain	Radial Strain	Hydrostatic Pressure		Volumetric Strain
	%	%	psi	kPa	%
HC 100					
HC100_1	0.29	0.51	103.9	716.6	1.31
HC100_2	0.33	0.49	99.4	685.5	1.30
HC100_3	0.36	0.56	99.3	684.9	1.49
HC100_4	0.27	0.46	93.4	644.2	1.20
Mean	0.31	0.51	99.0	682.8	1.33
$\sigma^*$	0.04	0.04	4.3	29.7	0.12
HC 80					
HC80_1	0.25	0.50	79.4	547.6	1.15

\* Standard Deviation

Crushed Limestone Type 610  
Hydrostatic Compression

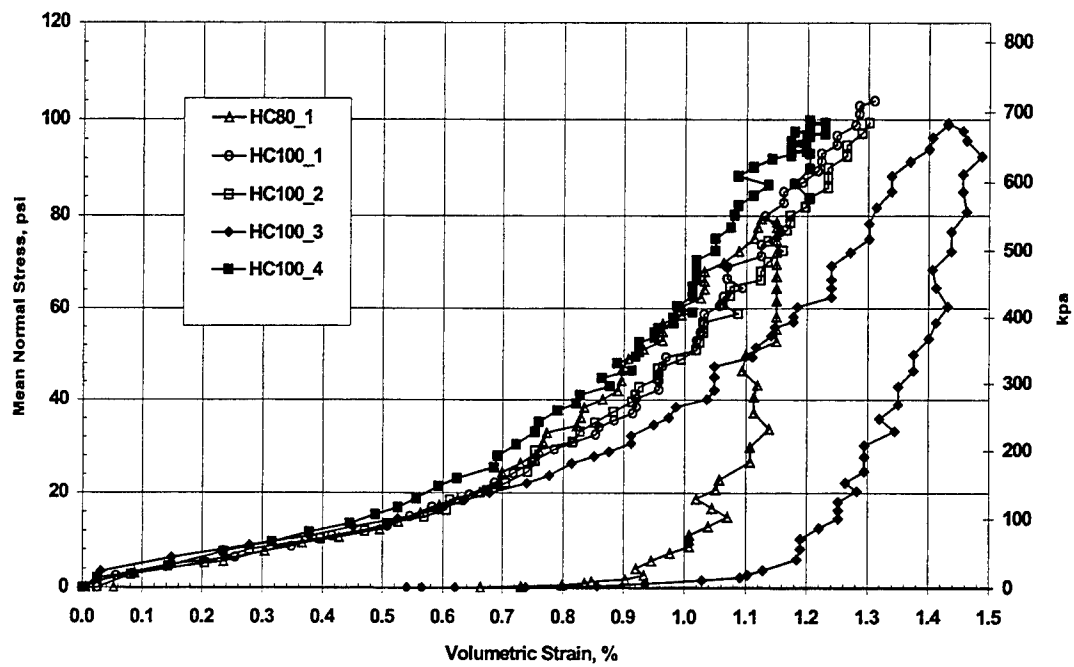


Figure 5.17. Mean normal stress versus volumetric strain for hydrostatic compression tests of granular limestone

## DETERMINATION OF ABAQUS DRUCKER-PRAGER MODEL PARAMETERS

The values for  $\beta$  (slope) and  $d$  (y intercept) for the DP model were determined from a composite plot of the failure points for the 15, 30, 50, and 80 psi (103.4, 206.8, 344.7, 551.6 kPa) conventional triaxial compression tests. The elliptical cap location is determined from the plastic volume change of a hydrostatic compression test. The granular limestone material tested was very dense and strong when compared to the types of materials that the Drucker-Prager model was originally intended to represent. The high density and strength of the material is attributed to the high level of compactive effort used in fabricating the specimens and placing this material in the field. As a result of, the hydrostatic stress regime under which one would see plastic volume change (i.e. cap location) is much higher than the service loads that even aircraft pavements would ever see. In essence, this reduces the cap model's operation back to a simpler two-parameter friction model. Figure 5.18 shows the failure points from the CTC test and the hydrostatic compression test plotted on a  $q$  (stress difference) versus  $\log p$  (mean normal stress) space. Figure 5.19 shows the composite stress strain response for the material. Figure 6.20 shows that the reference stress (virgin loading) line is beyond the line bounding the maximum void ratios for the CTC test results. This supports the conclusion that the cap for this material lies totally outside the stress regime of interest in this research.

A value of  $58.6^\circ$  for  $\beta$  and 11.25 psi (77.5 kPa) for  $d$  were calculated from the test data. A value of 26,000 psi (179.3 MPa) was calculated for the shear modulus of the base course as shown in Figure 5.19. From the plot of principal stress difference versus principal strain difference an initial tangent slope of 52,000 psi (358.5 MPa) was determined. This value of shear modulus,  $G$ , is used in calibrating both the Drucker-Prager and WES Multimechanical models. This initial shear modulus value is within the normal valid range for granular limestone base course materials as seen in many flexible pavements (Ulidtz, 1998).

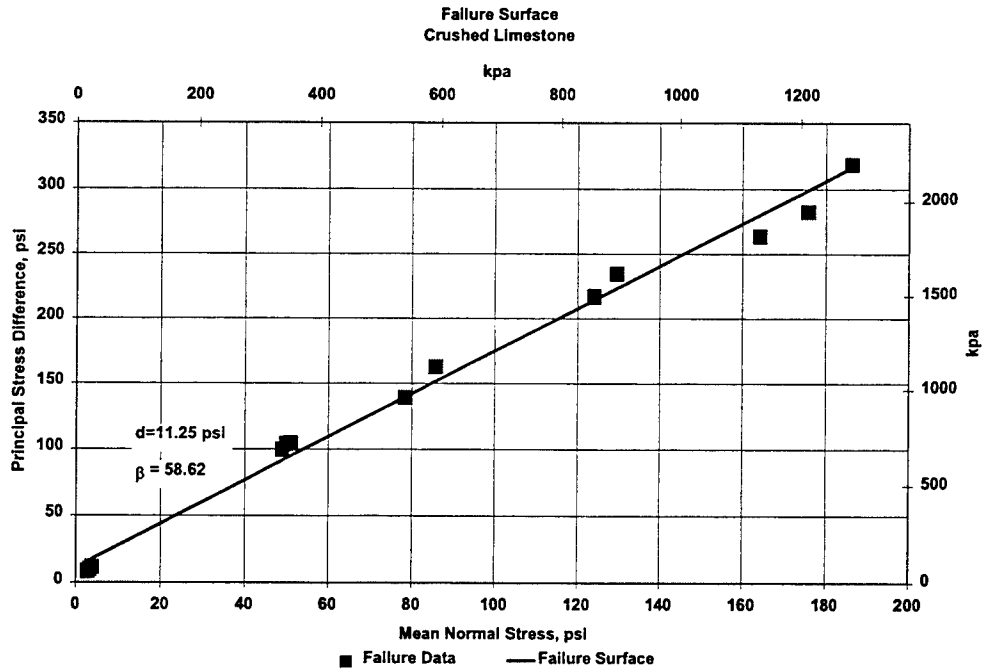


Figure 5.18. Failure surface for crushed limestone base course material

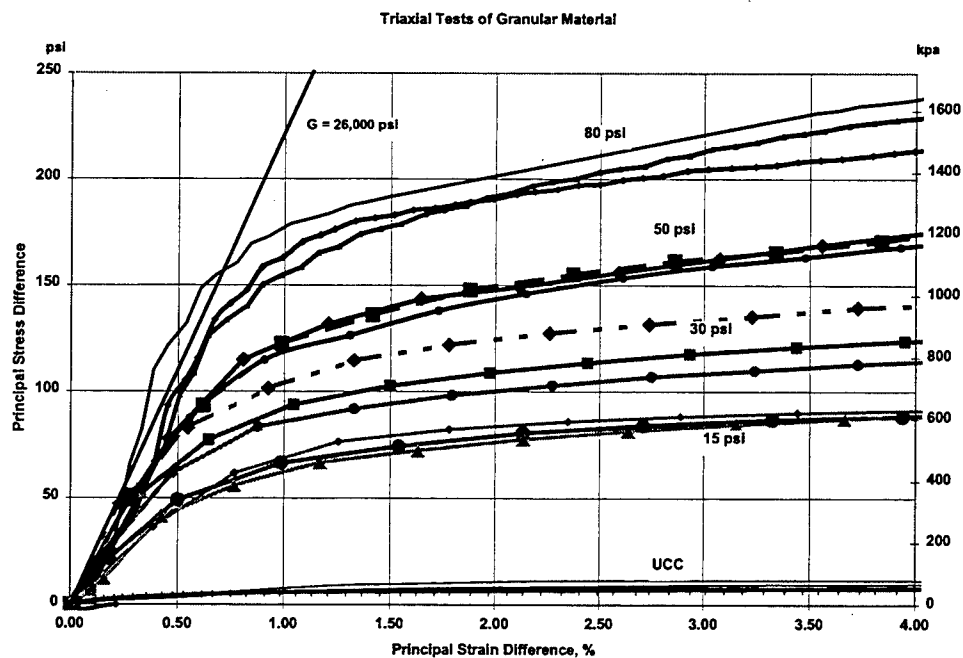


Figure 5.19. Composite plot of initial portion of principal stress difference versus principal strain difference showing shear modulus

## **DETERMINATION OF WES MULTIMECHANICAL MODEL PARAMETERS**

The global parameters were established using the following methods. A summary of the values is shown in Table 5.6. A stand-alone version of the WES MM model called MVIEWER was written to aid in determining those parameters that require trial-and-error methods. MVIEWER provides the analyst with a PC compatible platform to simulate laboratory tests relatively easily. A discussion of the MVIEWER program and its application is presented in Appendix G.

### **Strength Parameters**

The value for friction angle,  $\phi$ , was based on the 15-psi (103.4-kPa) triaxial compression tests and the unconfined compression tests. A value of 48 degrees was determined from the tests using the conventional Mohr's Circle technique described in Appendix H. The value for cohesion was selected based on fitting the model to unconfined compression tests and the 15-psi (103.4-kPa) CTC test data.

### **Stiffness Parameters**

The bulk modulus,  $K$ , is the slope of the Mean Normal Stress versus Volumetric Strain curve and was determined from a hydrostatic compression test. The shear modulus was determined from a plot of shear stress versus shear strain. The slope of the initial portions of the curves should be equal to twice the shear modulus,  $G$ . The value picked for  $G$  was more than 1.5 times greater than the  $K$ , thus the value of Poisson's ratio is slightly negative. Traditional engineering practice would consider reasonable values to range between 0 and 0.5. Theoretically admissible values range between  $-1$  and  $0.5$ . This material is nonlinear, anisotropic, and plastic from early loading such that the classical concept of Poisson's ratio is not truly applicable. The value for  $G$  represents the rate at which shear stress accumulates for a given amount a shear stress. A very stiff initial modulus is desirable so that plastic behavior under relatively low stresses can be simulated using an elastic-plastic model.

### Other Parameters

The  $e$ -log  $p$  curve from a hydrostatic compression test should normally be used to obtain a slope for the normal consolidation line, NCL. The intercept for the line is called the hydrostatic intercept. The hydrostatic compression tests did not produce an overwhelming plastic response, as is the case with clay or other fine-grained soils. The response had a significant elastic component since the preconsolidation pressure of the base course material was not reached during the test. Another approach was used to produce an  $e$ -log  $p$  relation for the limestone aggregate.

The approach was to plot the maximum void ratio achieved during the triaxial compression tests against the logarithm of the mean stress associated with the maximum void ratio. A plot of the 16 data points is shown in Figure 5.20. The model line (gray lower line) was drawn to provide an upper bound to the data. The line used for the  $e$ -log  $p$  relation was drawn parallel to the bounding line but with a slightly higher intercept of 0.7 psi. The reciprocal of  $C_c$  had a magnitude of 8.685. The values provided a reference stress,  $P_e$ , which was used to normalize the mean stress in the model.

The dilatancy factor rate is a scaling factor for shear-volume coupling. In CSSM only one factor is used to control shear-volume coupling. The shear-volume-coupling factor,  $M_c$ , is the ratio of shear stress to mean stress under constant volume.  $M_c$  should have a value of about 1.8 based on the triaxial tests but this magnitude produced contraction in the model during shearing. All of the test specimens dilated during shear and the value of  $M_c$  was adjusted to correctly simulate the volume change during shear.

The parameters for over consolidation (OC) factor and  $\phi$  ratio are intended to reduce the strength of the material as a function of confining stress. The strength parameters for the base course aggregate are shown in Table 5.7. The OC factor and  $\phi$  ratio provides a function to reduce  $\phi$  as the mean stress increases. The values adopted were chosen by trial and error.

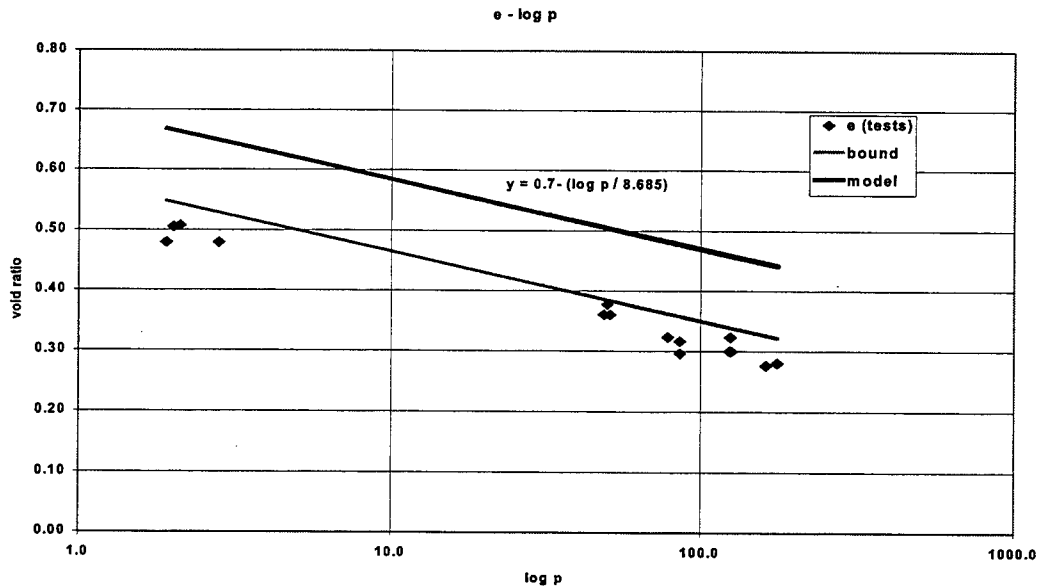


Figure 5.20. Plot used to determine NCL relationship for granular limestone material

Table 5.6. Global Properties for Granular Limestone

PROPERTY	MAGNITUDE	BASIS
Phi	48 degrees	tests at 15 psi confining pressure
Cohesion	0.25 psi	Unconfined Compression
Bulk Modulus	10000 psi	Hydrostatic Compression
Shear Modulus	26000 psi	Plot of shear stress vs. shear strain
Phi Ratio	0.50	adjust to CTC yield data
Hydrostatic Intercept $F_h$	0.70 psi	$e - \log p$ curve (or $e_{\max} - \log p$ from shear tests)
Reciprocal of $C_c$	8.685	$e - \log p$ curve (or $e_{\max} - \log p$ from shear tests)
Shear-Volume Factor MC	0.72	adjust to volume change data
OC Factor	1.80	adjust to yield data
Dilatancy Rate Factor	1.00	Set to unity as CSSM convention



Table 5.7. Strength Parameters by Confining Stress for Granular Limestone

Confining Stress (psi)	Mean Stress at Max Q	Cohesion (psi)	Friction Angle
15	40	2.1	48.2
30	85	1.9	44.5
50	124	1.8	42.7
80	186	1.6	39.8

### Mechanism Parameters

The mechanism parameters are shown in Table 5.8. The underlying philosophy for obtaining model parameters should follow the approach outlined in the earlier section entitled “Calibrating the model – General Approach.” In fact, the calibrations were done in an informal manner as the more subtle features of the model were being discovered through the act of calibration itself.

Table 5.8. Mechanism Properties for Granular Limestone

	Mechanism			
	1	2	3	4
Phi Fraction	0.350	0.420	0.820	0.88
Mean Stress Fraction	0.900	0.770	0.380	0.48
Shear Stiffness Distribution	0.702	0.148	0.058	0.0042
Compression Limit	0.018	0.9	1.00	1.00
Volumetric Stiffness Distribution	0.565	0.38	0.02	0.035

The mechanism parameters were adjusted through trial and error with the MVIEWER program to conform to the conventional triaxial test data. The following guidelines proved helpful in assigning values to the parameters.

1. Set the mechanism strength to yield for the 1<sup>st</sup> mechanism, then 2<sup>nd</sup>, 3<sup>rd</sup> and allow 4<sup>th</sup> mechanism to not yield at all. The phi factor was used to achieve control strength.
2. Use the PFact to alter strength by limiting the mean stress seen by each mechanism.

3. Use the shear ratio to adjust the stiffness of the shear mechanism. The 1<sup>st</sup> to yield should be stiffest. The last mechanism to yield should have the lowest stiffness.
4. Adjust  $M_c$  to provide a reasonable volume change during shearing.
5. Start the calibration with bulk ratio equal to 0.25 for all mechanisms and  $H_{limit}$  set to unity for all limits. Then, lower  $H_{limit}$  on 1<sup>st</sup> mechanism until a effect is achieved.
6. Special consideration is needed to match the unconfined compressive test results. The amount of mean stress applied to a mechanism should be adjusted with the parameter  $P_{Fact}$ .
7. The strongest mechanism (mechanism 4) should be adjusted with  $P_{Fact}$  such that the mechanism fails in unconfined compression and does not fail in confined triaxial compression tests.

### APPLICATION OF MVIEWER

The primary purpose of the MVIEWER program is to provide the analyst with the capability of easily evaluating the effect of changes in input parameters on the stress strain response of the model. The following section demonstrates this feature of the MVIEWER as the program is used to investigate the sensitivity of the stress strain response to some of the model parameters. As discussed earlier, there are ten global properties and twenty mechanism specific properties in the WES MM model. The material constants shown in Tables 5.6 through 5.8 contain the parameters used in the FEM analytical studies of the laboratory and field tests.

Changes in the global material properties have an effect on the response of all four mechanisms. The major parameters that effect the shear strength are the cohesion ( $c$ ) and friction angle ( $\phi$ ). Changes in the shear modulus ( $G$ ) and bulk modulus ( $K$ ) effect the stiffness of the model response. The remaining global parameters are used to adjust the model's dilatancy, and hydrostatic response. When the shear modulus is increased, the response of the entire constitutive model stiffens. In Figure 5.21,  $G$  has been changed from 30,000 psi (206.8 MPa) to 60,000 psi (413.6 MPa).

Similar behavior occurs as  $G$  is decreased from 30,000 psi (206.8 MPa) to 15,000 psi (103.4 MPa). The model response is softened as shown in Figure 5.22. Changes in the bulk modulus,  $k$ , have a smaller effect on the stress strain response of the model as shown in Figure 5.23. As one would expect, the  $K$  term primarily effects the volumetric strain response of the model.

The strength parameters,  $C$  and  $\phi$ , have a pronounced effect on the occurrence of yielding in the WES MM model. The effect of increasing  $\phi$  by only 10% (from  $48^\circ$  to  $52.8^\circ$ ) is shown in Figure 5.24.

The granular limestone material used in this study had a very low cohesion, and large changes in the cohesion parameter  $C$  had a much less pronounced effect on yield than did changes in  $\phi$ . The effect of increasing  $C$  by 10 times is picked up at only the higher stress level and is shown in Figure 5.25.

The PHIRATIO and DECAY parameters are used to adjust the friction angle as a function of mean stress and the degree of dilatancy experienced. Figure 5.26 shows the small effect that a change in PHIRATIO has on the stress strain response of this material.

Figure 5.27 shows the effect of a change in the DECAY parameter on the stress strain response of the WES MM model for this type of material. The effects of DECAY and PHIRATIO are seen primarily in the response of the model at higher strain levels when dilatancy has begun to occur.

The remaining global parameters are related to the hydrostatic response ( $M_c$ ) of the model and dilatancy scaling ( $\gamma$ ). The  $M_c$  parameter is used to normalize the hydrostatic stress to the reference stress ( $P_e$ ) from the Normal Consolidation Line. The dilatancy scaling factor,  $\gamma$ , is left at unity for the material used in this study. The twenty mechanism specific parameters effect the shape of the stress strain curve in the same manner their respective global counterparts.

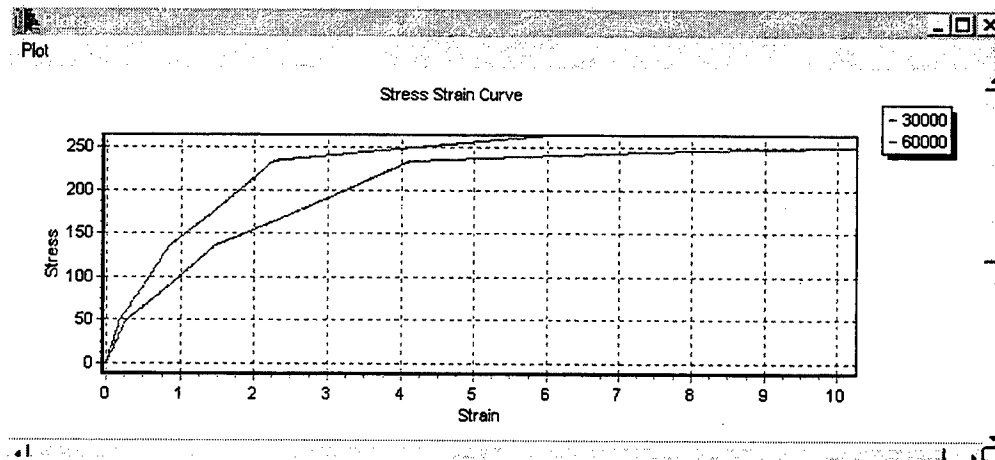


Figure 5.21. Stress strain response with  $G=30,000$  psi (206.8 MPa) (lower line) and  $G=60,000$  psi (413.6 MPa) (upper line)

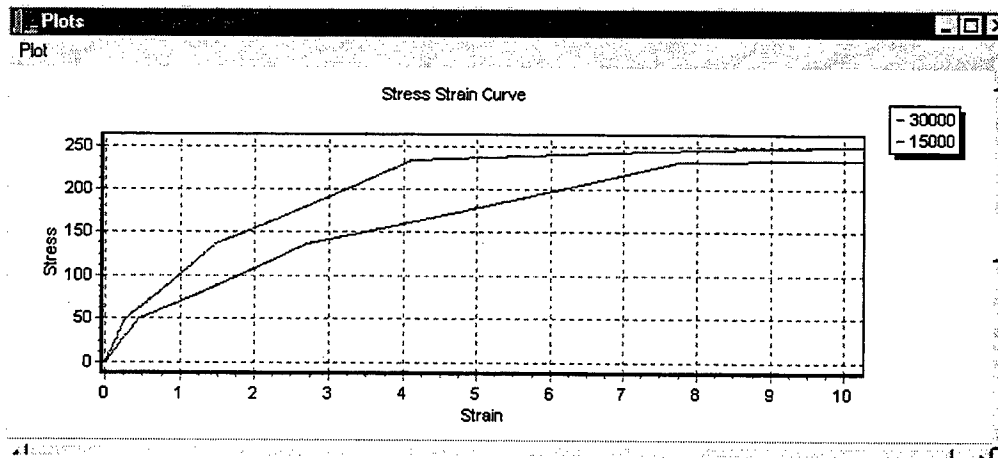


Figure 5.22. Stress strain response with  $G=30,000$  psi (206.8 MPa) (upper line) and 15,000 psi (103.4 MPa) (lower line)

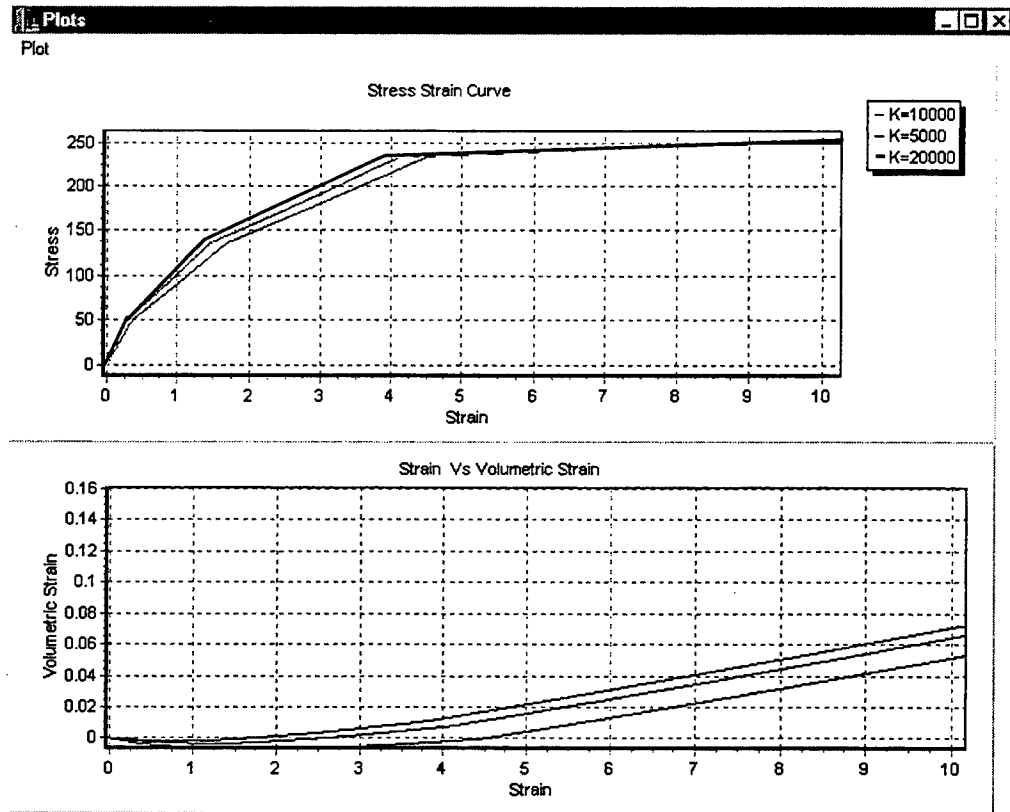


Figure 5.23. Stress strain response with  $K=20,000$  psi (137.9 MPa) (upper line), 10,000 psi (68.9 MPa) (middle line), and 5,000 psi (34.3 MPa) (lower line)

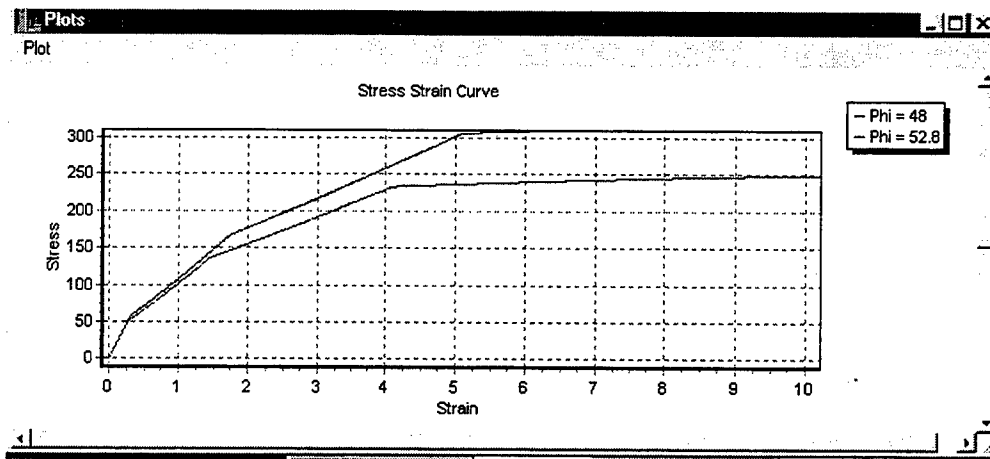


Figure 5.24. Stress strain response with  $\phi=48^\circ$  (lower line) and  $\phi=52.6^\circ$  (upper line)

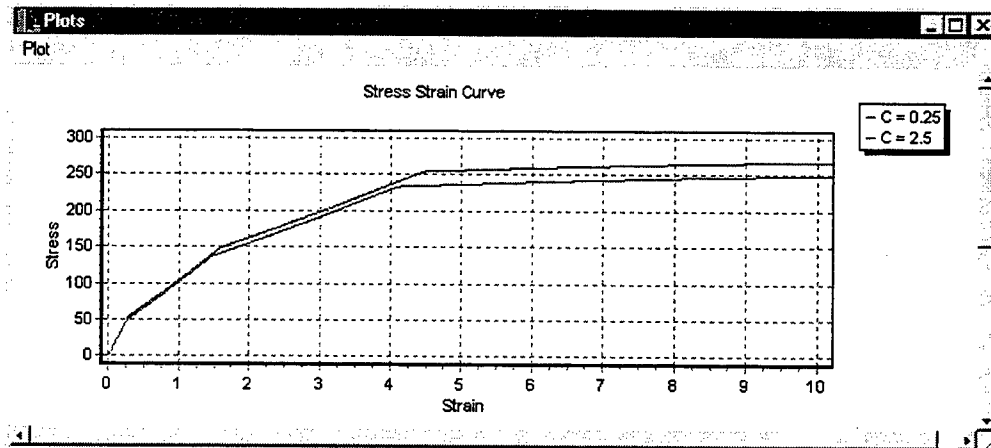


Figure 5.25. Stress strain response with  $C = 0.25$  (lower line) and  $C = 2.5$  (upper line)

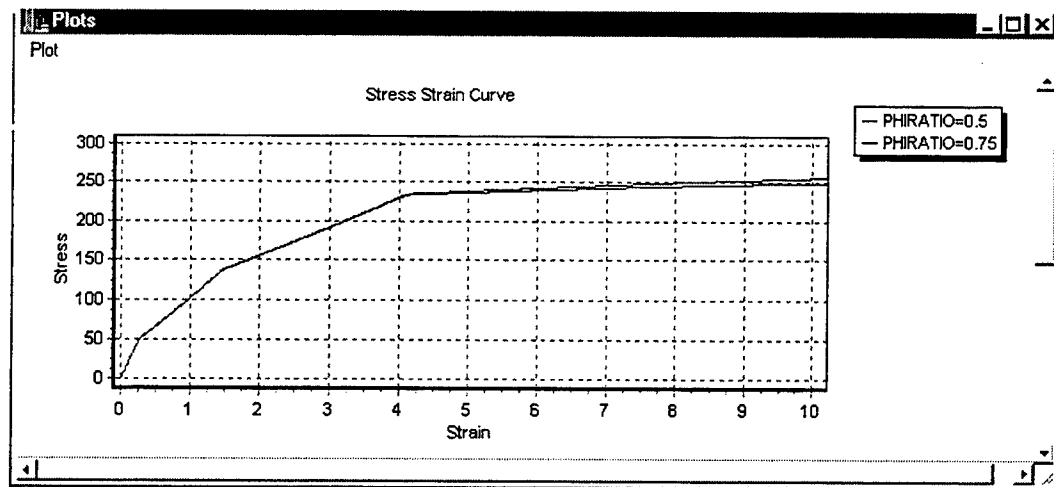


Figure 5.26. Stress strain response with PHIRATIO=0.5 (lower line) and PHIRATIO=0.75 (upper line)

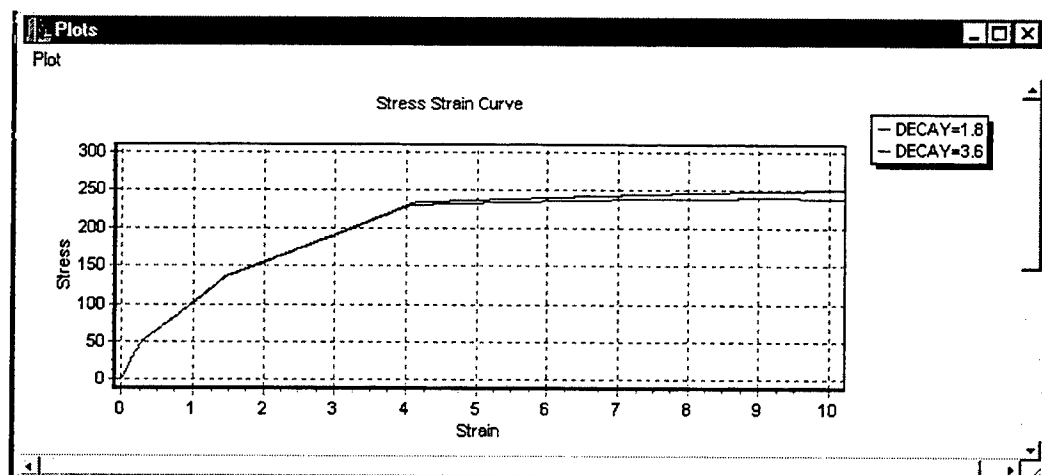


Figure 5.27. Stress strain response with DECAY=3.6 (lower line) and DECAY=1.8 (upper line)

## **CHAPTER 6: MODEL VERIFICATION**

### **VERIFICATION ANALYSES**

In order to verify that the parameters obtained in the calibration procedures provide adequate response predictions it was necessary to conduct analytical simulations of selected laboratory and field tests using the ABAQUS finite element code. The predicted response was compared to the measured response obtained during the tests to provide an indication of the accuracy of the model calibrations. Both constitutive models, Drucker Prager and WES MM, were used in the laboratory verification analyses. Only the WES model was used in the field test analyses.

### **ABAQUS ISSUES**

The ABAQUS user must enable some special features and change certain defaults to obtain a solution of a non-linear problem involving a frictional material. Three keywords are used, \*STEP, \*STATIC, and \*CONTROL. The use of the terms time step and load step are used interchangeably in static analysis problems with ABAQUS. Time is used as the arbitrary index upon which loads are incremented to arrive at a solution in all ABAQUS runs in this study. Each of the examples comes from the input file provided in Appendix A.

The \*STEP keyword should have NLGEOM, EXTRAPOLATION, UNSYMM, and INC features considered. The NLGEOM enables large deformation features. The EXTRAPOLATION feature may be set to EXTRAPOLATION=NO to suppress extrapolation of the strain increment to the next increment. The EXTRAPOLATION=YES is the default. The INC switch should be used to raise the number of increments above the default value of 10. Finally, the UNSYMM=YES should be enabled so that the entire stiffness matrix is used. ABAQUS uses a symmetric matrix as default. Frictional materials have an unsymmetrical stiffness matrix. A symmetric approximation may work, but convergence should be made easier if the unsymmetrical matrix is used. Once NLGEOM is turned on it remains on.



**\*STEP, EXTRAPOLATION=NO, INC=100, UNSYMM=YES, NLGEOM**

The **\*STATIC** keyword has four time parameters on one line: initial time increment, total step length, minimum time increment allowable, maximum time increment. Automatic time incrementation is used whenever possible. The time has no actual units of clock time unless some time dependant phenomenon is being considered. ABAQUS generates a warning about this situation on each static step. The default for minimum time increment is 1.0E-5 time the size of the step. The static parameters must be set each time the **\*STATIC** is used.

**\*STATIC**

0.1, 1.0, 1.E-8, 0.25

The **\*CONTROL** keyword has several important features. The **\*CONTROL** keyword can enable a line search that is particularly important during reversals of strain or stress. Enable the line search and allow 4 to 6 line search iterations. ABAQUS uses a displacement criterion in addition to a force residual criterion to determine equilibrium. The displacement criterion should be turned off with the **\*CONTROL** keyword. Finally the allowable number of attempts to reach equilibrium should be increased above the default values. The **\*CONTROL** keyword can be use to increase the time incrementation parameters to allow more attempts to reach equilibrium before cutting a time increment and allow more attempts to reach equilibrium in general. The defaults are too small for non-linear analyses. The control options are set once and stay in force on all subsequent steps unless changed. When the **FIELD** parameter is set to a **DISPLACEMENT** value it affects the tolerance of residual force that is allowed for an increment to converge. The **LINE SEARCH** parameter is used to set the solution technique to a more robust form than that used for linear problems. The value is basically a switch that enables the line search algorithm, if the value is anything other than zero. The **TIME INCREMENTATION** parameter is set to enable the automatic time

incrementation procedures in ABAQUS to be changed to obtain solutions to highly non-linear problems (Meade, 1997).

**\*CONTROLS, PARAMETERS=FIELD, FIELD=DISPLACEMENT**

0.07, 1.0, 1.0

(ratio of largest residual force to average model force, displacement criteria switches)

**\*CONTROLS, PARAMETERS=LINE SEARCH**

6 (enables line search to be performed)

**\*CONTROLS, PARAMETERS=TIME INCREMENTATION**

12, 18, 21, 50, 15, , , 15, ,6

(incrementation cut back factors)

These are general findings and are not absolute since each and every new non-linear FEM model or mesh may require different techniques to reach a convergent solution. Simple changes in material properties may create very complex model behaviors that become very difficult to solve numerically.

### **SIMULATION OF LABORATORY TESTS**

Analytical simulations of all four levels of conventional triaxial compression tests [15 psi (103.4 kPa), 30 psi (206.8 kPa), 50 psi (344.7 kPa), and 80 psi (551.6 kPa)], uniaxial strain tests, hydrostatic compression tests, and unconfined compression tests were conducted using both models. The WES MM model was used to simulate a repeated load conventional triaxial compression test at low strain levels.

#### **Conventional Triaxial Compression Tests**

Simulations of the 4 levels of conventional triaxial compression test were performed using both the DP model and the WES MM model. The stress-strain results of the simulations using both the DP model and the WES MM model are shown along with the test results in Figures 6.1 through 6.4.

The DP predicted failure surface was very close to that obtained from the laboratory with a predicted  $\beta$  of  $58.2^\circ$  and a  $d$  of 7 psi (82.74 kPa) compared with  $\beta = 58.6^\circ$  and  $d = 11.25$  psi (130.01 kPa) from the laboratory data. The failure points from the DP simulations are shown in Figure 6.5. The DP model behaves in a manner consistent with a classical elastic-plastic formulation. The pre-yield behavior is characterized by elastic response followed by plastic response when the yield stress is exceeded. The DP model was calibrated using the procedures outlined by the ABAQUS user documentation as described in Chapter 5. The model under predicts maximum stress in all 4 simulated tests. The predicted stress strain behavior of the granular material was quite different from the response measured in the tests. One of the shortcomings of the DP model is its inability to adequately capture the response of granular materials at low stress levels. Until the yield point is reached, purely elastic recoverable strain is incurred due to load application. The material will appear to be much stiffer in DP model predictions prior to yield than that seen in tests since only elastic behavior is modeled prior to the yield point.

The preconsolidation pressure for the material is well beyond the stress levels of interest in most pavements. This resulted in the cap portion of the DP model not coming into play for any of the simulations, which produced non-dilative response predictions. The non-dilative behavior of the DP model can be seen in Figure 6.6, where the mean normal stress is plotted versus volumetric strain.

The agreement of the WES MM model predictions with the test data is best for the 30-psi (206.8 kPa) test. The stress-strain response for all four CTC tests are very good. The basic shape of the curve and the maximum stress level reached is very close for all except the 80-psi (551.6 kPa) test. The accuracy of the 80-psi (551.6 kPa) test prediction was sacrificed to achieve a closer fit at lower stress levels (i.e., stress levels closer to those expected in field tests to be discussed later in this chapter). The predicted failure surface of the WES MM model, in a principal stress difference versus mean normal stress space, was very close to that

obtained from the laboratory with a predicted friction angle,  $\beta$ , of  $60^\circ$  and a cohesion,  $d$ , of 12 psi (82.74 kPa) compared with  $\beta = 58.6^\circ$  and  $d = 11.25$  psi (130.01 kPa) from the laboratory test data. A plot of the WES MM failure data is shown in Figure 6.7. This plot is very close to the failure surface plotted from the laboratory test data. The ability of the WES MM model to change friction angle with increasing mean normal stress is primarily responsible for the small differences.

The post yield shear dilatant behavior of the WES MM model is also demonstrated in the composite plot of mean normal stress versus volumetric strain shown in Figure 6.8. The breakpoints (changes in slope of the stress-strain curve) in the WES MM model are also very evident in the response shown in Figure 6.8.

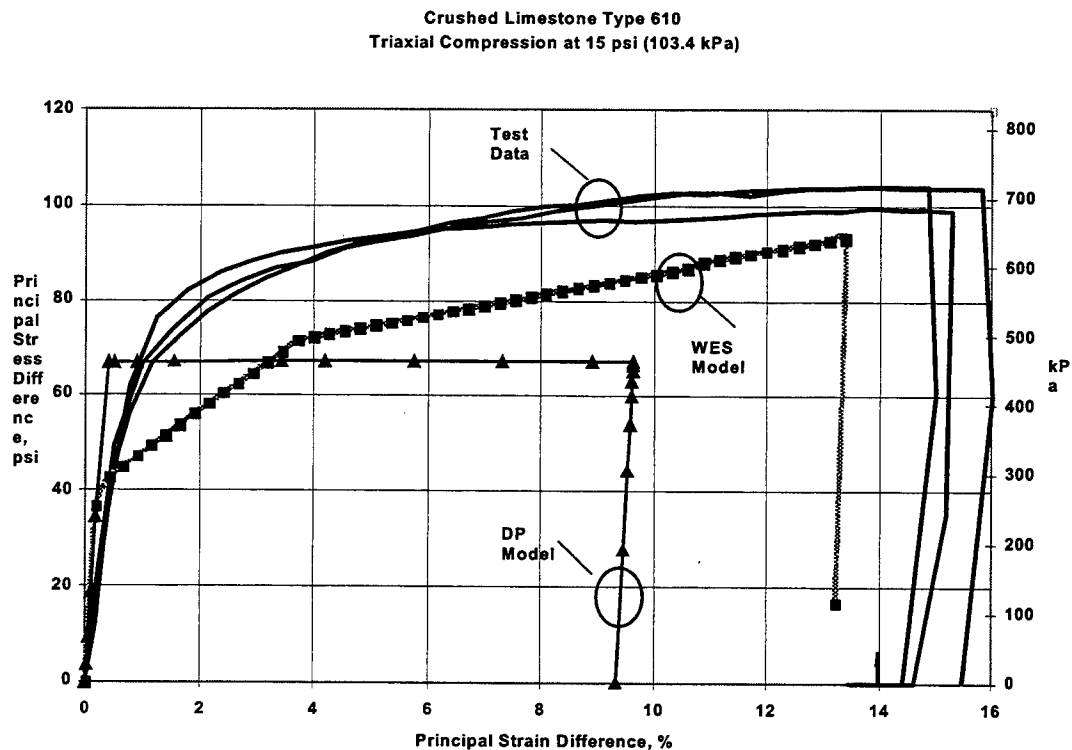


Figure 6.1. Composite plot of principal stress difference versus principal strain difference for 15 psi (103.4 kPa) test

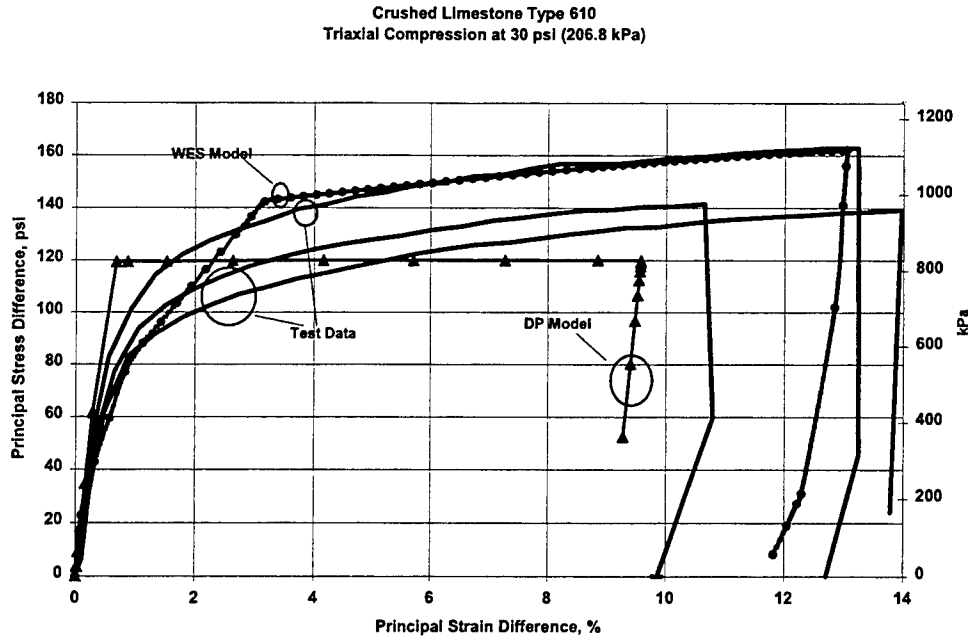


Figure 6.2. Composite plot of principal stress difference versus principal strain difference for 30 psi (206.8 kPa) test

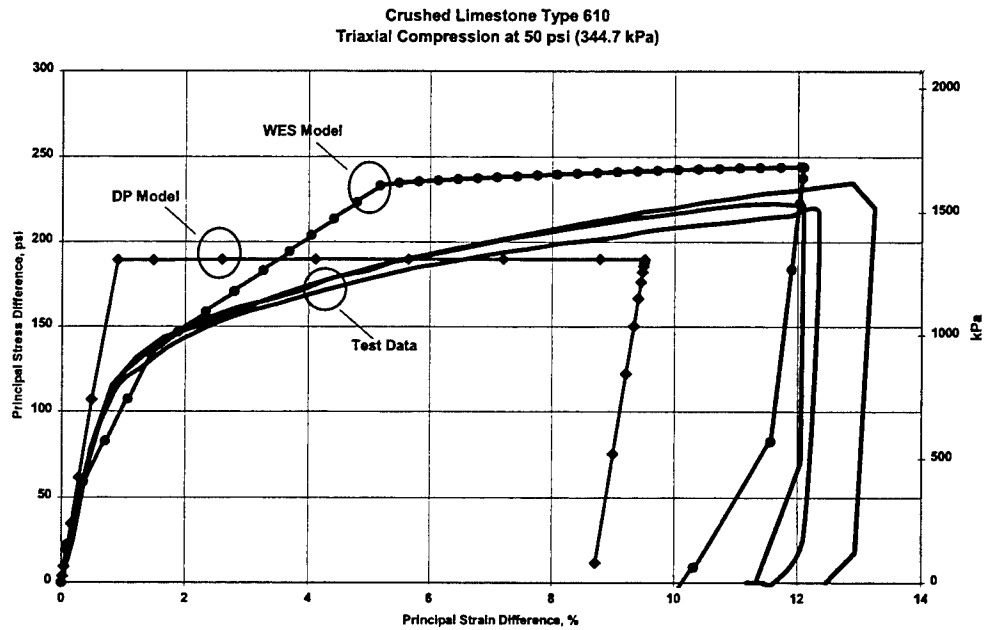


Figure 6.3. Composite plot of principal stress difference versus principal strain difference for 50 psi (344.7 kPa) test

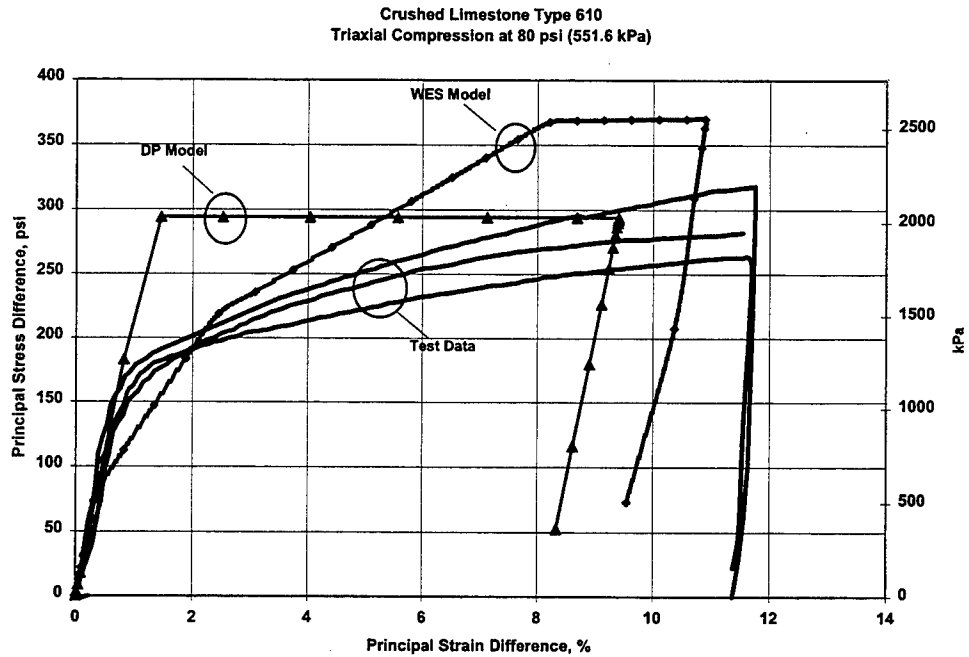


Figure 6.4. Composite plot of principal stress difference versus principal strain difference for 80 psi (551.6 kPa) test

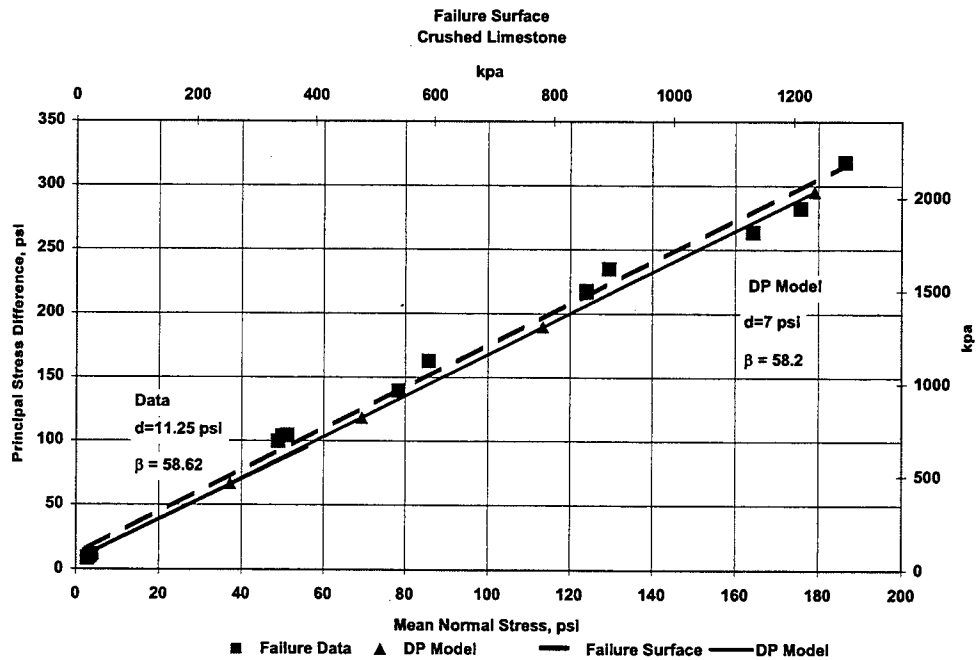


Figure 6.5. Predicted failure surface for Drucker-Prager model compared with test results

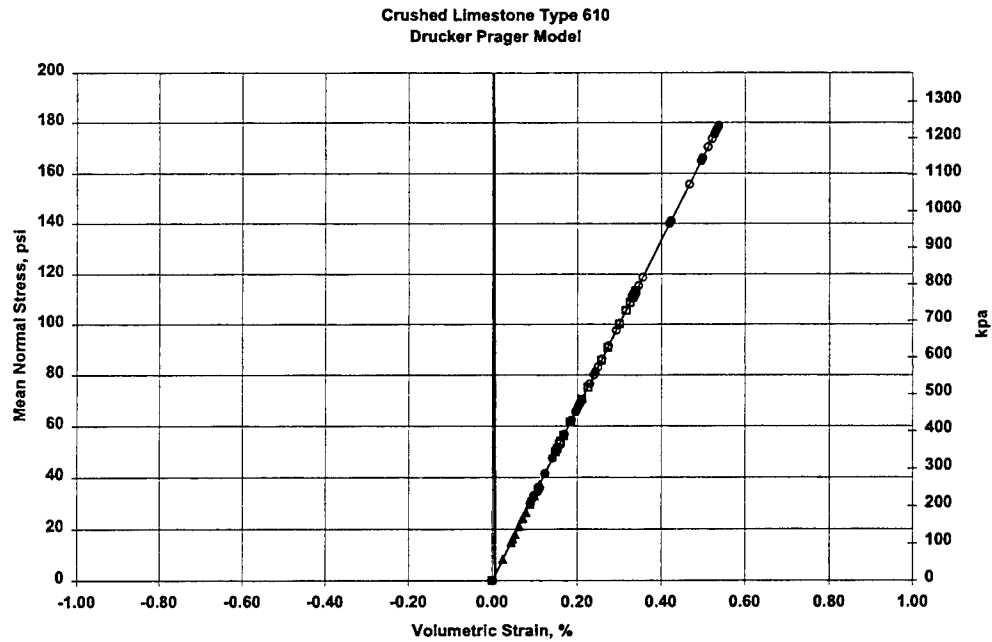


Figure 6.6. Composite plot of mean normal stress versus volumetric strain for DP predictions of CTC tests

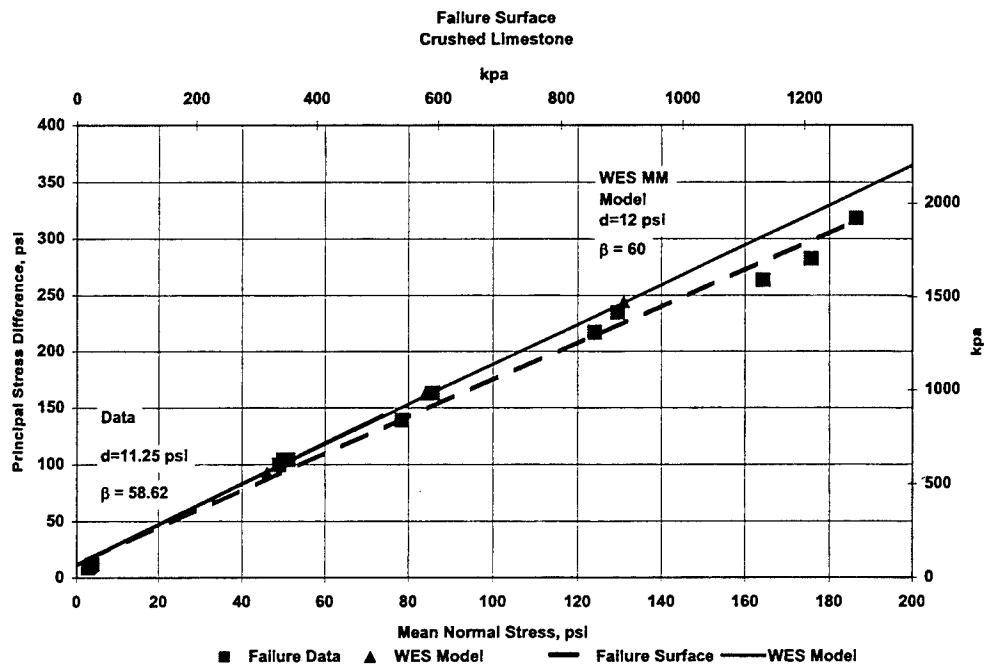


Figure 6.7. Predicted failure surface for WES MM model compared with test results

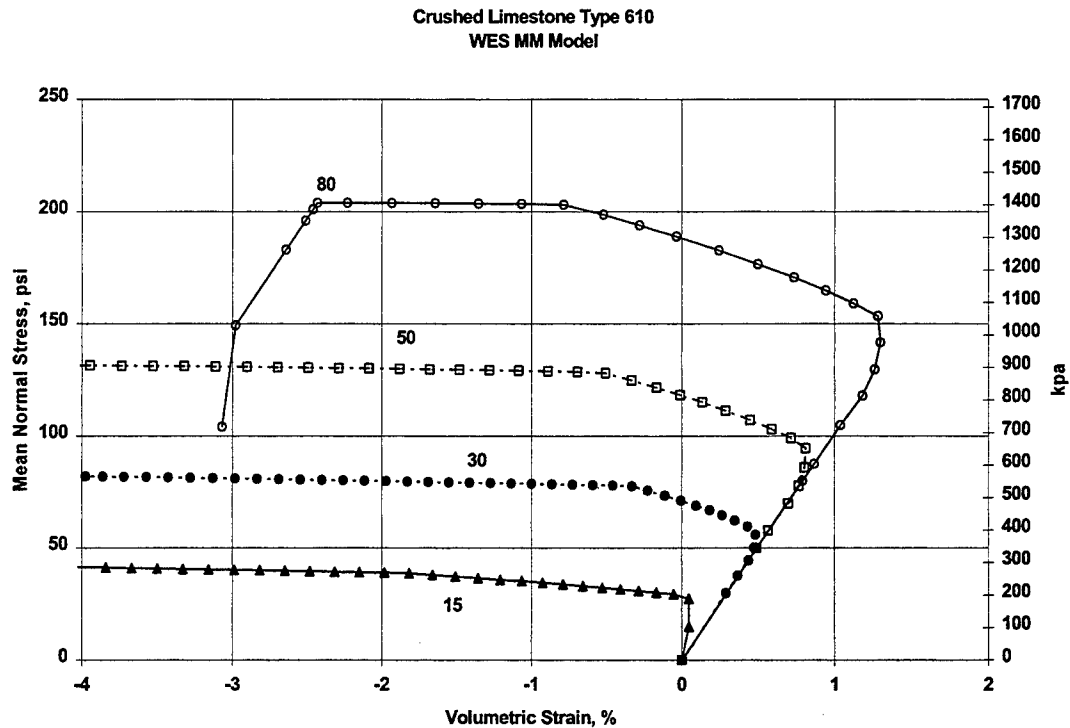


Figure 6.8. Composite plot of mean normal stress versus volumetric strain for WES MM predictions of CTC tests

### Uniaxial Strain Tests

Simulations of the uniaxial strain tests (UXE) were performed using both the DP model and the WES MM model. The stress-strain results of the UXE simulations using the DP model and the WES MM model are shown with the test results in Figures 6.9 through 6.11. The WES MM model demonstrates the ability to predict the stress path required to maintain uniaxial strain conditions through loading and unloading. The existence of a residual (locked in) stress is typical for this kind of test, and can be seen in the WES MM model as well as the test data shown in Figure 6.9. The DP model is unable to capture the shearing response that creates the “locked in” stress after unloading. This can be attributed to the fact that the UXE stress path never intersects the DP failure surface. That leaves only elastic response for the DP model during this test. The WES MM model is able to capture this behavior through the separation of hydrostatic and shear response in the HYDROS and



Amnos routines described in Chapter 4. The plot of mean normal stress versus volumetric strain shown in Figure 6.11 demonstrates the ability of the WES model to capture the overall stiffness of the material in hydrostatic conditions, but its shortcomings in modeling the true volumetric stress-strain response are also evident. Additional effort in the calibration of the hydrostatic mechanism parameters of the WES MM model may well provide the accuracy of response predictions missing in these analyses. Although this type of test is useful in exercising the model, it is not particularly representative of any real condition that exists in a loaded pavement.

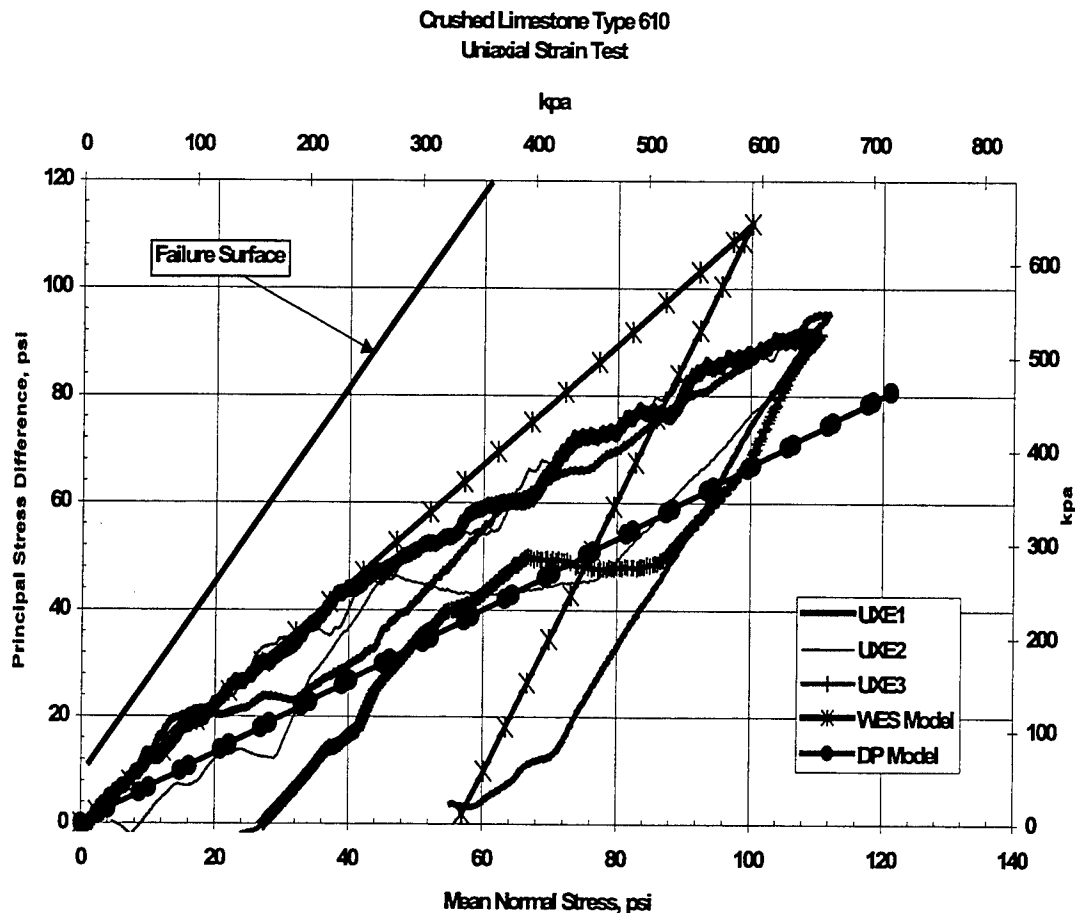


Figure 6.9. Composite plot of principal stress difference versus mean normal stress for uniaxial strain tests

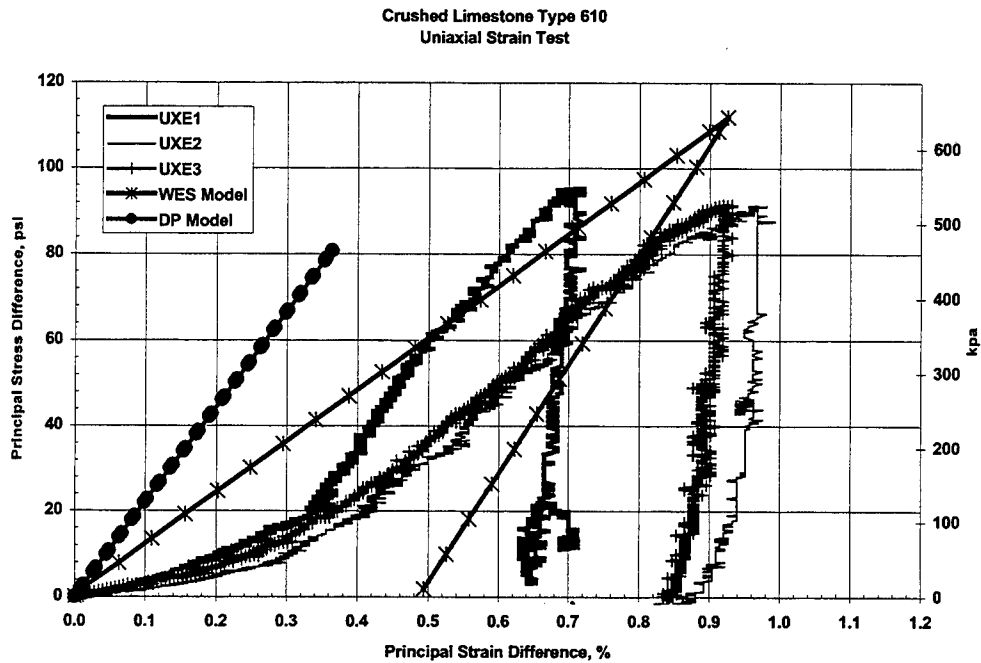


Figure 6.10. Composite plot of principal stress difference versus principal strain difference for uniaxial strain tests

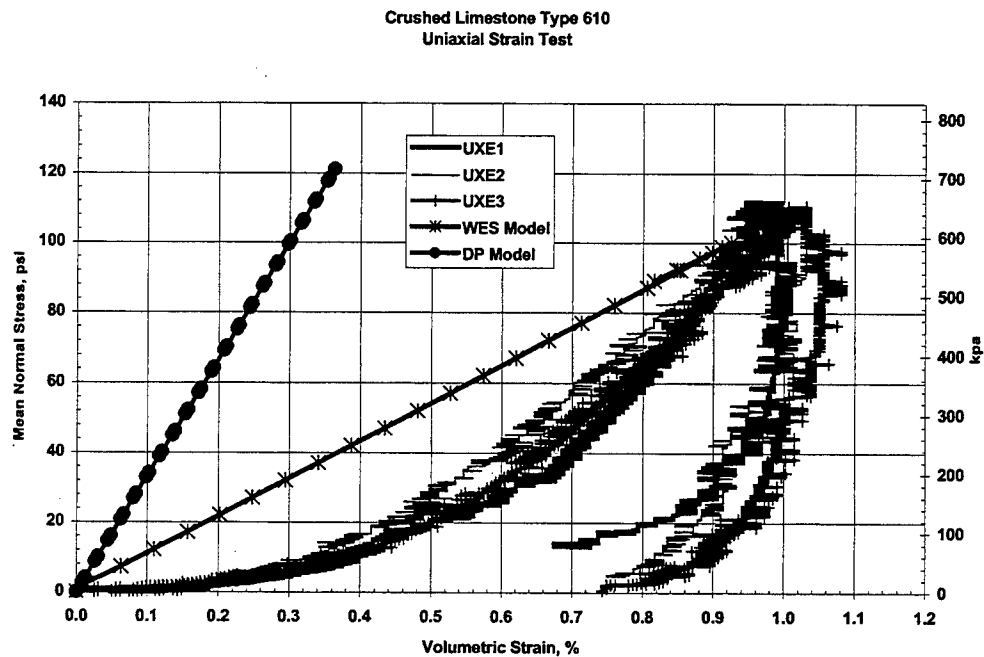


Figure 6.11. Composite plot of mean normal stress versus volumetric strain for uniaxial strain tests

### **Hydrostatic Compression Tests**

Simulations of the hydrostatic compression tests (HC) were performed using both the DP model and the WES MM model. The stress-strain results of the HC simulations using the DP model and WES MM model are shown with the test results in Figure 6.12. The DP model can only produce a linear response to hydrostatic state of stress that is a function of the bulk modulus that is fixed by selection of Young's modulus and Poisson's ratio. The response of the DP model is stiffer than the test data under hydrostatic conditions. However, matching the response of the DP model under CTC conditions was more crucial than matching hydrostatic response. Therefore the Young's modulus and Poisson's ratio were selected with the CTC tests as the benchmark test results. Such a trade off in performance is a shortfall of a simplistic model like DP. In essence, one only has four parameters to work with to produce stiffness and yield that can fit only a limited number of situations. The WES MM model did not perform as well for hydrostatic test conditions as it did in simulations of tests with a lot of shear stress. The response of the model is almost purely linear and does not exhibit yield in hydrostatic test conditions. As was the case with the DP model, matching the response of the WES MM model under CTC conditions was more crucial than matching the response of hydrostatic test conditions.

### **Unconfined Compression Tests**

Analytical simulations of the unconfined compression tests (UCC) were performed using both the DP model and the WES MM model. The stress-strain results of the HC simulations using the DP model and WES MM model are shown with the test results in Figures 6.13 and 6.14. The DP model provides an acceptable prediction of the yield stress, however it does only a minimal job of modeling the overall stress strain response of the unconfined tests. Again, a model like the DP is just too simple in nature to capture the complex response of an unconfined test of granular material. The WES MM model did a good job of modeling the overall stress strain response of the unconfined compression test. The WES

MM model also has the ability to capture both the dilative and softening response of the granular material under unconfined compression. These test also serve primarily as calibration tests and an index of a models applicability to a wide range of conditions and are not representative of conditions that would exist in the granular base course of a pavement.

### **Cyclic Triaxial Compression Tests**

Simulations of the cyclic triaxial compression tests (CTCR) were performed using the WES MM model. The analytical predictions made using the standard calibration presented in Chapter 5 produced cyclic behavior that was somewhat different form the laboratory tests. The model did produce hysteresis, but the shape and size of the hysteresis loops at low strain levels and the magnitude of the strain at which the cyclic behavior began was different from the test data as shown in Figure 6.15. A modified calibration was completed (Shown in Table 6.1 and Table 6.2), and the cyclic test was rerun with the new calibration. The ability of the WES MM model to closely capture cyclic response was clearly demonstrated in this analysis. However, obtaining this calibration required a lot of iterations and intimate knowledge of model behavior. One of the original goals of this model development was to produce a constitutive model that would be relatively easy to calibrate from standard geotechnical laboratory tests. This modified calibration also proved to create numerical convergence problems with ABAQUS when applied to the field test section FEM analyses. When using a commercial finite element code like ABAQUS, one does not have access to the source code for the finite element program. As a result, when problems with convergence are encountered and can not be solved through the use of \*CONTROL options, other avenues of completing an analysis, such as equivalent alternate material model calibrations, must be considered. Even though the modified cyclic calibration produces excellent stress-strain agreement with the test data at low stress levels, the amount of permanent strain accumulated from each cycle is very close for both calibration. Given these considerations, the original standard calibration was used for all test section analyses.

Table 6.1. Global Properties for Modified Calibration

PROPERTY	MAGNITUDE
Phi	48 degrees
Cohesion	0.25 psi (1.72 kPa)
Bulk Modulus	100000 psi (689.5 MPa)
Shear Modulus	200000 psi (689.5 MPa)
Phi Ratio	0.50
Hydrostatic Intercept	0.70 psi (4.82 kPa)
Reciprocal of Cc	8.685
Shear-volume Factor Mc	0.72
OC factor	1.80
Dilatancy Rate Factor	1.00

Table 6.2. Mechanism Properties for Modified Calibration

	Mechanism			
	1	2	3	4
Phi Fraction	0.1	0.25	0.6	0.9
Mean Stress Fraction	2.2	0.86	0.3	0.35
Shear Stiffness Distribution	0.49	0.26	0.068	0.011
Compression Limit	0.018	0.9	1.00	1.00
Volumetric Stiffness Distribution	0.565	0.38	0.02	0.035

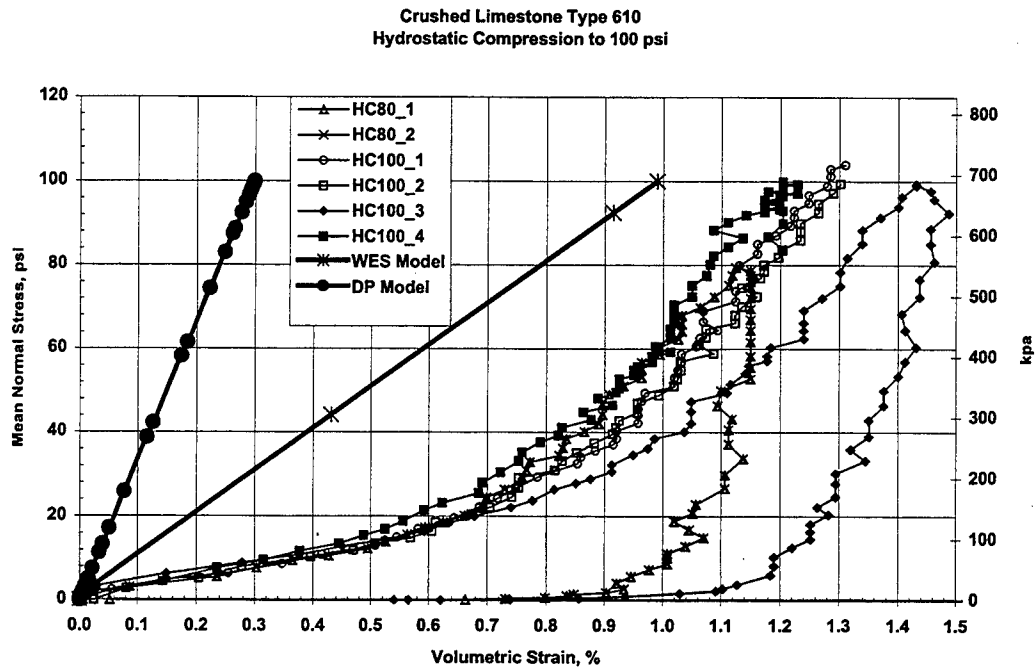


Figure 6.12. Composite plot of mean normal stress versus volumetric strain for hydrostatic compression tests

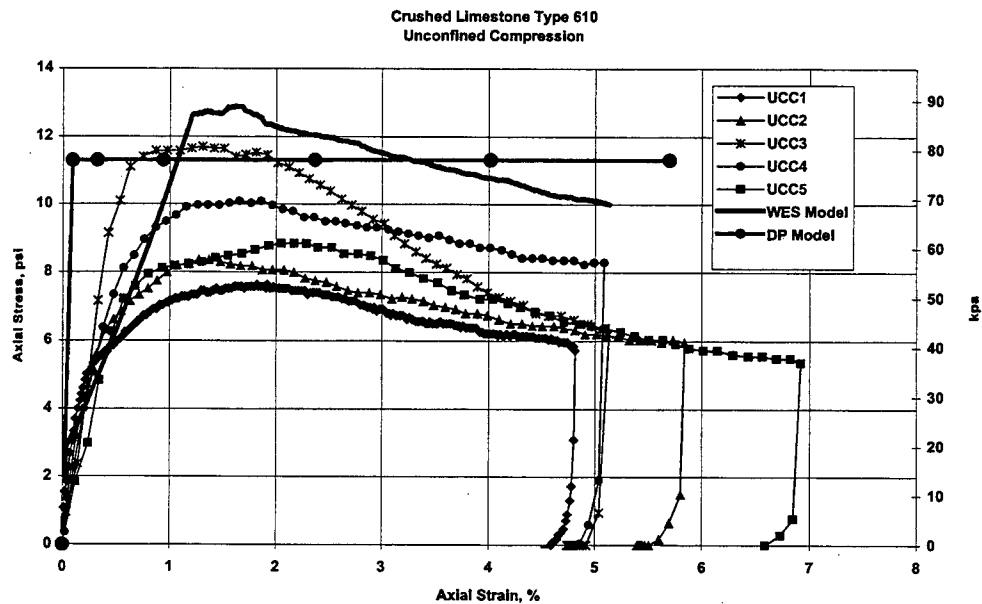


Figure 6.13. Composite plot of axial stress versus axial strain for unconfined compression tests

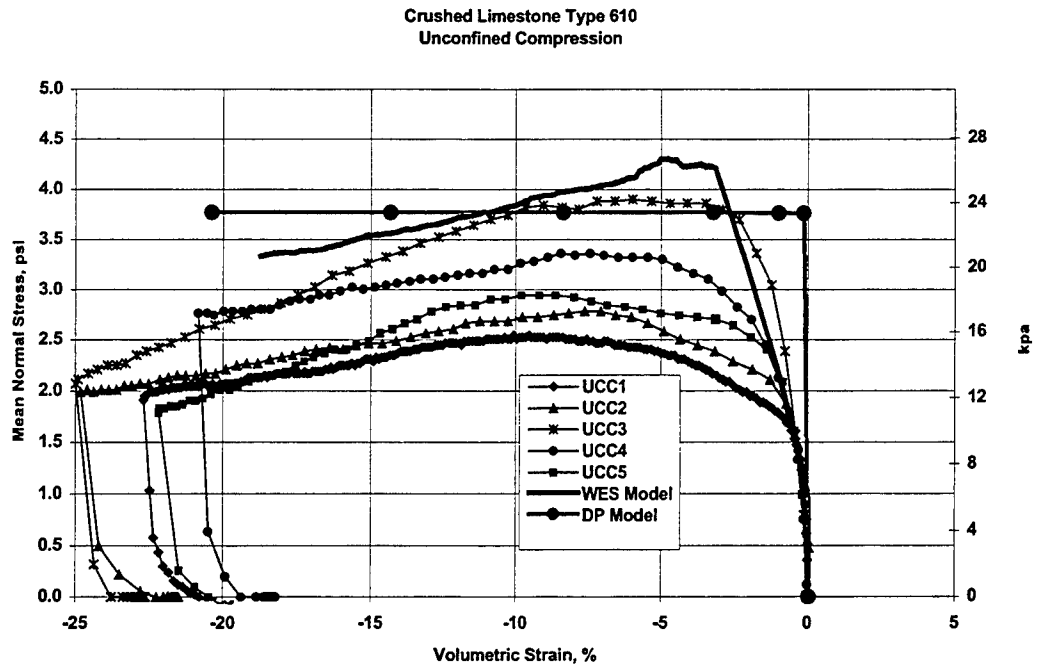


Figure 6.14. Composite plot of mean normal stress versus volumetric strain for unconfined compression tests

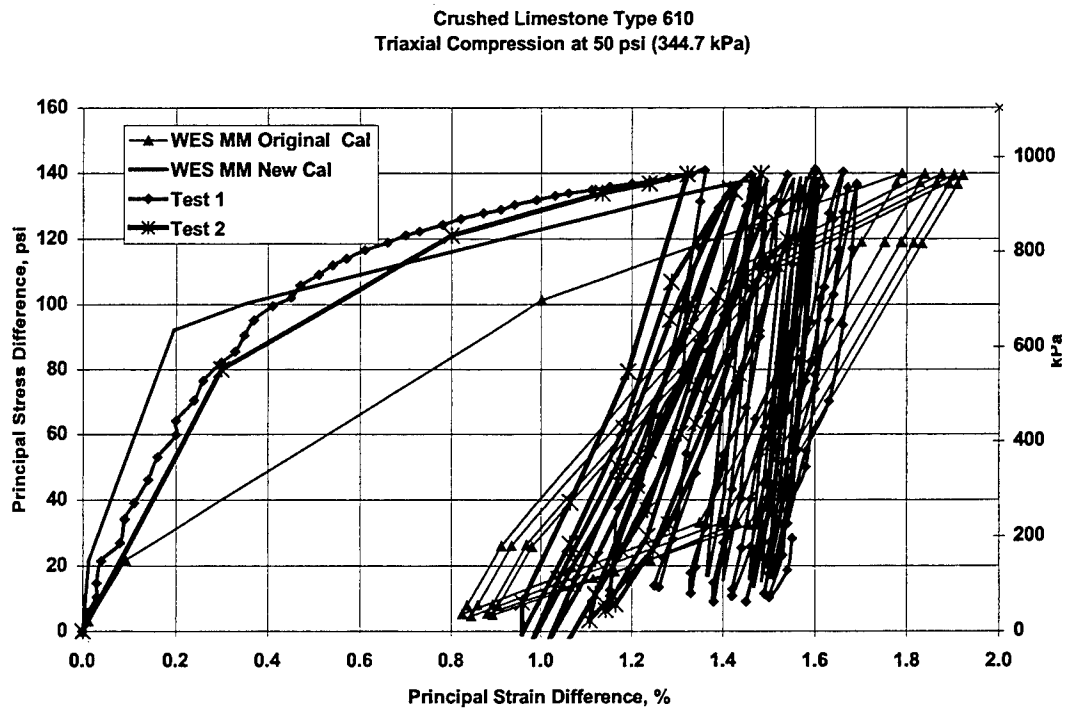


Figure 6.15. Comparison of FEM prediction of cyclic response with test data

## **FIELD TEST SECTIONS**

Cyclic tire loads of two test items from the selected test section (Webster, 1993) were simulated with the WES MM model being used to define the properties of the granular base course material. The remaining layers were modeled using linear elastic properties.

### **General Test Section Description**

Test sections were located at the U.S. Army Engineer Waterways Experiment Station (WES) in Vicksburg, MS. They were constructed within an aircraft hangar so that they could be sheltered from rain and sun. The existing soil floor was excavated to a depth of 40 in. (1016 mm) and the lean clay at the bottom of the trench was compacted to a CBR strength greater than 10. The bottom and sides of the trench were lined with sheets of polyethylene to minimize drying of the heavy clay subgrade during traffic tests.

The subgrade under all test items consisted of heavy clay (CH) material, according to the Unified Soil Classification System. This material had a liquid limit (LL) of 67 and a plasticity index (PI) of 45. When compacted in accordance with ASTM D 698 (standard Proctor), it had an optimum moisture content of 23 percent (by mass of dry material), corresponding to a maximum dry density of 92 lb/ft<sup>3</sup> (1475 kg/m<sup>3</sup>). Compaction was accomplished in 6-in. (152-mm) lifts with a rubber-tired roller. The final subgrade surface was smoothed with a vibratory steel drum roller.

The base course material was an MDOT type 610, crushed limestone. When compacted in accordance with ASTM D 1557 (modified Proctor), it had an optimum moisture content of 4.5 percent (by mass of dry material), corresponding to a maximum dry density of 144 lb/ft<sup>3</sup> (2307 kg/m<sup>3</sup>). The base course material was back-dumped, spread with a bulldozer and compacted in 6-in. (152-mm) lifts with a vibratory steel drum roller. The top lift of the base course was also compacted with a solid rubber-tired roller. All test items were surfaced with 2 in. (51 mm) of asphalt concrete (50-blow Marshall specification). The maximum aggregate size for the asphalt concrete was 0.5 in (12.5 mm) and the minimum Marshall



stability was 1500 lbs. (6.67 kN). The asphalt surfacing covered an area 50 ft (15.2 m) by 224 ft (68.3 m). This area included all test items and extended 40 ft (2.2 m) past each end of the test section.

### As-Constructed Properties

Cross-section level readings taken during construction indicated that the base layer thicknesses of all test items were constructed to within 1 in. (25 mm) of design thickness.

Thickness estimates for the asphalt concrete were obtained from twelve core samples.

Thicknesses ranged from 2.0 in. (51 mm) to 2.6 in (66 mm). Table 6.3 shows a summary of as-constructed data for base course and subgrade.

Table 6.3. As-constructed Properties for Subgrade and Base Course.

Test Lane	Material	Depth of Measurement in. (mm)	CBR	Moisture Content (%)	Dry Density, lb/ft <sup>3</sup> (kg/m <sup>3</sup> )	Percent of Maximum Density
1	base course	2 ( 51)	-----	4.1	137.2 (2198)	96
1	subgrade	10 (254)	7.1	26.3	92.8 (1487)	102
1		16 (406)	6.9	26.2	92.3 (1479)	101
1		22 (559)	7.3	25.9	93.5 (1498)	103
2	base course	2 ( 51)	-----	4.3	136.9 (2194)	95
2	subgrade	16 (406)	2.5	31.4	86.6 (1388)	98
2		22 (559)	2.7	30.5	86.9 (1393)	98
2		28 (711)	2.3	31.9	86.0 (1378)	98

### Instrumentation

Multi-depth deflectometers (MDD) were used to measure both recoverable and permanent deformations. A single MDD was installed in each of test items 1 and 2 in both traffic lanes 1 and 2. These MDDs consisted of a support shaft and up to four modules, each of which measured vertical deflection at a different depth. In plan view, the MDDs were

centered in the test items. The MDDs were retrofitted into the pavements by using an auger to dig a vertical hole, 1.5 in. (37.5 mm) in diameter, through the pavement system. The MDD shafts were anchored 8 ft (2.4 m) below the surface in order to provide a motionless reference for deflection measurements. Each MDD included a module at a depth just beneath the asphalt concrete layer and just beneath the base course layer. Figure 6.16 shows a general schematic of an MDD.

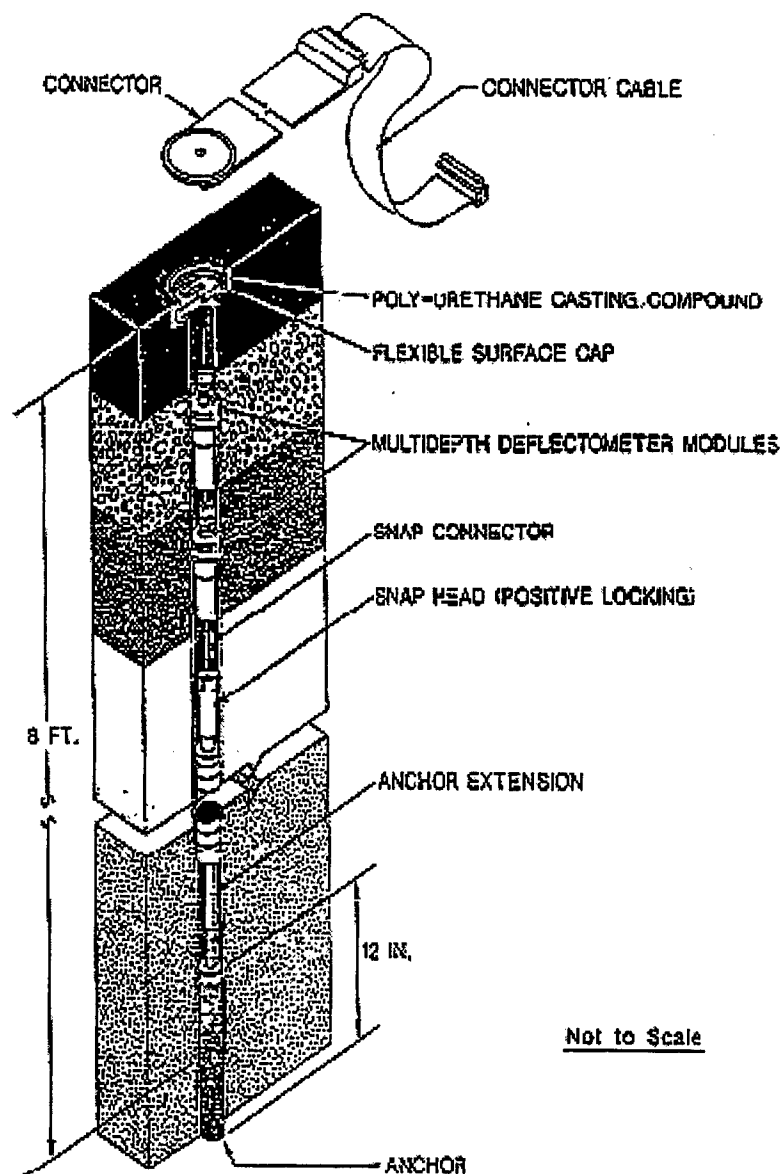


Figure 6.16. Typical cross-section of MDD after installation

## Traffic

Test traffic was applied using a single-wheel test cart with a wheel load of 30,000 lb (133 kN) as shown in Figure 6.17. The loaded tire, which was designed for a C-130 aircraft, was inflated to provide a contact pressure of 68 psi (468 kPa). The contact area was 442 in<sup>2</sup> (0.29 m<sup>2</sup>). The cart was powered by the front half of a four-wheel drive truck and was equipped with an outrigger wheel to prevent overturning. The load was produced using lead blocks located at the rear of the cart. The test traffic was applied to the pavement using the powered cart in both directions with the drivers manually operating and aligning the vehicle to insure that proper load distributions were maintained.

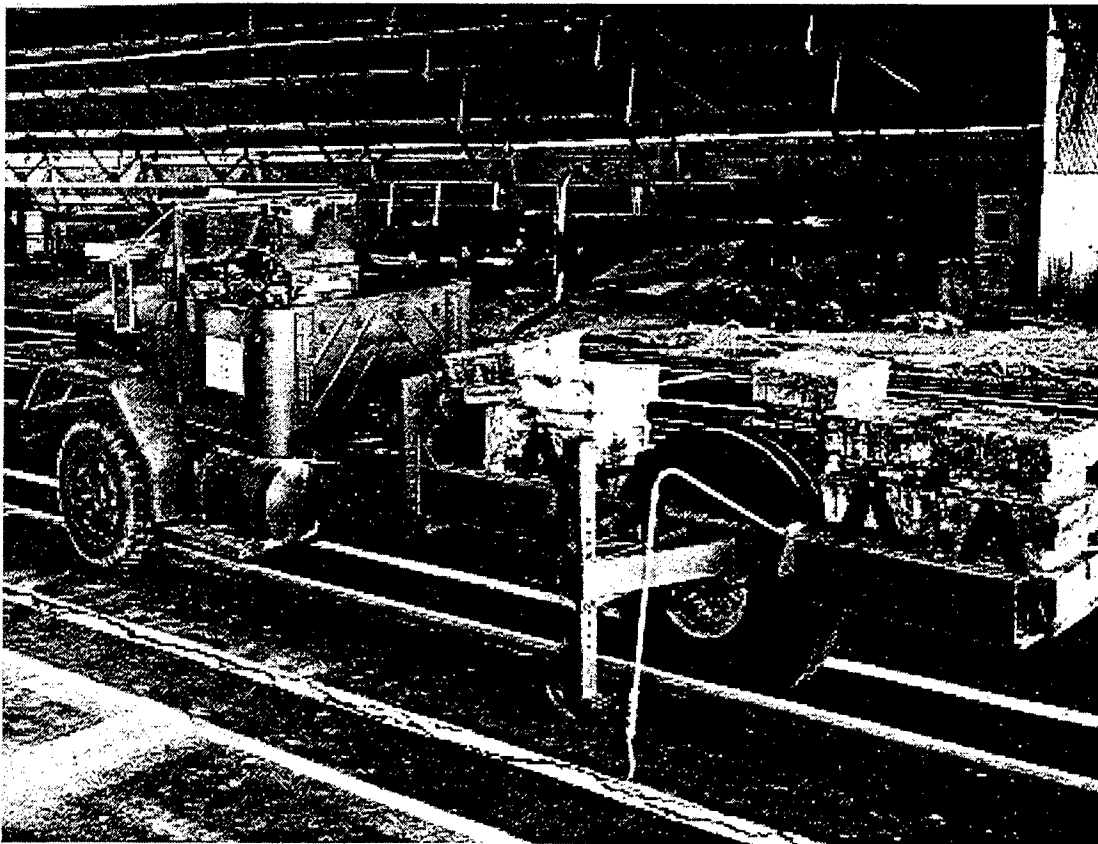


Figure 6.17. Loaded single wheel test cart with C-130 tire

## **ABAQUS FEM ANALYSIS OF TEST SECTION**

The ABAQUS FEM code was used to analyze the response of the two test sections of interest. All ABAQUS computations were conducted on SGI ORIGIN 2000 supercomputers. Finite element model development for ABAQUS was accomplished interactively on engineering workstations using The MacNeal-Schwendler Corporation's PATRAN software incorporating an ABAQUS application interface. PATRAN was also utilized to post-process many of the results from ABAQUS. A 2-D static axisymmetric analysis was performed using the WES MM model for the base course and linear elastic properties for the asphalt and subgrade layers. The purpose for this analysis was to demonstrate the ability to predict permanent deformation in a granular pavement layer using a non-linear elastic-plastic model.

### **Material Properties**

The information available from the test section data did not allow for direct calibration of the asphalt and subgrade properties. However, there was enough information to arrive at reasonable values for the elastic constants: Young's modulus ( $E$ ) and Poisson's ratio ( $\nu$ ). Typical values for these material constants can be found in a number of sources (Kulhawy, Mayne, 1990) (Ulidtz, 1998) (Tseng, 1988). The MDD deformation values were used to fine-tune these constants to produce reasonable values of deformation under load. In essence the MDD reading under load enabled a crude backcalculation of elastic constants to be performed, thus enabling the base course layer to see a stress state very similar to the true state of stress under load. Table 6.4 gives the values used for the elastic constants in both test sections. The values used for these elastic constants in the subgrade material represent more than just a material property. They are an effective foundation stiffness that allows for the subgrade material, lower supporting layers and far boundaries to be included in a simplified system model. The crushed limestone aggregate base course was modeled with the WES MM model as calibrated in Chapter 5.

Table 6.4. Material Properties Used for Asphalt and Subgrade Layers

Section ID	Asphalt Layer		Subgrade Layer	
	E, psi (MPa)	$\nu$	E, psi (MPa)	$\nu$
Lane 1-1	500,000 (3447.5)	0.35	18,000 (124.1)	0.35
Lane 2-1	500,000 (3447.5)	0.35	15,000 (103.4)	0.35

### FEM Mesh

The two test sections were modeled using standard 4 node quadrilateral axisymmetric elements from the ABAQUS element library as shown in Figure 6.18. In order to correctly model the C-130 wheel load, the load was simulated with a surface pressure of 68 psi (468.8 kPa) applied over a circular area of 442 square inches ( $0.29 \text{ m}^2$ ) to produce a total load of 30,000 lbs. (133 kN). The nominal layer thickness values are shown in Table 6.5. The total depth of the subgrade was 240 in. (6096 mm) yielding a total model depth of not less than 20 feet (6.25 m). This depth was similar to that arrived at for similar analyses in the literature. (Bryant 1998) (Yeh, 1989) (Barksdale, 1973)

Table 6.5. Layer Thickness Values

Section ID	Asphalt Layer	Base Course	Subgrade
Lane 1-1	2 in ( 50.8 mm)	10 in (254.0 mm)	240 in (6096 mm)
Lane 2-1	2 in ( 50.8 mm)	18 in (457.2 mm)	240 in (6096 mm)

The coordinate system used for the analysis denotes Y as the vertical direction and X as the horizontal direction. The meshes for both test sections were fixed in the X along the left side (line of symmetry) and the right hand side. The meshes were fixed against vertical translation along the bottom. Figures 6.19 a and b show the FEM mesh for the test sections. The elements ranged in size from the 3 in. by 2 in. elements directly under the loaded area to

the 12 in. square elements in the region farthest from the loaded area. The elements at the upper right hand corner and lower left hand corner of the model had aspect ratios on the order of 6:1 resulting in a few slender elements. Although these aspect ratios are fairly high, ABAQUS will support elements in this aspect ratio range, and the area undergoing load application was also very far from the slender elements.

The objective of this study was to develop a response model for granular pavement layers. Although that primarily involved the development and implementation of a constitutive model, it was necessary to apply said model to the analysis of a pavement system. For validation As the analysis phase of the study progressed it became obvious that obtaining a convergent solution with ABAQUS was a difficult task that changed with the inclusion of small differences in mesh or material model parameters. The FEM grids shown in Figures 6.19 and 6.20 were arrived at through trial and error attempts at defining the finest mesh that would provide reasonable response while still being able to converge to a solution during load application. The smallest element in these meshes is 2 in. by 3 in. In the earliest meshes developed during this study the elements were 1 in. by 1 in. under the loaded area. The nature of non-linear plastic analysis proved to counter intuitive to traditional finite element mesh concepts. In most cases the finer a mesh is made the easier and more accurate the solution will become until the accuracy reaches some asymptotic value. That concept relies on the fact that a solution can be obtained. In the case of non-linear elastic-plastic analysis there is a limit on the minimum element size that can provide a practical solution with reasonable load step sizes. As the size of the elements undergoing plastic deformation gets smaller it is also necessary to reduce the strain increment applied to those elements. If the strain increment is large relative to the element size then the entire element and its neighbors may yield in one increment. If that happens then the solution procedures used in codes like ABAQUS will not be able to converge.

A convergent solution was not possible until elements with minimum dimensions of at least 2 inches (5.08 mm) were used under the loaded area. Even then, extreme care was required in selecting the load step (strain increment) parameters required to obtain a convergent solution.. The formulation of the WES MM model produces breakpoints in the stress strain curve each time one of the four mechanisms in the model yields. In a pavement section FEM model any element in the base course was subject to yielding at up to four levels under load application due to these breakpoints. As the load was increased in each of the cycles of applied wheel load, the area of the model under the load would experience yield. The difficulty in reaching a convergent solution would increase each time the zone of plastic deformation would move far enough through the base course to encompass another element. In effect, plastic behavior in the material translates directly into increased difficulty in obtaining a convergent solution. This difficulty is coupled with the mesh fineness to produce a very complex challenge in conducting an analysis. The automatic time stepping methods used in ABAQUS enabled the user to specify parameters for controlling the size of the load step (strain increment). ABAQUS could use very small steps when solution convergence was difficult to obtain, and then use relatively large steps when the model was more numerically stable. The exact mesh dimensions and load step definitions can not be obtained through a direct method, but they are arrived at obtained through trial and error. Unlike many trial and error methods this procedure is basically a “GO” or “NO GO” proposition. One must also weight the advantages of a very accurate material calibration at low stress levels as compared with the increased difficulty in obtaining a solution. The cyclic calibration produced great response predictions for calibration verifications, but could not be made to converge with a pavement test section grid. The grids shown in Figures 6.19 and 6.20 did converge with the standard material calibration arrived at in Chapter 5 and the ABAQUS model definitions shown in Appendix B.

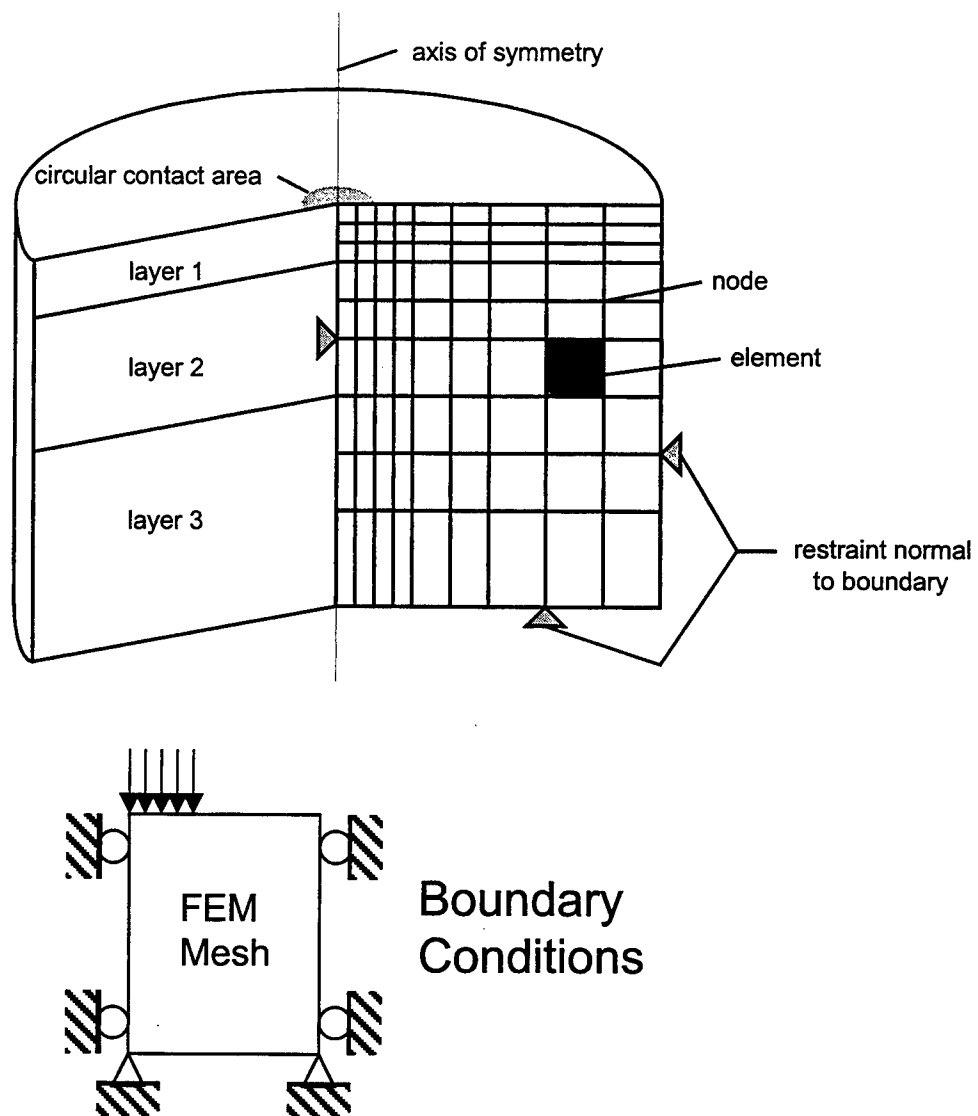


Figure 6.18. Typical axisymmetric FEM model of a pavement



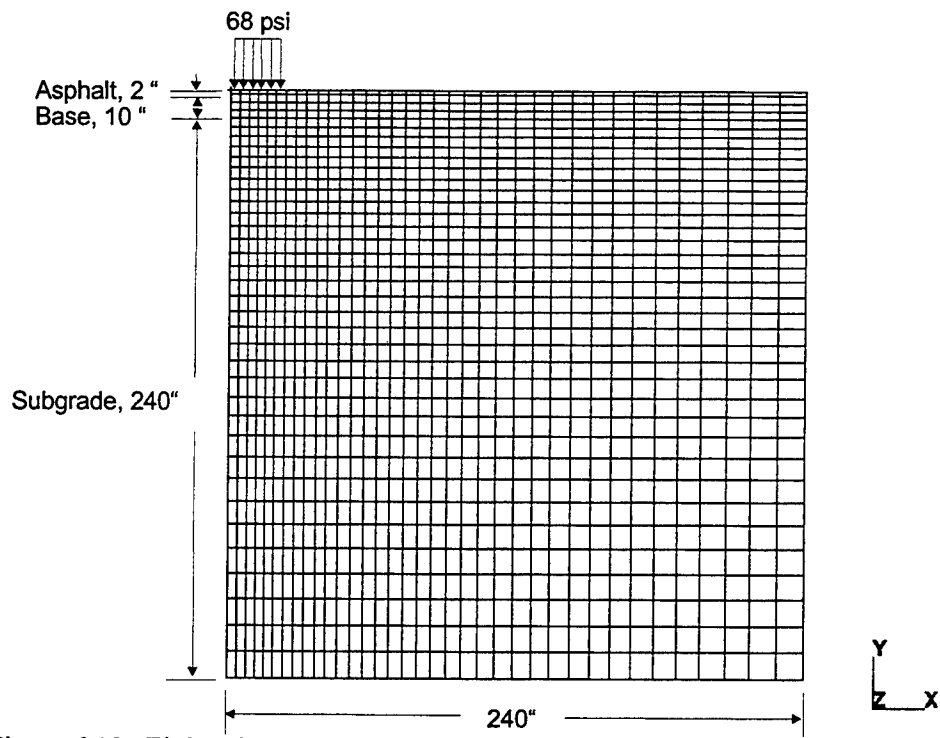


Figure 6.19. Finite element mesh for Lane 1-1

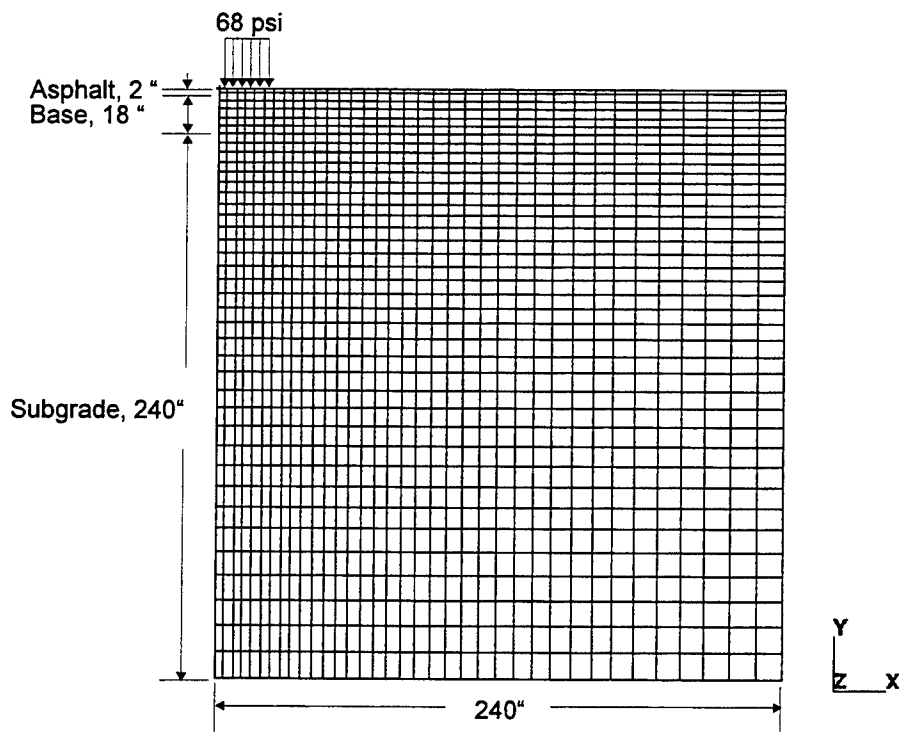


Figure 6.20. Finite element mesh for Lane 2-1

### Results of FEM Analyses of Test Sections

The test sections were subjected to 5 cycles of a simulated single C-130 tire load. The base course layer was modeled with the WES MM model, while the remaining layers were modeled as a linear elastic material. The results of these analyses were compared to MDD measurements from the field test sections to provide model validation and assessment.

Figure 6.21 shows the deformed shape of Lane 1-1 under the 5<sup>th</sup> load application. The value of deformation at the top of the base course was 173 mils (4.39 mm). Webster, 1993, reported the value of deformation at the top of the base course in Lane 1-1 to be 165 mils (4.19 mm) under the 5<sup>th</sup> load application. The predicted deformation under load at the top of the subgrade was 113 mils (2.87) as compared with a field value of 125 mils (3.17 mm). The agreement between these values verifies the relative accuracy of the overall system calibration for Lane 1-1.

In order to validate the ability of the WES MM model to predict plastic accumulated strain under repeated loads, the value of permanent deformation after removal of the load at the top of the base course, 33 mils (0.83 mm), was determined from the analysis and compared with the field value of 40 mils (1.02 mm) for Lane 1-1. Figure 6.22 shows the deformed shape of Lane 1-1 after removal of the 5<sup>th</sup> load.

Similar finite element calculations were made for Lane 2-1. Figure 6.23 shows the deformed shape of Lane 2-1 under the 5<sup>th</sup> load application. Figure 6.23 shows the deformed shape of Lane 2-1 after removal of the 5<sup>th</sup> load. The deformation at the top of the base course was predicted to be 243 mils (6.17 mm). Webster, 1993, reported the value of deformation at the top of the base course in Lane 2-1 to be 190 mils (4.83 mm) under the 5<sup>th</sup> load application. The predicted permanent deformation at the top of the base course was 93 mils (2.36 mm) as compared with the field value of 50 mils (1.27 mm). The predicted deformation under load at the top of the subgrade was 116 mils (2.94 mm) with a field value of 145 mils (3.68 mm).

Figures 6.25 and 6.26 show the deformation under load at the top of the base course and the top of the subgrade from the FEM predictions and the field measurements for Lanes 1-1 and 2-1 respectively. Figures 6.25 and 6.26 also show the FEM prediction of permanent deformation as a function of load cycles. The agreement between the FEM predictions and the field measurements are closer for Lane 1-1 than for Lane 2-1. The effects of the lower strength subgrade (3 CBR) in Lane 2-1 are much more difficult to model with linear elasticity than the higher strength (8 CBR) subgrade in Lane 1-1. The lower strength subgrades are also much harder to construct and much more susceptible to environmental changes, which resulted in higher variability of strength and stiffness within the test section (Webster, 1993). The magnitude of these deformations is very small when compared with the overall cross-sectional dimensions modeled. For instance, the deformation at the top of the base course under load in Lane 2-1 was predicted to be 243 mils (6.17 mm). This was 53 mils greater than the field measurement and only 0.3% of the layer thickness.

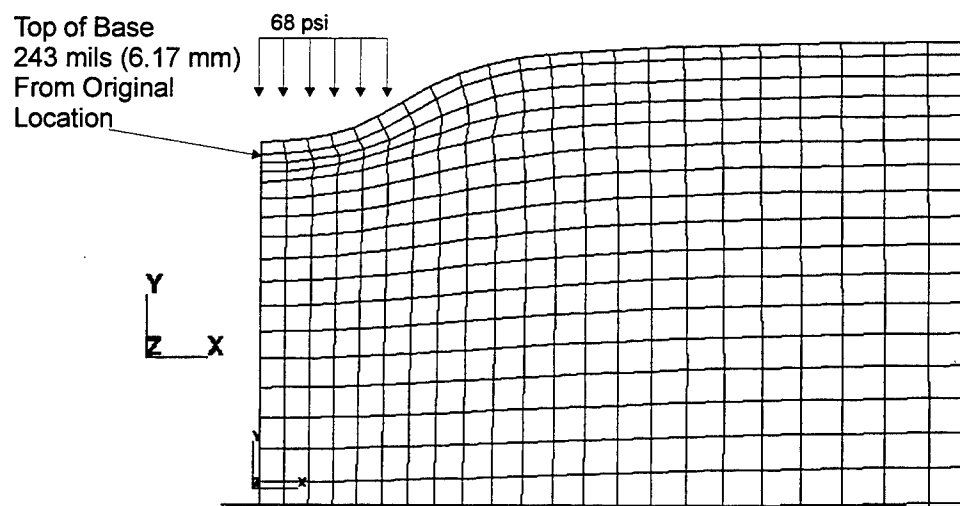


Figure 6.21. Deformed shape (100 X) under 5<sup>th</sup> load application for Lane 1-1

Top of Base  
33 mils (.84 mm)  
From Original  
Location

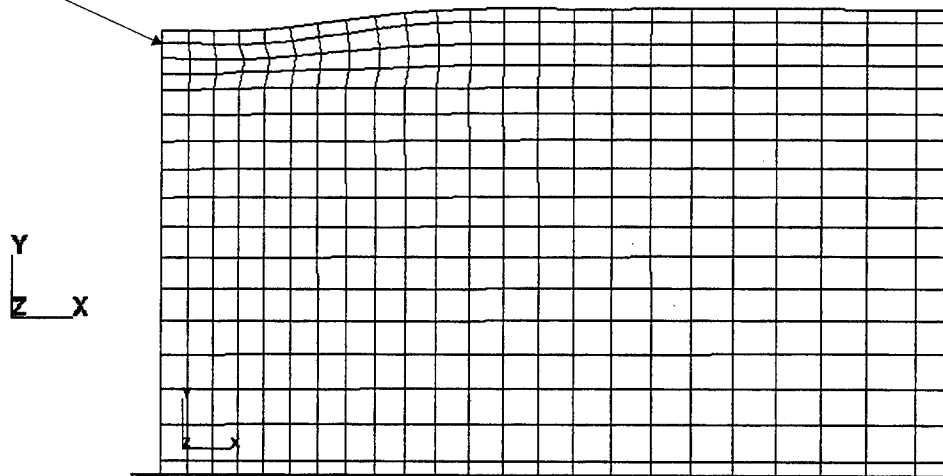


Figure 6.22. Deformed shape (100 X) after 5<sup>th</sup> load application for Lane 1-1

Top of Base  
243 mils (6.17 mm)  
From Original  
Location

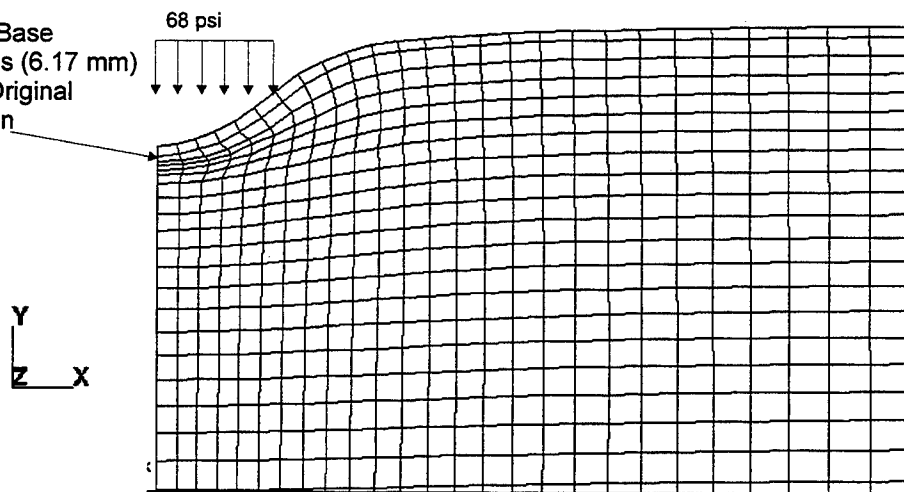


Figure 6.23. Deformed shape (100 X) under 5<sup>th</sup> load application for Lane 2 -1

Top of Base  
93 mils (2.36 mm)  
From Original  
Location

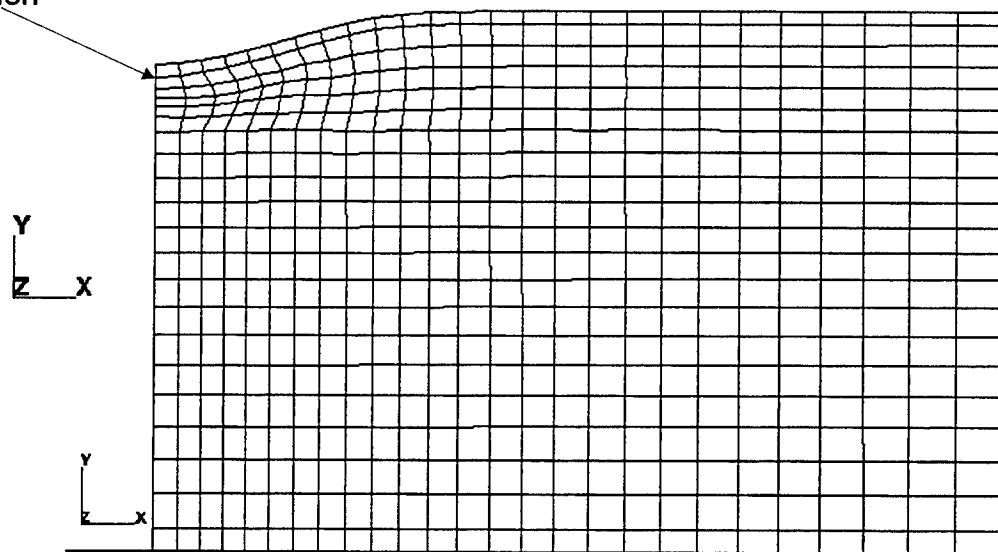


Figure 6.24. Deformed shape (100 X) after 5<sup>th</sup> load application for Lane 2-1

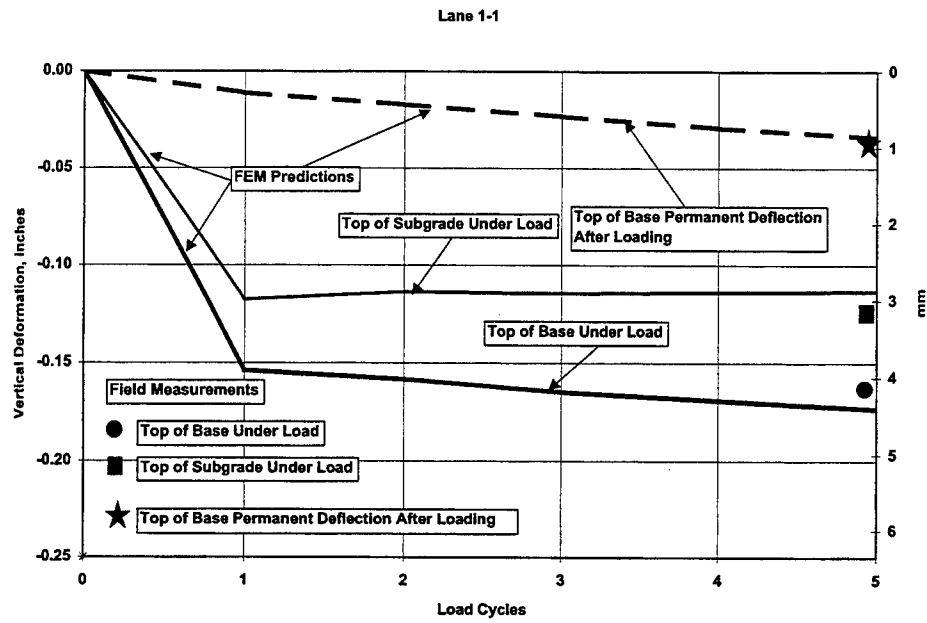


Figure 6.25. Vertical deformation versus load cycles from FEM simulation of Lane 1-1

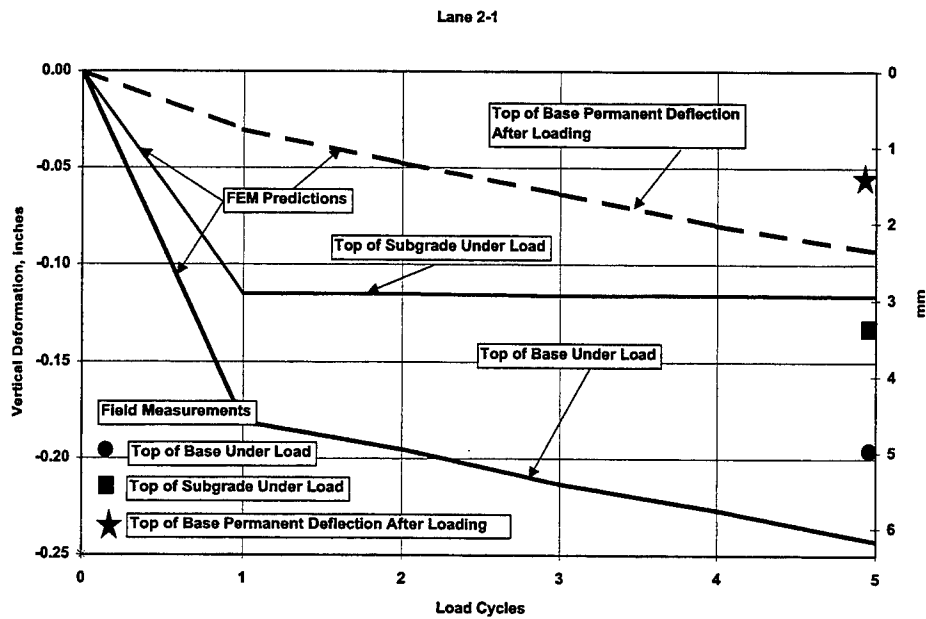


Figure 6.26. Vertical deformation versus load cycles from FEM simulation of Lane 2-1

An important feature for a model for granular layers in pavements is determined by its ability to predict the shear deformation of the base course under load and permanent shear strain under repeated load. This type of shearing failure is representative of the type of behavior seen in many pavements where the base course has failed (Ahlvin, 1991). Figures 6.27 through 6.30 show the evolution of shear strain through five load cycles in Lane 1-1. The shear strain or principal strain difference is shown as a color fringe plot to enable the area of permanent strain to be seen. The shear fringes are plotted on deformed meshes to aid in visualizing the results. As Load Cycle 1 was applied, the development of shear strain on the order of 0.5 % (the gray shaded region underneath the loaded area) is clearly seen in the base course (the 2<sup>nd</sup>, 3<sup>rd</sup>, and 4<sup>th</sup> rows of elements from the top) shown in Figure 6.27. After the removal of load cycle 1, a small residual shear strain was developed in the base course and can be seen in the light blue shaded region underneath the loaded area in Figure 6.28. In Figure 6.29 the shear strain under the 5<sup>th</sup> load cycle is plotted. The magnitude of the shear strain (>0.6%) is greater than that of the 1<sup>st</sup> load cycle due to the accumulation of shear strain during each of the five load applications. The region experiencing these higher strains (the darker shaded region) is also larger than that for one load cycle. Figure 6.30 shows the residual or permanent shear strain in the blue, green and pink region, after the removal of the 5<sup>th</sup> load cycle. The permanent shear strain not only increases in magnitude, but the number of elements experiencing plastic deformation also increases with the number of load repetitions. The maximum residual shear strain seen after the 5<sup>th</sup> load cycle was on the order of 0.45% . This type of behavior is quite representative of that seen in pavements subjected to repeated wheel loads.

Figures 6.31 through 6.34 show the evolution of shear strain through five load cycles in Lane 2-1. The magnitude of maximum shear strain under load is 0.5% under one load cycle and >1% under the 5<sup>th</sup> load cycle. This can be seen in the gray shaded area in Figure 6.31 and the gray/black shaded area in Figure 6.33 respectively. The magnitude and number of

elements experiencing permanent shear strain can be seen in the shaded regions in Figures 6.32 (after 1 load cycle) and 6.34 (after the 5<sup>th</sup> load cycle). The maximum residual shear strain after 5 load cycles is on the order of .9% for Lane 2-1 which is almost double that seen in Lane 1-1. This would agree with the differences in the two sections and the permanent deformation measurements and predictions. The trend seen of movement of material from underneath a loaded area is a very real phenomenon that is seen in pavements under all types of wheel loading conditions.

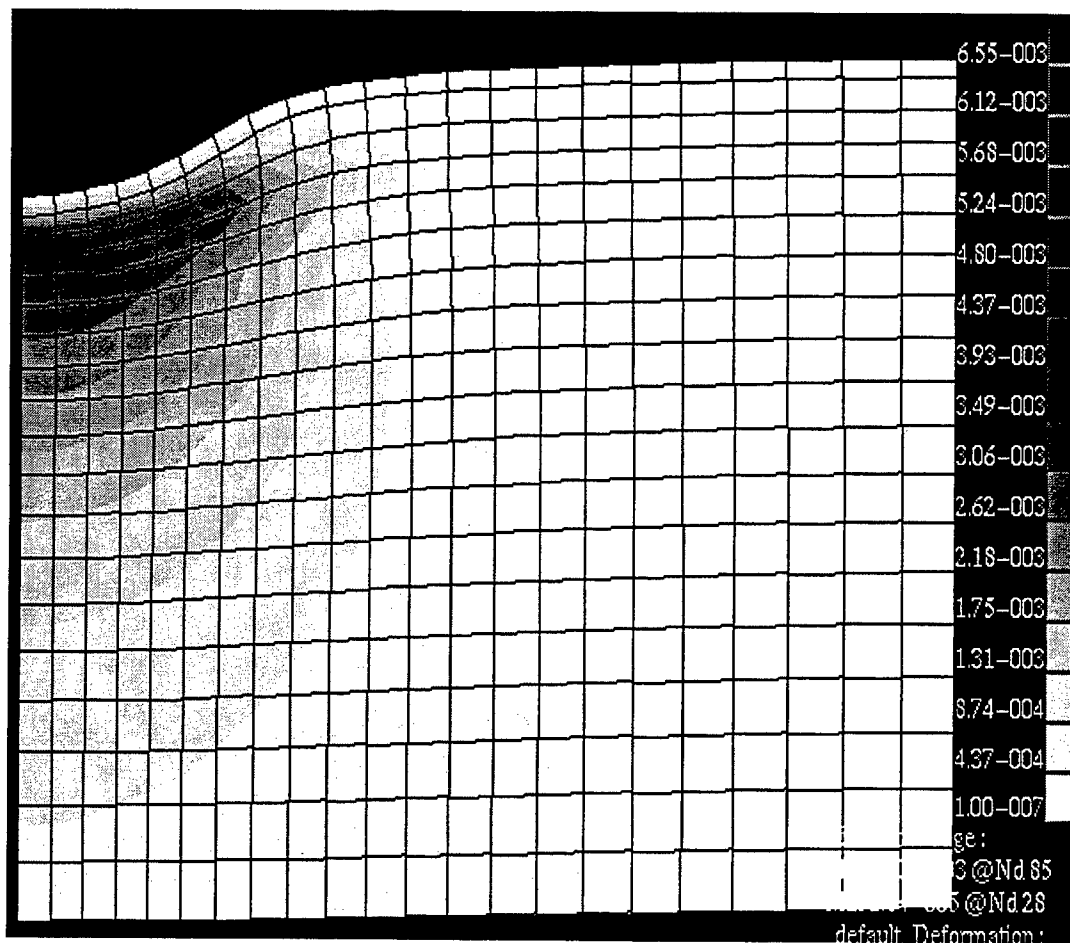


Figure 6.27. Principal strain difference in Lane 1-1 (i.e. shear strain) under load cycle 1



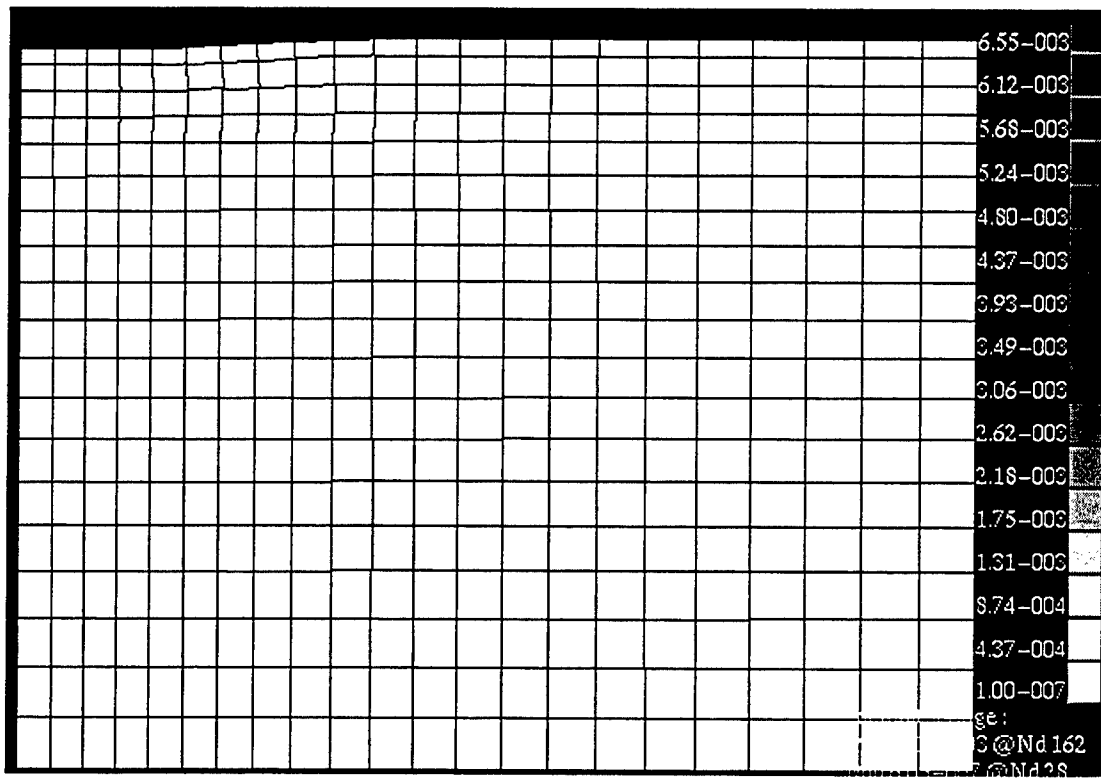


Figure 6.28. Principal strain difference in Lane 1-1 (i.e. shear strain) after load cycle 1

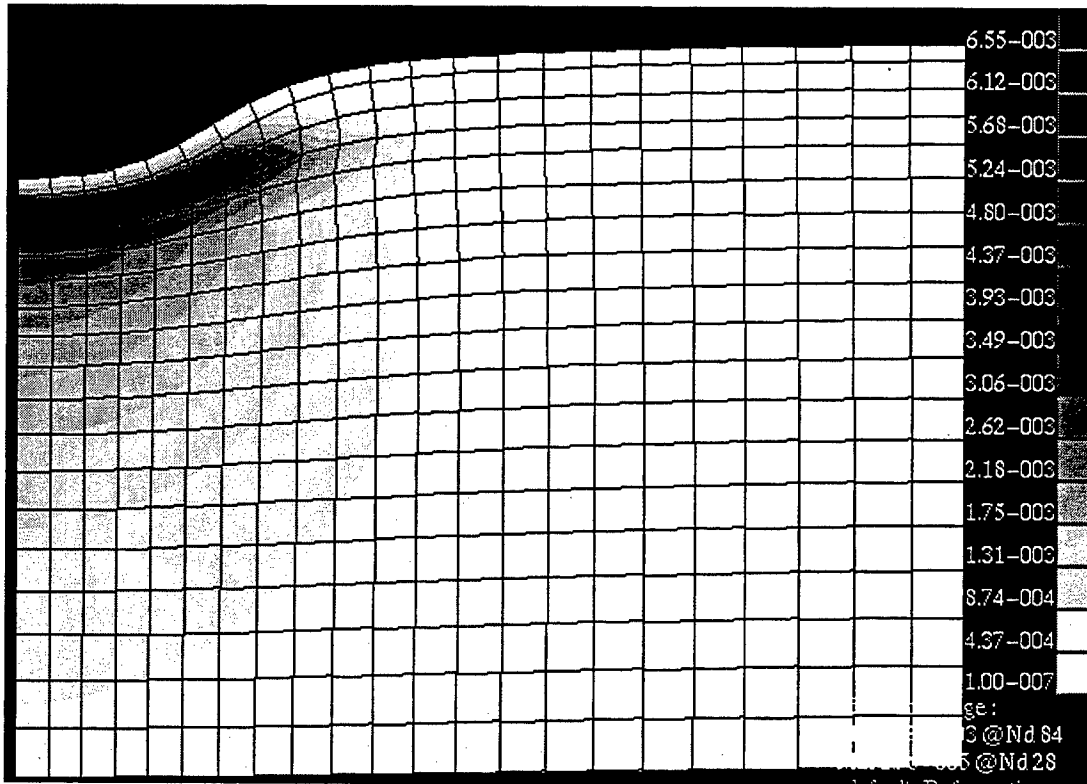


Figure 6.29. Principal strain difference in Lane 1-1 (i.e. shear strain) under load cycle 5

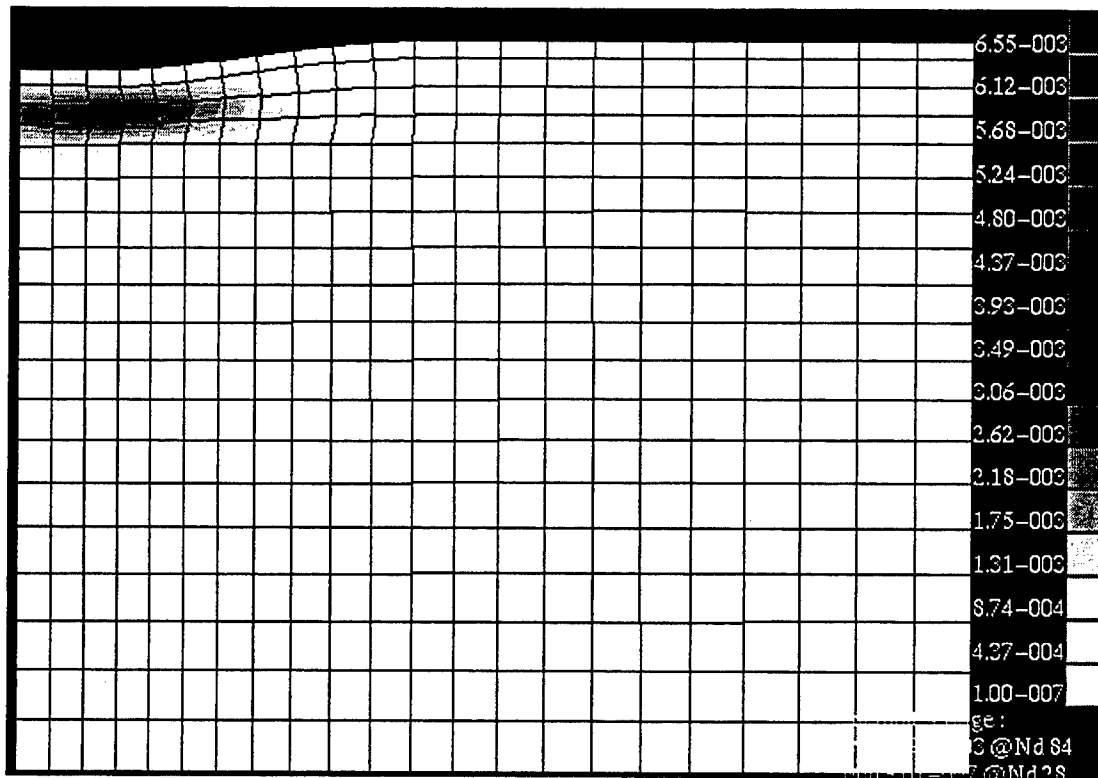


Figure 6.30. Principal strain difference in Lane 1-1 (i.e. shear strain) after load cycle 5

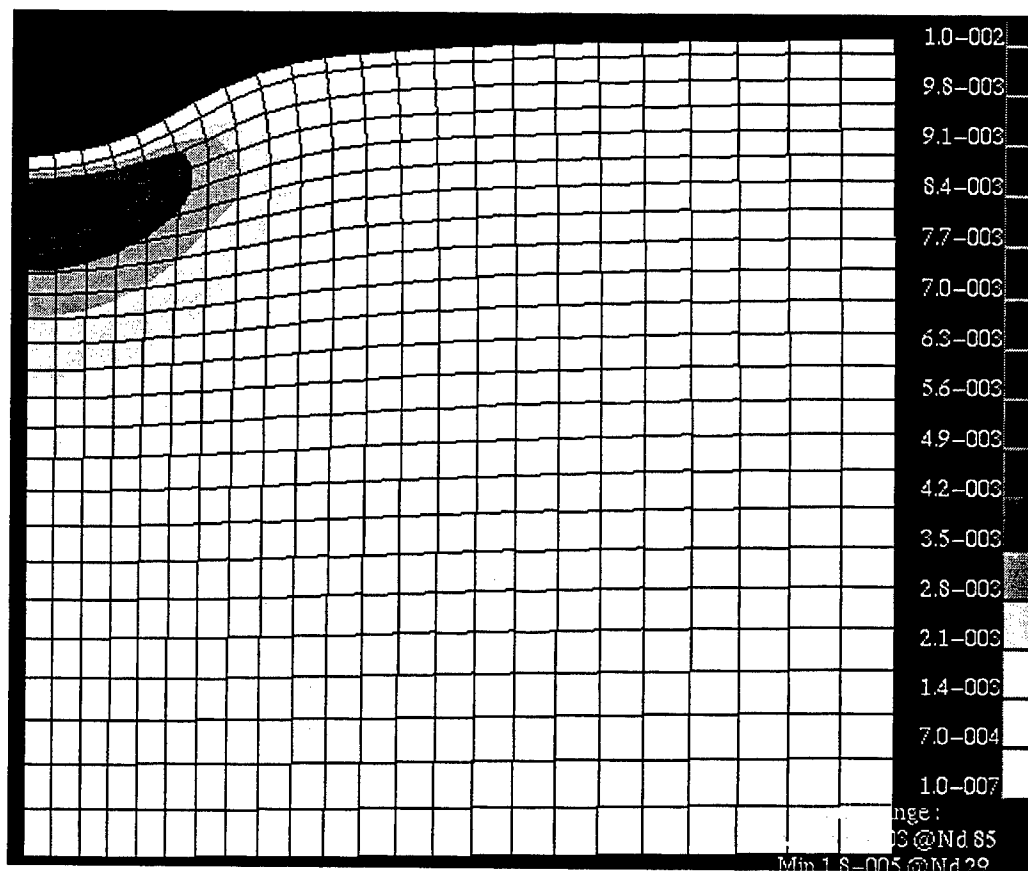


Figure 6.31. Principal strain difference in Lane 2-1 (i.e. shear strain) under load cycle 1

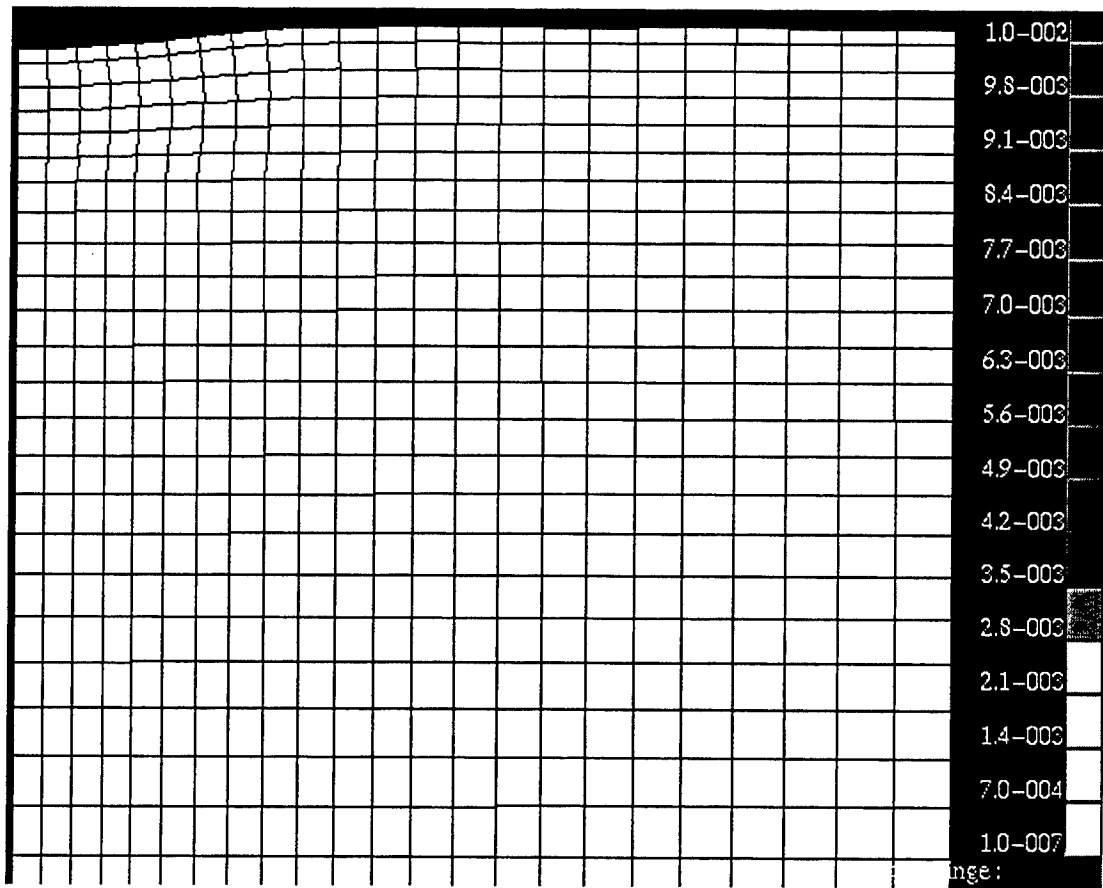


Figure 6.32. Principal strain difference in Lane 2-1 (i.e. shear strain) after load cycle 1

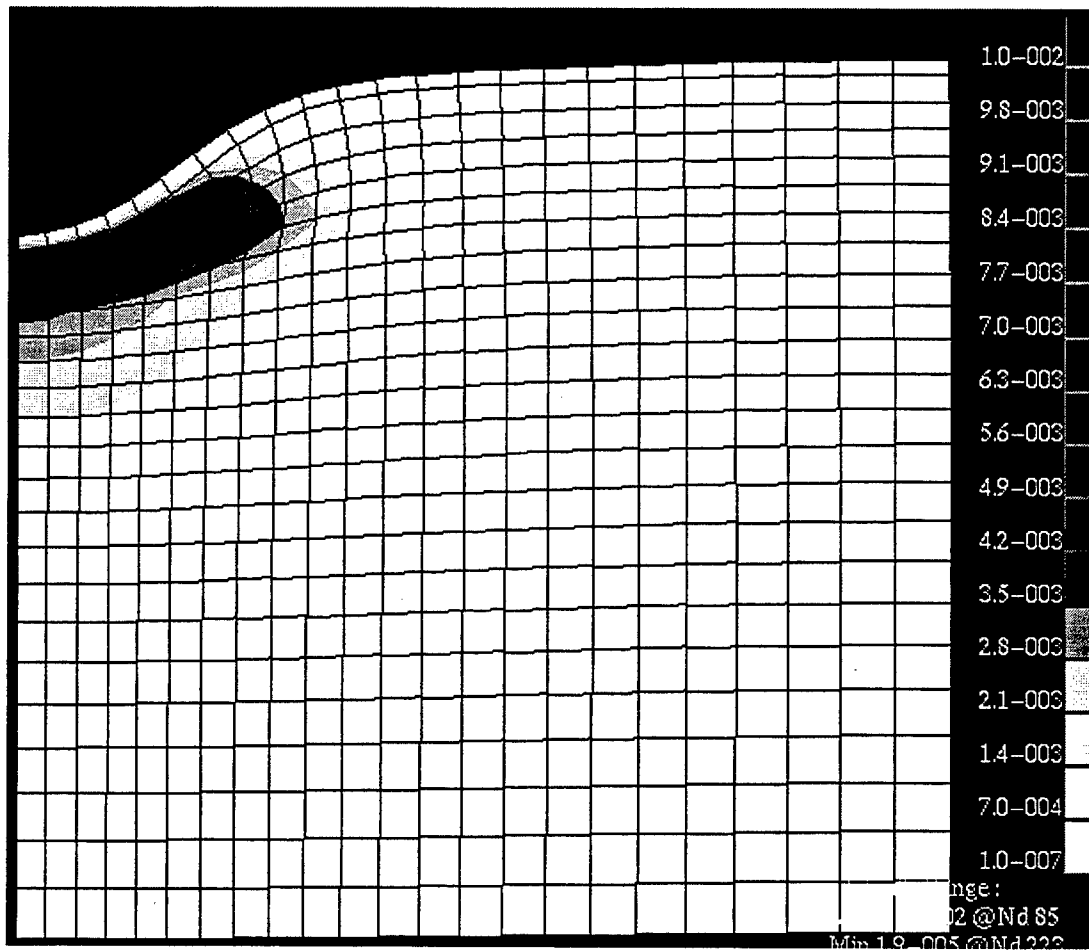


Figure 6.33. Principal strain difference in Lane 2-1 (i.e. shear strain) under load cycle 5

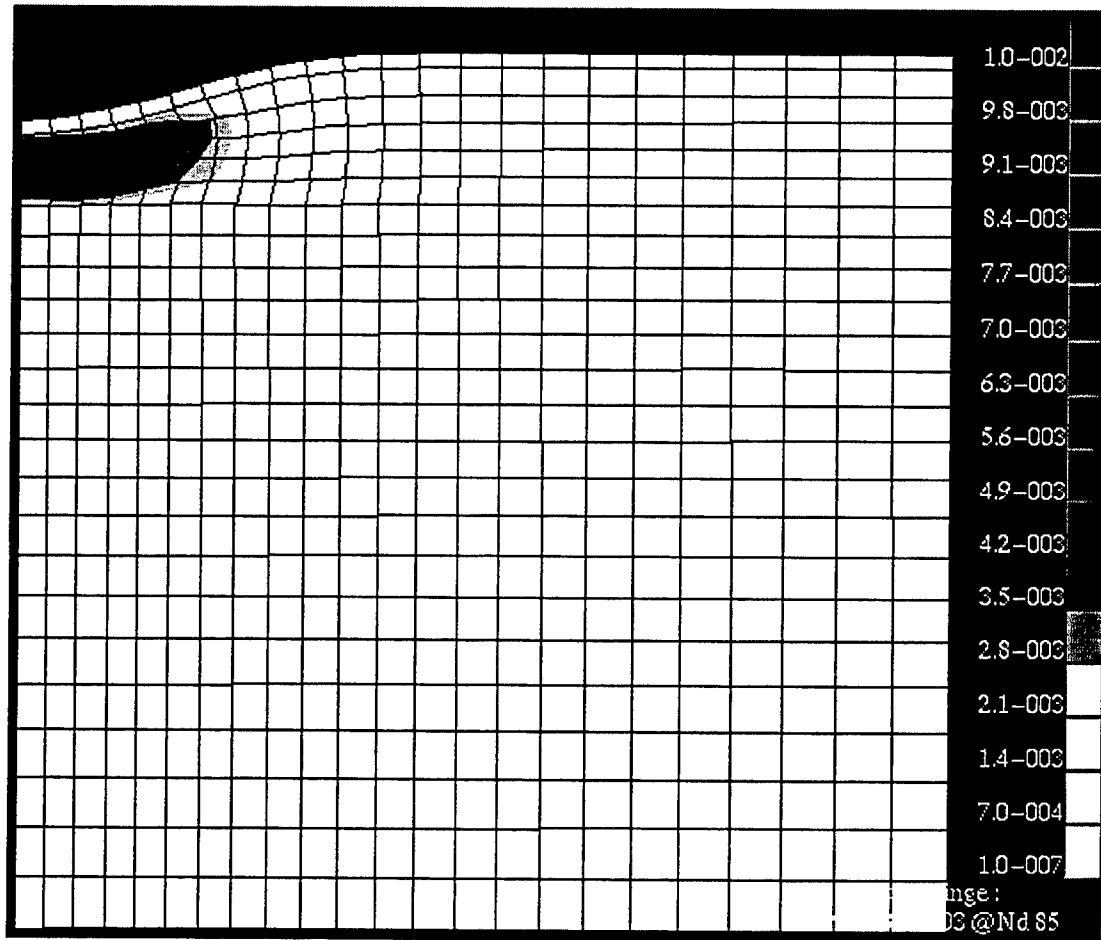


Figure 6.34. Principal strain difference in Lane 2-1 (i.e. shear strain) after load cycle 5

## Model Sensitivity

The sensitivity of the FEM response to changes in the Calibration Parameters for the WES MM model is an area that should be considered. It is recognized that the overall pavement system response is a function of the response of each layer of the systems acting as a whole. Changes in any parameter in the granular material model will effect the stress-strain response and yield properties of the material., although some parameters are less important for certain types of materials. This was demonstrated in Chapter 5 in the presentation of the MVIEWER results. The real question is not how do changes in the parameters effect the system response, but how do changes in the material density, compaction, moisture content, etc., effect the strength and stiffness of a base course material. A study to adequately define such relationships would be a huge effort requiring large amounts of manpower, laboratory testing, and time. The following table gives some limited insight into the question of the relationship between model parameters and system response. The global strength and stiffness parameters,  $\phi$  and  $G$ , respectively were changed from the original calibration and the analysis was rerun. The deformation in Lane 1-1 at the top of the base course under the 5<sup>th</sup> load, and the residual deformation at the top of the base course after removal of the 5<sup>th</sup> load are shown for 5 cases in Table 6.6.

The overall deformation under load was higher with the lower  $\phi$  (Case 2) and lower with the higher  $\phi$  (Case 1). As one would expect, when compared with the original calibration, the overall deformation under load was lower in Case 3 (higher shear modulus) and higher in Case 4 (lower shear modulus). The permanent deformations did not exhibit as much sensitivity to changes in  $G$  as did the total deformation under load, which contains a large elastic component. The changes in response due to changes in  $G$  are small when compared to the changes in  $\phi$ , especially in terms of accumulated deformation. The friction angle,  $\phi$ , was varied by +/- 10% to arrive at these results, while the shear modulus,  $G$ , was



changed by factors of 2.0 and 0.5. This would indicate that the definition of the yield surface parameters is crucial in properly modeling the response of granular layers in flexible pavement systems.

The WES MM model performs well with proper calibration and attention to detail in FEM model definition. The development and application of user defined material models is a complex task that requires the user to work “blind” with an analysis code that does not offer access to computational source code. Many of the difficulties experienced in applying the WES MM model may be eliminated if the code is actually incorporated into built-in material libraries instead of existing as a user defined subroutine. Such an endeavor would require a collaborative effort with a commercial analysis code producer like HKS/ABAQUS.

Table 6.6. Predicted Base Course Deformation in Lane 1-1 with Changes in  $\phi$  and G.

	Friction Angle $\phi$ , Degrees	Shear Modulus. G, ksi (MPa)	Predicted Deformation at Top of Base Course, mils (mm)	
			Under 5 <sup>th</sup> Load	After 5 <sup>th</sup> Load
Original Cal	48.0	30 (206.8)	165 (4.19)	33 (0.84)
Case 1	52.6	30 (206.8)	166 (4.22)	25 (1.00)
Case 2	43.2	30 (206.8)	188 (4.77)	46 (1.20)
Case 3	48.0	60 (413.7)	160 (4.06)	30 (0.76)
Case 4	48.0	15 (103.4)	193 (4.90)	36 (0.91)
Field Data	-----	-----	173 (4.39)	40 (1.02)

## **CHAPTER 7: CONCLUSIONS AND RECOMMENDATIONS**

### **CONCLUSIONS**

The response of a flexible pavement system subjected to aircraft loads is complex, and accurately predicting the response of such a system requires significant computational capabilities. For flexible pavements, the geometric modeling aspects of the problem are quite simple, but the materials exhibit very complex behavior. The application of computational models in pavements analysis requires the solution of many problems with both material constitutive models and system models. The materials exhibit viscous, viscoelastic, and plastic response to loads. Many times the deformations or deformation rates are non-linear functions of the stress state. The materials are often heterogenous, anisotropic, and particulate in nature. The pavement system is also quite complex and difficult to model. Pavement loads are often difficult to predict over time. Spatial variability of materials, and the effects of environment and aging present additional difficulties in modeling pavements. The purpose of this effort was to develop a model that addresses one of these many difficulties: prediction of response of granular pavement layers. It must be recognized that calculating the response of a pavement is of interest only because it allows one to use it to predict pavement performance. The links between pavement response and performance are not simple. One must have the proper tools to understand what happens in pavements, and theoretical models are needed

The development of the WES Multimechanical Model represents a significant advancement in the state-of-the-art of flexible pavement material response modeling. The essential features of pavement material response that are provided with the WES Multimechanical Model include: (1) non-linear elastic response, (2) permanent or plastic deformations after yield, (3) cyclic loading, (4) strain softening/hardening, and (5) shear dilatancy. A model of this type has the added benefit of calibration parameters that are physically significant. In effect, they are related directly to the properties of the material

determined from laboratory test data. The inclusion of the WES Multimechanical Model for granular materials in a new-generation analysis and design procedure should provide the pavements community with a tool for predicting the permanent deformation of unbound layers in flexible pavements. The following conclusions can be drawn from this study:

- The ability to predict permanent deformation under a relatively small number of load repetitions with relatively close agreement to field measurements has been demonstrated. When one considers the long-term effects of repeated loads, the analyst must consider many additional aspects of the total pavement system. The nonlinear plastic response of the surface layers and the subgrade layers are critical in understanding the behavior of a pavement over time. Variability in the material properties within a pavement structure is a systems level problem that must be addressed. The mechanical properties of granular base courses can vary widely from one location to another. The WES MM model is quite sensitive to some of these properties and can result in differences in predicted response.
- Historically no universally accepted rational and consistent constitutive model has been used in modeling granular pavement materials. A constitutive model that can capture the essential behavior of pavement materials under service environments has many requirements including simplicity of calibration and operation, physical significance of the model parameters, and the ability to be readily incorporated into analysis codes.
- The WES MM model performs well in modeling granular pavement materials with proper calibration and attention to detail in FEM model definition. It is essential that high quality laboratory test data be used to calibrate this model for any potential application. The selection of mesh definition for a pavement section is more of a learned skill than an exact science.

- This type of constitutive model, although simple in formulation, is quite sophisticated in operation. It remains a very high-end analysis tool, which can be very complex in its application to pavement analysis.
- The inclusion of granular base response models is critical when predictions of pavement behavior under repeated loads are required. Current aircraft pavement design procedures do not account for the performance of the granular base. Designers will need to incorporate criteria for base course response in future generation analysis, design, and performance models.
- Older classical soil models, like Drucker- Prager, appear to lack the sophistication required to properly model granular pavement materials. The Drucker-Prager model is not intended to handle cyclic loads. The Drucker-Prager models can not capture the non-linear pre-yield behavior of granular materials. The Drucker-Prager model does not have the ability to model shear dilatancy in materials which have been highly compacted.

## **RECOMMENDATIONS**

The following recommendations are made as a result of this study:

- Future generation pavement analysis and design procedures for aircraft loads should include models capable of predicting permanent deformation under repeated loads. The current pavement design procedures are capable of providing reasonable layer thickness designs for a wide range of aircraft. However, when the task is changed to predicting the performance of a pavement under non-standard conditions or designing a pavement with non-standard materials then the older procedures lack the sophistication required to handle that kind of requirement. This model would allow the designer or analyst the option of including permanent deformation under repeated load as criteria in layer thickness design.

- A database of test results necessary for WES MM model calibration for unbound pavement materials should be developed from laboratory tests to aid pavement analysts in predicting performance of pavements under repeated loads. Such a database would provide analysts with an advantage in obtaining values of parameters when new materials are encountered. The process of assembling such a database would provide the information required to characterize the sensitivity of the model and calibration parameters to changes in the physical and mechanical material properties of the material.
- The ABAQUS User Defined Material Model (WES MM) should be included in the standard material library for ABAQUS or a similar code.
- The WES MM model should be the basis for future model development to include features such as partially saturated soils and time dependent components for modeling asphalt cement concrete.
- The finding of this study should be used in designing and instrumenting a full scale test section that would enable the accumulation of surface and subsurface permanent deformation of a pavements under aircraft loads to be more accurately determined. These test results could then be used to further develop performance criteria based on the WES MM model.

## REFERENCES

- ABAQUS, 1998, Users Documentation, Version 5.8, "Drucker-Prager Model for Geologic Materials", Hibbitt, Karlsson, & Sorensen, Inc, Pawtucket, Rhode Island.
- Ahlrich, Randolph C., 1995, Influence of Aggregate Gradation and Particle Shape/Texture on Permanent Deformation of Hot Mix Asphalt Pavements, Ph.D. Dissertation, Auburn University, Auburn, AL.
- Ahlvin, Richard G., 1992, "Origin of Developments for Structural Design of Pavements", Technical Report GL-91-26, US Army Engineer Waterways Experiment Station, Vicksburg, MS.
- American Society for Testing and Materials, 1997, 1997 Annual Book of ASTM Standards, "Designation D2850 Standard Test Method for Unconsolidated, Undrained Compressive Strength of Cohesive Soils in Triaxial Compression", Philadelphia, PA.
- American Society for Testing and Materials, 1997, 1997 Annual Book of ASTM Standards, "Designation D3387 Standard Test Method for Compaction and Shear Properties of Bituminous Mixtures by Means of the US Army Corps of Engineers Gyratory Testing Machine", Philadelphia, PA.
- Baladi, G. Y. and Rohani, B., 1979, "Elasto-Plastic Model for Saturated Sand," Journal of the Geotechnical Engineering Division, American Society of Civil Engineers, Vol. 105, No. GT4, pp. 465-480, New York, NY.
- Barker, Walter R., and Gonzalez, Carlos R., 1991, "Pavement Design by Elastic Layer Theory", Proceedings of the ASCE Conference on Aircraft/Pavement Interaction, Kansas City, MO.
- Barksdale, R. D., and Hicks, R. G., 1973, "Material Characterization and Layered Theory for Use in Fatigue Analysis", Highway Research Board, Special Publication 140, Washington, DC.
- Bonaquist, R. F., 1996, Development and Application of a Comprehensive Constitutive Model for Granular Materials in Flexible Pavement Structures, Ph.D. Dissertation, University of Maryland, College Park, MD.
- Bryant, Larry M., 1998, "Preliminary Analytical Model for Flexible Pavements", Technical Report CR GL-98-4, US Army Engineer Waterways Experiment Station, Vicksburg, MS.
- Chen, W. F., and Mizuno, E., 1990, Nonlinear Analysis in Soil Mechanics, Elsevier Science, New York, NY.
- Chen, W. F., and Saleeb, A. F., 1982, Constitutive Equations for Engineering Materials, Volume 1: Elasticity and Modeling, John Wiley and Sons, New York, NY.
- Desai, C. S., Somasundaram, S., and Frantziskonis, G., 1986, "A Hierarchical Approach for Constitutive Modeling of Geologic Materials," International Journal for Numerical and Analytical Methods in Geomechanics, Vol. 10, pp. 225-257.

Desai, C. S. and Siriwardane, H. J., 1984, Constitutive Laws for Engineering Materials with Emphasis on Geologic Materials, Prentice Hall, Englewood Cliffs, NJ.

DiMaggio, F.L. and Sandler, I.S., 1971, "Material Model for Granular Soils," Journal of the Engineering Mechanics Division, American Society of Civil Engineers, Vol. 97, pp. 935-950, New York, NY.

Domaschuck, K. and Wade, N.H., 1969, "A Study of the Bulk and Shear Moduli of Sand," Journal of the Soil Mechanics and Foundation Division, American Society of Civil Engineers, Vol. 98, pp. 561-582, New York, NY.

Drucker, D. C. and Prager, W., 1957, "Soil Mechanics and Plastic Analysis or Limit Design," Quarterly Journal of Applied Mathematics, Vol. 10 No. 2, pp. 157-165.

Duncan, J.M. and Chang, C.Y., 1970, "Non-Linear Analysis of Stress and Strain in Soils", Journal of the Soil Mechanics and Foundation Division, American Society of Civil Engineers, Vol. 96, pp. 1629-1653, New York, NY.

Duncan, J.M., Byrne, P., Wong, K.S., and Mabry, P., 1978, Strength, Stress-Strain, and Bulk Modulus Parameters for Finite Element Analyses of Stresses and Movements in Soil Masses, Report UCB/GT/78-02, University of California, Berkeley, CA.

Headquarters, Department of the Army, 1989, "Flexible Pavement Design for Airfields (Elastic Layered Method)," TM 5-825-2-1, Washington, DC.

Headquarters, Department of the Army, 1989, "Graded-Crushed-Aggregate Base Course," CECS 02233 (Guide Specification), 16 pp., Washington, DC.

Hicks, R. G. and Monismith, C. L., 1971, "Factors Influencing the Resilient Properties of Granular Materials," Transportation Research Record 345, pp. 15-31, Washington, DC.

Hicks, R. G. and Finn, F. N., 1970, "Analysis of the Results From the San Diego Test Road," Proceedings, Association of Asphalt Paving Technologists, Vol. 39, pp. 153-185.

Horner, David R., 1997, Micro-Mechanical Theory for Large Deformations of Granular Media, Ph.D. Dissertation, University of Michigan, Ann Arbor, MI.

Horner, David R., 1997, "Application of DEM to Micro-Mechanical Theory for Large Deformations of Granular Media", Technical Report in Preparation, US Army Engineer Waterways Experiment Station, Vicksburg, MS.

Kulhawy, F. H., Mayne, P.W., 1990, Manual on Estimating Soil Properties for Foundation Design, Electric Power Research Institute, Palo Alto, California.

Lade, P. V. and Duncan, J.M., 1975, "Elastoplastic Stress-Strain Theory for Cohesionless Soil," Journal of the Geotechnical Engineering Division, American Society of Civil Engineers, Vol. 101, pp. 1037-1053, New York, NY.

- Lytton, R. L., Uzan, J., Fernando, E. G., Roque, R., Hiltunen, D., and Stoffels, S. M., 1993, Development and Validation of Performance Models and Specifications for Asphalt Binders and Paving Mixes, Report Number SHRP-A-357, Strategic Highway Research Program, National Research Council, Washington, DC.
- Matsuoka, H. and Nakai, T., 1977, "Stress-Strain Relationship of a Soil based on the 'Spatial Mobilized Plane', Soils and Foundations.
- May, R.W. and Witczak, M.W., 1981, "Effective Granular Modulus to Model Pavement Responses," Transportation Research Record 810, pp. 1-9, Washington, DC.
- Meade, Ron B., 1997, "Regarding the Development of a Micromechanically-based Elastic-plastic Constitutive Model for Soils", Internal Memorandum, Soils and Rock Mechanics Division, Geotechnical Laboratory, USAE Waterways Experiment Station, Vicksburg, MS.
- Meade, Ron B., 1998, "Regarding the Calibration of a Micromechanically-based Elastic-plastic Constitutive Model for Soils", Internal Memorandum, Soils and Rock Mechanics Division, Geotechnical Laboratory, USAE Waterways Experiment Station, Vicksburg, MS.
- MS State Department of Transportation, (MDOT), 1990, MS Standard Specification for Road and Bridge Construction, Jackson, MS.
- Peters, John F., 1991, "Computational Aspects of Endochronic Plasticity", Proceedings, Seventh International Conference on Computer Methods and Advances in Geomechanics, Cairns, Australia.
- Peters, John F., 1997, "Regarding Development of a Micromechanically-based Elastic-plastic Constitutive Model for Soils", Internal Memorandum, Soil and Rock Mechanics Division, Geotechnical Laboratory, USAE Waterways Experiment Station, Vicksburg, MS.
- Peters, John F., 1998, "Regarding Implementation of a Micromechanically-based Elastic-plastic Constitutive Model for Soils", Internal Memorandum, Soil and Rock Mechanics Division, Geotechnical Laboratory, USAE Waterways Experiment Station, Vicksburg, MS.
- Peters, John F., 1983, Constitutive Theory for Stress-Strain Behavior of Frictional Materials, Ph.D. Dissertation, University of Illinois, Chicago, Illinois, 1983.
- Prevost, J. H. and Popescu, R., 1996, "Constitutive Relations for Soil Materials", The Electronic Journal of Geotechnical Engineering, Volume 1. <http://geotech.civen.okstate.edu/ejge>.
- Rada, G. and Witczak, M.W., 1981, "Comprehensive Evaluation of Laboratory Resilient Moduli Results for Granular Materials," Transportation Research Record 810, pp. 23-33, Washington, DC.
- Salami, M. Reza, 1994, Failure Mechanisms for Granular Materials, WES Contract DACA39-93-C-0083 Final Report, Department of Civil Engineering, North Carolina A&T State University.
- Schofield, A.N. and Wroth, C.P., 1968, Critical State Soil Mechanics, McGraw-Hill, London.



Seed, H.B., Mitry, F.G., Monismith, C.L., and Chan, C.K., 1967, "Factors Influencing the Resilient Deformations of Untreated Aggregate Base in Two-Layer Pavements Subjected to Repeated Loading," Highway Research Record 190, pp. 19-57.

Tseng, Kuo-Hung, 1988, A Finite Element Method for the Performance Analysis of Flexible Pavements, Ph.D. Dissertation, Texas A and M University, College Station, TX.

Ulitz, Per, 1998, Modeling Flexible Pavement Response and Performance, Polyteknisk Forlag, Denmark.

University of Michigan, 1962, Proceedings, International Conference on the Structural Design of Asphalt Pavements.

University of Michigan, 1967, Proceedings, Second International Conference on the Structural Design of Asphalt Pavements.

University of Michigan, 1972, Proceedings, Third International Conference on the Structural Design of Asphalt Pavements, Volumes I and II.

University of Michigan, 1977, Proceedings, Fourth International Conference on the Structural Design of Asphalt Pavements, Volumes I and II.

University of Michigan and The Delft University of Technology, 1982, Proceedings, Fifth International Conference on the Structural Design of Asphalt Pavements,

University of Michigan, 1987, Proceedings, Sixth International Conference on the Structural Design of Asphalt Pavements, Volumes I and II.

University of Michigan, 1992, Proceedings, Seventh International Conference on the Structural Design of Asphalt Pavements, Volumes I and II.

Uzan, J., A., 1985, "Characterization of Granular Material", Transportation Research Record 1022, National Research Council, Washington, DC.

Uzan, J., Witczak, M.W., Scullion, T., and Lytton, R.L., 1992. "Development and Validation of Realistic Pavement Response Models", Proceedings, Seventh International Conference on the Structural Design of Asphalt Pavements, Volume 1, pages 334-350.

Webster, Steve L, 1993, "Geogrid Reinforced Base Courses for Flexible Pavements for Light Aircraft: Test Section Construction, Behavior Under Traffic, Laboratory Tests, and Design Criteria", US Army Engineer Waterways Experiment Station, Vicksburg, MS.

Valanis, K. C., and Read, H. E. , 1987, "An Endochronic Plasticity Theory for Concrete", Mechanics of Materials 5, pages 227-295.

Valanis, K. C., 1971, "A Theory of Viscoplasticity Without a Yield Surface", Archives of Mechanics, Vol. 23, pp. 517-551.

Yeh, Meng-Shan, 1989, Nonlinear Finite Element Analysis and Design of Flexible Pavements, Ph.D. Dissertation, Michigan State University.

**APPENDIX A**  
**WES MM MODEL UMAT SOURCE CODE**

```

C      Last change:  DMS  13 Jul 1999    7:57 am
      SUBROUTINE UMAT(STRESS,STATEV,DDSDDE,SSE,SPD,SCD,
1 RPL,DDSDDT,DRPLDE,DRPLDT,STRAN,DSTRAN,
2 TIME,DTIME,TEMP,DTMP,PREDEF,DPRED,CMNAME,NDI,NSHR,NTENS,
3 NSTATV,PROPS,NPROPS,COORDS,DROT,PNEWDT,CELENT,
4 DFGRD0,DFGRD1,NOEL,NPT,LAYER,KSPT,KSTEP,KINC)
      INCLUDE 'ABA_PARAM.INC'

      CHARACTER*8 CMNAME
      REAL*8 STRESS(NTENS),STATEV(NSTATV),
1 DDSDDE(NTENS,NTENS),DDSDDT(NTENS),DRPLDE(NTENS),
2 STRAN(NTENS),DSTRAN(NTENS),TIME(2),PREDEF(1),DPRED(1),
3 PROPS(NPROPS),COORDS(3),DROT(3,3),DFGRD0(3,3),DFGRD1(3,3)

C!      LOGICAL DRAINED,  Sflag(4), Hflag(4),HflagSave(4) ,
SflagSave(4)

C!      INTEGER*4 Ntimes, iprint, Numout, im, iter, icode, smech,
hmech

      LOGICAL Sflag(4)
      LOGICAL Hflag(4)
      LOGICAL Sflagd

      INTEGER*4 r
C!      Index for mechanism

      INTEGER*4 counter

      REAL*8 State
C!      Void ratio

      REAL*8 Qs(6,4), JQs(6,4)
C!      Internal shear forces

      REAL*8 Qh(4), JQh(4)
C!      Internal hydrostatic forces

      REAL*8 StateSave
C!      Void ratio

      REAL*8 QsSave(6,4)
C!      Internal shear forces

      REAL*8 QhSave(4)
C!      Internal hydrostatic forces

      REAL*8 D(3,3)
C!      Strain Increment tensor

C!      REAL*8 Eps(3,3)
C!      Strain

      REAL*8 Ds(6)
C!      Strain increment vector

```

```

      REAL*8  Sigma(3,3)
C!    Stress tensor

      REAL*8  KStress(6)
C!    STRESS VECTOR USED IN MAIN PROGRAM SO AS NOT TO CONFUSE WITH
ABAQUS STRESS

      REAL*8  Sigc
C!    Confinning stress

      REAL*8  DeltaEps
C!    Strain increment

      REAL*8  TotalEps
C!    Total strain

      REAL*8  Fh, beta, Pe
C!    Parameters defining volumetric state

      REAL*8  Mc
C!    Shear-volume coupling parameter

      REAL*8  Cohesion
C!    Cohesion parameter

      REAL*8  Gamma

      REAL*8  C
C!    Mohr-Coulomb cohesion

      REAL*8  Decay
C!    Defines rate that PhiLim falls with OCR

      REAL*8  PhiRatio
C!    Ratio of maximum and minimum PhiLim

      REAL*8  PhiLim
C!    Mohr-Coulomb friction angle

      REAL*8  PhiR
C!    Friction angle in radians

      REAL*8  BulkMod
C!    Elastic Bulk Modulus

      REAL*8  ShearMod
C!    Elastic Shear Modulus

      REAL*8  PhiFrac(4)
C!    Fraction of PhiLim for each shear mechanism

      REAL*8  Pfact(4)
C!    factor to apportion mean stress to mechanism

      REAL*8  ShearRatio(4)
C!    Shear modulus for internal mechanism

```

```

REAL*8  Hlimit(4)
C!      Limit of internal hydrostatic mechanism

REAL*8  BulkRatio(4)
C!      Bulk modulus for internal mechanism

REAL*8  SPARMS(27)

C      Counters used in Do Loops

INTEGER*4  I,J, IR, IQ, II, IA

C      Variables to calculate Jacobian
REAL*8  SML_STRAIN(3,3),JAC(NTENS)
REAL*8  JState, BSTATE, JSIGMA(3,3), JSTRESS(6), JDs(6)
REAL*8  JACO(NTENS,NTENS), ASIGMA(3,3), blend1, blend2
PARAMETER(ALPHA = -0.00001)

C      OPEN FILE FOR DEBUG DATA
C
C
C      OPEN (14, FILE = './MDUMP.OUT')
C      WRITE (14,*) 'START EXECUTABLE STATEMENTS', KSTEP, KINC,
NPROPS
C      CALL FLUSH (14)
C      CALL FLUSH (6)
C      CALL FLUSH (8)
      SIGMA(1,1) = STRESS(1)
      SIGMA(2,2) = STRESS(2)
      SIGMA(3,3) = STRESS(3)
      SIGMA(1,2) = STRESS(4)
      SIGMA(2,1) = SIGMA(1,2)
      SIGMA(1,3) = 0
      SIGMA(3,1) = SIGMA(1,3)
      SIGMA(2,3) = 0
      SIGMA(3,2) = SIGMA(2,3)
C      WRITE (14,*) 'SIGMA INITIALIZED', KSTEP, KINC
C      CALL FLUSH (14)
C      CALL FLUSH (6)
C      CALL FLUSH (8)

C      PROPS(ERTIES)
      beta          = PROPS(1)
      Fh            = PROPS(2)
      C             = PROPS(3)
      Mc            = PROPS(4)
      Gamma         = PROPS(5)
      PhiLim        = PROPS(6)
      Decay         = PROPS(7)
      PhiRatio      = PROPS(8)
      BulkMod       = PROPS(9)
      ShearMod      = PROPS(10)
      PhiFrac(1)    = PROPS(11)
      PhiFrac(2)    = PROPS(12)
      PhiFrac(3)    = PROPS(13)

```

```

        PhiFrac(4)      = PROPS(14)
        Pfact(1)        = PROPS(15)
        Pfact(2)        = PROPS(16)
        Pfact(3)        = PROPS(17)
        Pfact(4)        = PROPS(18)
        ShearRatio(1)   = PROPS(19)
        ShearRatio(2)   = PROPS(20)
        ShearRatio(3)   = PROPS(21)
        ShearRatio(4)   = PROPS(22)
        Hlimit(1)       = PROPS(23)
        Hlimit(2)       = PROPS(24)
        Hlimit(3)       = PROPS(25)
        Hlimit(4)       = PROPS(26)
        BulkRatio(1)    = PROPS(27)
        BulkRatio(2)    = PROPS(28)
        BulkRatio(3)    = PROPS(29)
        BulkRatio(4)    = PROPS(30)

C      WRITE (14,*) 'PROPS INITIALIZED', KSTEP, KINC

C      WRITE (14,*) ' beta', beta
C      WRITE (14,*) ' Fh', Fh
C      WRITE (14,*) ' C', C
C      WRITE (14,*) ' Mc', Mc
C      WRITE (14,*) ' Gamma', Gamma
C      WRITE (14,*) ' PhiLim', PhiLim
C      WRITE (14,*) ' Decay', Decay
C      WRITE (14,*) ' PhiRatio', PhiRatio
C      WRITE (14,*) ' BulkMod', BulkMod
C      WRITE (14,*) ' ShearMod', ShearMod
C      WRITE (14,*) ' PhiFrac(1)', PhiFrac(1)
C      WRITE (14,*) ' PhiFrac(2)', PhiFrac(2)
C      WRITE (14,*) ' PhiFrac(3)', PhiFrac(3)
C      WRITE (14,*) ' PhiFrac(4)', PhiFrac(4)
C      WRITE (14,*) ' Pfact(1)', Pfact(1)
C      WRITE (14,*) ' Pfact(2)', Pfact(2)
C      WRITE (14,*) ' Pfact(3)', Pfact(3)
C      WRITE (14,*) ' Pfact(4)', Pfact(4)
C      WRITE (14,*) ' ShearRatio(1)', ShearRatio(1)
C      WRITE (14,*) ' ShearRatio(2)', ShearRatio(2)
C      WRITE (14,*) ' ShearRatio(3)', ShearRatio(3)
C      WRITE (14,*) ' ShearRatio(4)', ShearRatio(4)
C      WRITE (14,*) ' Hlimit(1)', Hlimit(1)
C      WRITE (14,*) ' Hlimit(2)', Hlimit(2)
C      WRITE (14,*) ' Hlimit(3)', Hlimit(3)
C      WRITE (14,*) ' Hlimit(4)', Hlimit(4)
C      WRITE (14,*) ' BulkRatio(1)', BulkRatio(1)
C      WRITE (14,*) ' BulkRatio(2)', BulkRatio(2)
C      WRITE (14,*) ' BulkRatio(3)', BulkRatio(3)
C      WRITE (14,*) ' BulkRatio(4)', BulkRatio(4)
C      WRITE (14,*) 'PROPS INITIALIZED', KSTEP, KINC
C      WRITE (14,*) 'COHESION VALS', PhiLim, Cohesion
C      WRITE (14,*) 'PhiLim = ', PhiLim
C      WRITE (14,*) 'Cohesion = ', Cohesion
C      WRITE (14,*) 'C = ', C
C      CALL FLUSH (14)
C      CALL FLUSH (6)

```

```

c      CALL FLUSH (8)

C      Convert cohesion to a hydrostatic offset
      PhiR = PhiLim * 3.141592/180.

      Cohesion = C * ( 3. - SIN(PhiR) ) * COS(PhiR) / SIN(PhiR)

C      Define ParmS
      SParms( 1) = beta
      SParms( 2) = Fh
      SParms( 3) = Cohesion
      SParms( 4) = PhiFrac(1) * PhiLim
      SParms( 5) = PhiFrac(2) * PhiLim
      SParms( 6) = PhiFrac(3) * PhiLim
      SParms( 7) = PhiFrac(4) * PhiLim
      SParms( 8) = ShearRatio(1) * ShearMod
      SParms( 9) = ShearRatio(2) * ShearMod
      SParms(10) = ShearRatio(3) * ShearMod
      SParms(11) = ShearRatio(4) * ShearMod
      SParms(12) = Pfact(1)
      SParms(13) = Pfact(2)
      SParms(14) = Pfact(3)
      SParms(15) = Pfact(4)
      SParms(16) = Hlimit(1)
      SParms(17) = Hlimit(2)
      SParms(18) = Hlimit(3)
      SParms(19) = Hlimit(4)
      SParms(20) = BulkRatio(1) * BulkMod
      SParms(21) = BulkRatio(2) * BulkMod
      SParms(22) = BulkRatio(3) * BulkMod
      SParms(23) = BulkRatio(4) * BulkMod
      SParms(24) = Mc
      SParms(25) = Decay
      SParms(26) = PhiRatio
      SParms(27) = Gamma

      STATE = STATEV(29)

C      Load Strain increment from DSTRAN(6) array
      D(1,1) = DSTRAN(1)
      D(2,2) = DSTRAN(2)
      D(3,3) = DSTRAN(3)
      D(1,2) = DSTRAN(4)*0.5
      D(2,1) = D(1,2)
      D(1,3) = 0
      D(3,1) = D(1,3)
      D(2,3) = 0
      D(3,2) = D(2,3)

c      Load strain increment vector Ds from Strain increment Array D

```

```

      Ds(1) = D(1,1)
      Ds(2) = D(2,2)
      Ds(3) = D(3,3)
      Ds(4) = D(1,2)
      Ds(5) = D(1,3)
      Ds(6) = D(2,3)

C      Stuff STATE into BSTATE
      BSTATE = STATE

C
C      Bring Qs, Qh, and Void Ration in from Statev array.

      COUNTER=0
      DO i=1,6
        DO r=1,4
          COUNTER=COUNTER+1
          Qs(i,r)= statev(COUNTER)
        END DO
      END DO
      DO r=1,4
        COUNTER=COUNTER+1
        Qh(r)= statev(COUNTER)
      END DO

      COUNTER=COUNTER+1
      STATE=STATEV(COUNTER)

c      WRITE (14,*) "Before", state, counter , "(sv-29)",
statev(29)
c      DO r=1,4
c      WRITE (14,*) "Qh(",R,")",Qh(r)
c      CALL FLUSH (14)
c      CALL FLUSH (6)
c      CALL FLUSH (8)
c      END DO
c      SUBROSand_Driver(Ds, State, Qs, Qh, Stress, Sparms,
Sflag,Hflag)
      CALL Sand_Driver(Ds, State, Qs, Qh, KStress, Sparms,
Sflag,Hflag)

c      WRITE (14,*) "AFTER", state
c      DO r=1,4
c      WRITE (14,*) "Qh(",R,")",Qh(r)
c      CALL FLUSH (14)
c      CALL FLUSH (6)
c      CALL FLUSH (8)
c      END DO
c      CALL FLUSH (14)
c      CALL FLUSH (6)
c      CALL FLUSH (8)

C      Fill Qs, Qh and Void Ratio back into STATE variables

      COUNTER=0
      DO I=1,6

```



```

        DO R=1,4
            COUNTER=COUNTER+1
            STATEV(COUNTER) = Qs(I,R)
        END DO
    END DO
    DO R=1,4
        COUNTER=COUNTER+1
        STATEV(COUNTER) = Qh(R)
    END DO
    COUNTER=COUNTER+1
    STATEV(COUNTER)=State

C      Put KStress into stress variable from abaqus
    DO I=1,NTENS
        STRESS(I) = KSTRESS(I)
c      WRITE(14,*) 'STRESS ', I, STRESS(I)
    END DO

C      End : boss loop

C      CALCULATE THE JACOBIAN.

C      Make a copy of Current Qs, Qh and Void Ratio for a dummy call.

        DO i=1,6
            DO r=1,4
                QsSave(i,r)= Qs(i,r)
                QhSave(r) = Qh(r)
            END DO
        END DO
        JState=State

C      Zero out JACO(NTENS,NTENS)

        DO I = 1,NTENS
            DO J = 1, NTENS
                JACO(I,J) = 0.0
            END DO
        END DO

C      Loop: JACK

        DO I = 1,NTENS

C      Reset Strain Increment to 0.0

            DO II = 1,3
                DO IQ = 1,3
                    SML_STRAIN(II,IQ) = 0.0
                END DO
            END DO

```

```

        ASIGMA(1,1) = KSTRESS(1)
        ASIGMA(2,2) = KSTRESS(2)
        ASIGMA(3,3) = KSTRESS(3)
        ASIGMA(1,2) = KSTRESS(4)
        ASIGMA(1,3) = KSTRESS(5)
        ASIGMA(2,3) = KSTRESS(6)
        ASIGMA(2,1) = ASIGMA(1,2)
        ASIGMA(3,1) = ASIGMA(1,3)
        ASIGMA(3,2) = ASIGMA(2,3)

C      Set SML_STRAIN inc for partial

        IF (I.EQ.1) SML_STRAIN(1,1) = ALPHA
        IF (I.EQ.2) SML_STRAIN(2,2) = ALPHA
        IF (I.EQ.3) SML_STRAIN(3,3) = ALPHA
        IF (I.EQ.4) SML_STRAIN(1,2) = ALPHA*0.5
        IF (I.EQ.5) SML_STRAIN(1,3) = ALPHA*0.5
        IF (I.EQ.6) SML_STRAIN(2,3) = ALPHA*0.5
        SML_STRAIN(2,1) = SML_STRAIN(1,2)
        SML_STRAIN(3,1) = SML_STRAIN(1,3)
        SML_STRAIN(3,2) = SML_STRAIN(2,3)

c      Load strain increment vector Ds from Strain increment Array D

        JDs(1) = SML_STRAIN(1,1)
        JDs(2) = SML_STRAIN(2,2)
        JDs(3) = SML_STRAIN(3,3)
        JDs(4) = SML_STRAIN(1,2)
        JDs(5) = SML_STRAIN(1,3)
        JDs(6) = SML_STRAIN(2,3)

C      Load the Original Q Values in to the Call Arrays Qs, Qh
DO ia=1,6
    DO r=1,4
        JQs(ia,r)= QsSave(ia,r)
        JQh(r)   = QhSave(r)
    END DO
END DO

C      Dummy call to the sand_driver for calculation of
C      Jacobian.

        CALL Sand_Driver(JDs, JState, JQs, JQh, JStress,
            Sparms, Sflag, Hflag)

C      Map JStress from Sand Driver into JSigma for JACO

        JSIGMA(1,1) = JSTRESS(1)
        JSIGMA(2,2) = JSTRESS(2)
        JSIGMA(3,3) = JSTRESS(3)
        JSIGMA(1,2) = JSTRESS(4)
        JSIGMA(1,3) = JSTRESS(5)
        JSIGMA(2,3) = JSTRESS(6)

```

```

        JSIGMA(2,1) = JSIGMA(1,2)
        JSIGMA(3,1) = JSIGMA(1,3)
        JSIGMA(3,2) = JSIGMA(2,3)

C      Compute a Jacobian term
      IF (I.LE.3) THEN
        DO J = 1,3
          JACO(J,I) = (JSIGMA(J,I)-ASIGMA(J,I))/ALPHA
        END DO

      ELSE

        blend1 = JSIGMA(1,2)-ASIGMA(1,2)
        blend2 = JSIGMA(2,1)-ASIGMA(2,1)
        JACO(I,I) = (blend1+blend2)/(1*ALPHA)

      END IF
    END DO
  C    End of JACK loop

  C    Zero out the Jacobian Matrix.

    DO I=1,NTENS
      DO J=1,NTENS
        DDSDE(I,J) = 0.0
      END DO
    END DO

  C    Fill up the Jacobian Matrix

    DO I = 1,NTENS
      DO J = 1, NTENS
        DDSDE(I,J) = JACO(I,J)
      END DO
    END DO

    END

  C    End Program Main

  C
  *****
  *****
  C
  *****
  *****
  C
  *****
  *****
  C
  *****
  *****

```

SUBROUTINE  
Sand\_Driver(Ds, State, Qs, Qh, Stress, Sparms, Sflag, Hflag)

INCLUDE 'ABA\_PARAM.INC'

IMPLICIT NONE

C! YIELD SURFACE

REAL\*8 Fy

C! REAL\*8 A(6), B(6), TDOT

REAL\*8 TDOT

LOGICAL Sflag(4)

LOGICAL Hflag(4)

LOGICAL Sflagd

INTEGER\*4 r

C! Index for mechanism

INTEGER\*4 i

C! index for stress component

REAL\*8 Sparms(40)

C! Parameters

REAL\*8 Ds(6)

C! Strain increment

REAL\*8 Ds0(6)

C! Null strain increment

REAL\*8 State

C! Void ratio

REAL\*8 Qs(6,4)

C! Internal shear forces

REAL\*8 Qh(4)

C! Internal hydrostatic forces

REAL\*8 Sigma

C! Mean stress

REAL\*8 S(6)

C! Shear stress

REAL\*8 S0(6)

C! Initial shear stress

REAL\*8 Stress(6)

C! Stress

REAL\*8 Sig, Sig0

C! Mean stress parameter

REAL\*8 ShearMod

C! Elastic Shear Modulus

```

      REAL*8  Fh, beta, Pe
C!    Parameters defining volumetric state

      REAL*8  Mc
C!    Shear-volume coupling parameter

      REAL*8  Cohesion
C!    Cohesion parameter

      REAL*8  Decay
C!    Defines rate that PhiLim falls with OCR

      REAL*8  PhiRatio
C!    Ratio of maximum and minimum PhiLim

      REAL*8  PhiR
C!    Friction angle in radians

      REAL*8  SinPhi
C!    Sine of friction angle

      REAL*8  Gamma
C!    What is Gamma ????????

      REAL*8  Phi(4)
C!    Fraction of PhiLim for each shear mechanism

      REAL*8  Ylimit(4)
C!    Limit of internal shear mechanism

      REAL*8  Shear(4)
C!    Shear modulus for internal mechanism

      REAL*8  Hlimit(4)
C!    Limit of internal hydrostatic mechanism

      REAL*8  Pfact(4)
C!    factor to apportion mean stress to mechanism

      REAL*8  Bulk(4)
C!    Bulk modulus for internal mechanism

      REAL*8  desp(6)
C!    Plastic shear strain returned for rth mechanism

      REAL*8  despt(6)
C!    Total plastic shear strain

      REAL*8  depd
C!    Hydrostatic strain due to shear-volume coupling

      REAL*8  dEps
C!    Total hydrostatic strain increment

C!    Hydrostatic Strain increment
      dEps = Ds(1) + Ds(2) + Ds(3)

```

```

do I = 1,6
  desp(i) = 0.
END do

C!   Account for void ratio
State = (1. + State)* EXP(dEps) - 1.
beta = SParms(1)
Fh   = SParms(2)
Pe = 10.**((Fh - State )* beta)

c      WRITE (14,*)   "Inside", state
c      CALL FLUSH (14)
c      CALL FLUSH (6)
c      CALL FLUSH (8)

C!   Fill in parameters
Cohesion   = SParms( 3)
Phi(1)     = SParms( 4)
Phi(2)     = SParms( 5)
Phi(3)     = SParms( 6)
Phi(4)     = SParms( 7)
Shear(1)   = SParms( 8)
Shear(2)   = SParms( 9)
Shear(3)   = SParms(10)
Shear(4)   = SParms(11)
Pfact(1)   = SParms(12)
Pfact(2)   = SParms(13)
Pfact(3)   = SParms(14)
Pfact(4)   = SParms(15)
Hlimit(1)  = - SParms(16) * Pe
Hlimit(2)  = - SParms(17) * Pe
Hlimit(3)  = - SParms(18) * Pe
Hlimit(4)  = - SParms(19) * Pe
Bulk(1)    = SParms(20)
Bulk(2)    = SParms(21)
Bulk(3)    = SParms(22)
Bulk(4)    = SParms(23)
Mc         = SParms(24)
Decay      = SParms(25)
PhiRatio   = SParms(26)
Gamma      = SParms(27)

ShearMod = Shear(1) + Shear(2) + Shear(3) + Shear(4)

C!   Hydrostatic stress parameter
Sig = Qh(1) + Qh(2) + Qh(3) + Qh(4) - Cohesion

C!   Convert friction angle to yield limit by building a principal
C   stress state at the limit and computing Fy for that state.
DO r=1,4
  PhiR=(3.141592*Phi(r)/180.)*
1(PhiRatio+(1.0-PhiRatio)*EXP(Decay*Sig/Pe))
  SinPhi = SIN(PhiR)

  Stress(1) = (1. + SinPhi)/(1.-SinPhi)
  Stress(2) = 1.0

```

```

        Stress(3) = 1.0
        Stress(4) = 0.0
        Stress(5) = 0.0
        Stress(6) = 0.0
        Ylimit(r) = Fy(Stress)
    END DO

C!   Initialize stress
    do i=1,6
        S(i)      = 0.0
        S0(i)     = 0.0
        despt(i)  = 0.0
        desp(i)   = 0.0
    END DO

    Sigma = 0.0
    Sig0 = Sig

C! Update each sand shearing mechanism and shear accumulate stress
    DO r = 1,4

C! Save initial shear stress for stress dilatancy computation
        DO i=1,6
            S0(i) = S0(i) + Qs(i,r)
        END DO

        CALL Ammos(Ds, Qs(1,r), Sig*Pfact(r), desp,
            Ylimit(r), Shear(r), Sflag(r) )

        DO i=1,6
            despt(i) = despt(i) + Shear(r) * desp(i) / ShearMod
            S(i) = S(i) + Qs(i,r)
        END DO

    END DO

C! Shear coupling strain. Dilation is positive.
    depd =Gamma*(TDOT(S0, despt)/(-Sig0)-
    Mc*SQRT(TDOT(despt,despt)))

C! Update each hydrostatic mechanism and accumulate hydrostatic
stress
    DO r = 1,4
        CALL Hydros(dEps-depd, Qh(r), Bulk(r), Hlimit(r), Hflag(r))
        Sigma = Sigma + Qh(r)
    END DO

C! Rescale shear stress to account for reduction in mean stress
    Sig = Sigma - Cohesion

    DO I=1,6
        Ds0(I) = 0.
        S(I) = 0.
    END DO

```

```

DO r = 1,4
    DO I=1,6
        desp(I) =0.0
    END DO

    CALL Ammos(Ds0, Qs(1,r), Sig*Pfact(r), desp, Ylimit(r),
        Shear(r),Sflagd)

    DO i=1,6
        S(i) = S(i) + Qs(i,r)
        Stress(I) = S(i)
    END DO

    DO i=1,6
        Stress(I) = S(i)
    END DO

END DO

Stress(1) = S(1) + Sigma
Stress(2) = S(2) + Sigma
Stress(3) = S(3) + Sigma

c      WRITE (14,*)    "Inside # 2", state
c      CALL FLUSH (14)
c      CALL FLUSH (6)
c      CALL FLUSH (8)

      RETURN
      END
C      End Subroutine SAND_DRIVER

C
*****
C
*****
C
*****
C
*****
C
*****

SUBROUTINE Ammos( Ds, Qs, Sig, desp, Ylimit, Shear, Sflag)
INCLUDE 'ABA_PARAM.INC'
IMPLICIT NONE

REAL*8  Fy
C!      Scalar

REAL*8  FGrad(6)
C!      Array Giving Gadients

```



```

REAL*8 TDOT

LOGICAL Sflag

REAL*8 Y, Y0
C!   Value of yield function

REAL*8 Fc
C!   Fraction of coupling plastic strain

REAL*8 Sig
C!   Mean stress

REAL*8 Ylimit
C!   Limiting value of yield function

REAL*8 Shear
C!   Shear modulus

c!   REAL*8 Gamma
C!   Coupling parameter

REAL*8 Rho
C!   Interpolation parameter

REAL*8 dLamda
C!   plastic strain magnitude

REAL*8 Ds(6)
C!   Strain magnitude

REAL*8 Id(6)
C!   Identity tensor

REAL*8 Qm(6)
C!   Mean stress tensor

REAL*8 Qs(6), Qs0(6)
C!   Shear stress

REAL*8 Q(6)
C!   Stress

REAL*8 des(6)
C!   Shear strain increment tensor

REAL*8 dem(6)
C!   Volumetric strain increment tensor

REAL*8 dQsE(6)
C!   Elastic strain increment

REAL*8 P(6)
C!   Plastic strain direction

REAL*8 desp(6)

```

```

C!      Plastic strain increment tensor

      INTEGER I
C!      COUNTERS

!c      INITIALIZE COUNTING VARIABLES
      I=0
C!      J=0
C!      K=0
C!      L=0


C!      Identity tensor

      Id(1) = 1.0
      Id(2) = 1.0
      Id(3) = 1.0
      Id(4) = 0.0
      Id(5) = 0.0
      Id(6) = 0.0

C!      CHECK FOR NON-COMPRESSION
      IF (SIG.GE.0.0) THEN
        SIG=-0.001
      END IF
C!      Hydrostatic stress


C!      BEGIN VECTOR COUNTER LOOP

      DO I=1,6
        Qm(I) = Id(I) * Sig
      END do


C!      Save initial value
      Do I = 1,6
        Qs0(I) = Qs(I)
      END Do


C!      Hydrostatic increment

      DO I=1,6
        dem(I) = Id(I) * (Ds(1) + Ds(2) + Ds(3))/3.0
      END DO


C!      Shear part

      Do i=1,6
        des(I) = Ds(I) - dem(I)
      END DO


C!      Apply elastic Law with coupling plastic strain

```

```

C!      CALL FGradient(Q,FGrad)

      DO I=1,6

          dQsE(I) = Shear * des(I)

      END DO

      DO I=1,6

          Qs(I) = Qs(I) + dQsE(I)

      END DO

C!      Updated stress

      DO I=1,6
          Q(I) = Qs(I) + Qm(I)
      END DO

C!      Trial yield surface
      Y = Fy(Q)

c!      Adjust stress for yield condition
      IF(Y .GT. Ylimit .OR. Y .LE. 9.0) THEN
c!          Scale back stress
          CALL RadialReturn(Q, Ylimit)
c!          Qs = Q - Qm
          DO I=1,6
              Qs(I) = Q(I) - Qm(I)
          END DO

c!          IF(sdump) WRITE(13,*) q(1), q(2), q(3)

C!          Plastic shear strain increment

          do i=1,6
              desp(i) =( dQsE(i) - (Qs(i) - Qs0(i)))/Shear
          end do
C!          Signal that limit was hit
              Sflag = .True.

      ELSE
C!          Plastic strain is zero
              desp(1)=0.0
              desp(2)=0.0
              desp(3)=0.0
              desp(4)=0.0
              desp(5)=0.0
              desp(6)=0.0
C!          Signal that limit was not hit
              Sflag = .False.

      END IF

      RETURN

```

```

      END
C      End of Subroutine AMMOS

C!
*****
C!
*****
C!
*****
C!
*****
C      Last change:  PC      1 Apr 1999      12:49 pm
C!      Last change:  PC      1 Apr 1999      12:26 pm

C!      Subroutine to perform radial return of stress
C!      point to yield function given
C!      by  $F_y(Q) = I_1 I_2 / I_3$ . A transformation
C!      is first performed to principal
C!      stress space, then the return is performed
C!      such that  $I_1$  and  $(Pv_2 - Pv_3) / (Pv_1 - Pv_3)$ 
C!      are held constant. This these constraints,
C!       $F_y = Y_{limit}$  becomes a cubic equation.
C!      The stress tensor is computed from
C!      the eigen vectors and adjusted eigenvalues.
C!      Therefore, the adjusted stress tensor has
C!      the same principal axes, mean stress,
C!      and Lode parameter as the original stress tensor.
      SUBROUTINE RadialReturn(Q, Ylimit)
      INCLUDE 'ABA_PARAM.INC'
      IMPLICIT NONE

      LOGICAL sdump

      LOGICAL Reversed

      INTEGER i, j, iv, ib
      INTEGER it

      REAL*8 Qm1, Qm2, Qm3
      REAL*8 Qm
      REAL*8 Pmag
      REAL*8 I1, I2, I3, B1
      REAL*8 A, B, C, D
      REAL*8 alpha, beta, gamma, omega

      REAL*8 m(3)
      REAL*8 fi(3)
      REAL*8 S(3,3)
      REAL*8 Pv(3), Ev(3,3)

      REAL*8 Q(6)
      REAL*8 Ylimit, Rmax

C!      Initially principal values not reversed in order
      Reversed = .False.

```

```

C!      First estimate the maximum eigenvalue using Gershgorin's
theorem
      Qm1 = Q(1)      + ABS(Q(4)) + ABS(Q(5))
      Qm2 = ABS(Q(4)) + Q(2)      + ABS(Q(6))
      Qm3 = ABS(Q(5)) + ABS(Q(6)) + Q(3)

      Qm = MAX(Qm1, Qm2, Qm3)

C!      ....Compute principal values

C!      Invariants I1, I2, I3
      I1 = Q(1) + Q(2) + Q(3)

      I2 = Q(1)*Q(2)+Q(1)*Q(3)+Q(2)*Q(3) - (Q(4)**2+Q(5)**2+Q(6)**2)

      I3 = Q(1)*Q(2)*Q(3) -
      .      Q(1)*Q(6)**2 - Q(2)*Q(5)**2 - Q(3)*Q(4)**2 +
      .      2.0*Q(4)*Q(5)*Q(6)

C!      Use Newton iteration to get largest eigenvalue
      it = 0
      DO WHILE (ABS(Qm*(Qm*(I1-Qm)-I2)+I3).GT.1E-7.AND. it .LE. 50)
          it = it+1
          Qm = (Qm*Qm*(2.*Qm-I1) + I3)/(Qm*(3.*Qm-2.*I1) + I2)
      END DO

C!      Compute other two values using quadratic obtained from
synthetic division
C!      A = -1.0
      B = I1 - Qm
      C = Qm * B - I2

      D = B*B + 4.0 * C

C!      D can be <0 because of roundoff if there are repeated roots.
      IF(D .GT. 0.) THEN
          D = SQRT(D)
      ELSE
          D=0.0
      END IF

C!      Put in order of compressive magnitude
      Pv(3) = Qm
      Pv(2) = MAX(B+D, B-D)/2.0
      Pv(1) = MIN(B+D, B-D)/2.0

      Pmag = MAX( ABS(Pv(1)), ABS(Pv(2)), ABS(Pv(3)) )

C!      Check for null tensor
      IF(Pmag .LT. 1.E-12) GOTO 777

C!      Check for near-hydrostatic conditions.
      IF( ( ABS(Pv(1)-Pv(2)) )/Pmag .LT. 1.e-3) THEN
          IF(( ABS(Pv(1)-Pv(3)) )/Pmag .LT. 1.e-3) THEN
C!          Tensor is close to hydrostatic.
          GOTO 777

```

```

        END IF
    END IF

C!    Save principal values in normalized form for use later
    fi(1) = -Pv(1)/I1
    fi(2) = -Pv(2)/I1
    fi(3) = -Pv(3)/I1

C!    Compute principal directions. Note that by
C!    this point at least two eigenvalues
C!    have been determined to be distinct.
C!    Order eigenvalues to insure the first
C!    one is distinct. Note that they are
C!    now in order of magnitude. Thus Pv(1) and
C!    Pv(3) cannot be equal because the
C!    hydrostatic case has been ruled out.

    IF(ABS(Pv(1)-Pv(2)) .LT. ABS(Pv(1)-Pv(3)) .AND.
      . ABS(Pv(1)-Pv(2)) .LT. ABS(Pv(2)-Pv(3)) ) THEN
C!    Pv(1) and Pv(2) could be equal. Switch order

        Reversed = .true.
        A = Pv(3)
        Pv(3) = Pv(1)
        Pv(1) = A
    END IF

    DO i=1,2
        IF(i .EQ. 1 ) THEN
C!    First eigenvector. First eigenvalue is distinct.
            iv = 1
        ELSE
C!    Pick eigenvector with the "most distinct" eigenvalue.
            IF(ABS(Pv(1)-Pv(2)) .LT. ABS(Pv(1)-Pv(3)) ) THEN
                iv = 3
                ib = 2
            ELSE
                iv = 2
                ib=3
            END IF
        END IF
    END IF

C!    Set up the singular matrix
    S(1,1) = Q(1) - Pv(iv)
    S(1,2) = Q(4)
    S(1,3) = Q(5)

    S(2,1) = S(1,2)
    S(2,2) = Q(2) - Pv(iv)
    S(2,3) = Q(6)

    S(3,1) = S(1,3)
    S(3,2) = S(2,3)
    S(3,3) = Q(3) - Pv(iv)

    Pmag = Pmag * Pmag

```

```

C!      Pick the appropriate set of equations for eigenvector
components.
      IF(ABS(S(2,2) * S(3,3) - S(2,3) * S(3,2))/Pmag .GT. 1.E-5)
THEN
      D = S(2,2) * S(3,3) - S(2,3) * S(3,2)
      A = 1.0
      B = (-S(2,1) * S(3,3) + S(3,1) * S(2,3))/D
      C = (-S(2,2) * S(3,1) + S(2,1) * S(2,3))/D

      ELSE IF(ABS(S(1,1)*S(3,3)-S(1,3)*S(3,1))/Pmag.GT.1.E-5) THEN
      D = S(1,1) * S(3,3) - S(1,3) * S(3,1)
      A = (-S(1,2) * S(1,1) + S(3,2) * S(1,3))/D
      B = 1.0
      C = (-S(1,1) * S(3,2) + S(3,1) * S(1,2))/D

      ELSE IF(ABS(S(1,1)*S(2,2)-S(1,2)*S(2,1))/Pmag.GT.1.E-5) THEN
      D = S(1,1) * S(2,2) - S(1,2) * S(2,1)
      A = (-S(2,2) * S(1,3) + S(2,1) * S(1,3))/D
      B = (-S(1,1) * S(2,3) + S(2,1) * S(1,3))/D
      C = 1.0

      ELSE
C!      Repeated eigenvalue. Make a vector that is normal to first
C!      and direction m(i)that is not colinear to Ev(i,1)

      IF(ABS(Ev(1,1)) .GT. ABS(Ev(1,2)) ) THEN
      IF(ABS(Ev(1,1)) .GT. ABS(EV(1,3)) ) THEN
      m(1)= Ev(3,1)
      m(2)= Ev(2,1)
      m(3)= -Ev(1,1)
      ELSE
      m(1)= -Ev(3,1)
      m(2)= Ev(2,1)
      m(3)= Ev(1,1)
      END IF
      ELSE
      IF(ABS(Ev(1,2)) .GT. ABS(EV(1,3)) ) THEN
      m(1)= Ev(3,1)
      m(2)= -Ev(2,1)
      m(3)= Ev(1,1)
      ELSE
      m(1)= -Ev(3,1)
      m(2)= Ev(2,1)
      m(3)= Ev(1,1)
      END IF
      END IF

      A = m(2) * Ev(3,1) - m(3) * Ev(2,1)
      B = m(3) * Ev(1,1) - m(1) * Ev(3,1)
      C = m(1) * Ev(2,1) - m(2) * Ev(1,1)
END IF

C!      Normalize vector
D = SQRT(A*A + B*B + C*C)
Ev(1,iv) = A/D
Ev(2,iv) = B/D
Ev(3,iv) = C/D

```

```

END DO

C!   Use cross product to find third eigenvector
A = Ev(2,1) * Ev(3,iv) - Ev(2,iv) * Ev(3,1)
B = -Ev(1,1) * Ev(3,iv) + Ev(1,iv) * Ev(3,1)
C = Ev(1,1) * Ev(2,iv) - Ev(1,iv) * Ev(2,1)

C!   Normalize vector
D = SQRT(A*A + B*B + C*C)
Ev(1,ib) = A/D
Ev(2,ib) = B/D
Ev(3,ib) = C/D

C!   Adjust eigenvalues for yield condition
C!   assuming radial return in pi plane.
C!   The radial return requires solution
C!   of the cubic equation that is obtained by
C!   substitution of fi(1)+fi(2)+fi(3)=1
C!   and B1 into the equation for the yield
C!   function. The root rendering the
C!   largest negative value (most compressive)
C!   is the correct root. The cubic
C!   is in the form of
C!   alpha * Qm**3 + beta * Qm**2 + gamma * Qm + omega = 0

B1 = (fi(2)-fi(3))/(fi(1)-fi(3))
A = -(1.-B1)/(2.-B1)
B = (2*B1-1.)/(2.-B1)
C = -1./(2.-B1)
D = -(1.+B1)/(2.-B1)

alpha = B*D*Ylimit
beta = B + B*D + D + (A*D+B*C)*Ylimit
gamma = A + C + A*D + B*C + A*C*Ylimit
omega = A * C

C!   Use Newton iteration to get largest
C!   eigenvalue. Use approximation from Mohr-
C!   Coulomb yield surface as first guess
Rmax = 0.25 * ( (Ylimit - 5.) + SQRT((Ylimit-9.0)*(Ylimit-1.0))
)
Qm = -Rmax/(Rmax*(B1 + 1.0)-(B1-2.0))

it = 0
DO WHILE (ABS(Qm*(Qm*(alpha*Qm+beta)+gamma)+omega).GT.1E-7
.      .AND. it .LE. 50)
    it = it+1
    Qm = (Qm*Qm * (2.*alpha*Qm + beta) - omega)/
        (Qm * (3.*alpha*Qm + 2.*beta) + gamma)
END DO

C!   Revised principal values that meet yield condition
fi(1) = Qm
fi(2) = A + B*fi(1)
fi(3) = C + D*fi(1)

C!   Fill back in to eigenvalues

```



```

      IF(Reversed) THEN
        Pv(3) = -fi(1) * I1
        Pv(2) = -fi(2) * I1
        Pv(1) = -fi(3) * I1
      ELSE
        Pv(1) = -fi(1) * I1
        Pv(2) = -fi(2) * I1
        Pv(3) = -fi(3) * I1
      END IF

C!      Rebuild tensor from its spectral decomposition
      DO i=1,3
        DO j=i,3
          S(i,j) = Pv(1)*Ev(i,1)*Ev(j,1) +
            Pv(2)*Ev(i,2)*Ev(j,2) + Pv(3)*Ev(i,3)*Ev(j,3)
          S(j,i) = S(i,j)
        END DO
      END DO

C!      Put into vector form.
      Q(1) = S(1,1)
      Q(4) = S(1,2)
      Q(5) = S(1,3)

      Q(2) = S(2,2)
      Q(6) = S(2,3)
      Q(3) = S(3,3)

      777 CONTINUE
      RETURN
      END

C!
*****
C!
*****
C!
*****
C!
*****

      FUNCTION Fy(Q)

      IMPLICIT NONE

      REAL*8 Q(6)
      REAL*8 I1, I2, I3

      REAL*8 Fy

C!      Invariants I1, I2, I3
      I1 = Q(1) + Q(2) + Q(3)

      I2 = Q(1)*Q(2)+Q(1)*Q(3)+Q(2)*Q(3)-(Q(4)**2+Q(5)**2+Q(6)**2)

```

```

      I3 = Q(1)*Q(2)*Q(3) -
      .      Q(1)*Q(6)**2 - Q(2)*Q(4)**2 - Q(3)*Q(5)**2 +
      .      2.0*Q(4)*Q(5)*Q(6)

C!      Yield Function
      Fy = I1*I2/I3

      END

C!      =====

C!      *****
C!      *****
C!      *****
C!      *                      *HYDROS*                      *
C!      *****
C!      *****
C!      *****
C!      SUBROUTINE Hydros(dEps, Sigma, Bulk, Hlimit, Hflag)

      IMPLICIT NONE

      LOGICAL Hflag

      REAL*8 dEps
      REAL*8 Bulk
      REAL*8 Hlimit
      REAL*8 dSigmaE
      REAL*8 Sigma

C!      Stress increment
      dSigmaE = Bulk * dEps

C!      Elastic stress
      Sigma = Sigma + dSigmaE

C!      Limit condition (note tension--positive convention)
      IF(Sigma .LT. Hlimit) THEN
C!      Compression limit
          Sigma = Hlimit
          Hflag = .True.
      ELSE IF(Sigma .GT. 0.) THEN
C!      Tension Limit
          Sigma = 0.0
          Hflag = .True.
      ELSE
          Hflag = .False.
      END IF

      END

C!      *****
C!      *                      * T D O T *                      *
C!      *****

```

```

      FUNCTION TDOT(A,B)

      IMPLICIT NONE

C!
C!      Function to compute scalar product of two symmetric tensors
C!      given in 6 vector format
C!
      REAL*8 A(6),B(6), TDOT
C!
      TDOT = A(1) * B(1) + A(2) * B(2) + A(3) * B(3) +
      .           2.D0 * (A(4) * B(4) + A(5) * B(5) + A(6) *
B(6))
C!      Return TDOT a scalar quantity
      RETURN
      END

C!
*****
*****
C!      This is a subroutine TO RETURN THE GRADIENT OF A STRESS VECTOR
Q(6)      *
C!
*****
*****

      SUBROUTINE FGradient(Q, FGrad)

      IMPLICIT NONE
      INTEGER I
      REAL*8 TDOT
      REAL*8 Q(6)
      REAL*8 Iso(6)
      REAL*8 P(6)
      REAL*8 I1, I2, I3
      REAL*8 dFdI1, dFdI2, dFdI3
      REAL*8 dI1dQ(6), dI2dQ(6), dI3dQ(6)
      REAL*8 Pbar,PSUM
      REAL*8 FGrad(6)

C!      Mean tensor

      DO I=1,6
         Iso(I)=0.0
      END DO

      Iso(1) = 1.0/3.0
      Iso(2) = Iso(1)
      Iso(3) = Iso(1)

C!      Invarients I1, I2, I3
      I1 = Q(1) + Q(2) + Q(3)

      I2 = Q(1)*Q(2)+Q(1)*Q(3)+Q(2)*Q(3)-(Q(4)**2+Q(5)**2+Q(6)**2)

      I3 = Q(1)*Q(2)*Q(3) -
      .      Q(1)*Q(6)**2 - Q(2)*Q(4)**2 - Q(3)*Q(5)**2 +

```

```

      2.0*Q(4)*Q(5)*Q(6)

dFdI1 = I2/I3
dFdI2 = I1/I3
dFdI3 = -I1*I2/I3**2

DO I=1,6
  dI1dQ(I) = Iso(I)
END DO
dI2dQ(1) = Q(2) + Q(3)
dI2dQ(2) = Q(1) + Q(3)
dI2dQ(3) = Q(1) + Q(2)
dI2dQ(4) = -2.0 *Q(4)
dI2dQ(5) = -2.0 *Q(5)
dI2dQ(6) = -2.0 *Q(6)

dI3dQ(1) = Q(2)*Q(3) - Q(6)**2
dI3dQ(2) = Q(1)*Q(3) - Q(4)**2
dI3dQ(3) = Q(1)*Q(2) - Q(5)**2
dI3dQ(4) = -2.0 *(Q(2)*Q(4) + Q(5)*Q(6))
dI3dQ(5) = -2.0 *(Q(3)*Q(5) + Q(4)*Q(6))
dI3dQ(6) = -2.0 *(Q(1)*Q(6) + Q(4)*Q(5))

DO I=1,6
  P(I) = dFdI1 * dI1dQ(I) + dFdI2 * dI2dQ(I) + dFdI3 * dI3dQ(I)
END DO

PSUM = P(1)+P(2)+P(3)
DO I=1,6
  P(I) = P(I) - (PSUM)*Iso(I)
END DO

PBar = SQRT( TDOT(P,P) )

DO I=1,6
  FGrad(I) = P(I)/Pbar
END DO

RETURN
END

C
*****
C This is a subroutine to intialize the state variable array for
ABAQUS
      SUBROUTINE SDVINI (STATEV,COORDS,NSTATV,NCRDS,NOEL,NPT,
1  LAYER,KSPT)
      INCLUDE 'ABA_PARAM.INC'

      REAL*8 STATEV(NSTATV),COORDS(NCRDS)
      REAL*8 VERT,Hpart(4)
      INTEGER counter
C      COORDS are the coordinates of the point Zero must be at the
top of the System
C      NOEL is element number
C      NPT is integration point
C      LAYER is for a composite shell or layered solid

```

```

C      KSPT is a section point with a curent layer or section
C      Hpart is the fraction of the bulk modulus in each mechanism
C      Hydrostatic condition is set to 3*stress

      Hpart(1) = 0.6
      Hpart(2) = 0.38
      Hpart(3) = 0.01
      Hpart(4) = 0.01

      VERT = COORDS(3)*0.0868

      COUNTER=0
      DO I=1,6
        DO R=1,4
          COUNTER=COUNTER+1
          STATEV(COUNTER) = 0.0
        END DO
      END DO
      DO R=1,4
        COUNTER=COUNTER+1
C
C
        STATEV(COUNTER) = -Hpart(R)*1.0
      END DO

C      Set intial void ratio as state dependant variable 29
      STATEV(29) = 0.21

      RETURN
      END

```

**APPENDIX B**

**SAMPLE ABAQUS INPUT FILE**

Input File for Item 1-1	Comments
<p>*HEADING</p> <p>3X3 Grid for Lane 2</p> <p>**</p> <p>*NODE</p> <p>1, 0., 0.</p> <p>2, 4., 0.</p> <p>3, 8., 0.</p> <p>4, 12., 0.</p> <p>27, 12., -260.</p> <p>1428, 15.9827, -260.</p> <p>•</p> <p>•</p> <p>•</p> <p>1593, 0., -260.</p> <p>1594, 4., -260.</p> <p>1595, 8., -260.</p> <p>**</p> <p>**</p> <p>*ELEMENT, TYPE=CAX4, ELSET=AC_SURF</p> <p>1, 1, 5, 6, 2</p> <p>2, 2, 6, 7, 3</p> <p>3, 3, 7, 8, 4</p> <p>4, 4, 8, 44, 10</p> <p>34, 39, 73, 74, 40</p> <p>35, 40, 74, 75, 41</p> <p>36, 41, 75, 76, 42</p> <p>•</p> <p>•</p> <p>•</p> <p>*ELEMENT, TYPE=CAX4, ELSET=BASE</p> <p>37, 5, 81, 82, 6</p> <p>38, 6, 82, 83, 7</p> <p>•</p> <p>•</p> <p>•</p> <p>189, 242, 276, 277, 243</p> <p>*ELEMENT, TYPE=CAX4, ELSET=SUBGRADE</p> <p>217, 100, 339, 340, 272</p> <p>218, 272, 340, 341, 273</p> <p>•</p> <p>•</p> <p>•</p> <p>1404, 1591, 1595, 1427, 1393</p> <p>**</p> <p>**</p> <p>**</p> <p>**</p> <p>**</p> <p>**</p> <p>**</p> <p>**</p>	<p><u>Begin Model Definition</u></p> <p>Definition of nodes</p> <p>Node Number, r coordinate, z coordinate</p> <p>(Lines deleted for brevity)</p> <p>Definition of 4-node axysynetric elements</p> <p>Element number, nodes defining element</p> <p>(Lines deleted for brevity)</p> <p>(Lines deleted for brevity)</p> <p>(Lines deleted for brevity)</p> <p>(Lines deleted for brevity)</p> <p><u>End of Model Definition</u></p>

<pre> ** AC_SURF ** *SOLID SECTION, ELSET=AC_SURF, MATERIAL=AC_ELE     1., ** ** BASE ** *SOLID SECTION, ELSET=BASE, MATERIAL=BASE_ELE     1., ** ** SUBGRADE ** *SOLID SECTION, ELSET=SUBGRADE, MATERIAL=CH6000     1., ** ** AC_ELE ** Date: 19-Jul-99      Time: 15:36:49 ** *MATERIAL, NAME=AC_ELE ** *DENSITY     0.029, ** *ELASTIC, TYPE=ISO     500000.,    0.35 ** ** CH6000 ** Date: 19-Jul-99      Time: 15:36:49 ** *MATERIAL, NAME=CH6000 ** *DENSITY     0.023, ** *ELASTIC, TYPE=ISO     12000.,    0.35 ** ** ** ** *MATERIAL, NAME=UMAT ** *DENSITY     0.029, *DEPVAR     29 ** *USER MATERIAL, TYPE=MECHANICAL, CONSTANTS=30, UNSYMM 8.685,0.70,0.25,0.72,1.0,48.0,1.8,0.50 10000.,26000.0,0.35,0.42,0.82,0.88,0.9,0.77 0.38,0.48,0.702,0.148,0.058,0.0042,0.018,0.9 0.1,0.0,0.565,0.38,0.02,0.035 </pre>	<p><u>Material Definition</u></p> <p>Specifies element properties for solid elements</p> <p>Specifies elastic properties for asphalt layer</p> <p>Density in lbs./cubic inch</p> <p>Modulus of elasticity (psi), Poisson's ratio</p> <p>Specifies elastic properties for subgrade layer</p> <p>Density in lbs./cubic inch</p> <p>Modulus of elasticity (psi), Poisson's ratio</p> <p>Specifies userdefined material for base course</p> <p>Density in lbs./cubic inch</p> <p>Specifies number for state-dependent variables</p> <p>User defined material definition</p> <p>UMAT calibration constants</p>
--	---





<pre> ** ** RHS_FIX ** *BOUNDARY, OP=NEW     42, 1,,    0.     76, 1,,    0. . . .     1460, 2,,    0. ** ** ** ** Step 1, Gravity ** LoadCase, Geostatic ** *STEP, AMPLITUDE=RAMP, EXTRAPOLATION=NO, INC=10000, UNSYMM=YES, NLGEOM Application of Geostatic Gravity Load ** *STATIC     .01, 1. ** ** *CONTROLS, PARAMETERS=FIELD, FIELD=DISPLACEMENT 0.03, 1.0, 1.0, , *CONTROLS, PARAMETERS=LINE SEARCH 6, *CONTROLS, PARAMETERS=TIME INCREMENTATION 10, 15, 21, 50, 15, , , 15, , 6 , , , , , 1.1 ** ** ** *DLOAD, OP=NEW AC_SURF, GRAV, -2.68, 0.0, 1.0, 0.0 BASE, GRAV, -2.68, 0.0, 1.0, 0.0 SUBGRADE, GRAV, -2.68, 0.0, 1.0, 0.0 ** ** *FILE FORMAT, ASCII *NODE PRINT, FREQ=1 U, *NODE FILE, FREQ=1 U, ** *EL PRINT, POS=INTEG, FREQ=1 S, E, *EL FILE, POS=INTEG, FREQ=1 S, E, </pre>	<p>(Lines deleted for brevity)</p> <p><u>End Boundary Condition Definition</u></p> <p><u>Begin Definition of Load Steps</u></p> <p>Begin Step 1: Gravity Load</p> <p>Specify static analysis Initial time increment, total time</p> <p>Specify solution control parameters</p> <p>Apply distributed gravity load</p> <p>Specify output options Displacements and rotations</p> <p>Stress and strain</p>
---	---

<pre> ** *PRINT, FREQ=1 ** *END STEP ** ** Step 2, Load ** LoadCase, Default ** *STEP, AMPLITUDE=RAMP, INC=10000, NLGEOM, EXTRAPOLATION=NO Application of 68 psi Tire ** *STATIC     0.001,    1.,    1.E-8,    0.08 ** ** *CONTROLS, PARAMETERS=FIELD, FIELD=DISPLACEMENT 0.075, 1.0, 1.0, , *CONTROLS, PARAMETERS=LINE SEARCH 6, *CONTROLS, PARAMETERS=TIME INCREMENTATION 10, 15, 21, 50, 15, , 15, 6 , , , , , 1.1 ** *ELSET, ELSET=TIRE, GENERATE     1,    6,    1 ** ** ** TIRE ** *DLOAD, OP=MOD TIRE, P4,    68. ** *NODE PRINT, FREQ=20 U, *NODE FILE, FREQ=20 U, ** *EL PRINT, POS=CENTR, FREQ=20 S, E, *EL FILE, POS=CENTR, FREQ=20 S, E, ** ** *PRINT, FREQ=1 ** *END STEP ** ** ** ** ** </pre>	<p>End of Step 1</p> <p>Begin Step 2: Application of tire load</p> <p>Specify static analysis Initial time increment, total time, minimum time increment, maximum time increment</p> <p>Specify solution control parameters</p> <p>Define element set for tire load</p> <p>Apply distributed tire load</p> <p>Specify output options</p> <p>Displacements and rotations</p> <p>Stress and strain</p> <p>End of Step 1</p> <p>Begin Step 3: Removal of tire load</p>
---	---

<pre> ** ** ** ** Step 3, Un Load ** LoadCase, Default ** STEP, AMPLITUDE=RAMP, INC=10000, NLGEOM, EXTRAPOLATION=NO Removal of 68 psi Tire ** *STATIC     0.001,    1.,    1.E-8,    0.08 ** ** TIRE ** *DLOAD, OP=MOD TIRE, P4,    0.01 ** ** *END STEP </pre>	<p>Specify static analysis Initial time increment, total time, minimum time increment, maximum time increment</p> <p>Apply distributed tire load</p> <p>End of Step 3</p> <p>Load Steps 2 and 3 are repeated each time a load cycle is added</p>
---	--

**APPENDIX C**

**RESULTS OF TRIAXIAL COMPRESSION TESTS**

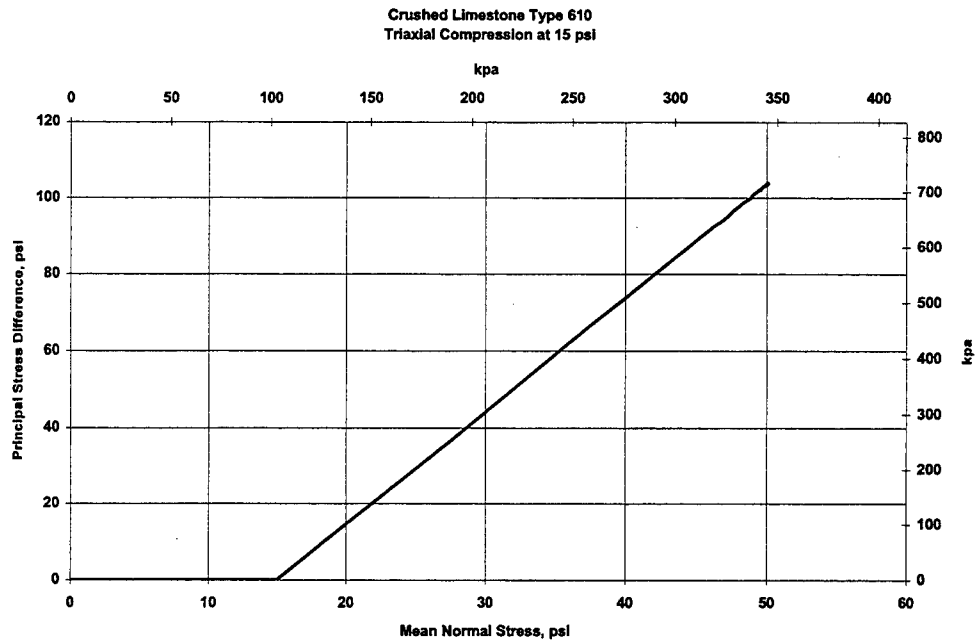


Figure C-1. CTC15-1

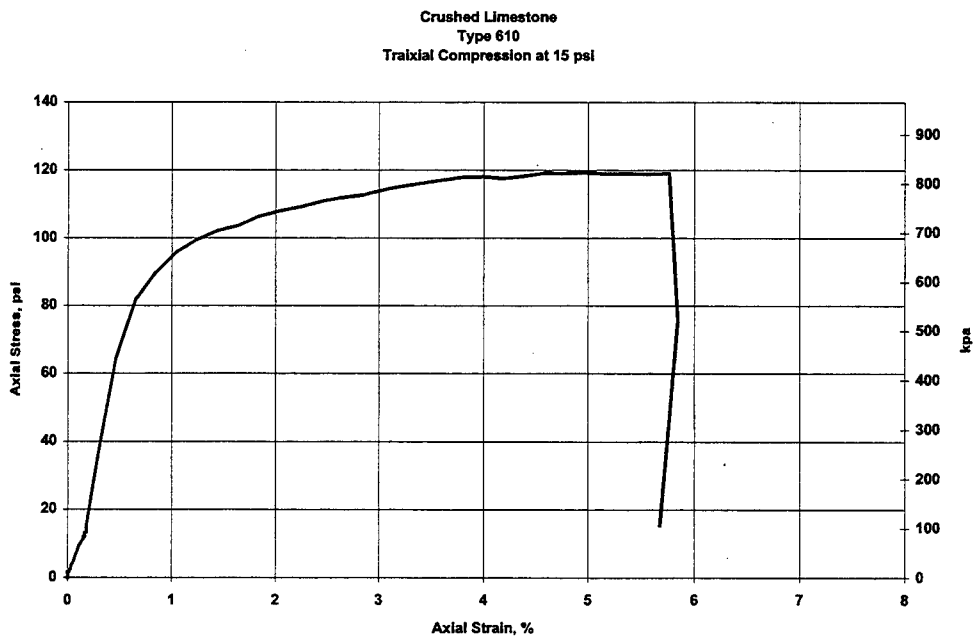


Figure C- 2. CTC15-1

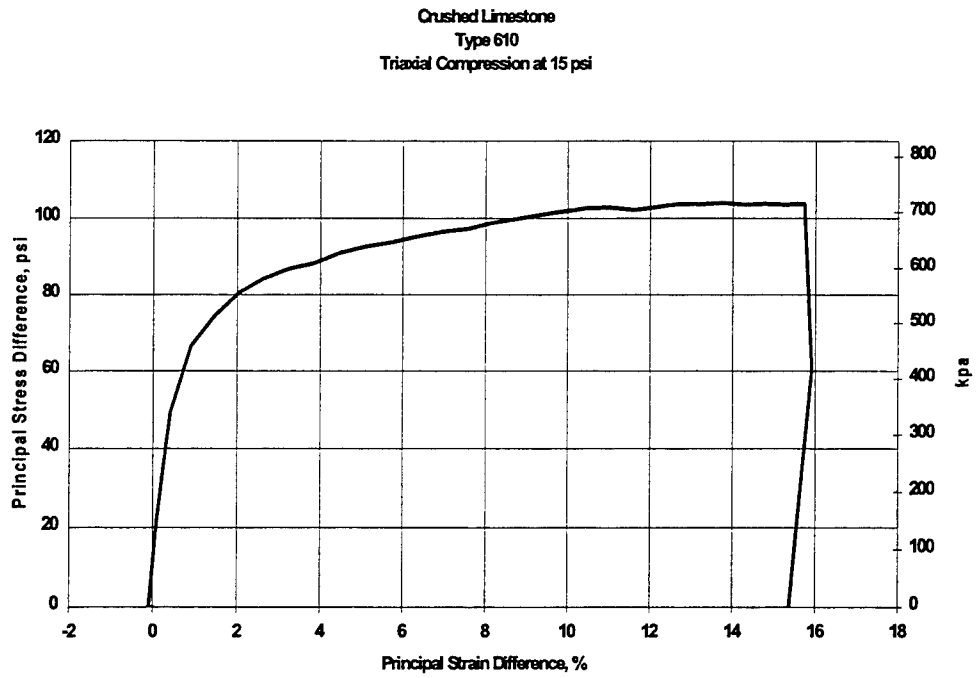


Figure C- 3. CTC15-1

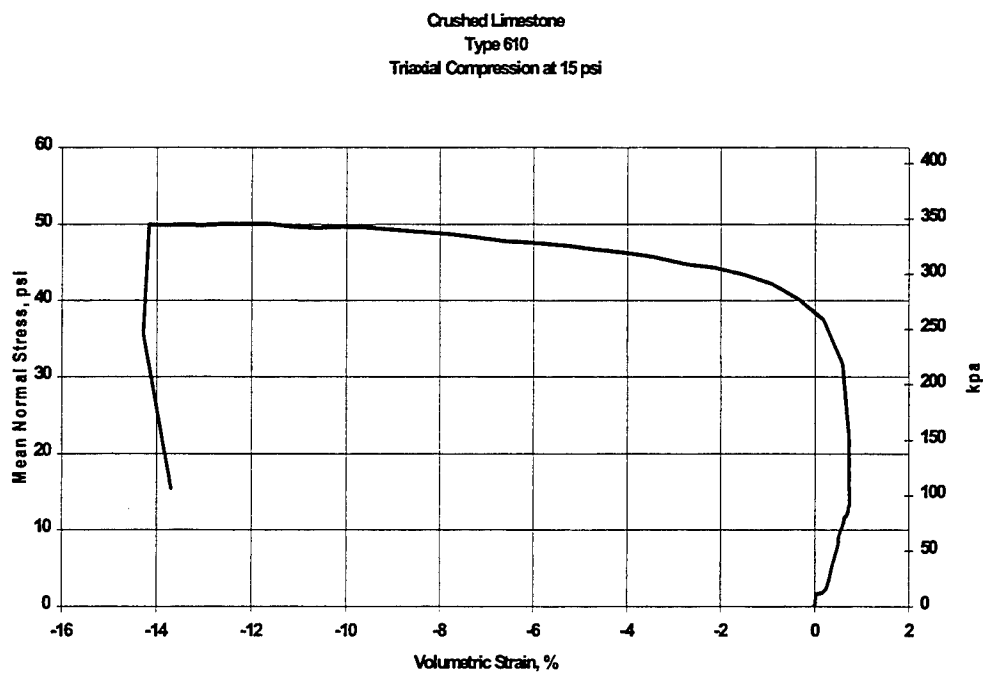


Figure C- 4. CTC15-1

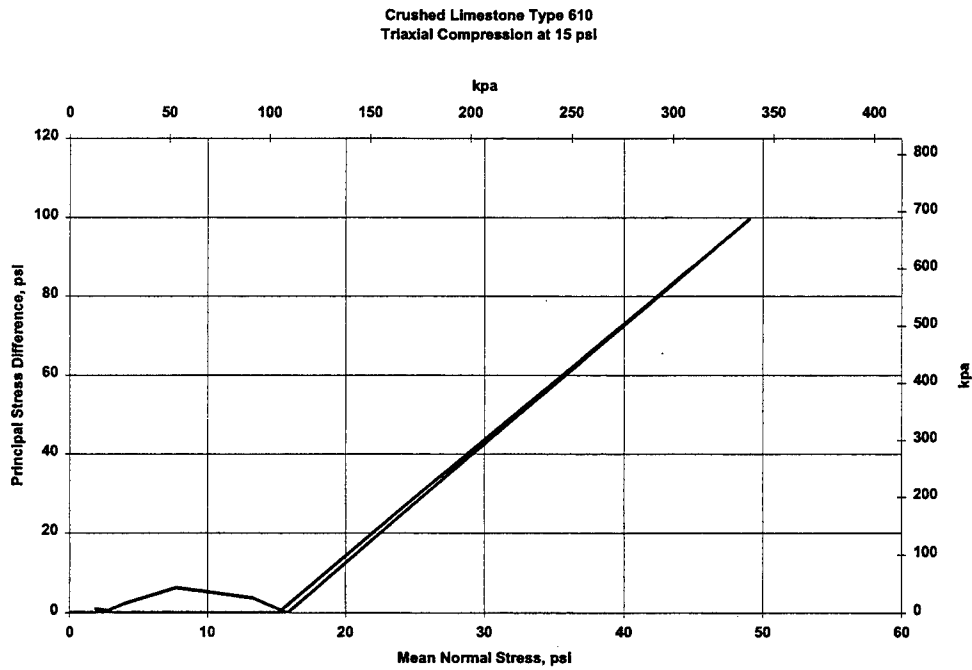


Figure C- 5. CTC15-2

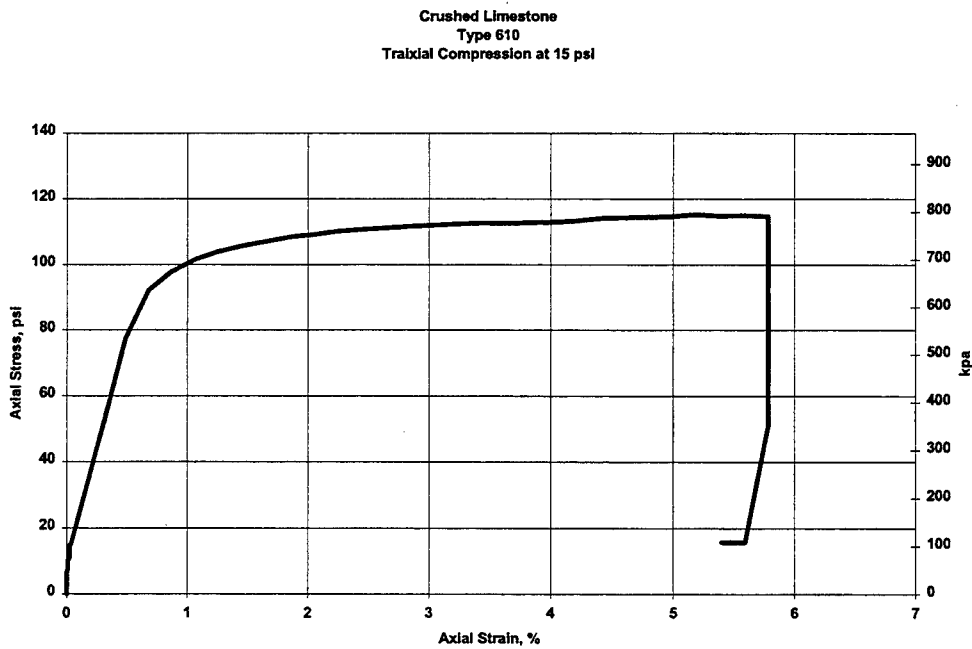


Figure C- 6. CTC15-2



Crushed Limestone  
Type 610  
Triaxial Compression at 15 psi

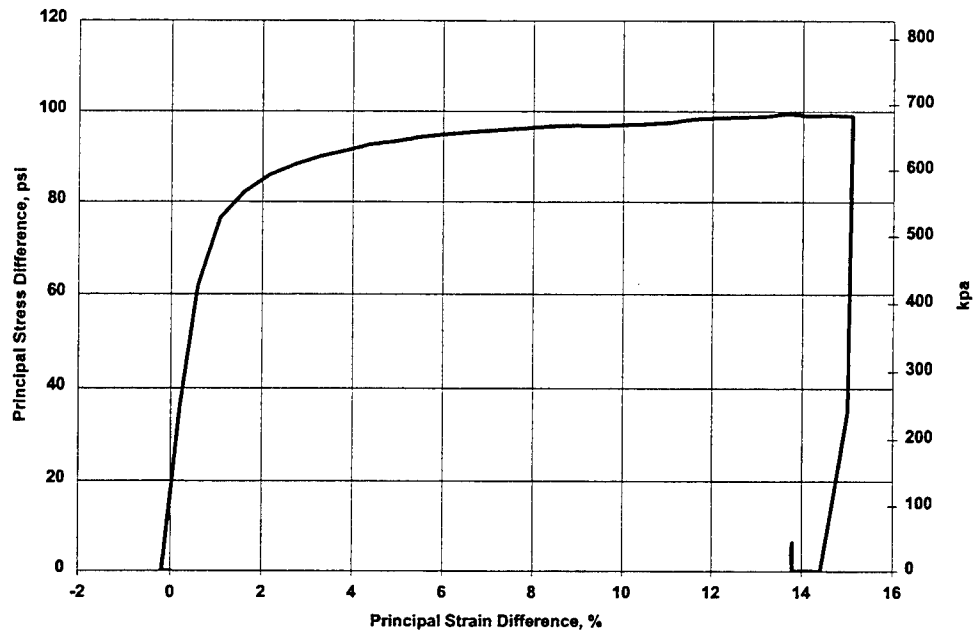


Figure C- 7. CTC15-2

Crushed Limestone  
Type 610  
Triaxial Compression at 15 psi

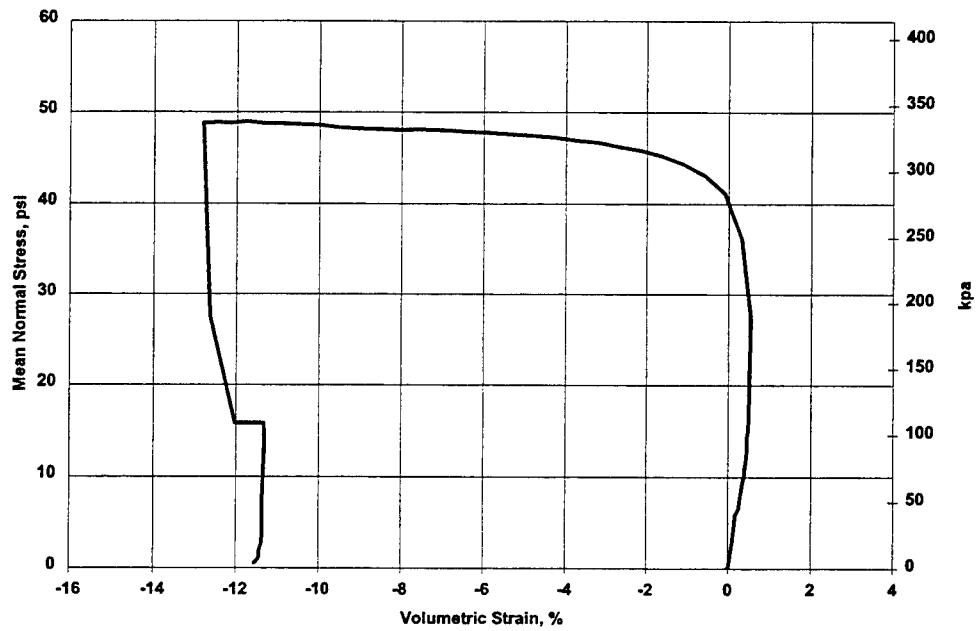


Figure C- 8. CTC15-2

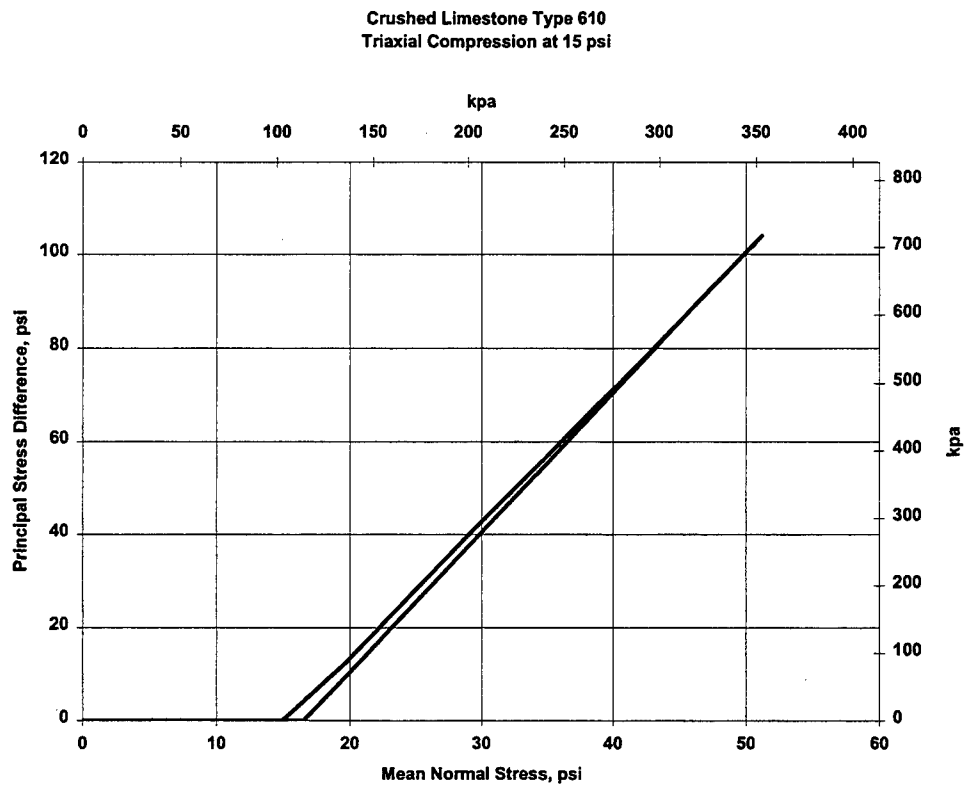


Figure C- 9. CTC15-3

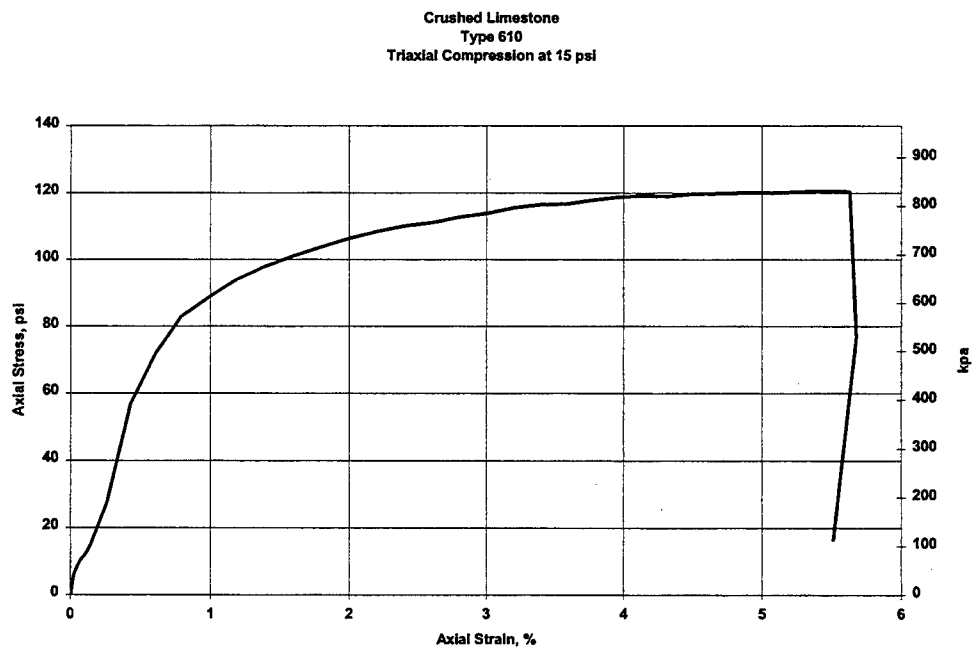


Figure C- 10. CTC15-3

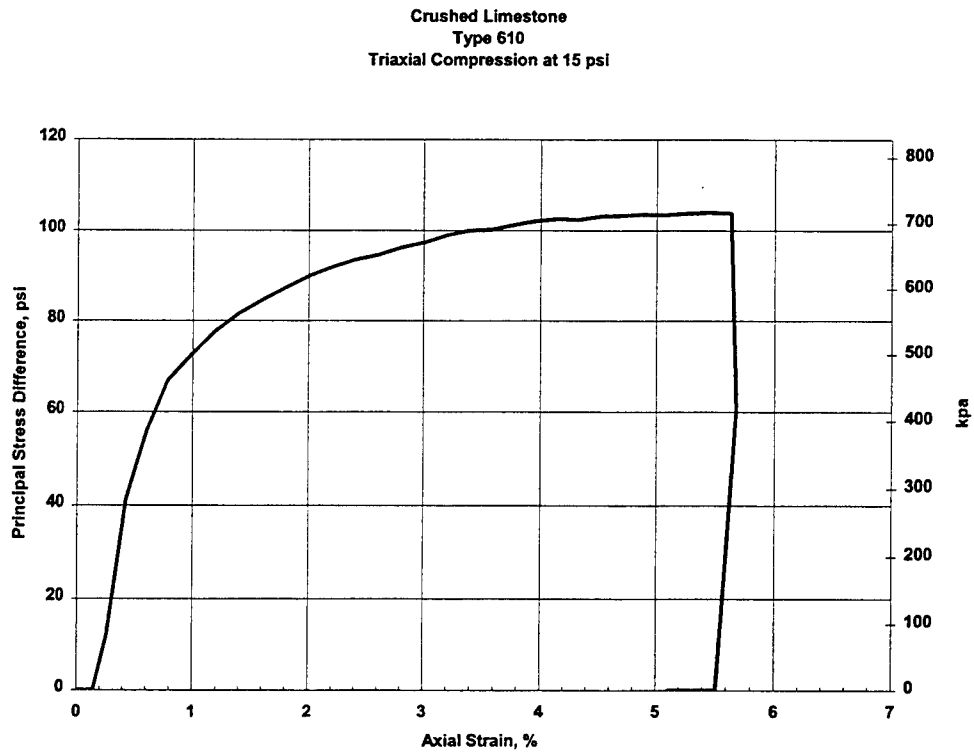


Figure C- 11. CTC15-3

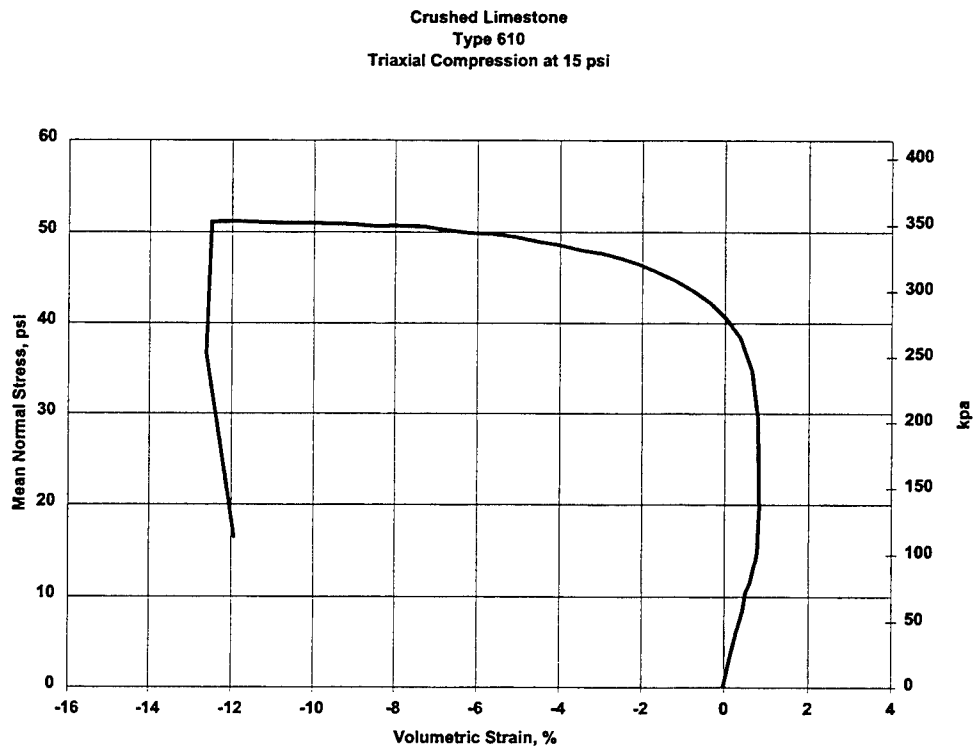


Figure C- 12. CTC15-3

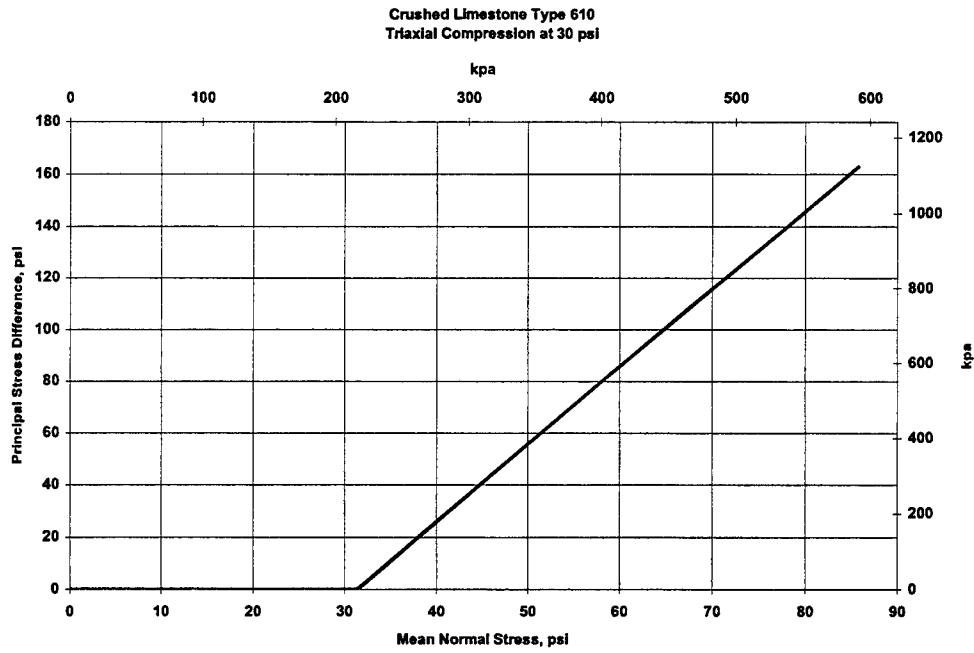


Figure C- 13. CTC30-1

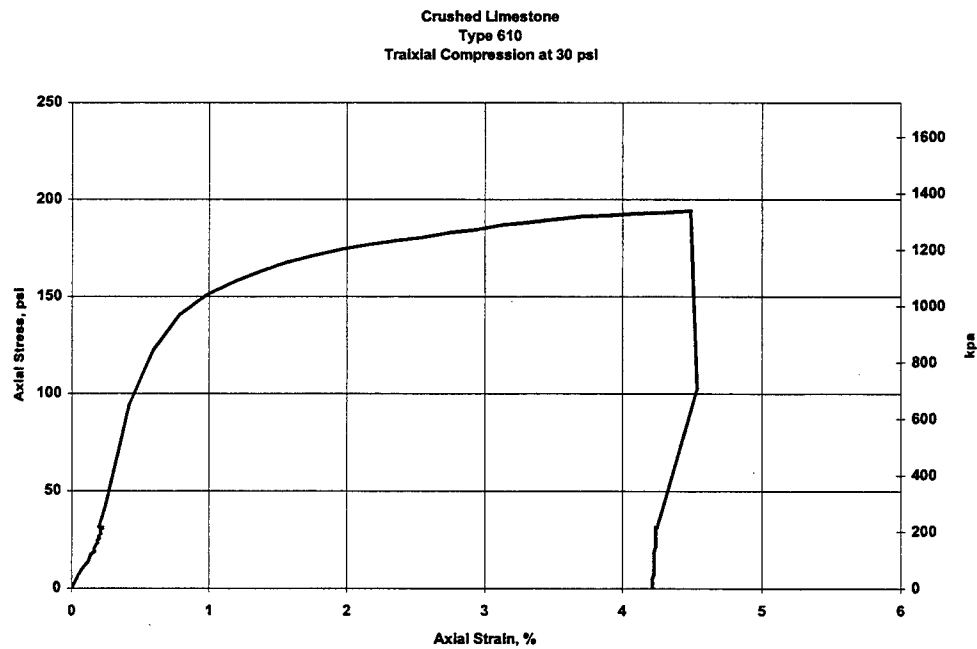


Figure C- 14. CTC30-1

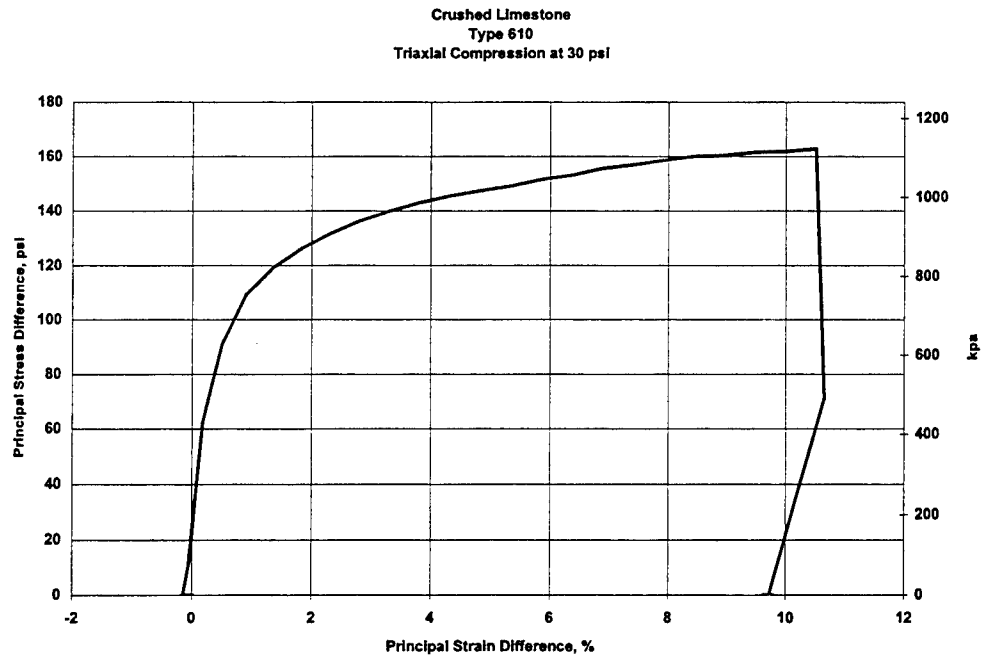


Figure C- 15. CTC30-1

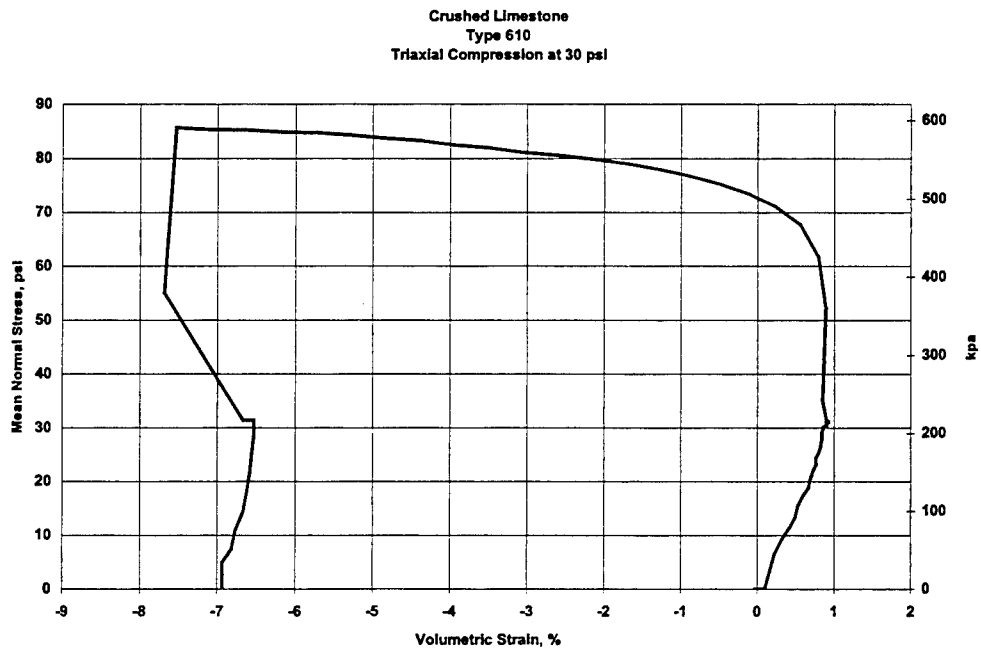


Figure C- 16. CTC30-1

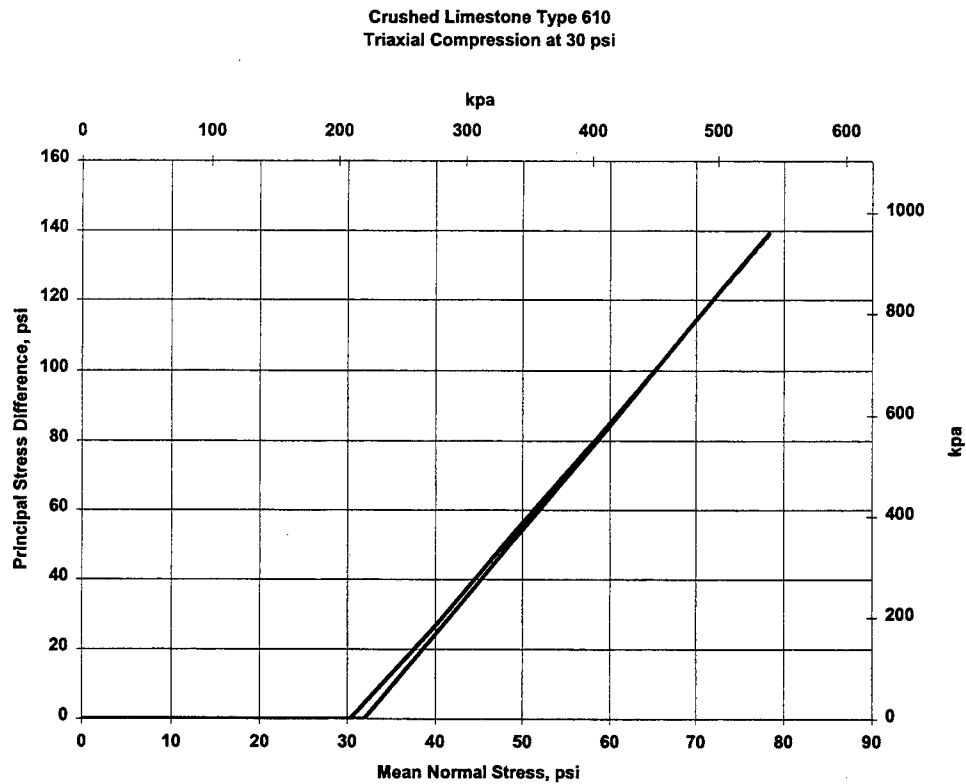


Figure C- 17. CTC30-2

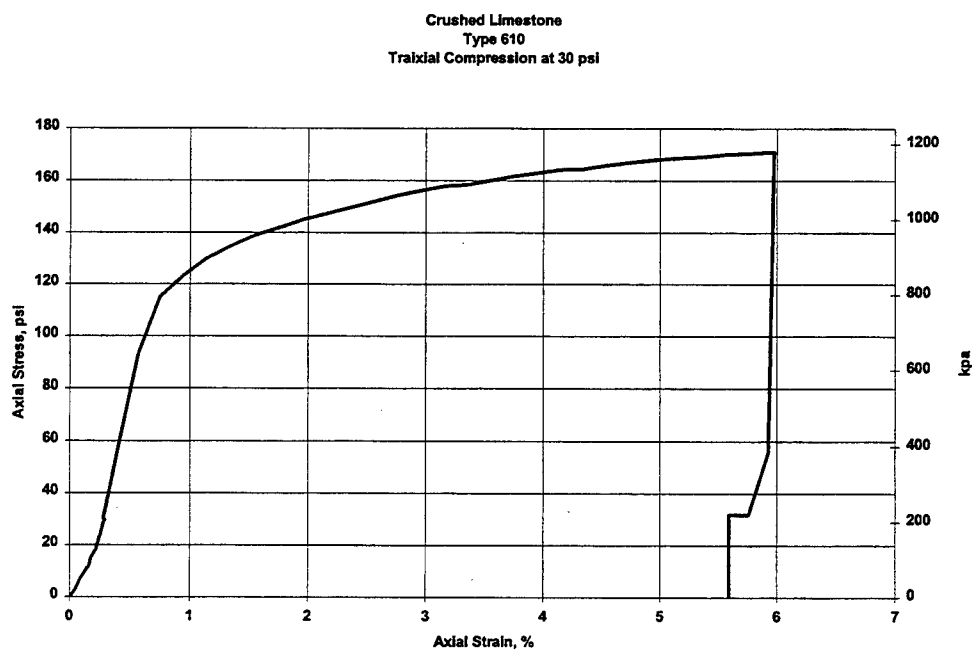


Figure C- 18. CTC30-2

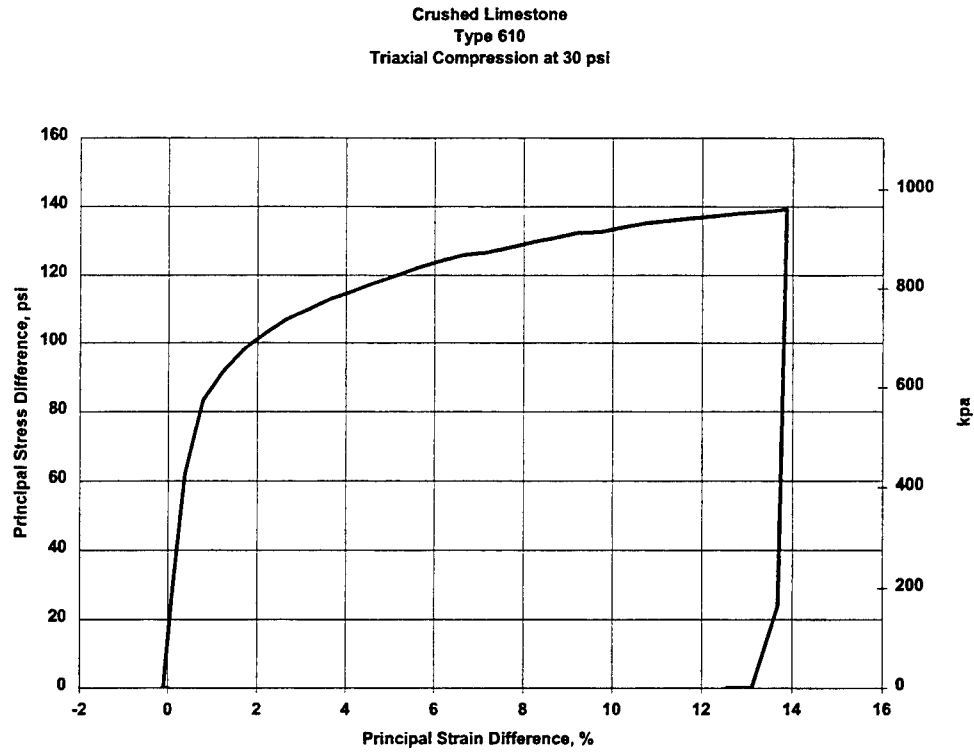


Figure C-19. CTC30-2

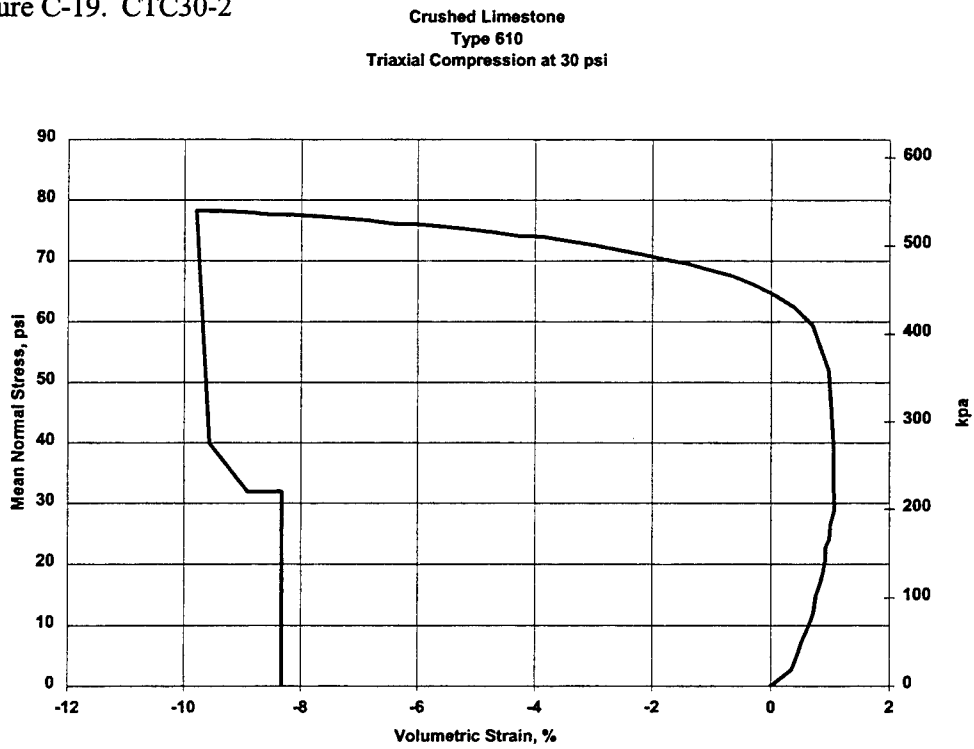


Figure C- 20. CTC30-2

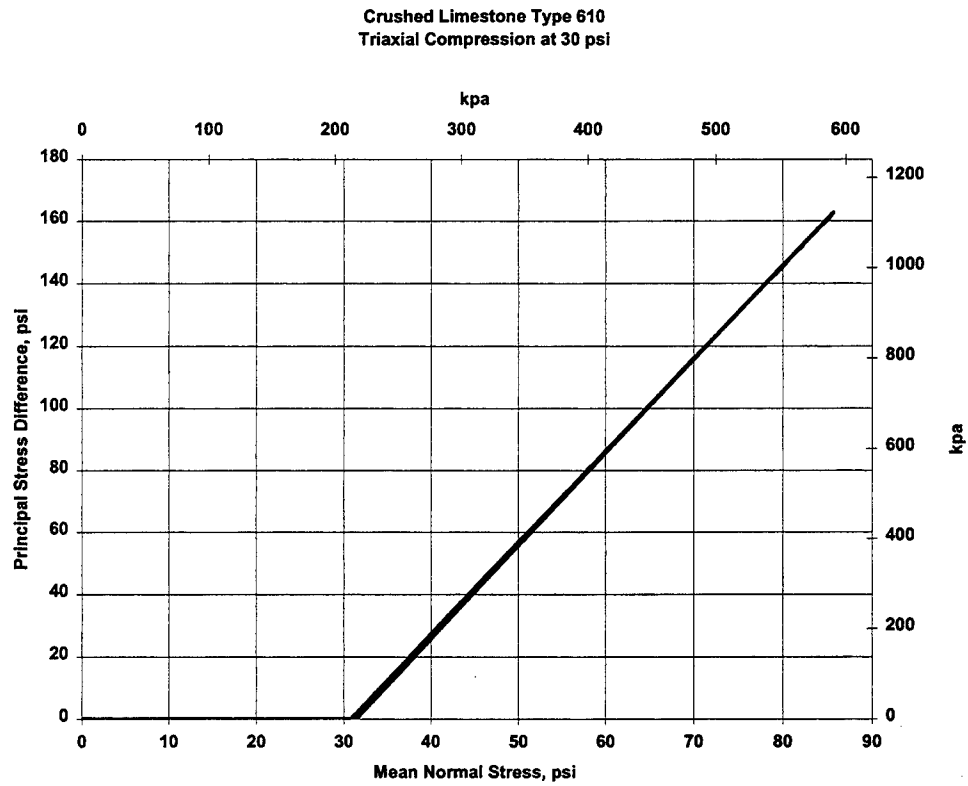


Figure C- 21. CTC30-3

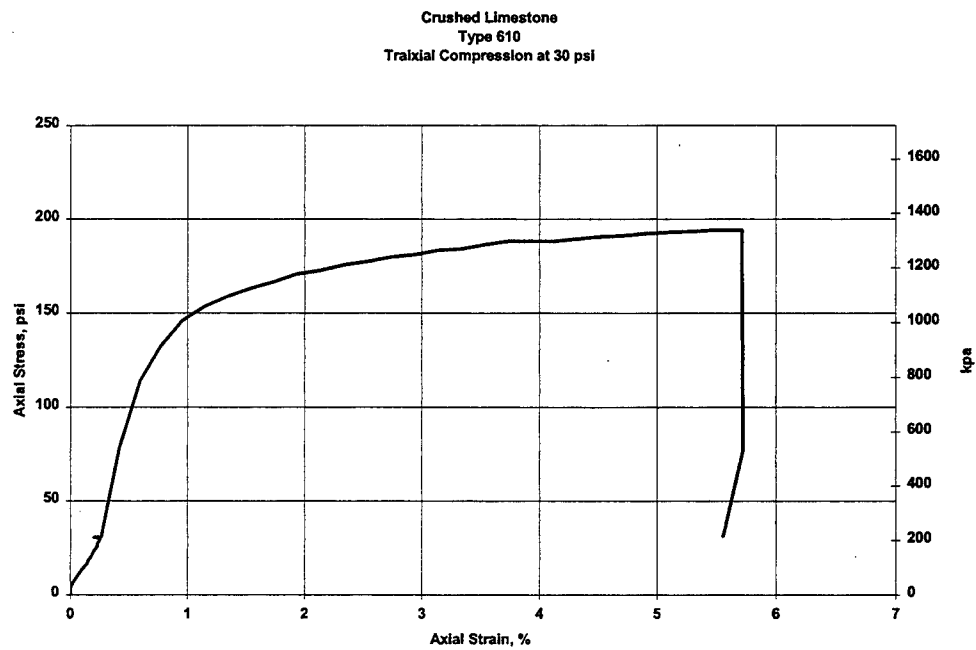


Figure C- 22. CTC30-3



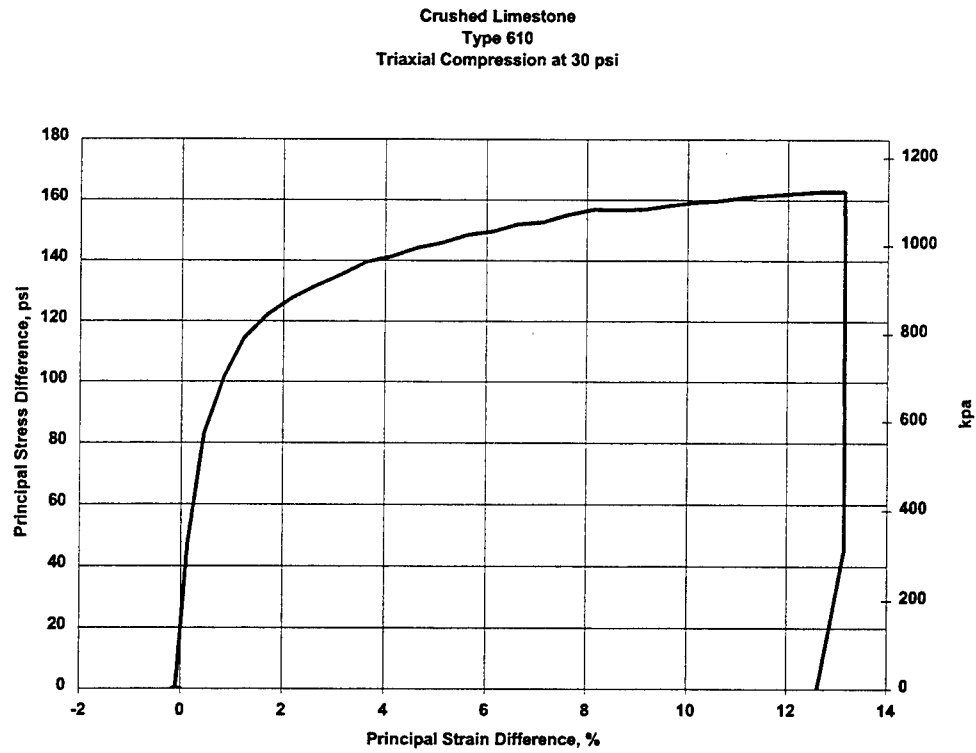


Figure C- 23. CTC30-3

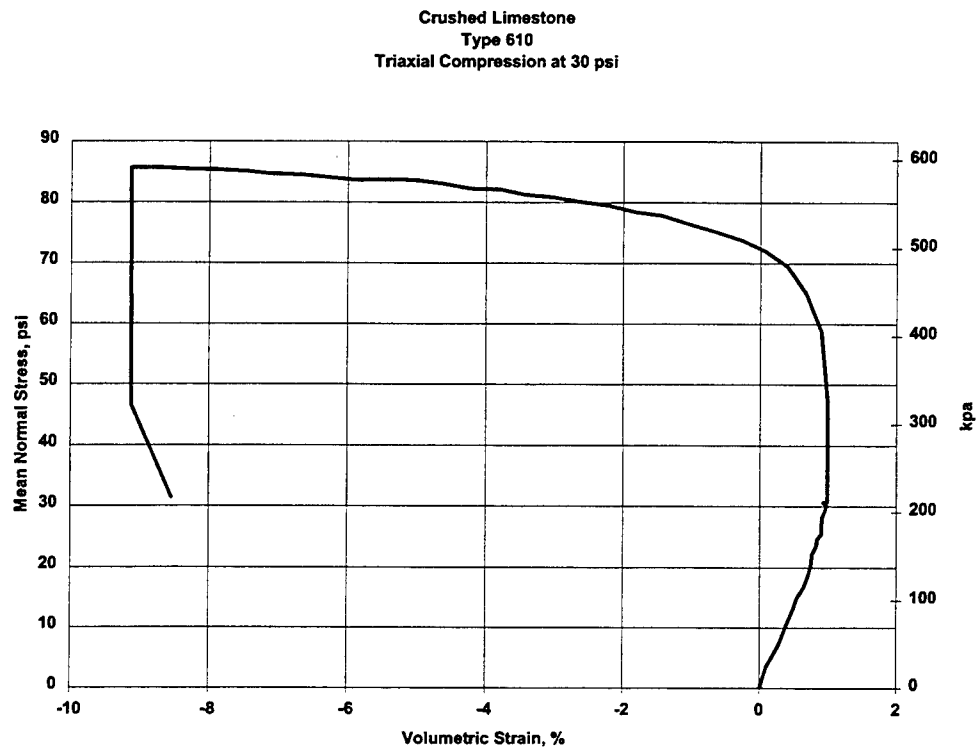


Figure C- 24. CTC30-3

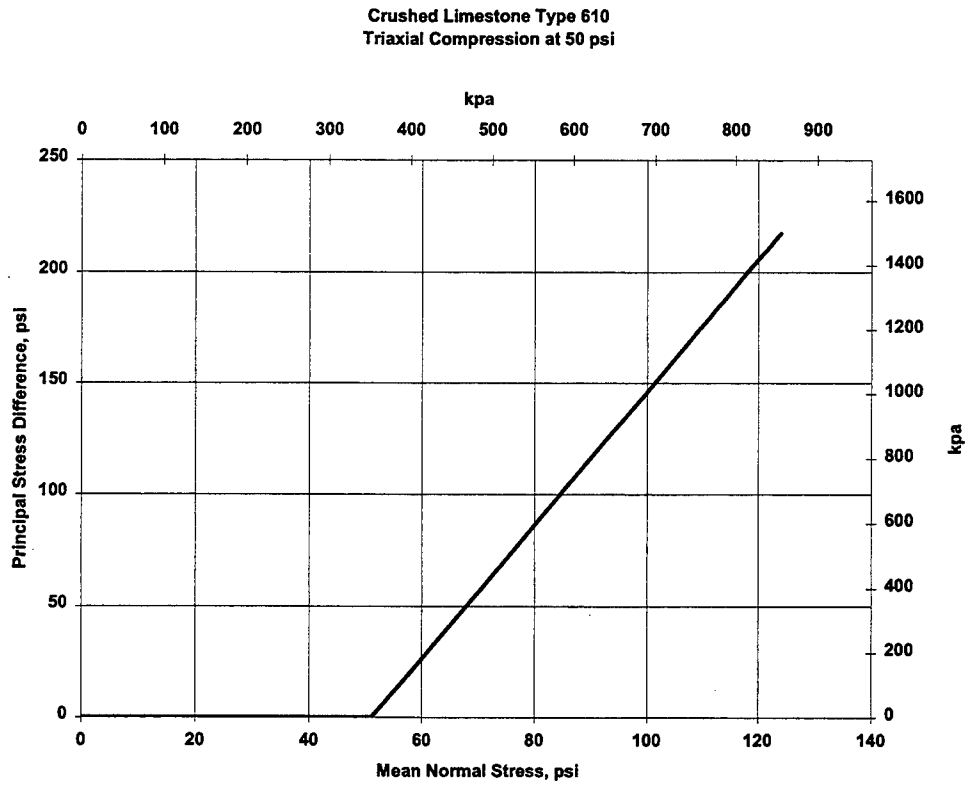


Figure C- 25. CTC50-1

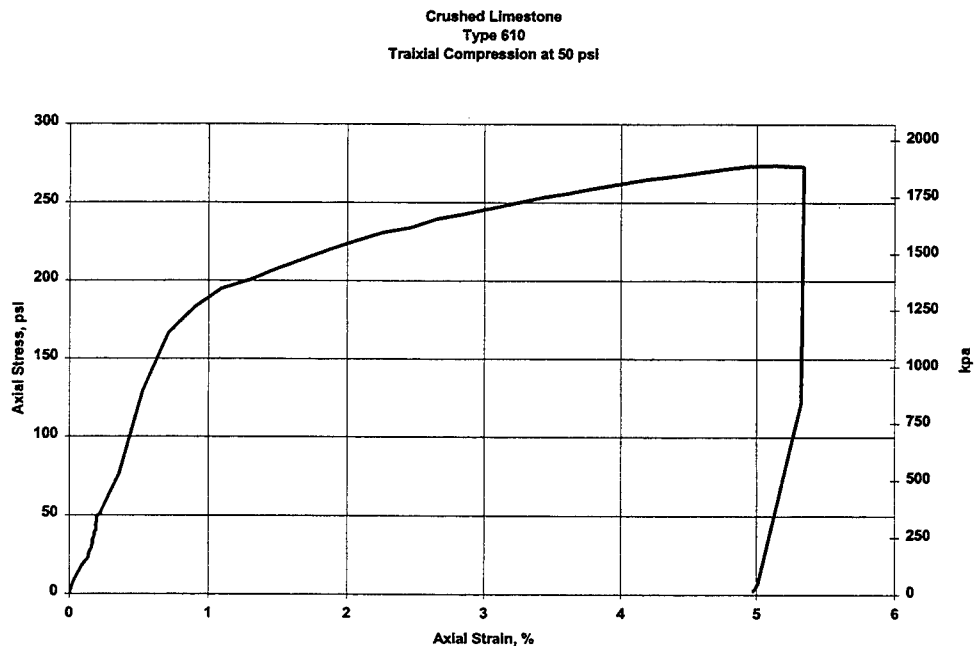


Figure C- 26. CTC50-1

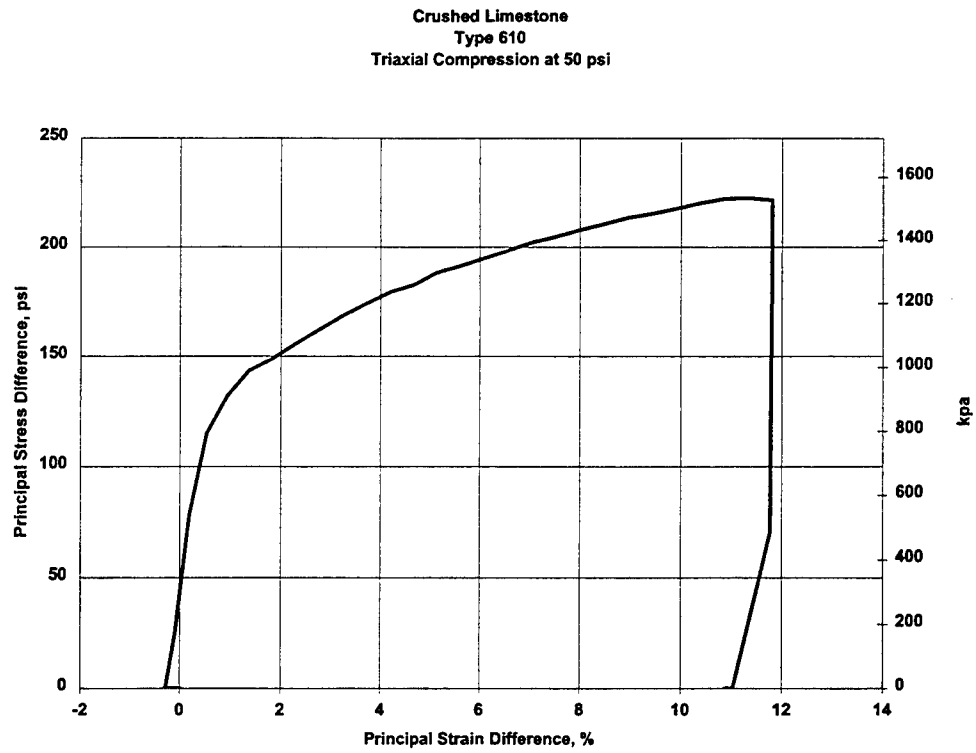


Figure C- 27. CTC50-1

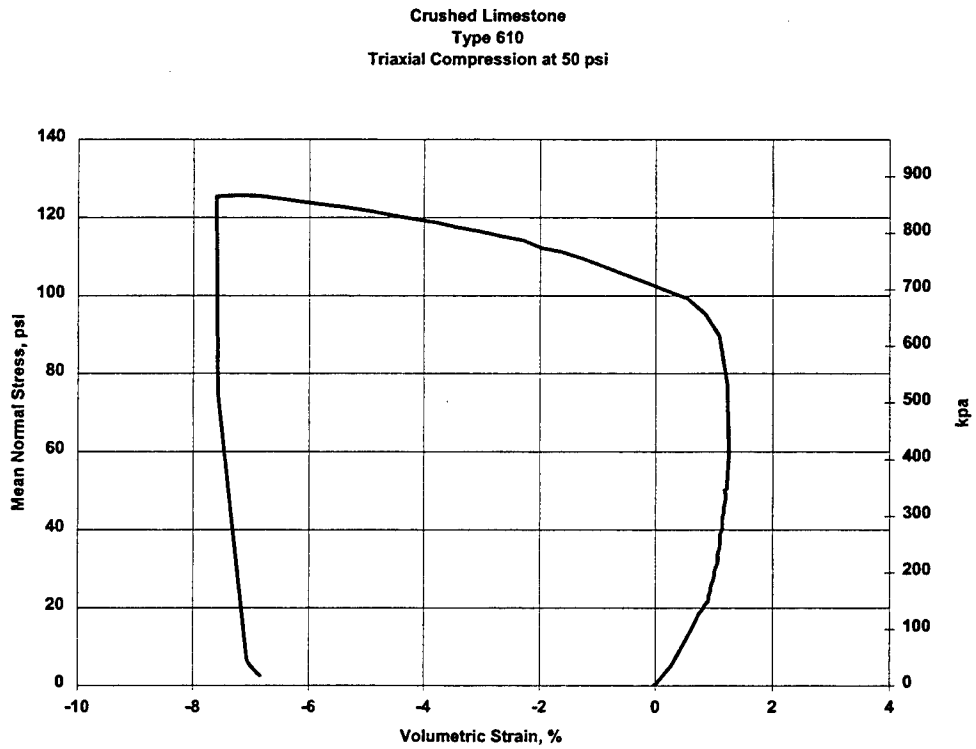


Figure C- 28. CTC50-1

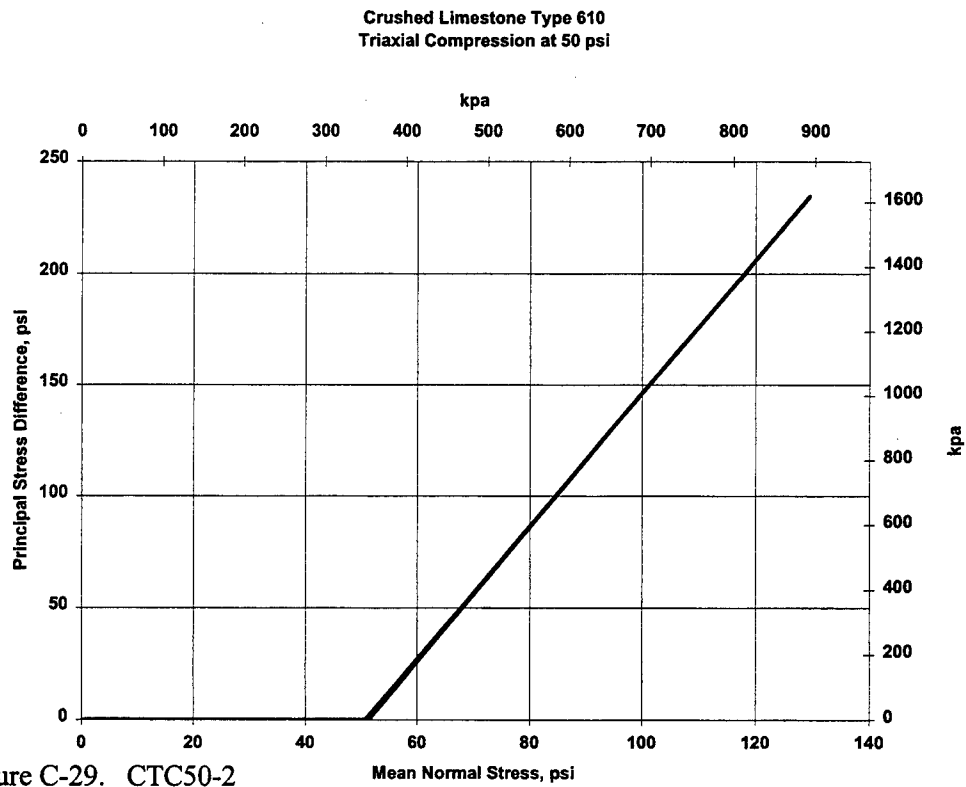


Figure C-29. CTC50-2

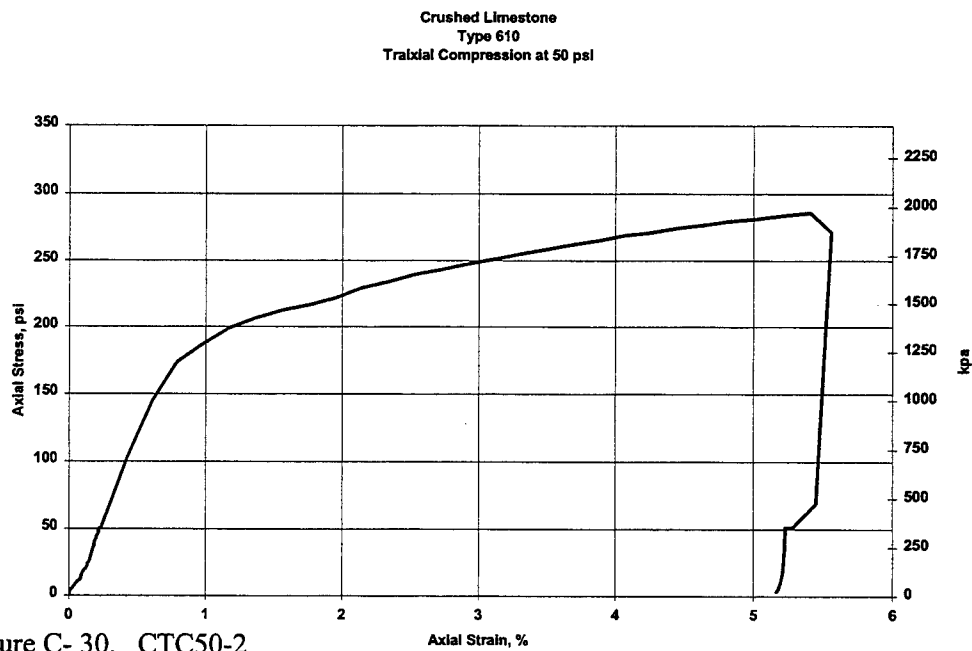


Figure C- 30. CTC50-2

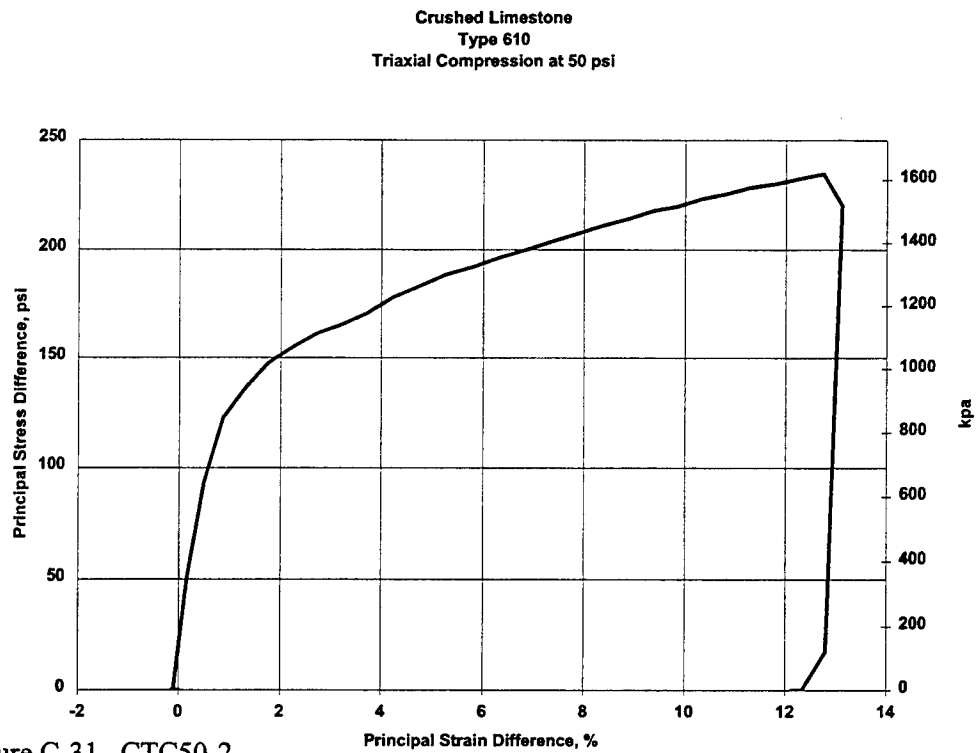


Figure C-31. CTC50-2

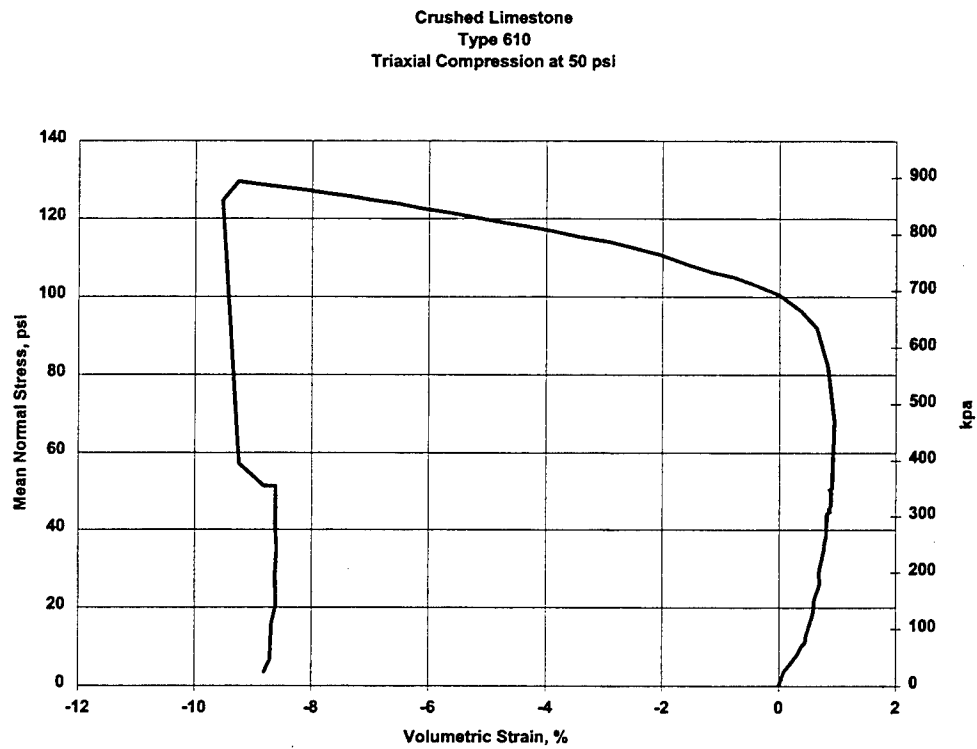


Figure C- 32. CTC50-2

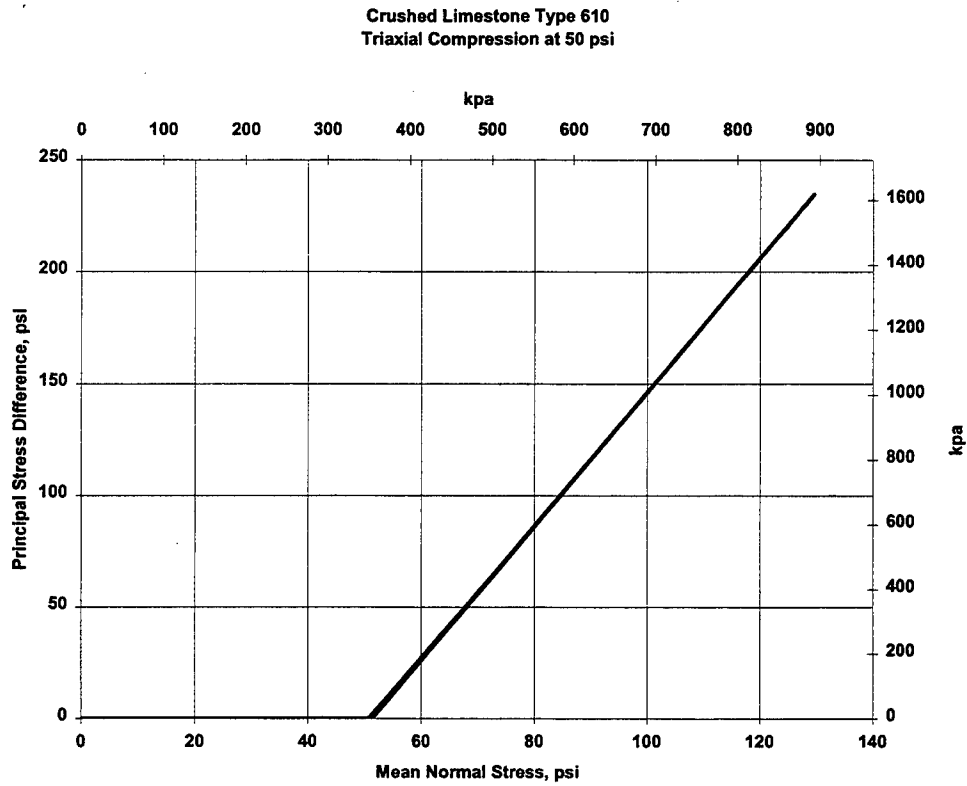


Figure C- 33. CTC50-3

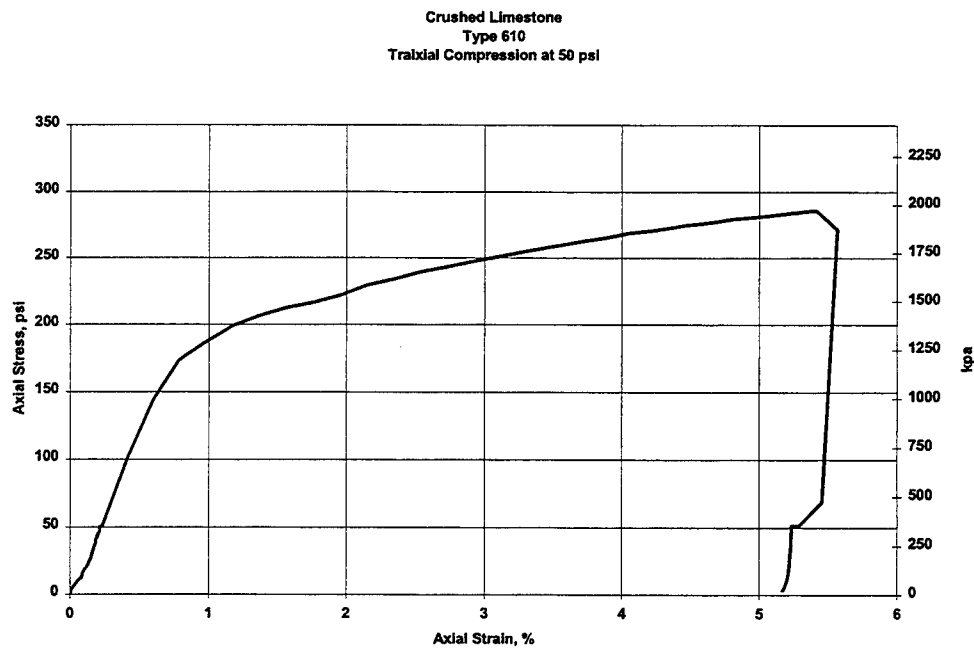


Figure C- 34. CTC50-3

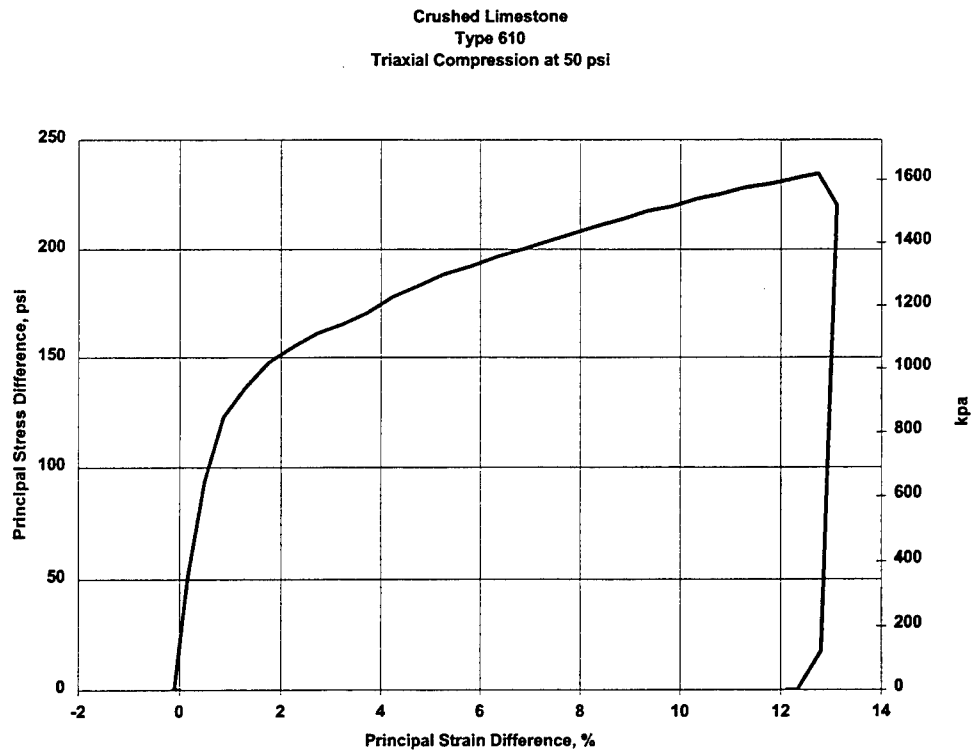


Figure C- 35. CTC50-3

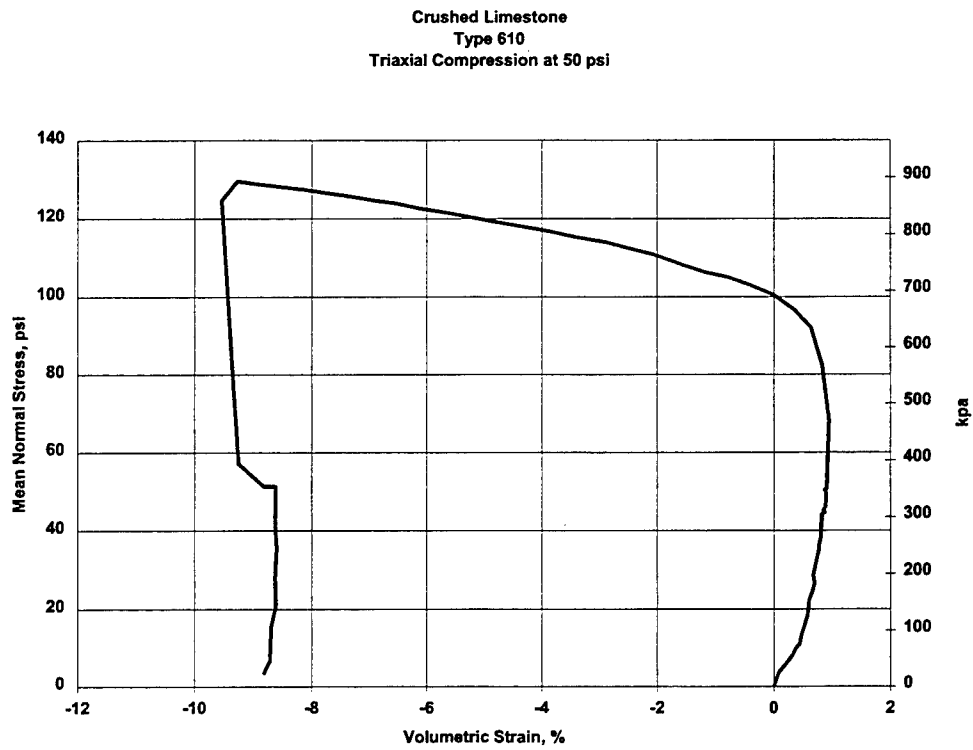


Figure C- 36. CTC50-3

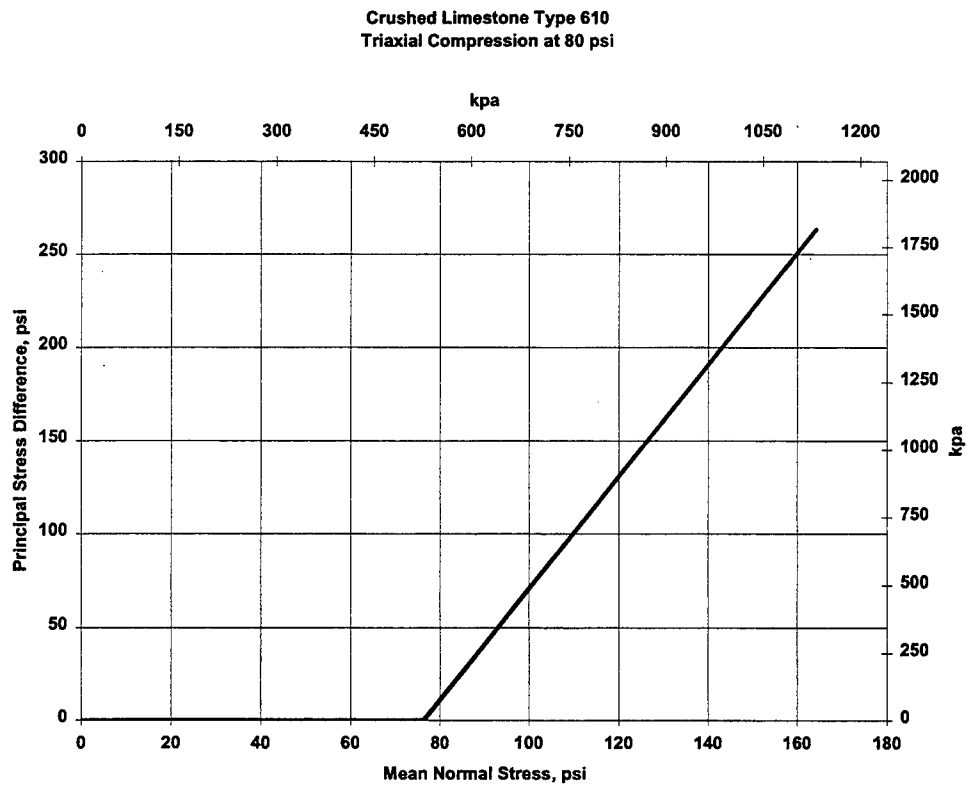


Figure C- 37. CTC80-1

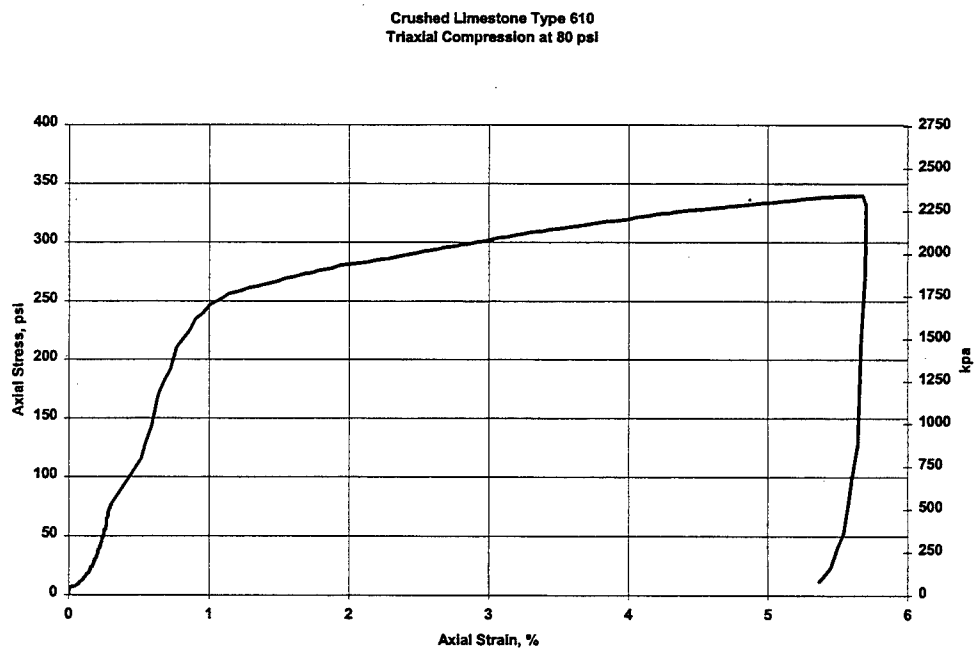


Figure C- 38. CTC80-1



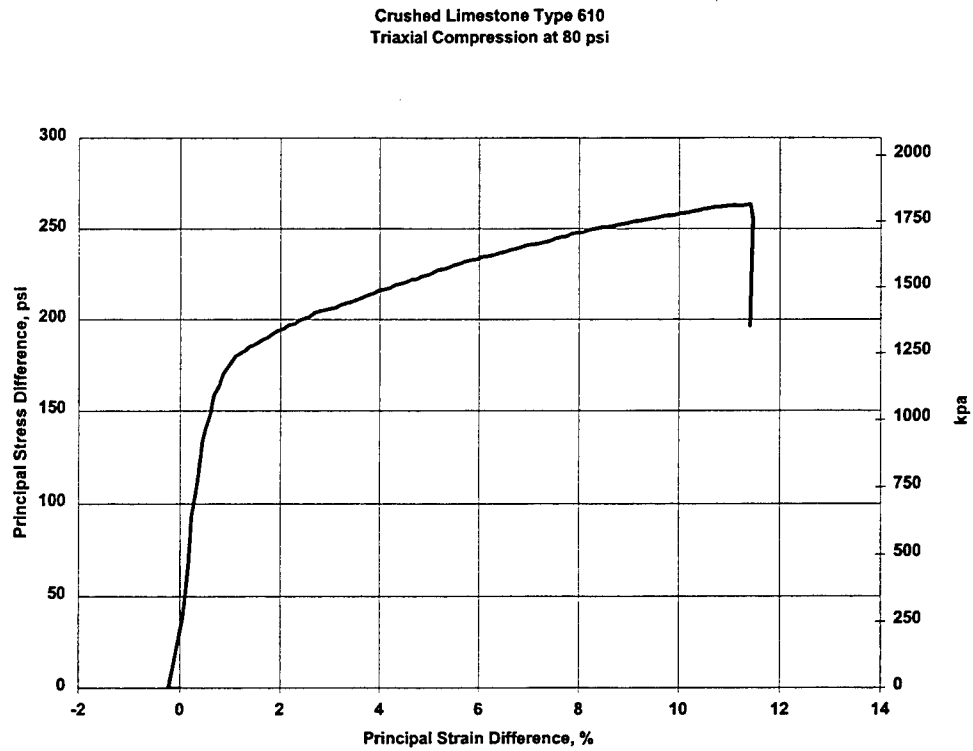


Figure C- 39. CTC80-1

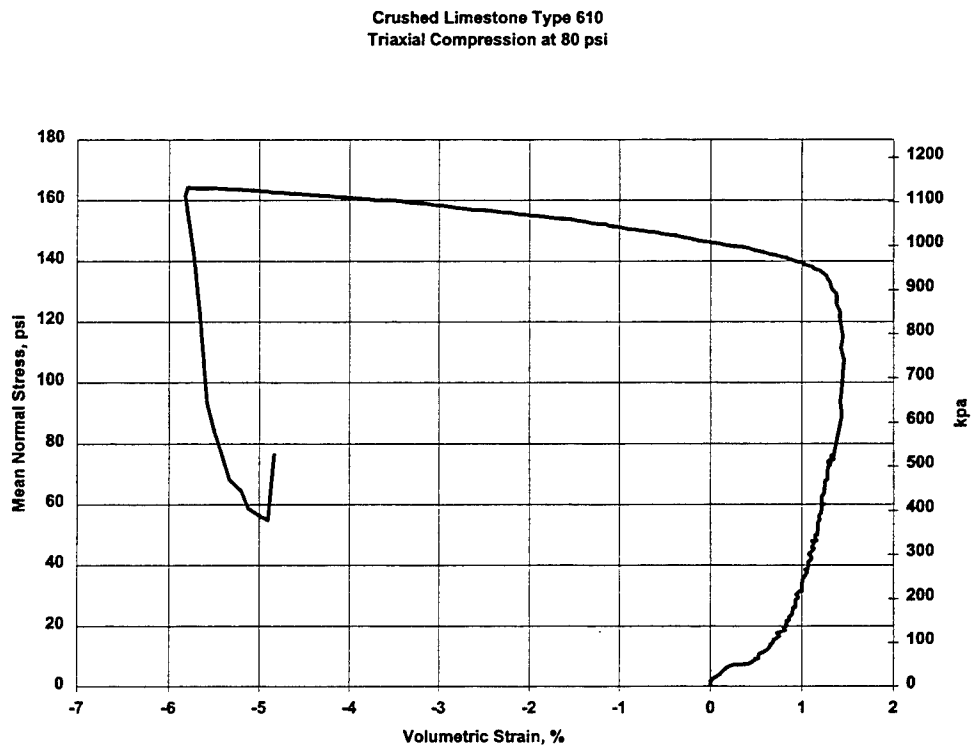


Figure C- 40. CTC80-1

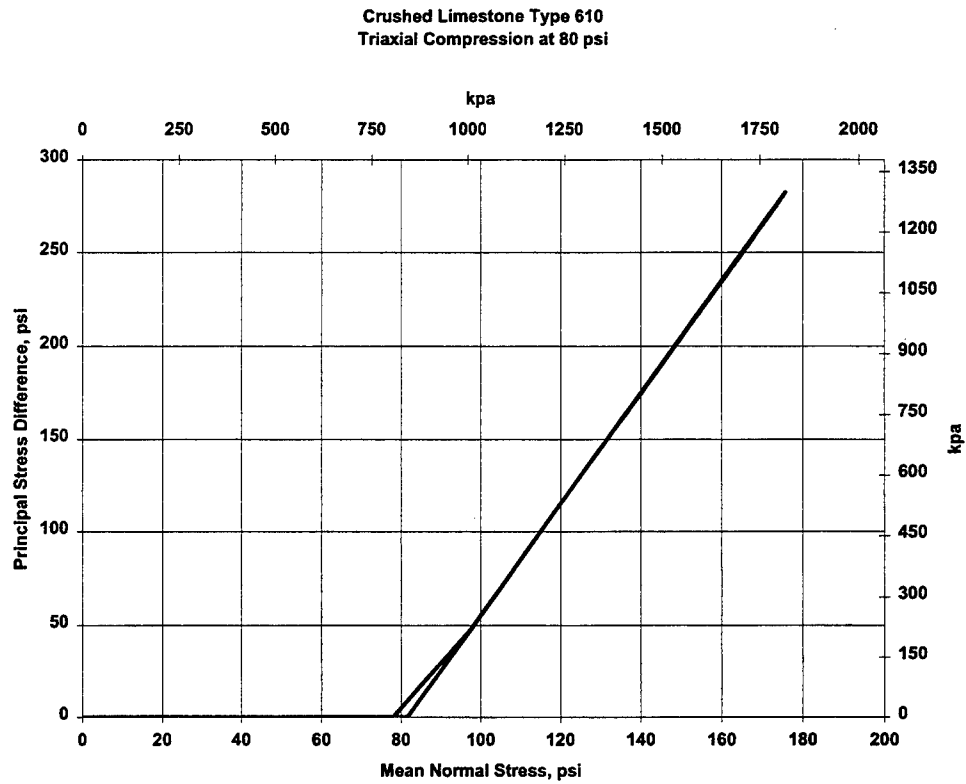


Figure C- 41. CTC80-2

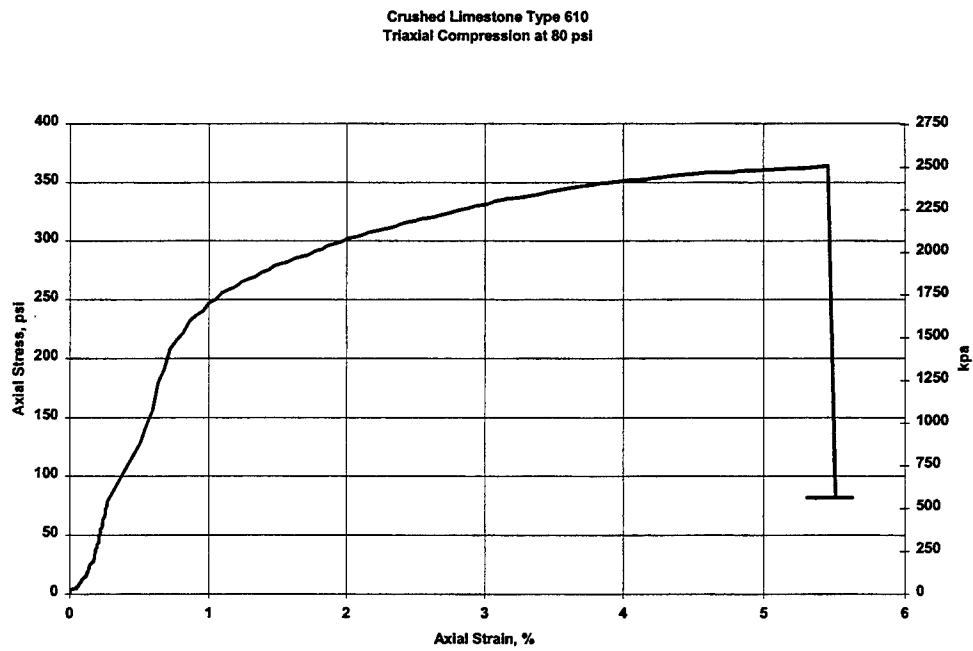


Figure C- 42. CTC80-2

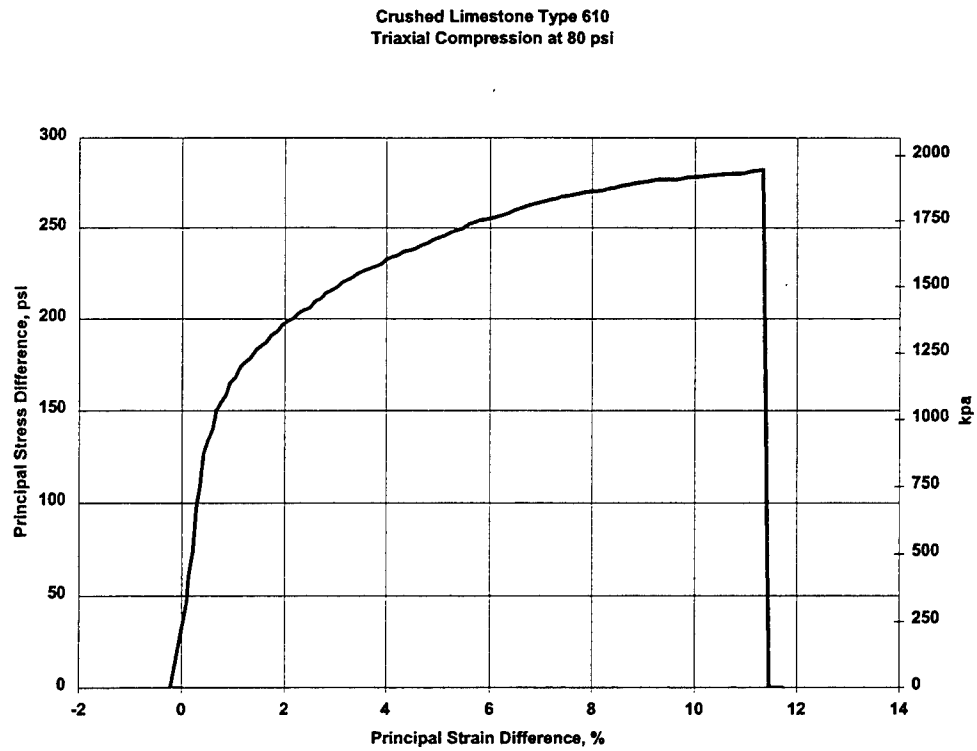
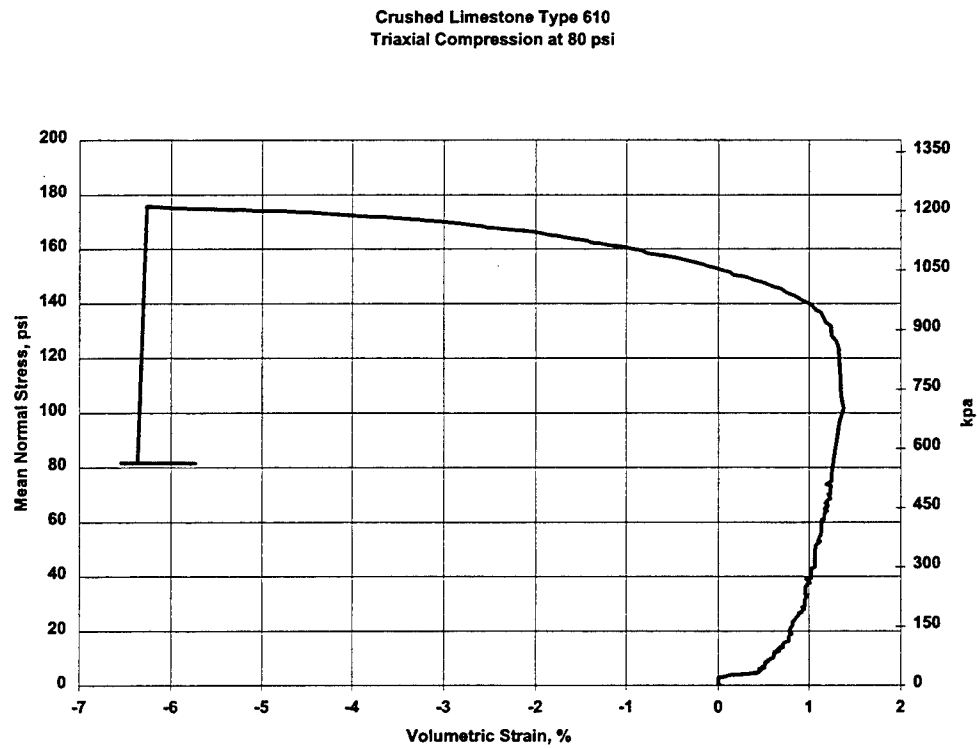


Figure C- 43. CTC80-2



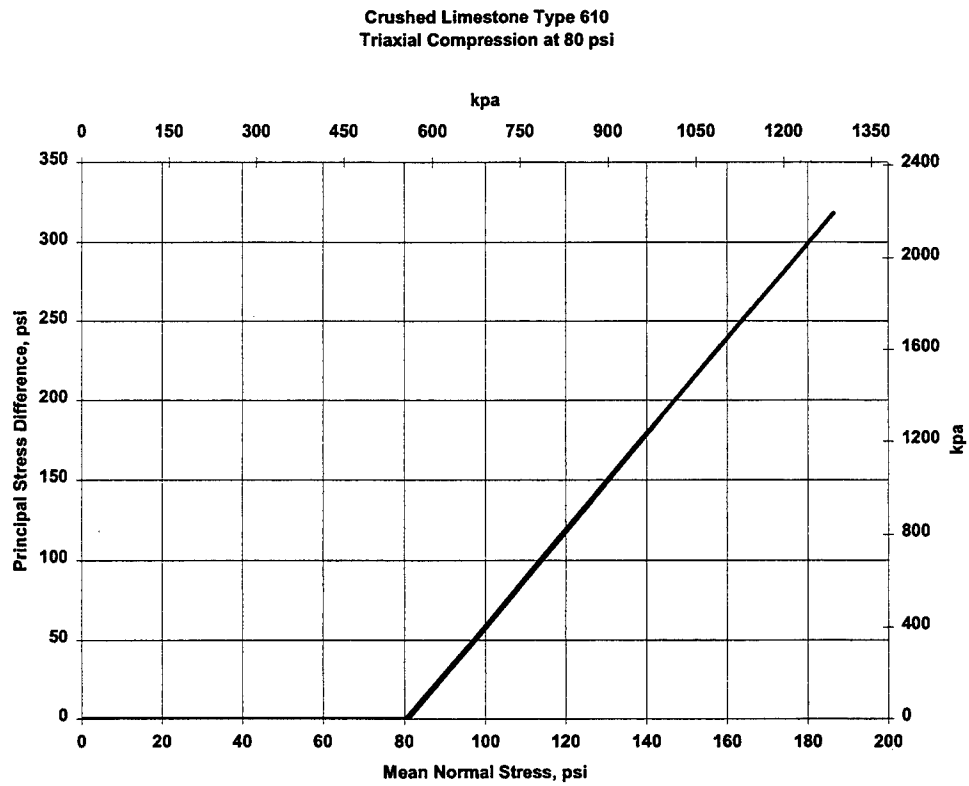


Figure C- 45. CTC80-3

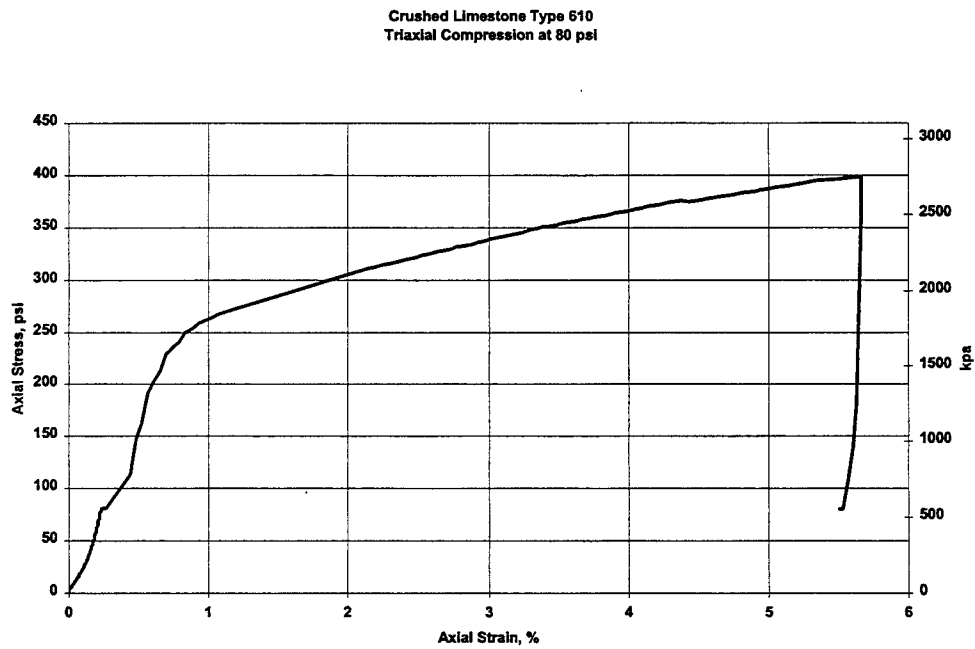


Figure C- 46. CTC80-3

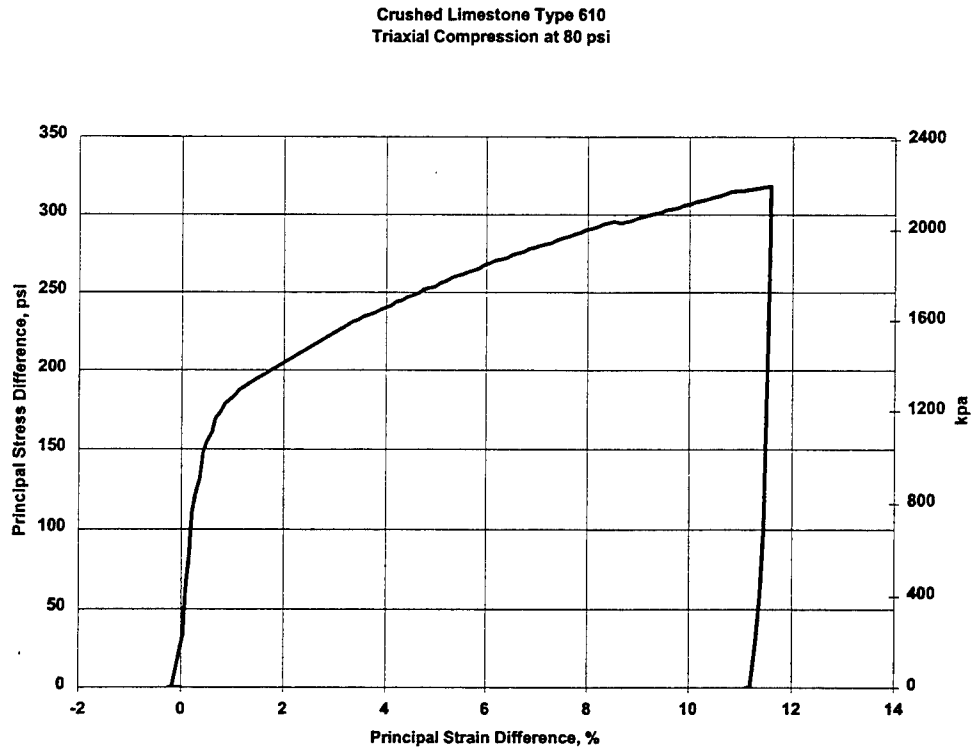


Figure C- 47. CTC80-3

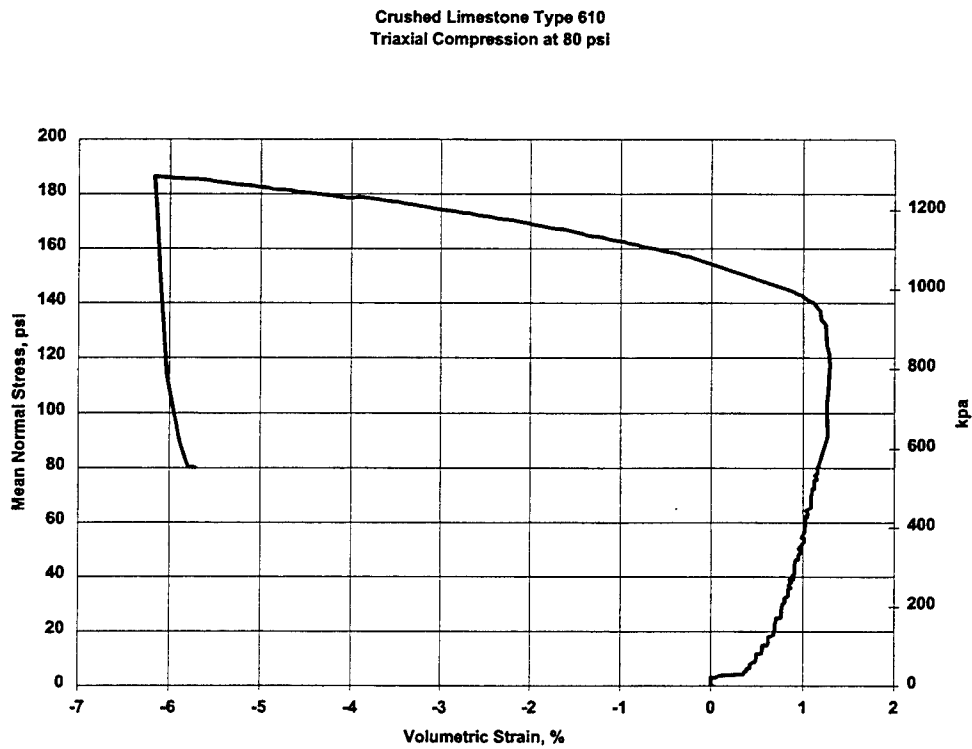


Figure C- 48. CTC80-3

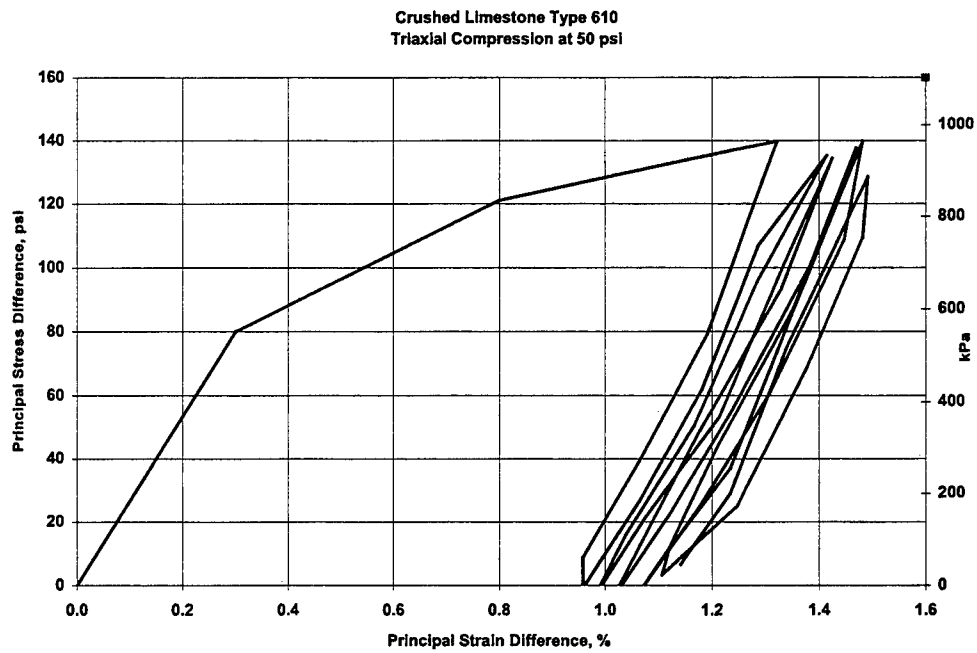


Figure C- 49. CTR50-1

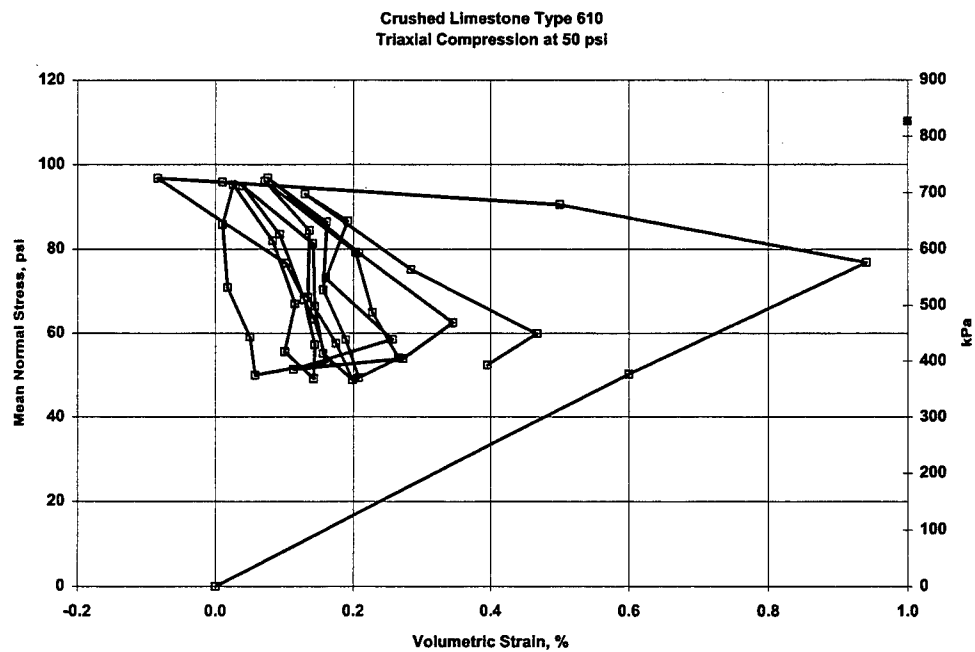


Figure C- 50. CTR50-1

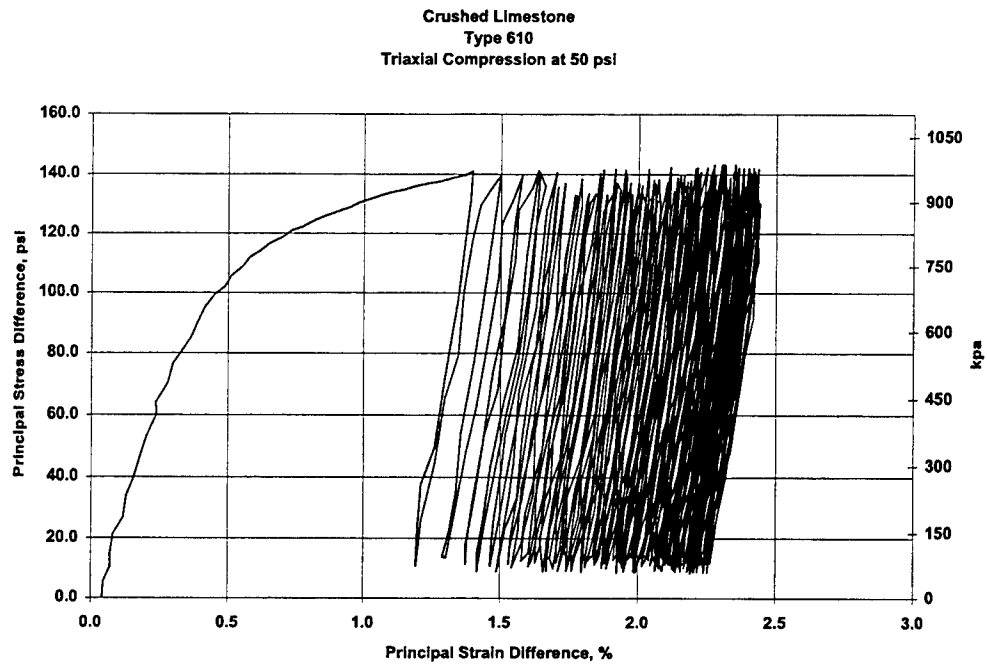


Figure C- 51. CTCR50-2

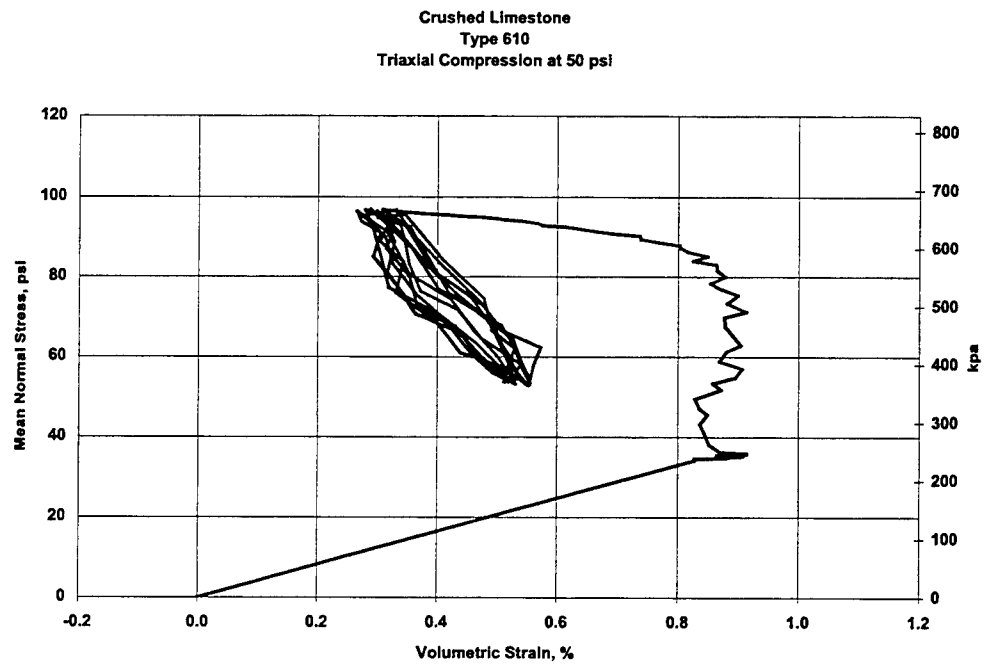


Figure C- 52. CTCR50-2

**APPENDIX D**

**RESULTS OF HYDROSTATIC COMPRESSION TESTS**



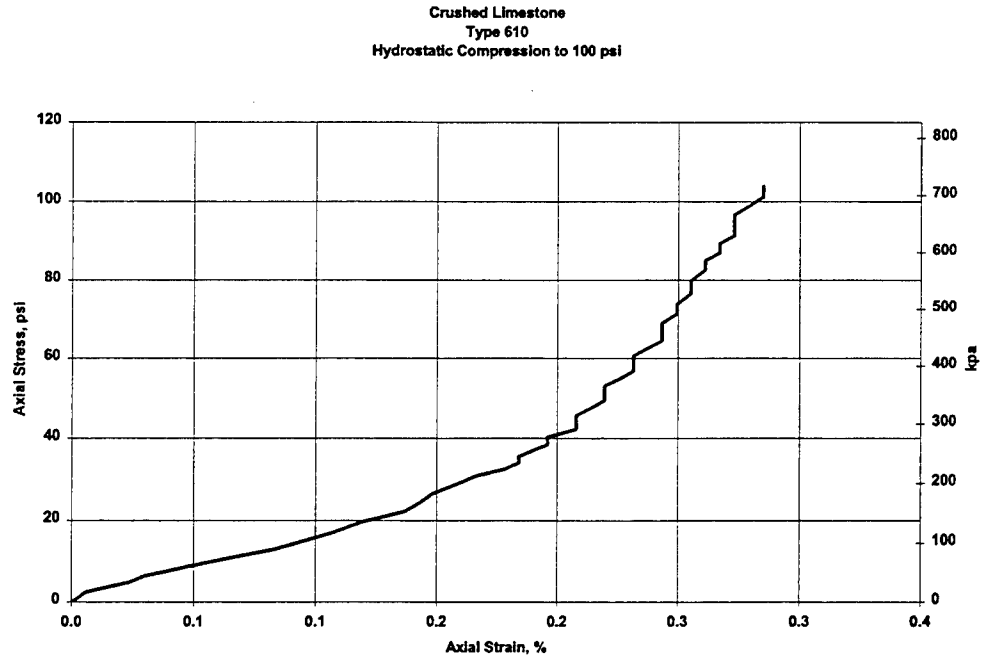


Figure D- 1. HC100-1

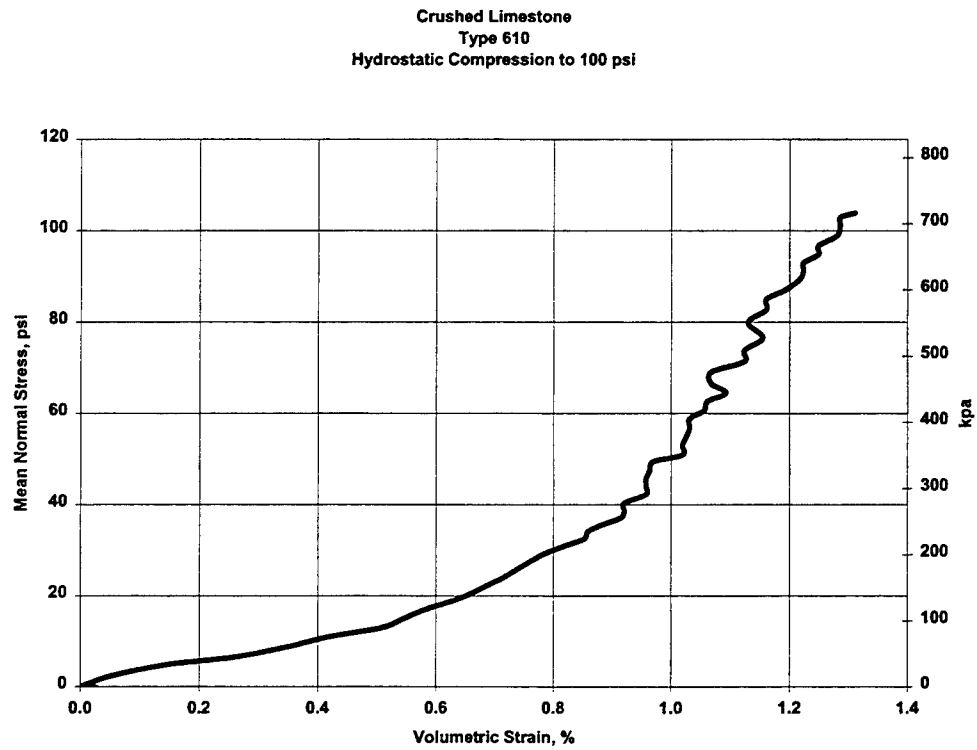


Figure D- 2. HC100-1

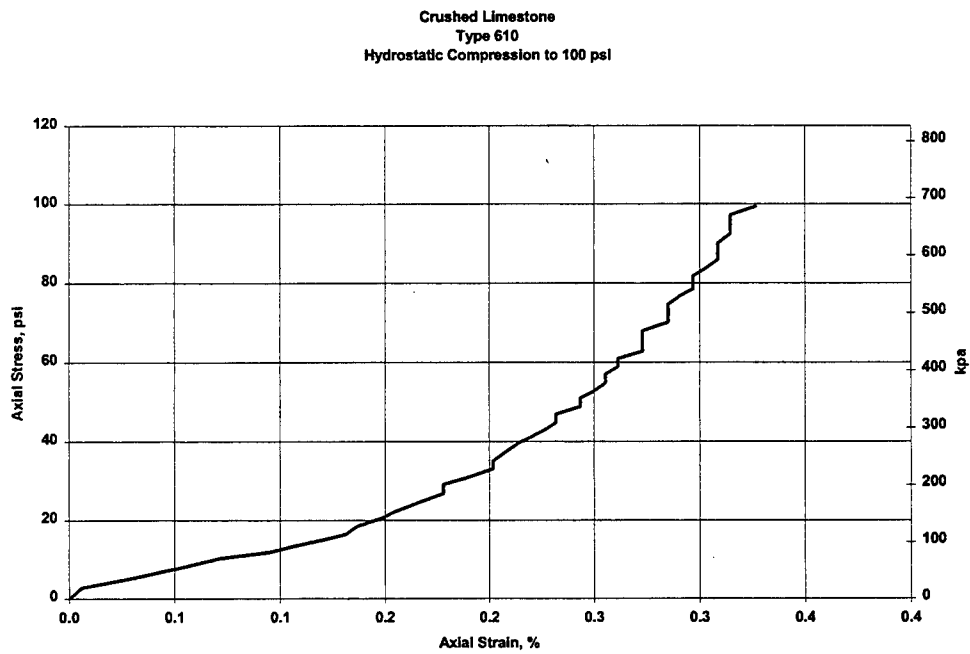


Figure D- 3. HC100-2

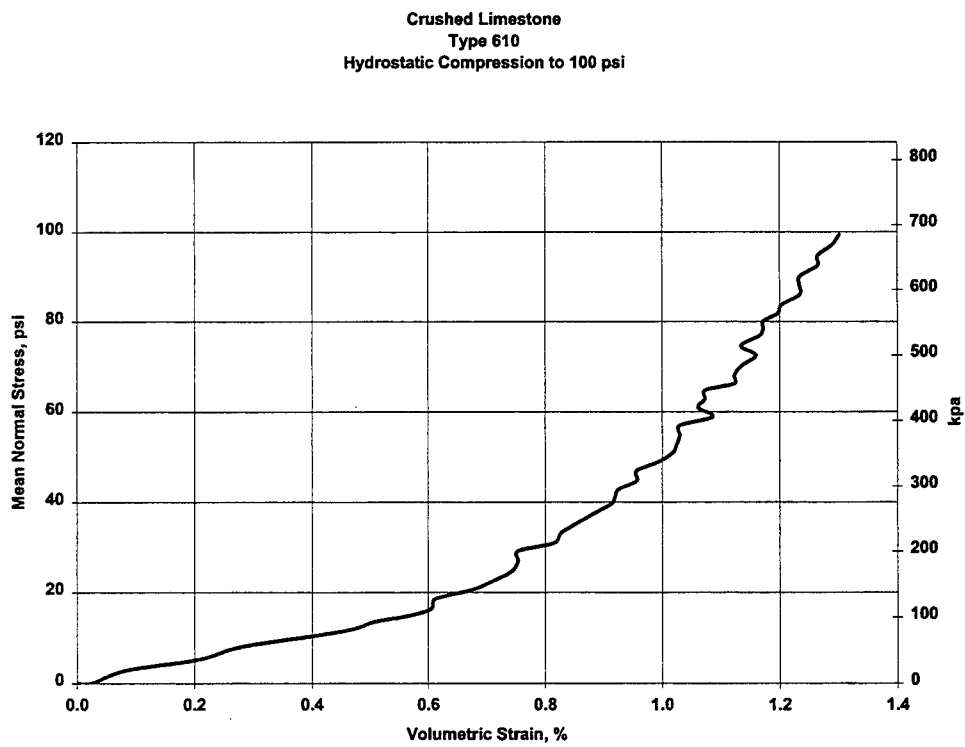


Figure D- 4. HC100-2

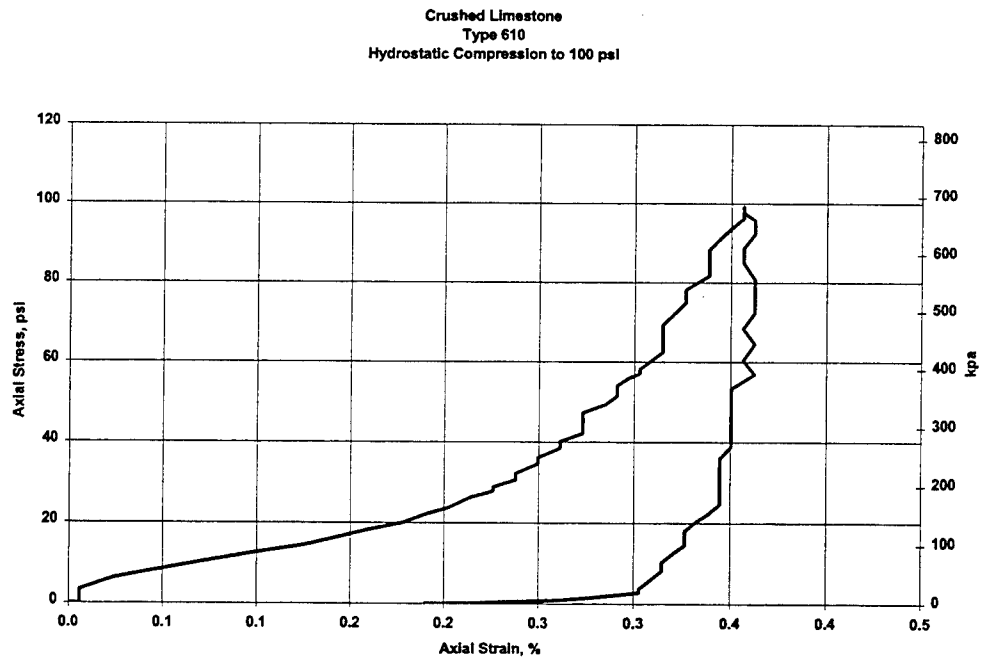


Figure D- 5. HC100-3

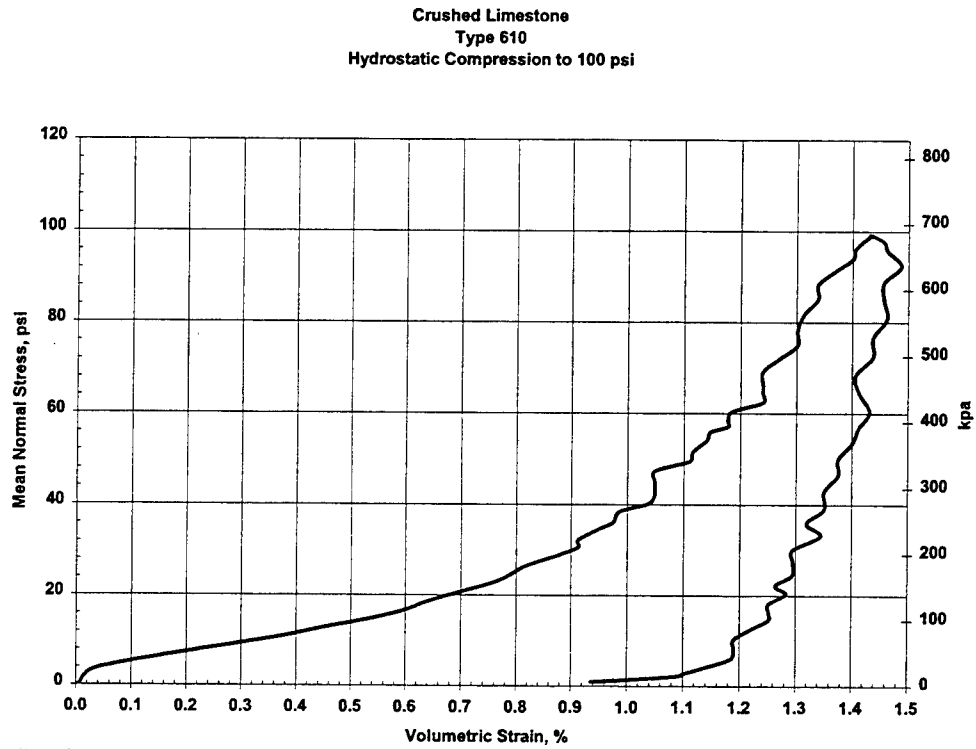


Figure D- 6. HC100-3

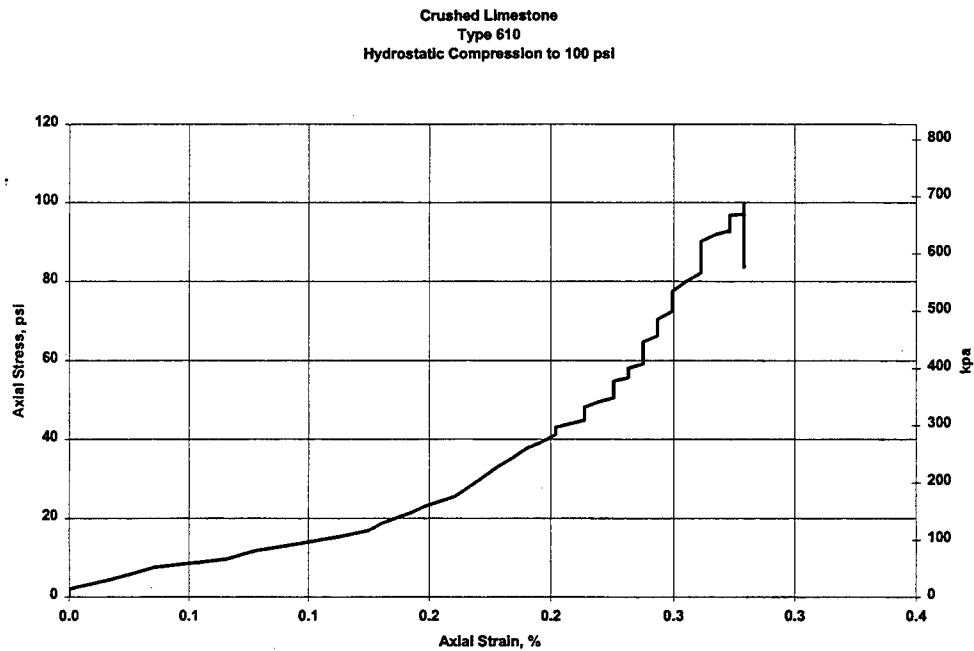


Figure D- 7. HC100-4

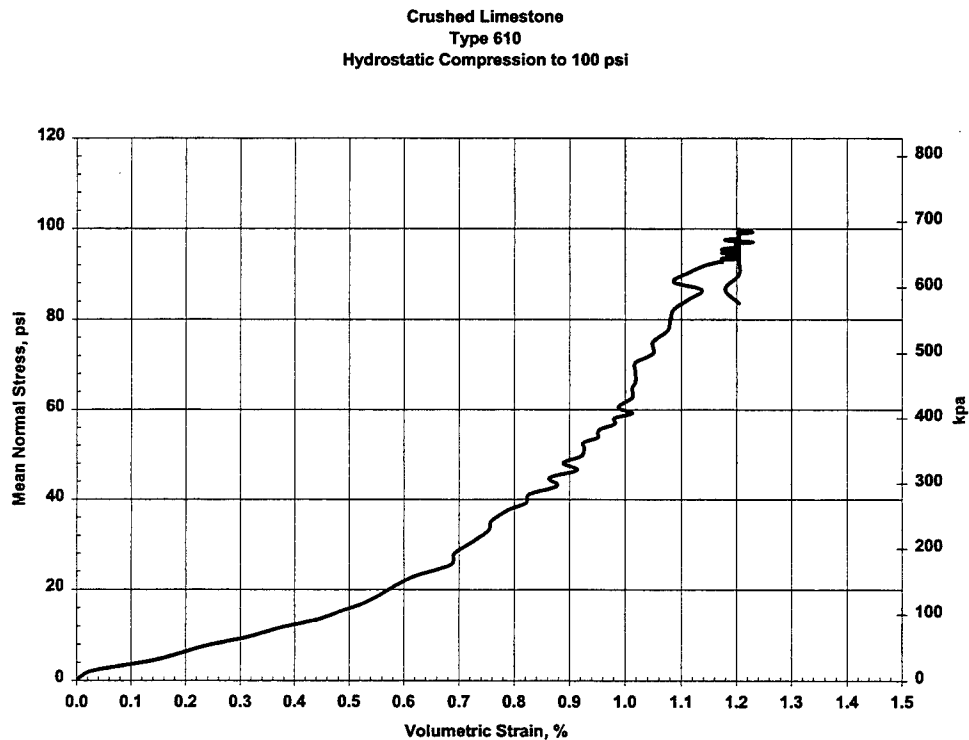


Figure D- 8. HC100-4

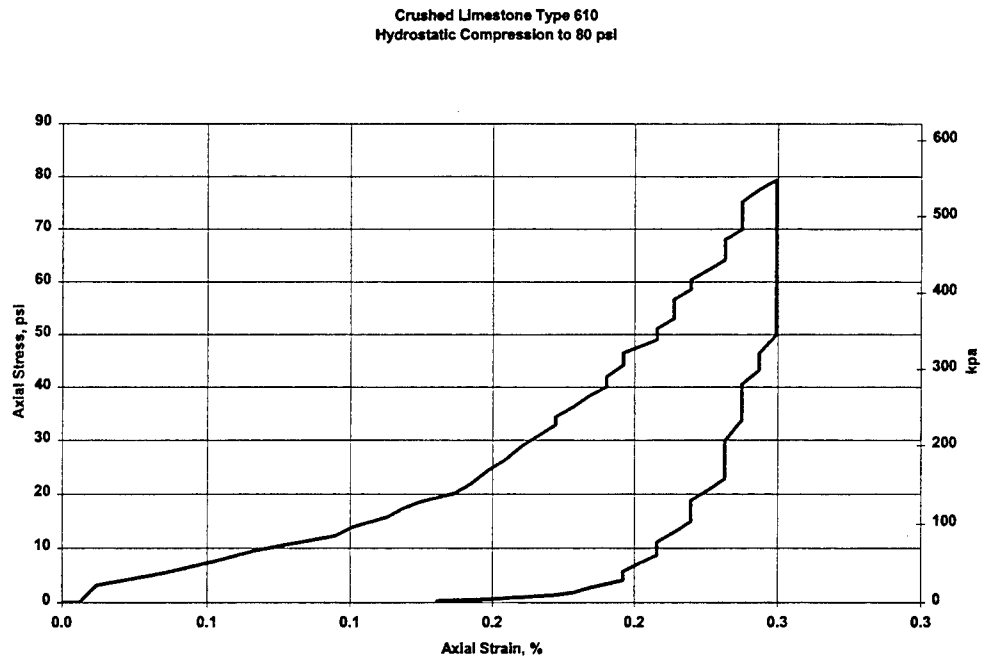


Figure D- 9. HC80-1

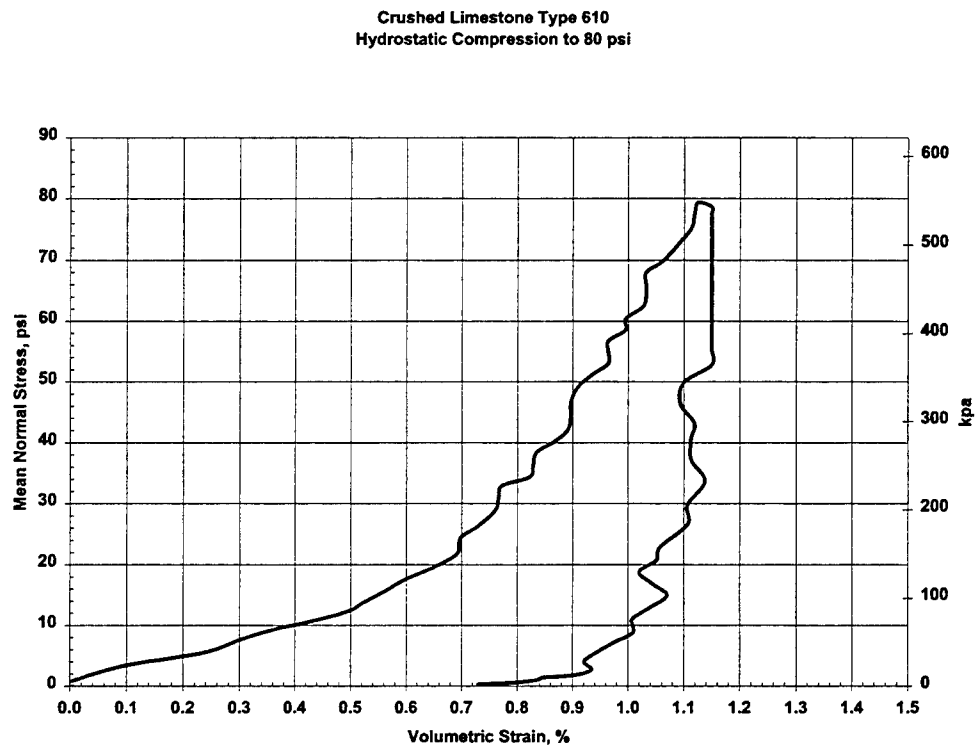


Figure D- 10. HC80-1

**APPENDIX E**

**RESULTS OF UNCONFINED COMPRESSION TESTS**

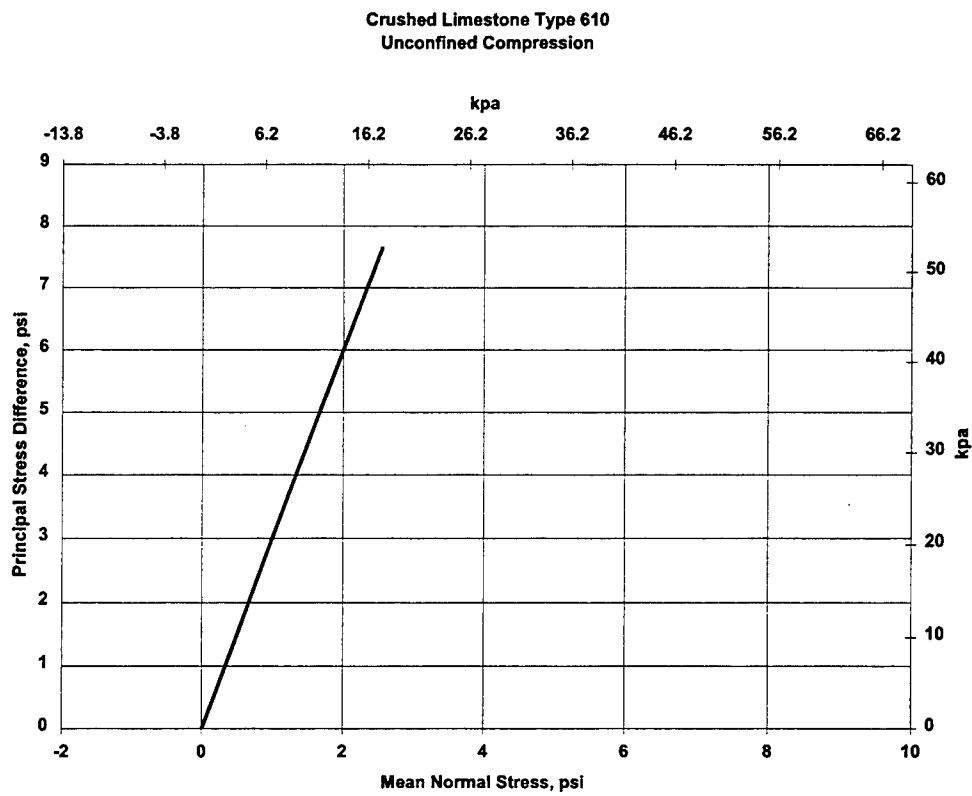


Figure E- 1. UCC1

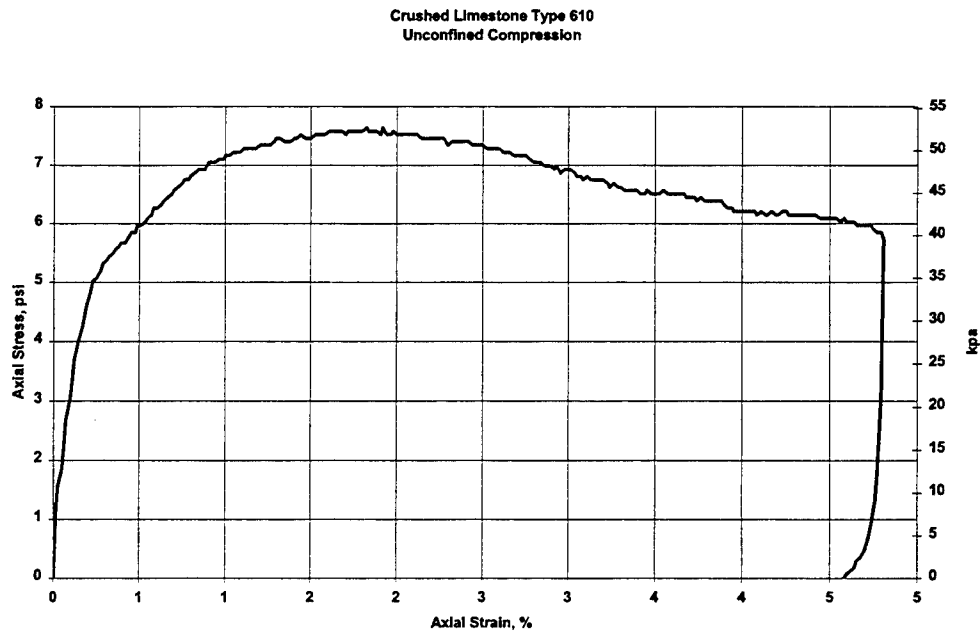


Figure E- 2. UCC1

Crushed Limestone Type 610  
Unconfined Compression

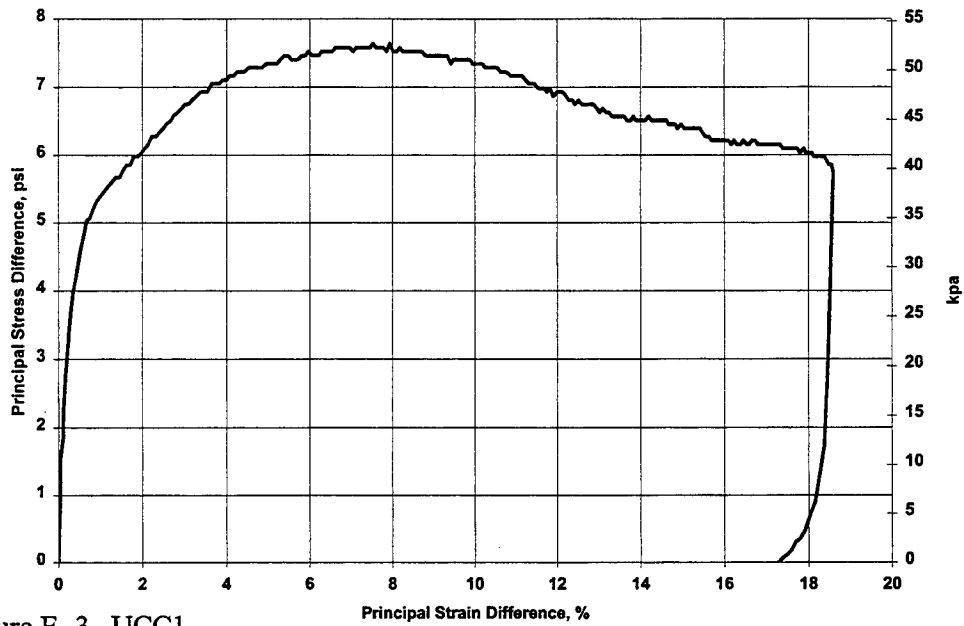


Figure E- 3. UCC1

Crushed Limestone Type 610  
Unconfined Compression

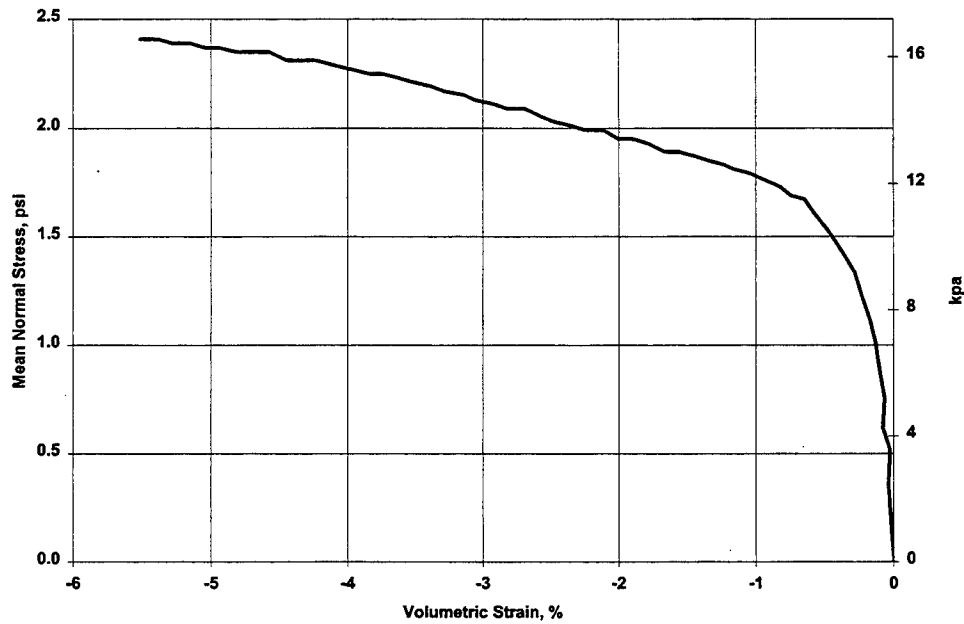


Figure E- 4. UCC1



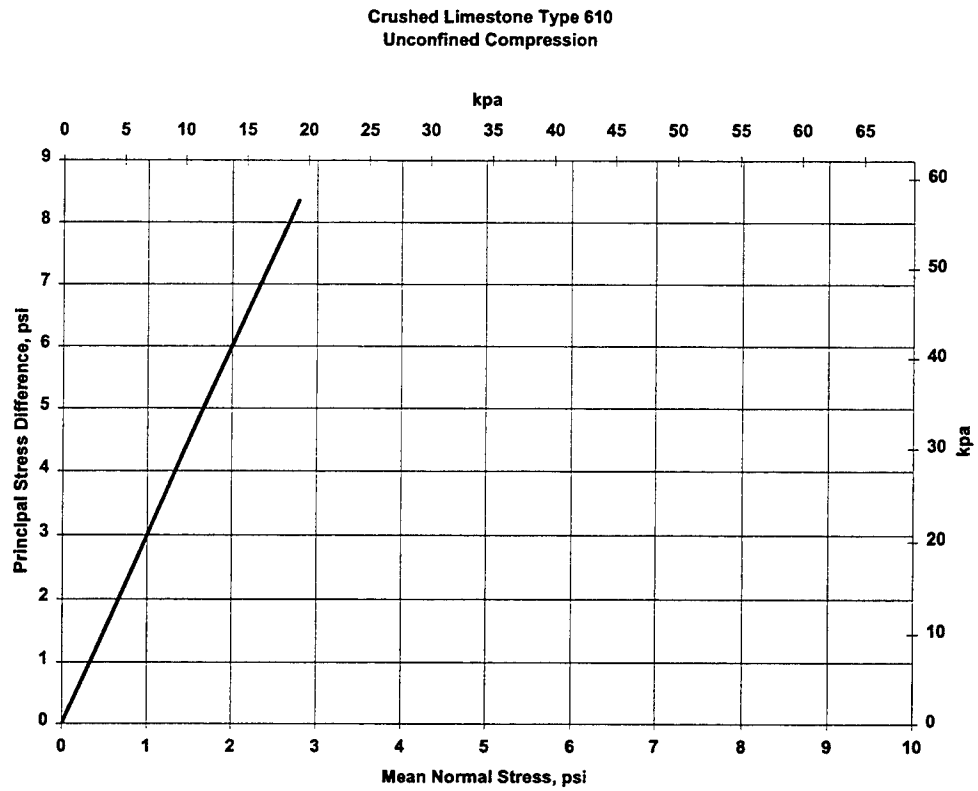


Figure E- 5. UCC2

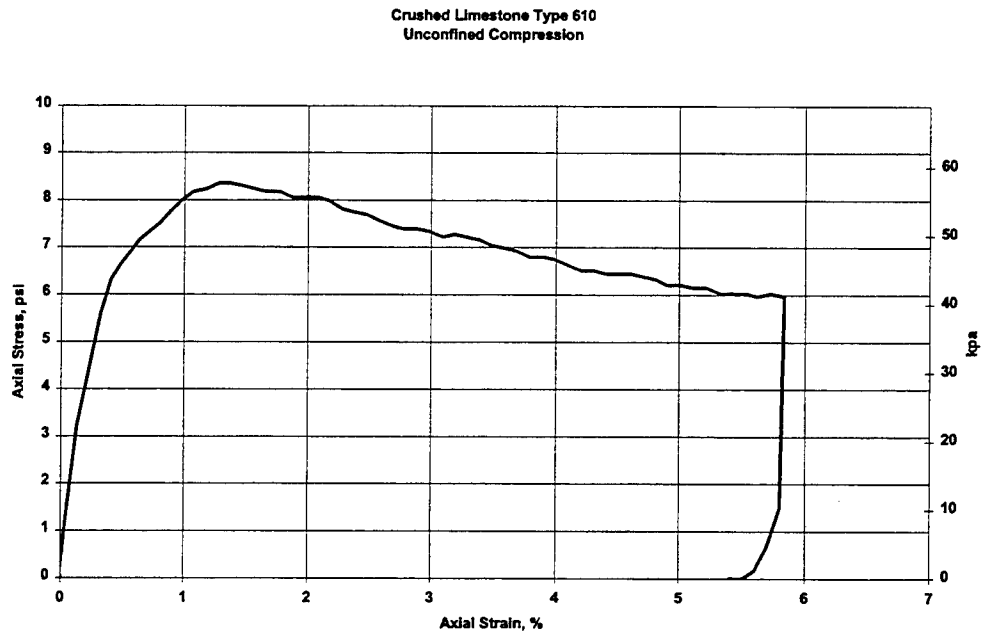


Figure E- 6. UCC2

Crushed Limestone Type 610  
Unconfined Compression

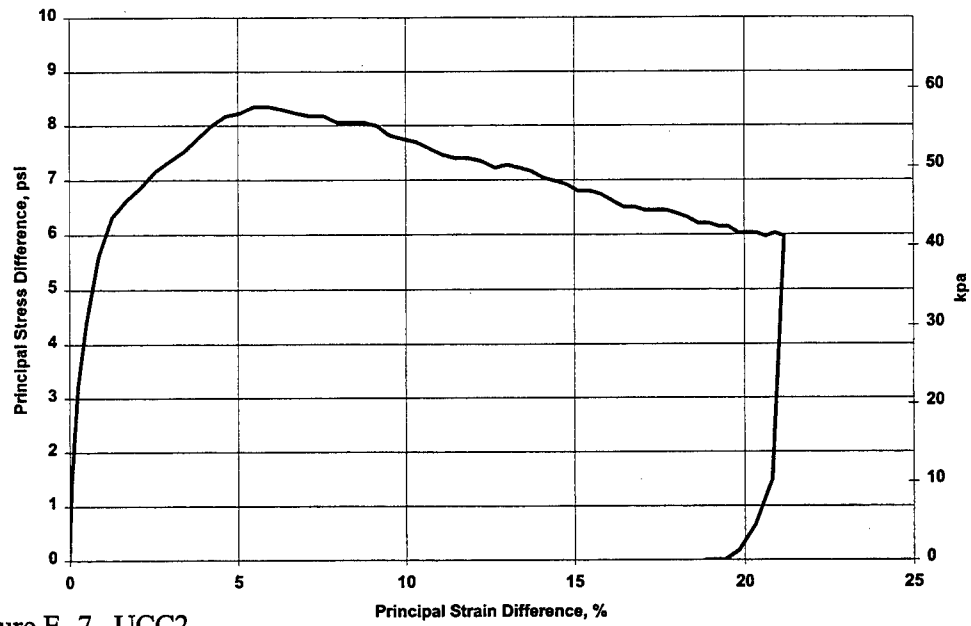


Figure E- 7. UCC2

Crushed Limestone Type 610  
Unconfined Compression

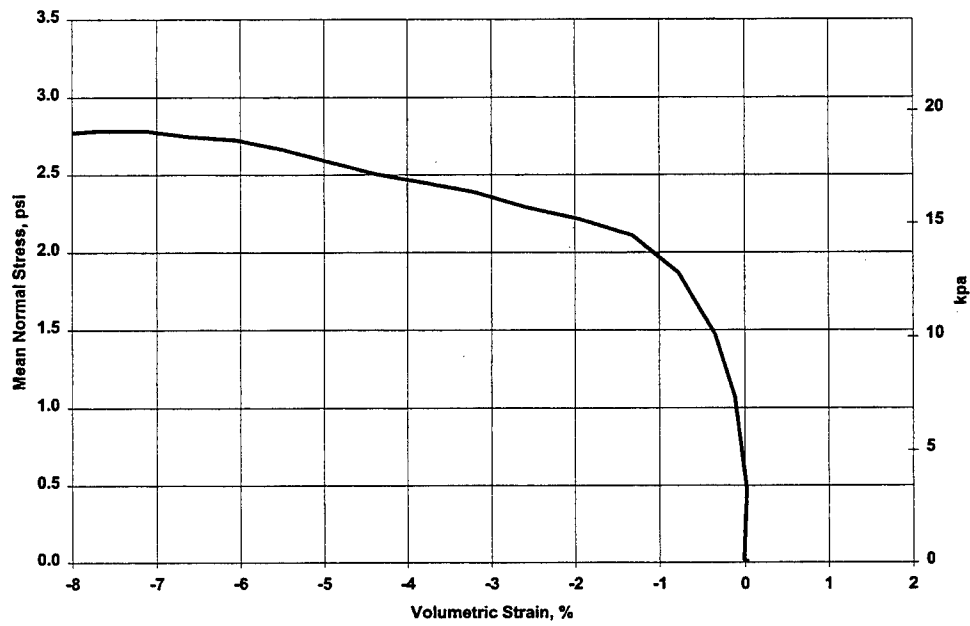


Figure E- 8. UCC2

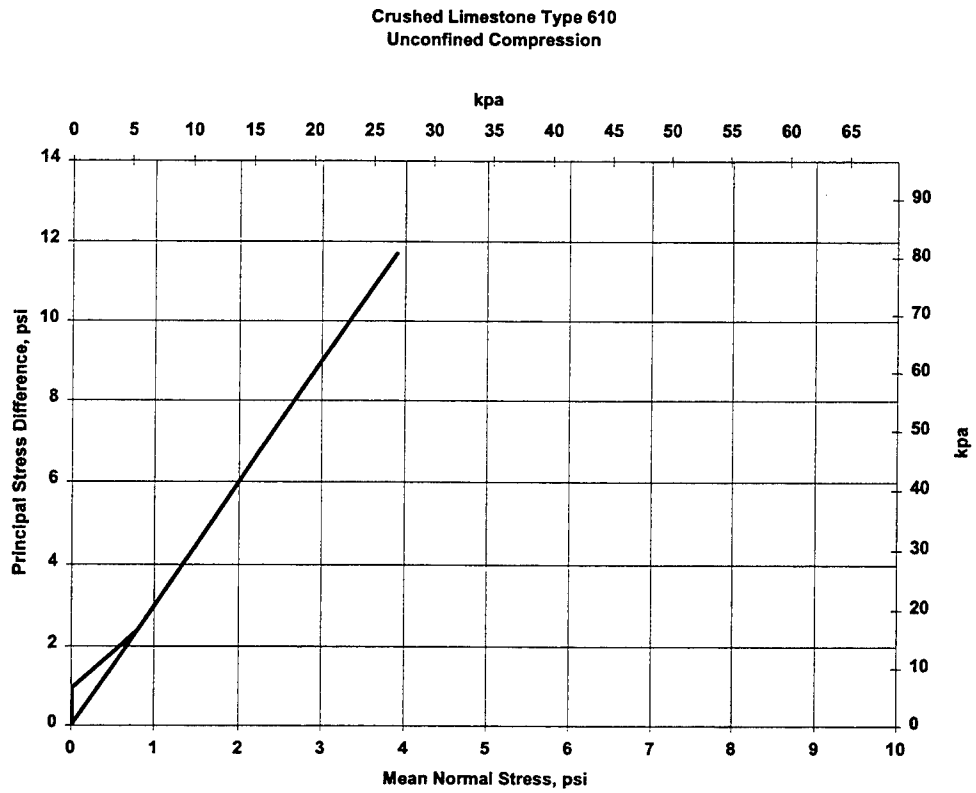


Figure E- 9. UCC3

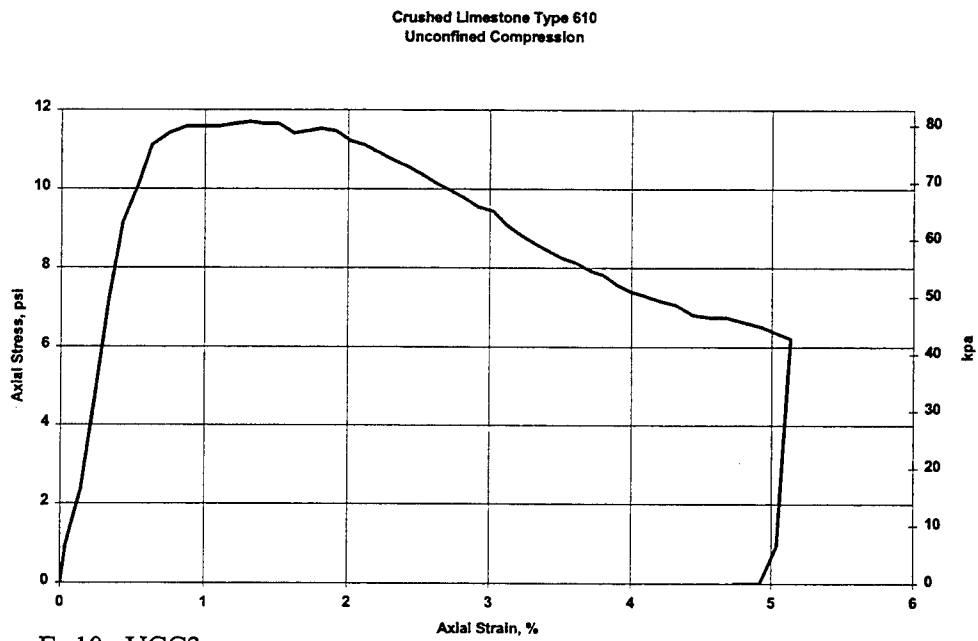


Figure E- 10. UCC3

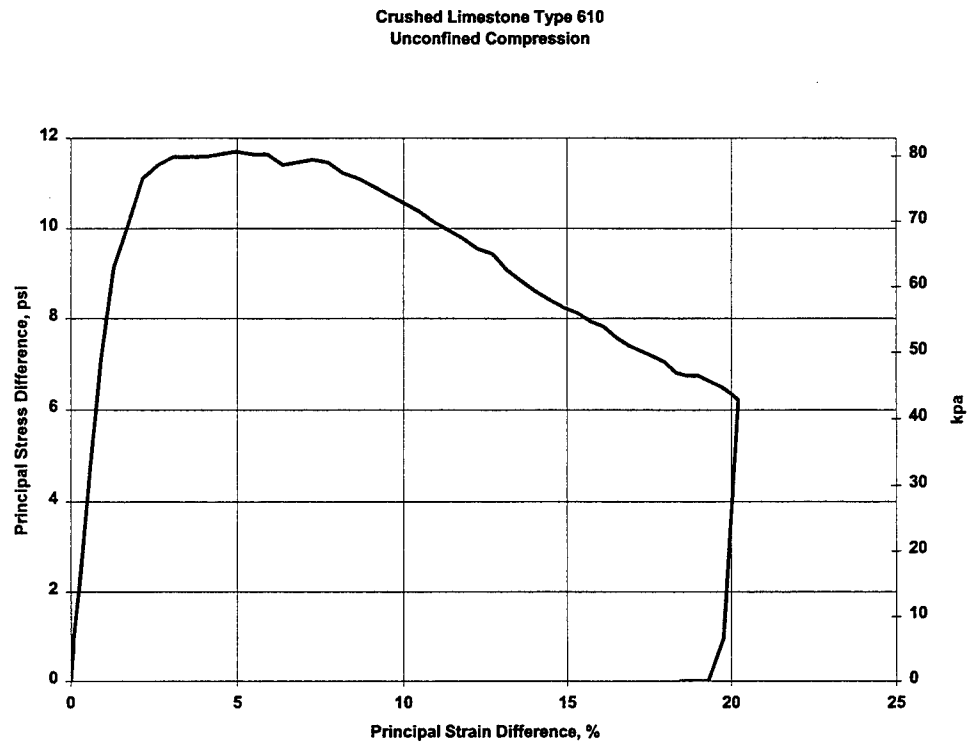


Figure E- 11. UCC3

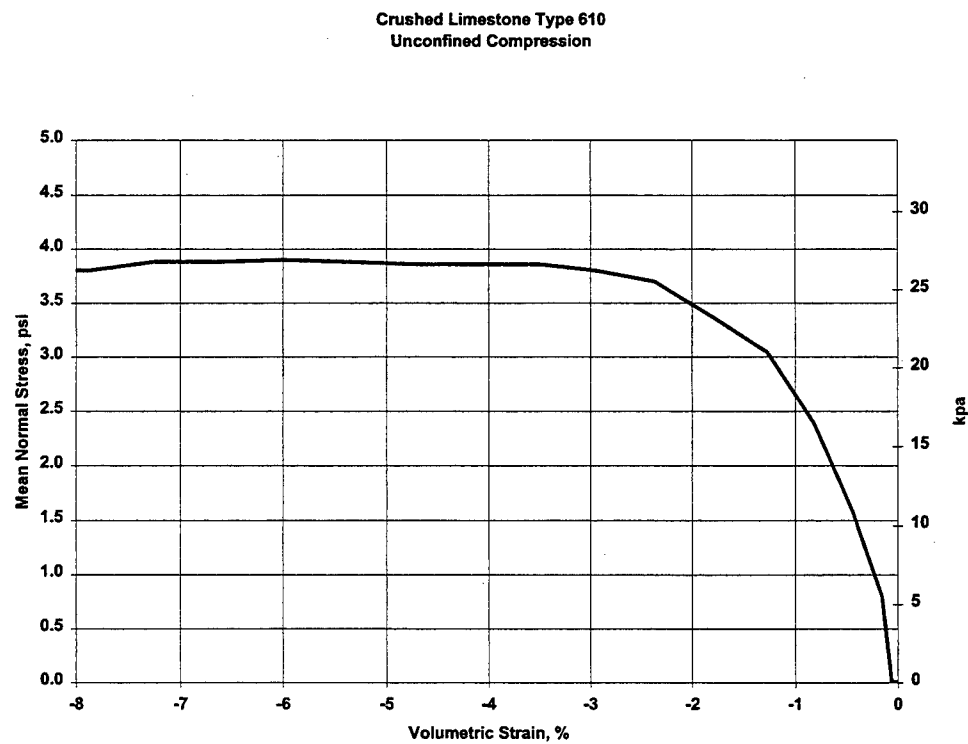


Figure E- 12. UCC3

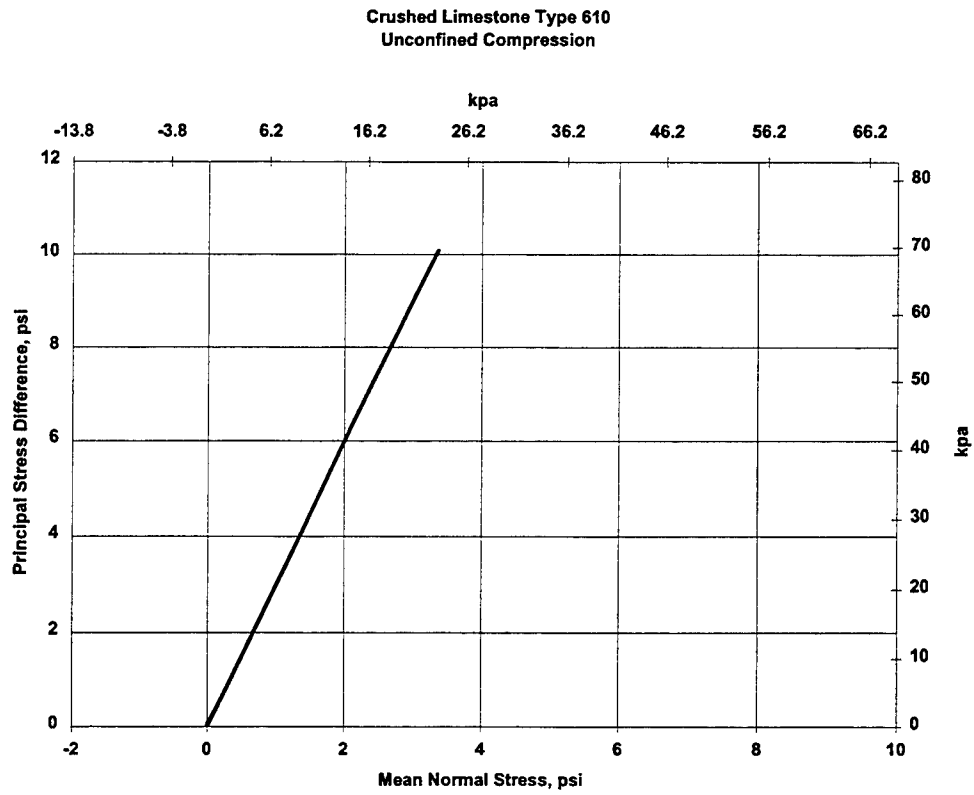


Figure E- 13. UCC4

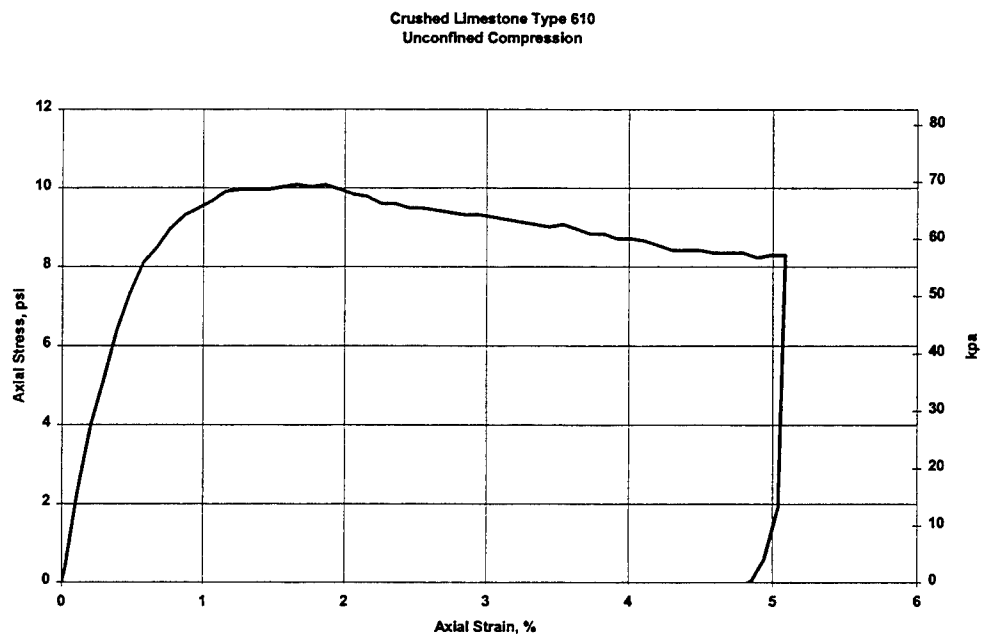


Figure E- 14. UCC4

Crushed Limestone Type 610  
Unconfined Compression

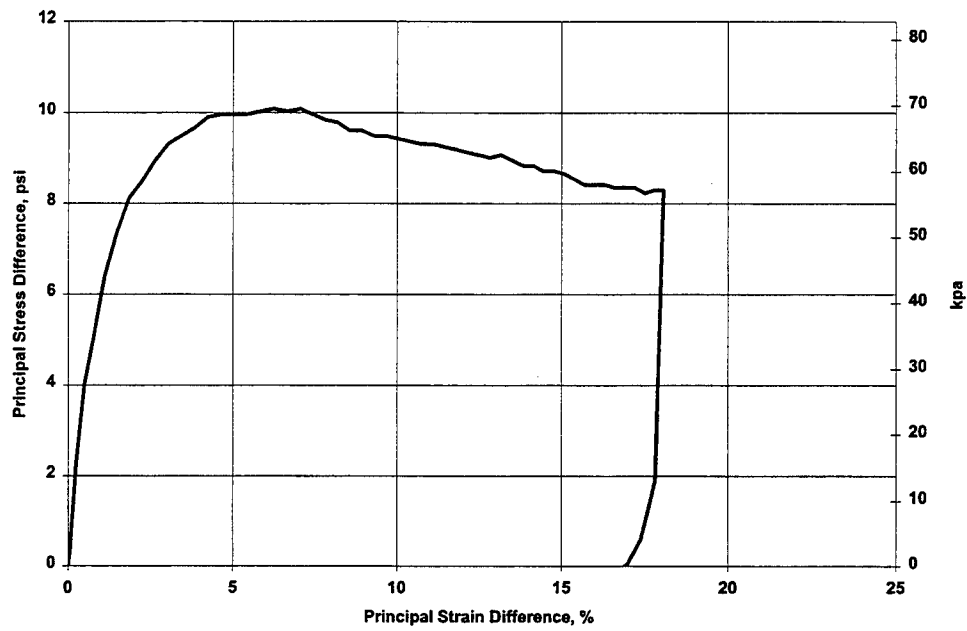


Figure E- 15. UCC4

Crushed Limestone Type 610  
Unconfined Compression

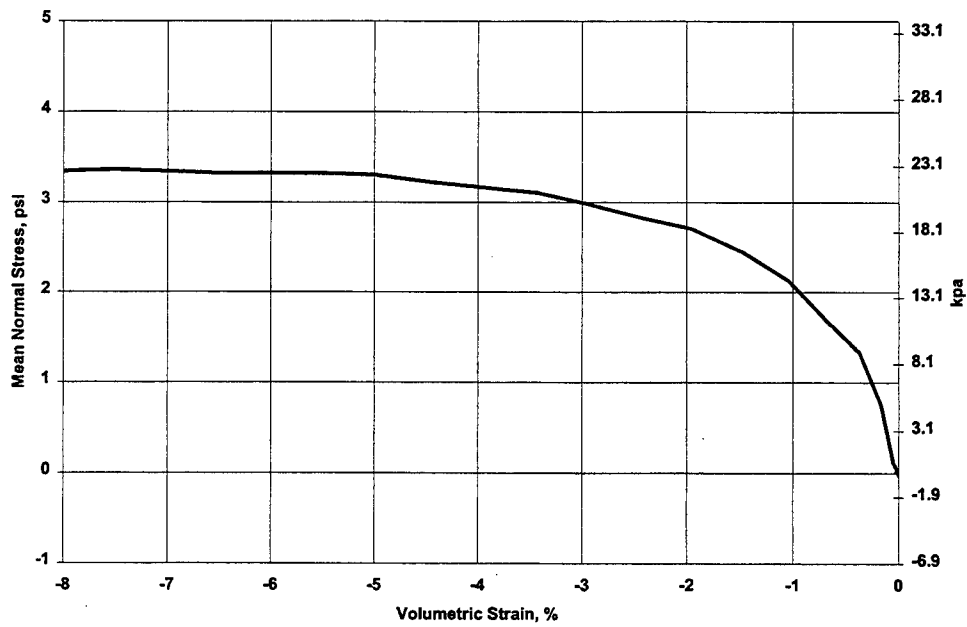


Figure E- 16. UCC4

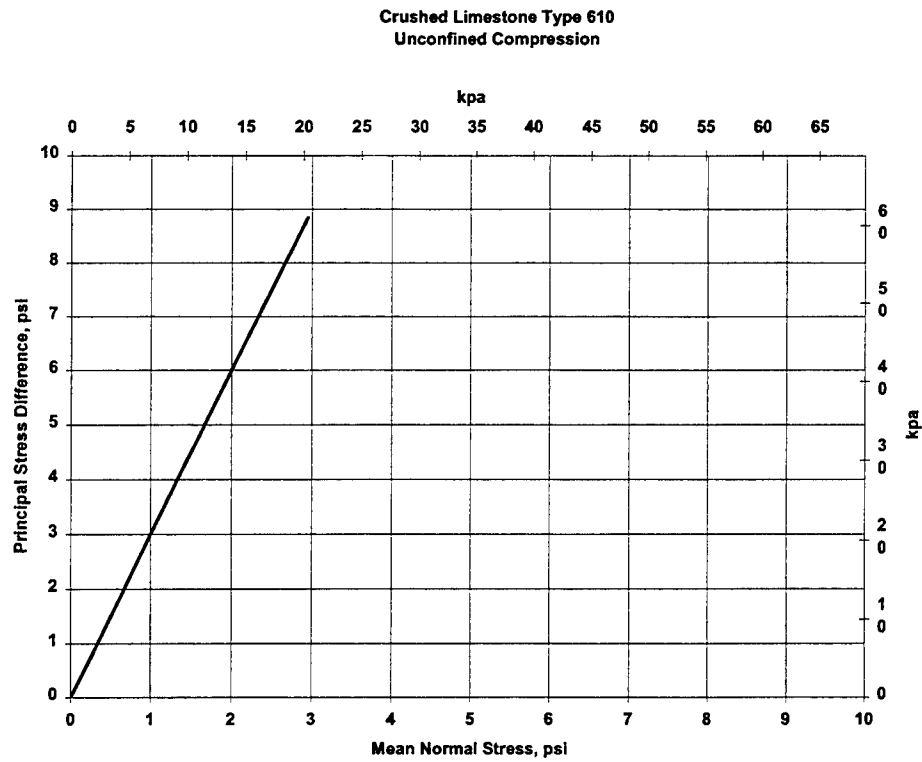


Figure E- 17. UCC5

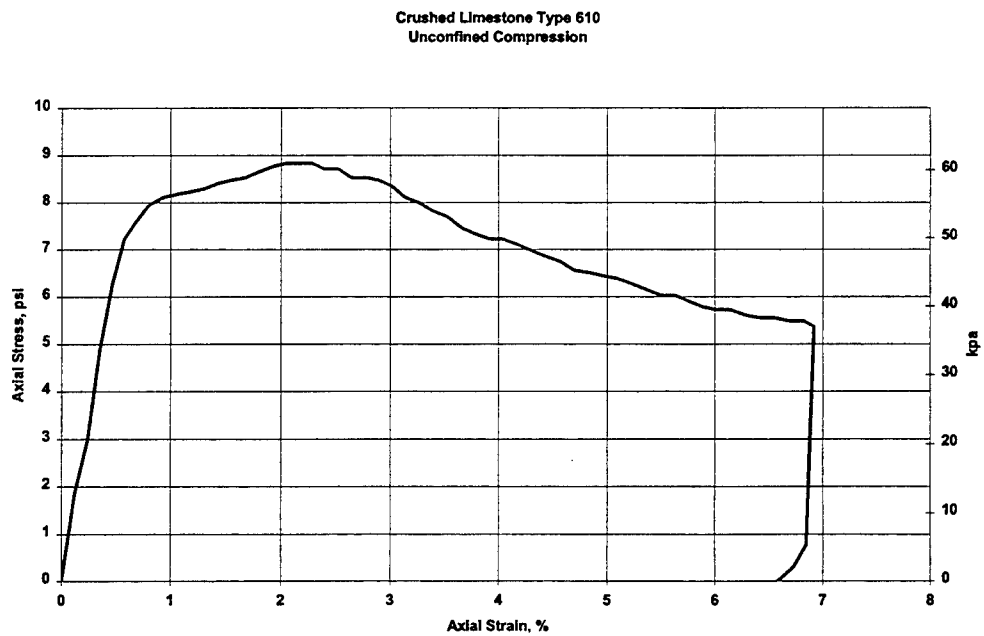


Figure E- 18. UCC5

Crushed Limestone Type 610  
Unconfined Compression

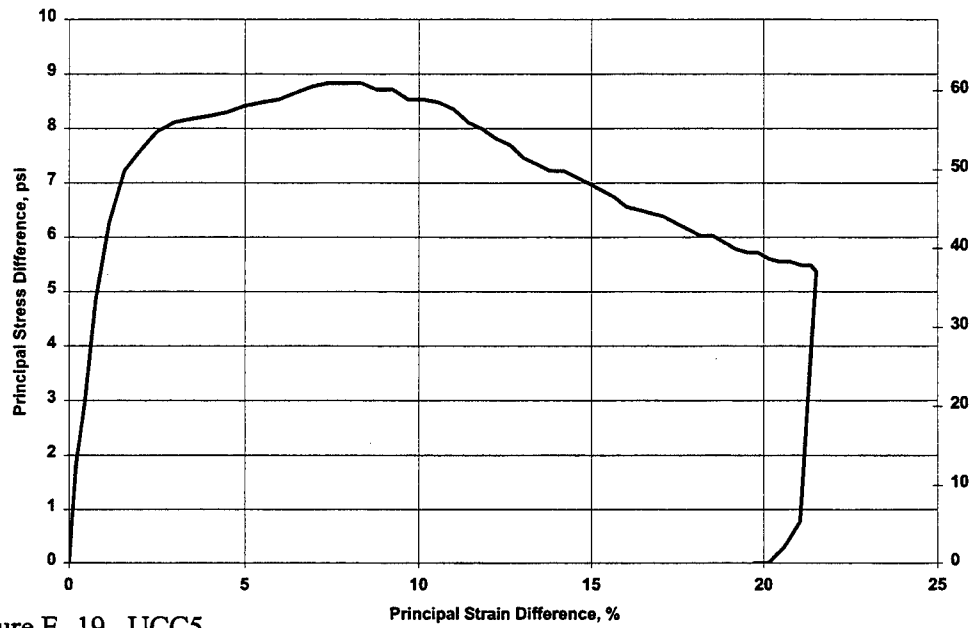


Figure E- 19. UCC5

Crushed Limestone Type 610  
Unconfined Compression

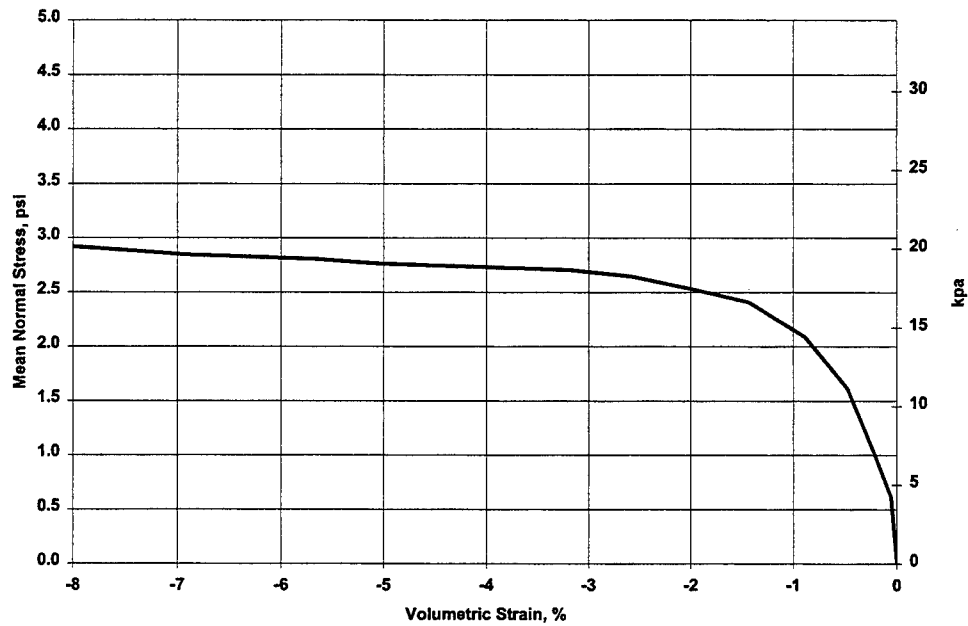


Figure E- 20. UCC5



**APPENDIX F**

**RESULTS OF UNIAXIAL STRAIN TESTS**

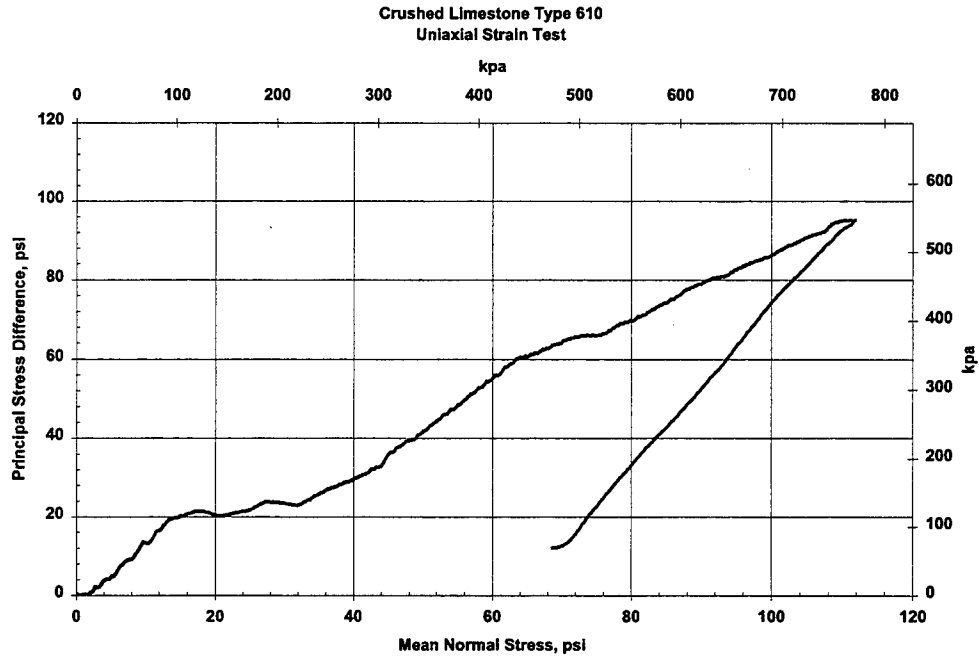


Figure F- 1. UXE1

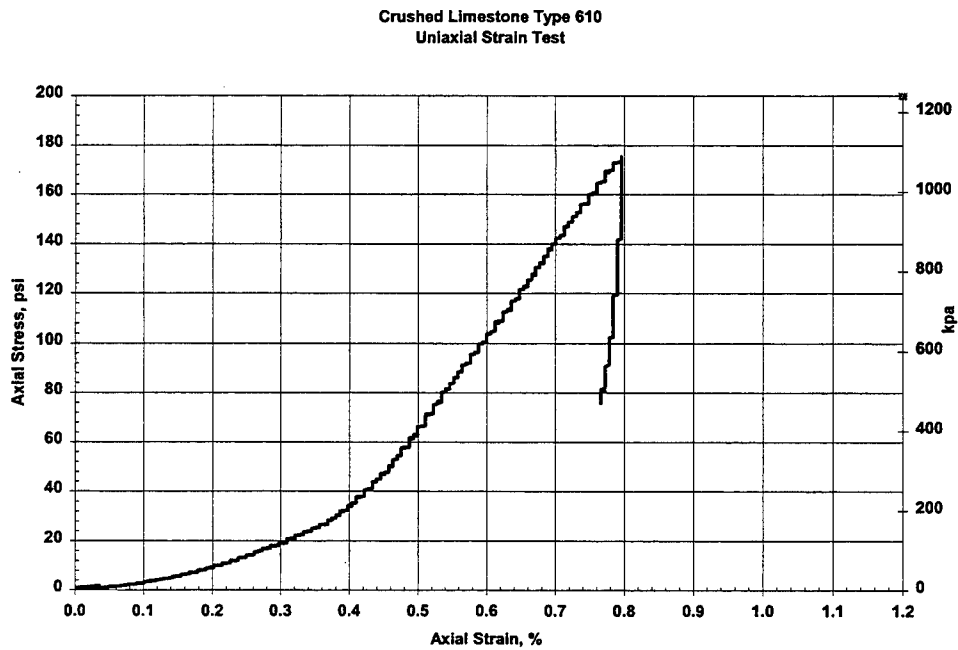


Figure F- 2. UXE1

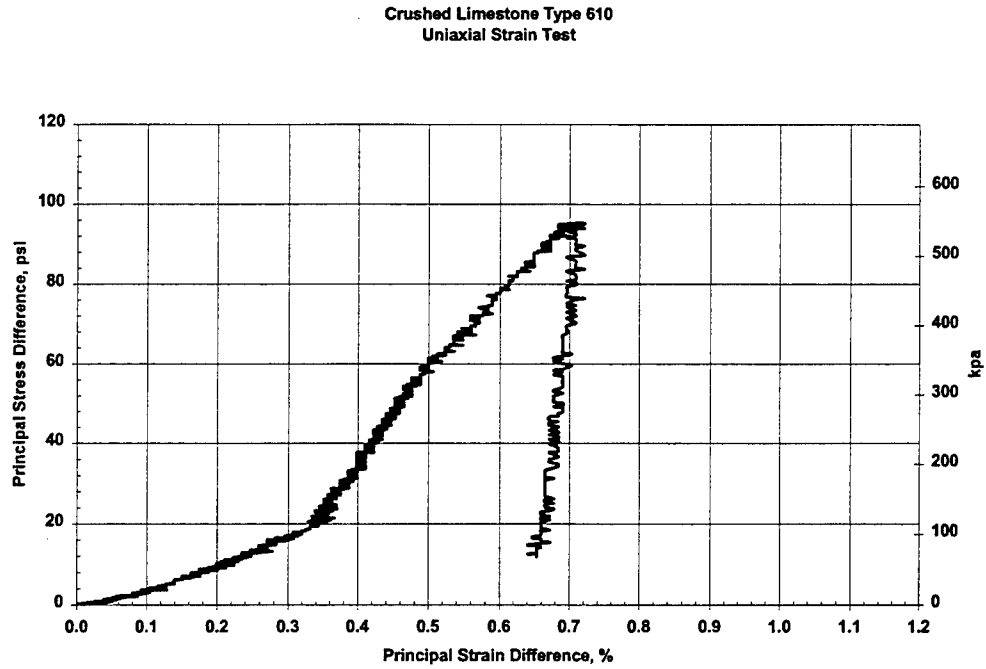


Figure F- 3. UXE1

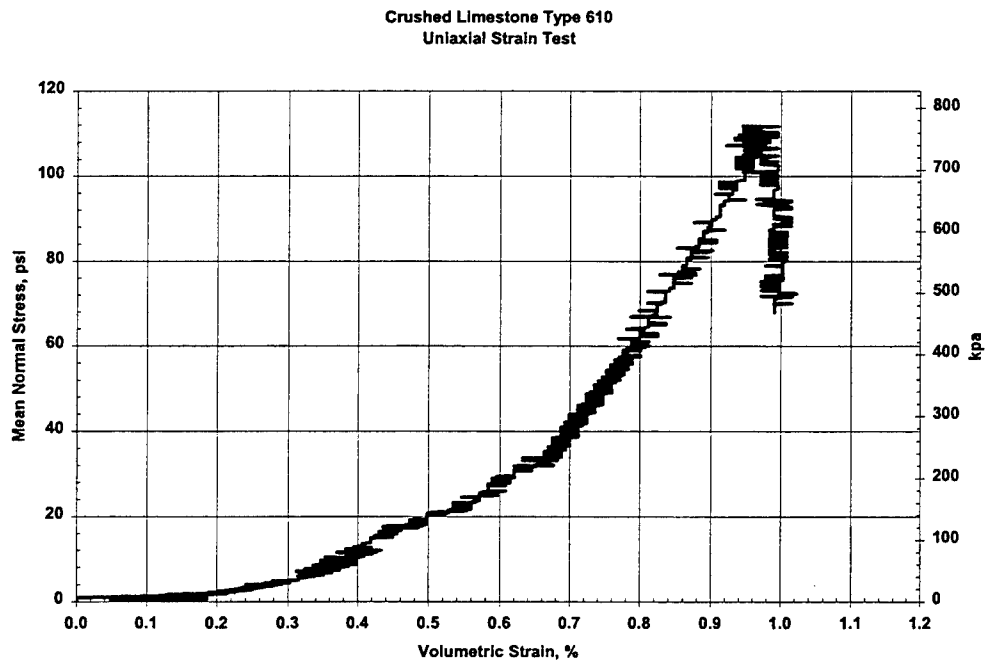


Figure F- 4 . UXE1

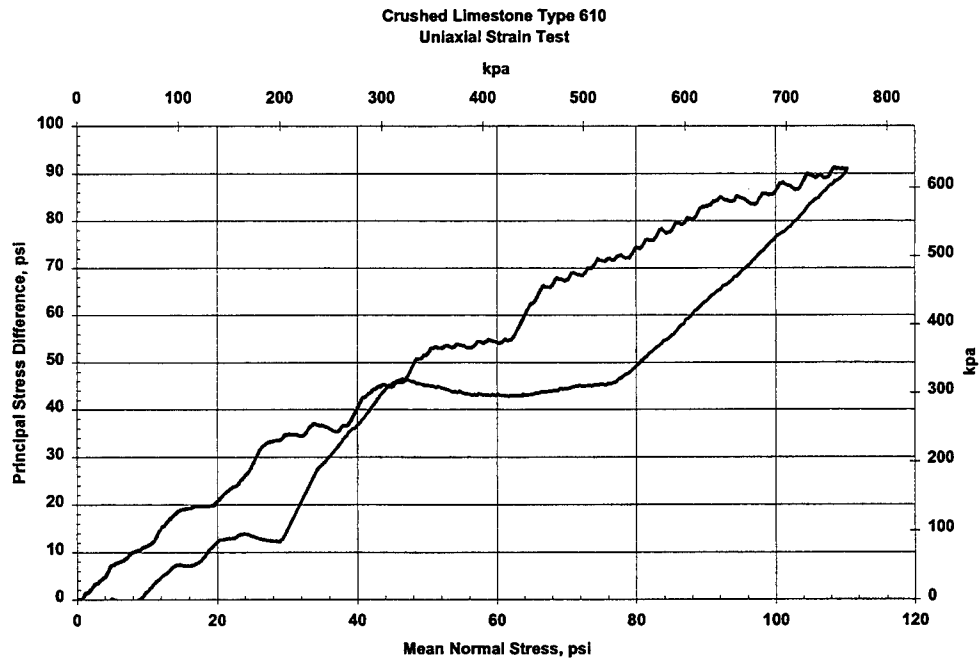


Figure F-5. UXE2

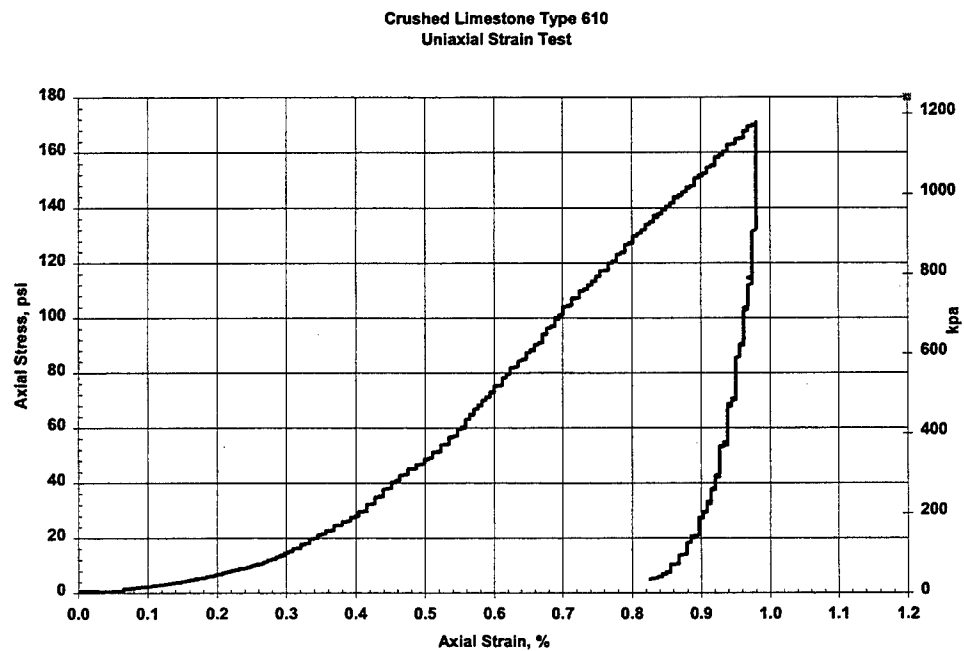


Figure F-6. UXE2

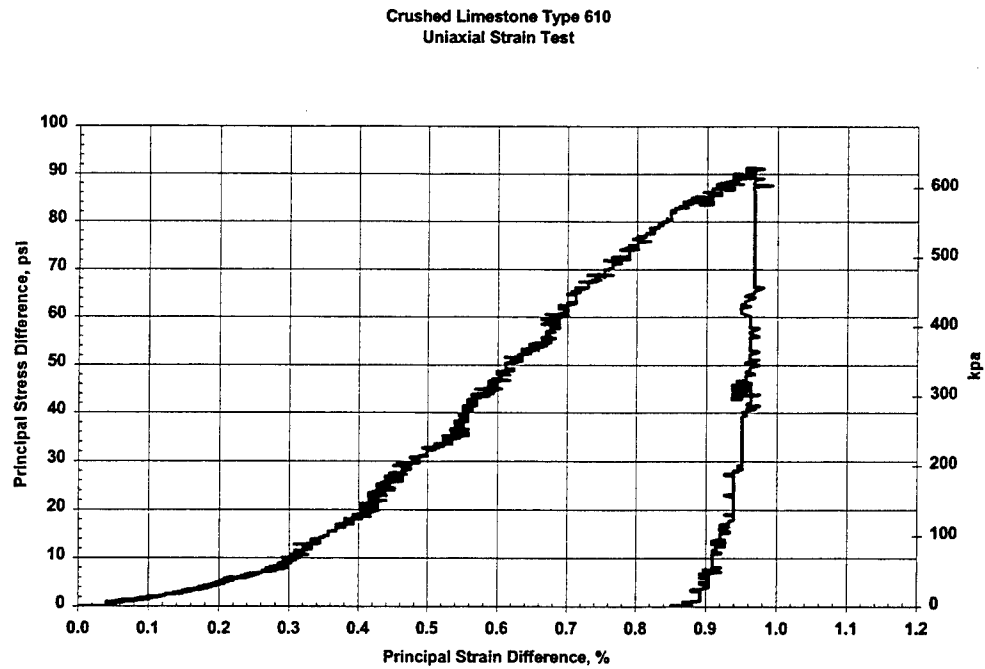


Figure F-7. UXE2

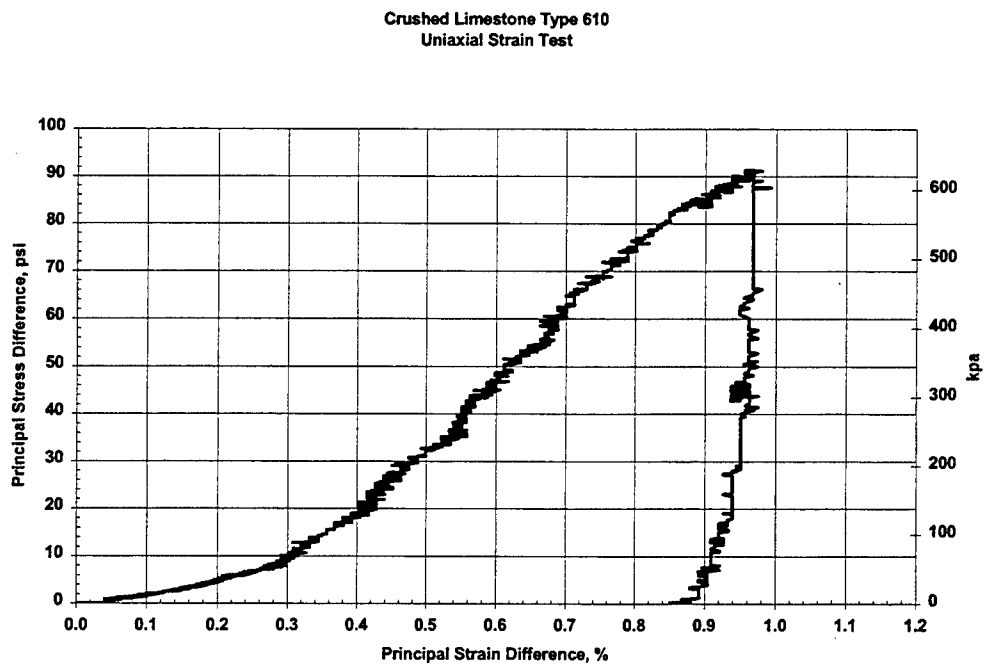


Figure F-8. UXE2

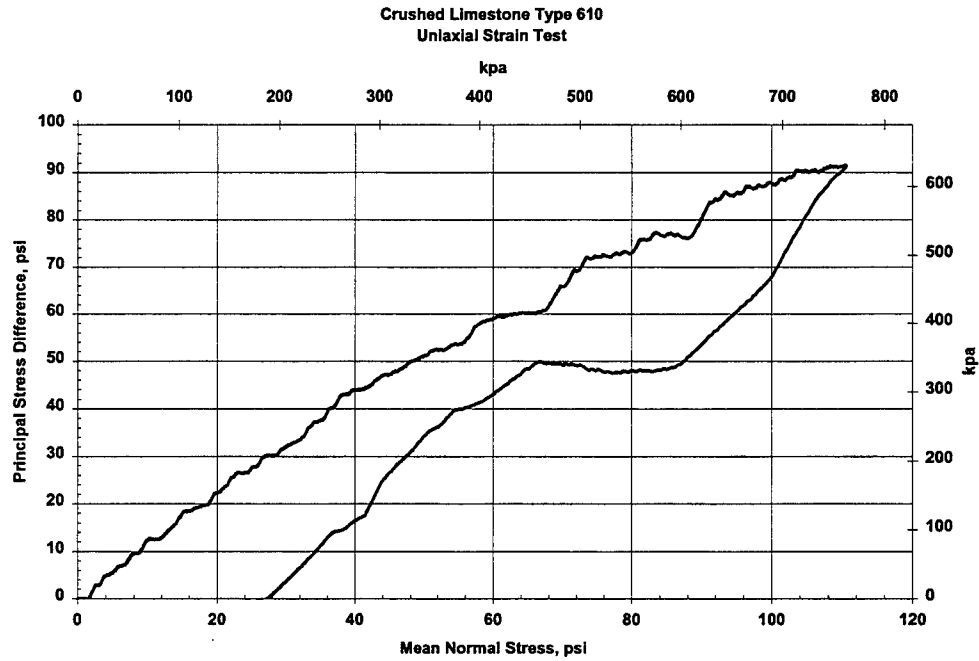


Figure F-9. UXE3

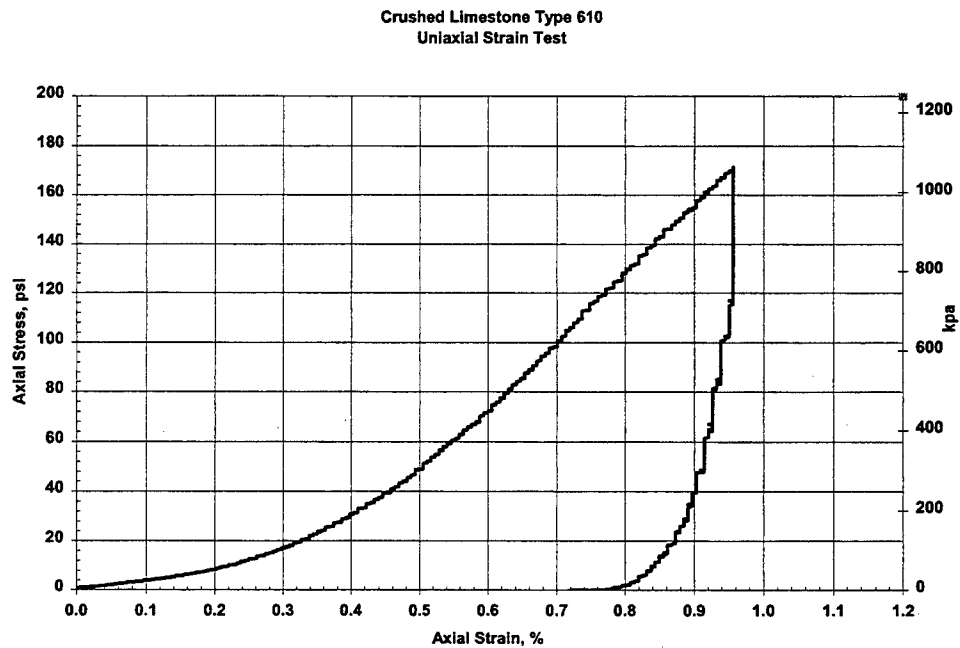


Figure F-10. UXE3

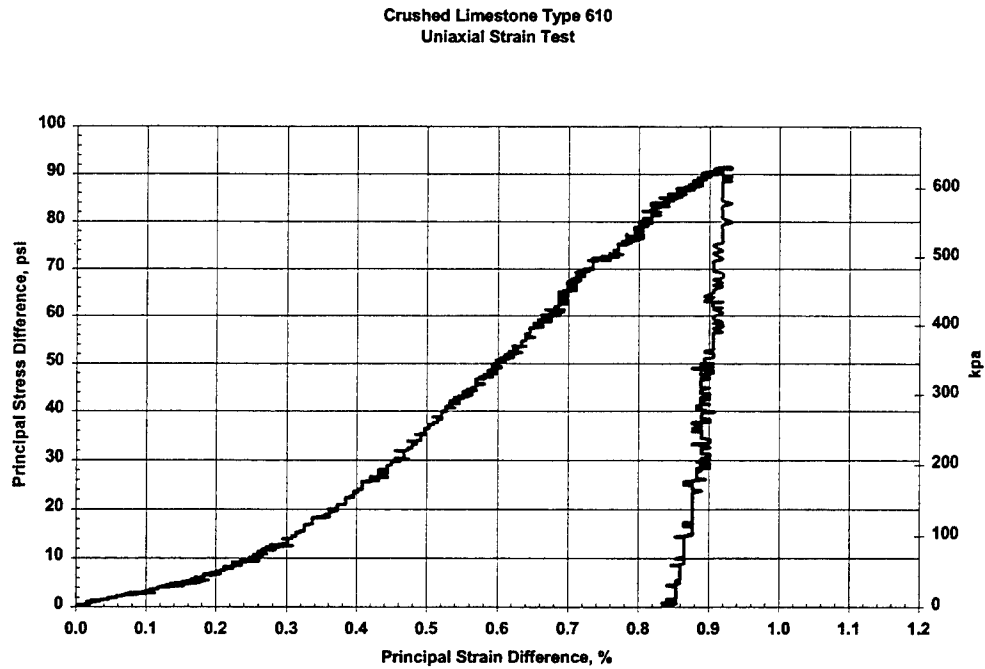


Figure F-11. UXE3

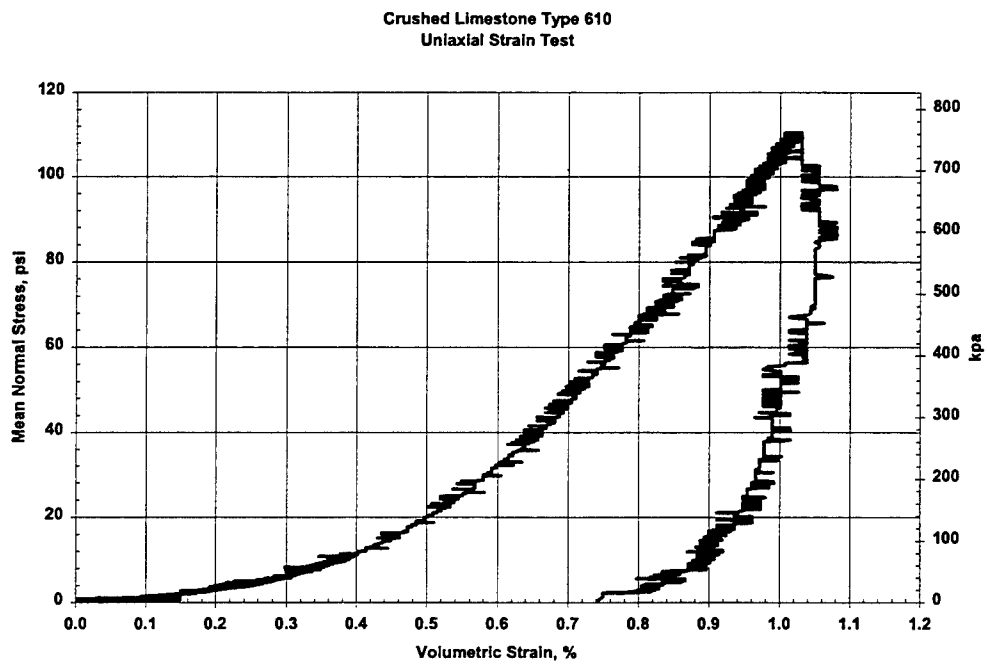


Figure F-12. UXE3

**APPENDIX G**

**OPERATION OF THE WES  
MULTIMECHANICAL MODEL VIEWER**



A stand-alone version of the WES MM model called MVIEWER was written to aid in determining those parameters that require trial-and-error methods. MVIEWER provides the analyst with a PC compatible platform to simulate laboratory tests relatively easily. A discussion of the MVIEWER program and its application is presented in this appendix.

Thirty material property calibration parameters are required for the WES MM model. Ten of these properties are global (Table G.1) and the remaining twenty are associated with each of the four mechanisms (Table G.2).

Table G.1 Global Properties

Name	Label in code	Comments
Phi	PHILIMIT	friction angle
Cohesion	C	cohesion
Bulk Modulus	K	
Shear Modulus	G	
phi ratio	PHIRATIO	
Hydrostatic Intercept	Fh	Intercept of Normal Consolidation Line (NCL)
Reciprocal of Cc	BETA	Reciprocal of the slope of NCL
Shear-volume factor	Mc	shear-volume coupling term
OC factor	Decay	strength reduction term
dilatancy scaling factor	GAMMA	

Table G.2 Mechanism Properties

Name	Label in code	Comments
Strength factor	PHIFRAC	scales friction angle
Mean Stress factor	PFACT	scales mean stress
Shear Stiffness factor	SHEARRATIO	distributes shear stiffness
Compression limit	HLIMIT	absolute compression limit
Volumetric Stiffness factor	BULKRATIO	distributes volumetric stiffness

The stand-alone model, MVIEWER, was used to provide quick feedback during the iterative calibration process for the WES model. The MVIEWER was compiled using a LeHey PC compatible FORTRAN 77/90 Compiler. The MVIEWER program uses either an ASCII input file or an interactive dialogue window to input the material properties and provide for an easy way of determining the sensitivity of the WES MM model to changes in these properties. The main starting screen for MVIEWER is shown in Figure G.1.

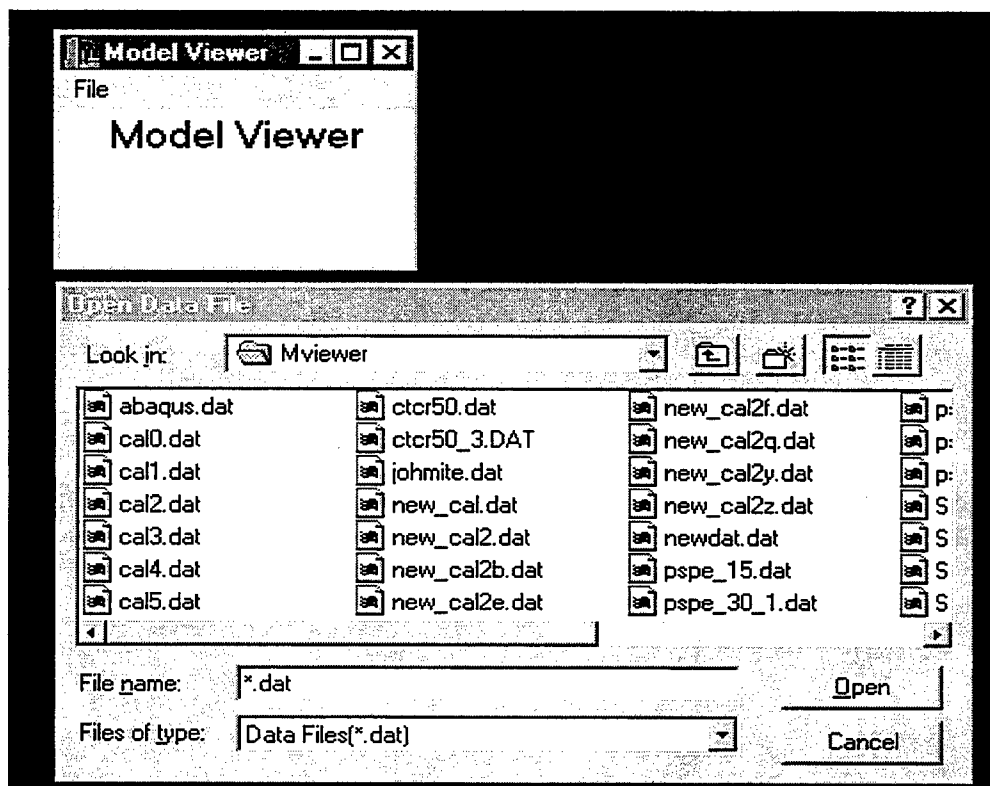


Figure G.1. Main starting screen for MVIEWER program

From this screen, an ASCII data file containing the input data and 30 material properties can be selected. The data is in the form shown in Figure G.2. The first 5 entries in the data file are used to simulate the conditions of the conventional triaxial test. In addition to the file retrieval method of inputting data, the user can directly type data into the appropriate locations shown in Figure G.3.

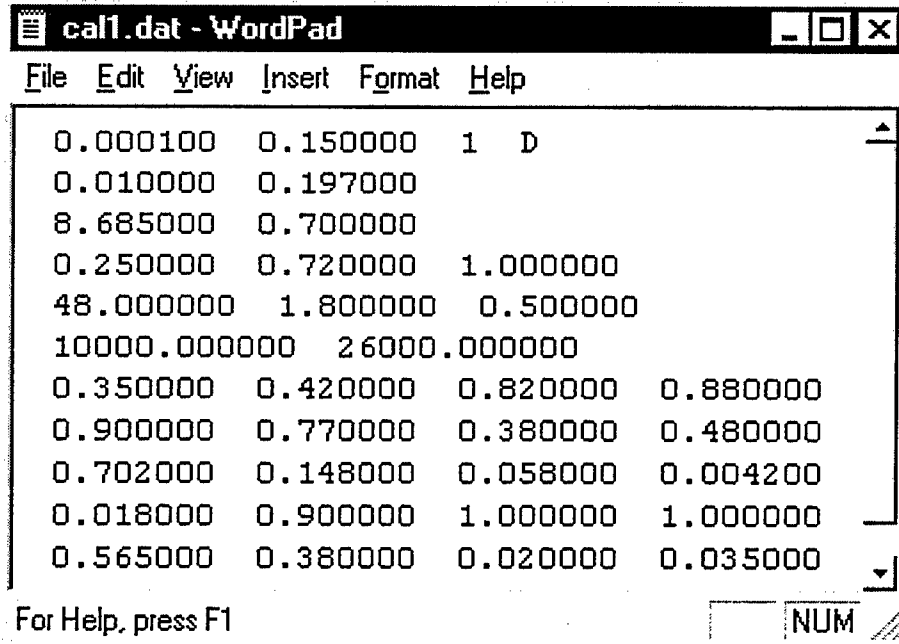


Figure G.2. Sample input data file for MVIEWER program

Data Editor

$\Delta\epsilon$	0.0001	$\epsilon$	0.15
Output Freq.	1	<input checked="" type="radio"/> Drained	<input type="radio"/> Undrained
$\sigma$	50	Void Ratio	0.197
$\beta$	8.685	Fh	0.7
Cohesion	0.25	Mc	0.72
$\phi$	48	Decay	1.8
$K$	10000	$G$	30000
PhiFrac	0.35	0.42	0.82
PFact	0.9	0.77	0.38
Shear Ratio	0.702	0.148	0.058
H Limit	0.018	0.9	1
Bulk Ratio	0.565	0.38	0.02
Cyclic Loading Conditions			<input type="checkbox"/> Off
Cyclic Modes	<input type="radio"/> Stress Mode	<input type="radio"/> Strain Mode	<input type="radio"/> Combo Mode
Start Value	0.0	End Value	0.0
Number of Cycles	0		
Compute	Plot Data		

Figure G.3. Sample input screen for MVIEWER program

The MVIEWER program also allows the analyst the opportunity to produce plots of principal stress difference versus principal strain difference and volumetric strain versus principal strain difference (Figure G.3). Multiple plots from several runs may be viewed together to aid the user in visualizing the effects of changing the material properties on the stress strain response of the model. The MVIEWER plot routine also allows the user to plot of principal stress difference versus principal strain difference from test results stored in an ASCII file (Figure G.4) Strains are given in %, while the units of stress are determined by the system used in the calibration (psi or kPa). For these plots stress is given in psi and strain in %.

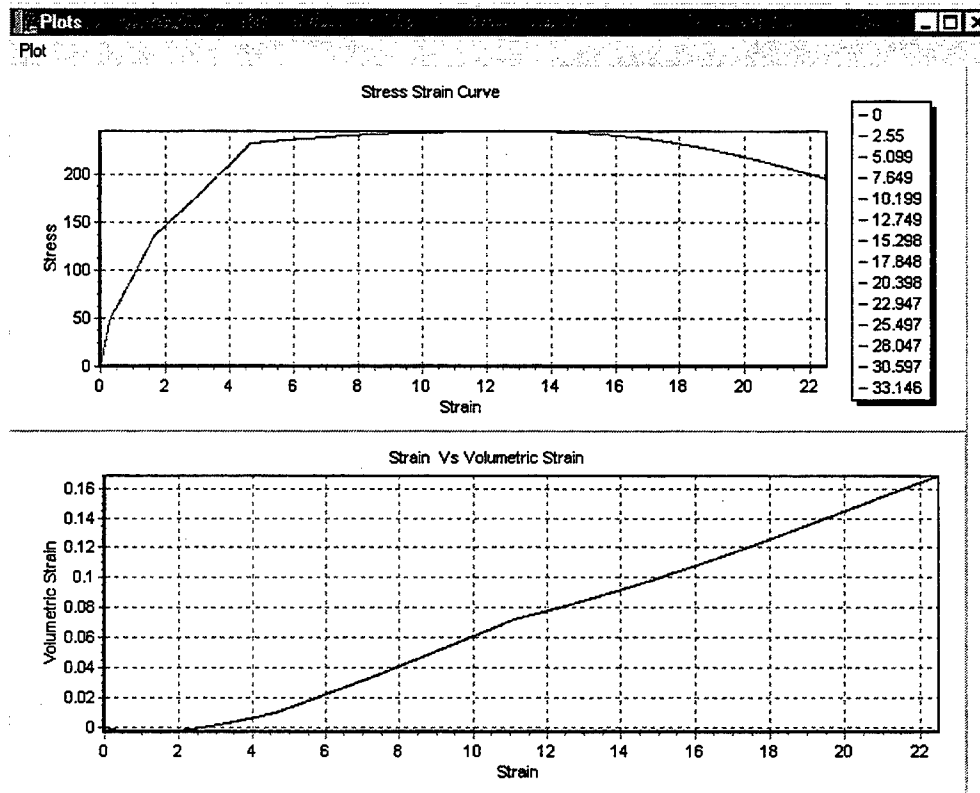


Figure G.4. Stress-Strain plots from MVIEWER model results

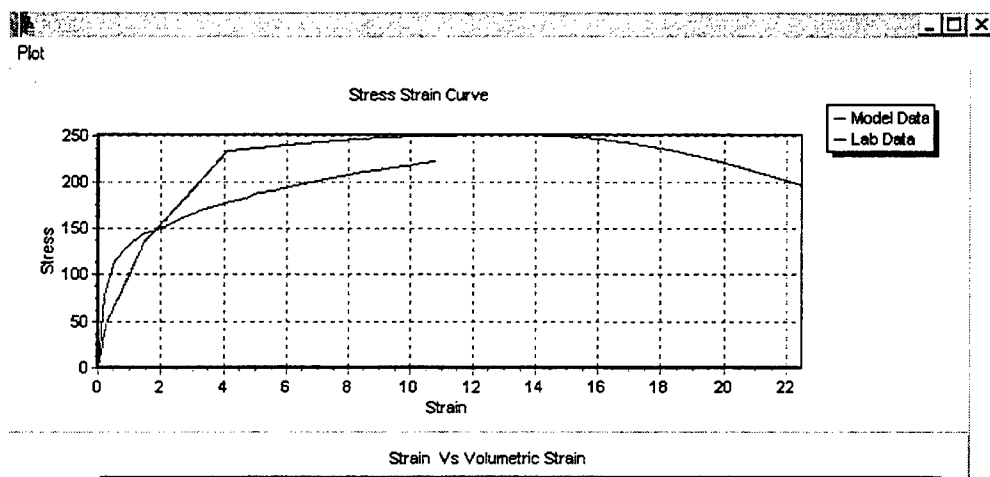


Figure G.5. Stress-Strain plots from MVIEWER model results (longer upper line) and test data (lower shorter line)

**APPENDIX H**

**DETERMINATION OF STRENGTH PARAMETERS**

The Mohr circle of stress provides a convenient method of analyzing two-dimensional stress states. In order to apply the method, the values and directions of the principal stress must be known. In the case of conventional triaxial tests of soils the applied stresses are the principal stresses. The axial stress is the maximum principal stress ( $\sigma_1$ ) and the confining stress is the minimum principal stress ( $\sigma_3$ ). The maximum shear stress has the coordinates of (s, t) as shown in Figure H.1.

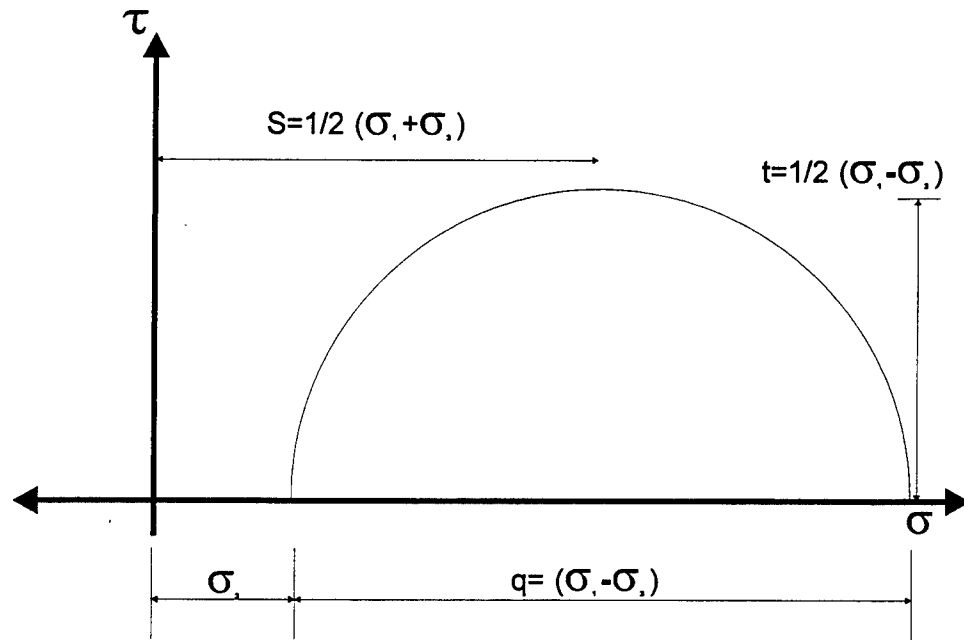


Figure H.1. Mohr circle of stress for a conventional triaxial compression test

In the case of plastic analysis of soils behavior, the Mohr circle containing the normal and shear stresses at failure is a limiting circle. Limiting circles at different values of normal stress will all touch at a common tangent, which is called a failure envelope (Figure H.2). The equation of this failure envelope is referred to as Coulomb's equation:

$$\tau = c + \sigma \tan \phi \quad (\text{H.1})$$

Where:

$\tau$  = shear stress

$c$  = cohesion

$\sigma$  = normal stress

$\phi$  = angle of internal friction

A line drawn through the point of maximum shear stress ( $s, t$ ) for a series of conventional triaxial compression tests will produce a maximum stress point failure envelope.

The equation of this line is given as:

$$t = a + s \tan \alpha \quad (\text{H.2})$$

Where:

$t = 1/2 (\sigma_1 - \sigma_3)$

$s = 1/2 (\sigma_1 + \sigma_3)$

$a$  = intercept ( $c \cos \alpha = a$ )

$\alpha$  = friction angle ( $\sin \phi = \tan \alpha$ )



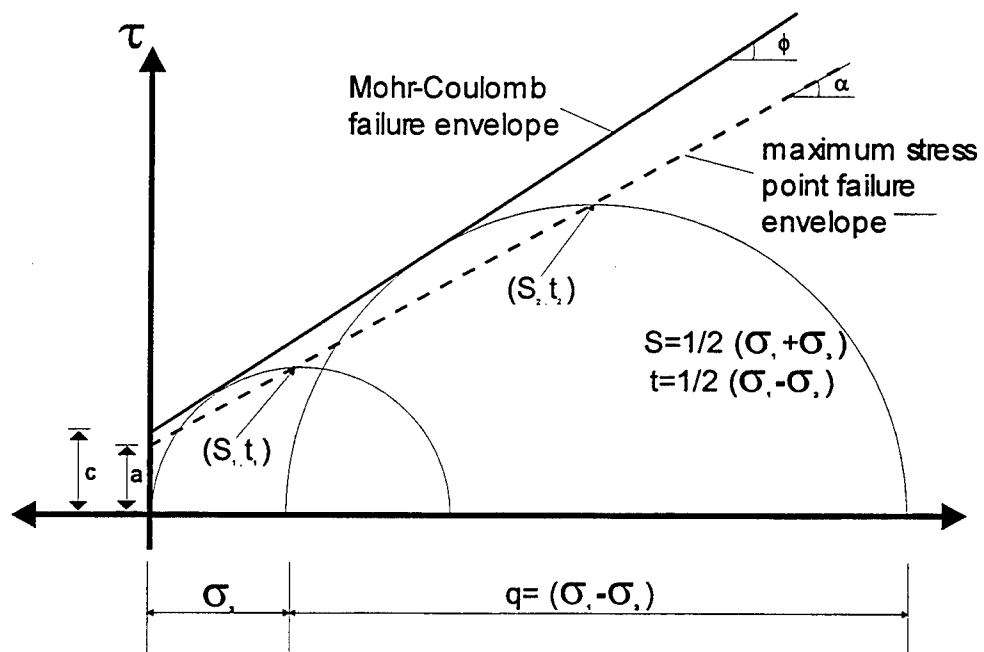


Figure H.2. Failure envelopes from Mohr's circle of stress for two conventional triaxial compression tests

**APPENDIX I**

**THREE DIMENSIONAL VERIFICATION**

The version of the WES Multimechanical Constitutive Model (WES MM) used in the research reported in the main body of this dissertation was originally formulated for full three dimensional (3D) analyses. The model was simplified to operate in a two dimensional axis-symmetric case. The laboratory and field tests analyzed were well-suited to an axisymmetric analysis. In future analyses the investigation of multiple wheel response and moving loads will require that the pavement system to be modeled in a full three dimensional setting.

Since the original formulation of the WES MM was 3D, it was relatively simple to set the model back to operate with a 3-D 8-node isoparametric brick element. In order to demonstrate the effectiveness of the model in three-dimensional analysis, a single 1-in. cubical element was subjected to the same stress path as the 50-psi conventional triaxial compression test. The element was subjected to the 3-D equivalent of the load and boundary conditions in the axisymmetric analysis presented in Chapter 6. The horizontal stresses ( $\sigma_2$  and  $\sigma_3$ ) are held at 50 psi, while the vertical stress ( $\sigma_1$ ) was increased until a vertical strain ( $\epsilon_1$ ) of approximately 5% was achieved. The element and the boundary conditions are shown in Figure I.1.

The laboratory test results and FEM predictions are shown in Figure I.2 and I.3. The 3D analysis is slightly stiffer at high strain levels than the 2D analysis. This can be attributed to the differences in element formulation in ABAQUS and small differences in convergence criteria. The maximum difference between the 2D and 3D predicted stress is only 3%. The application of the WES MM to 3D problems is an area for future exploration with many applications in pavement analysis.

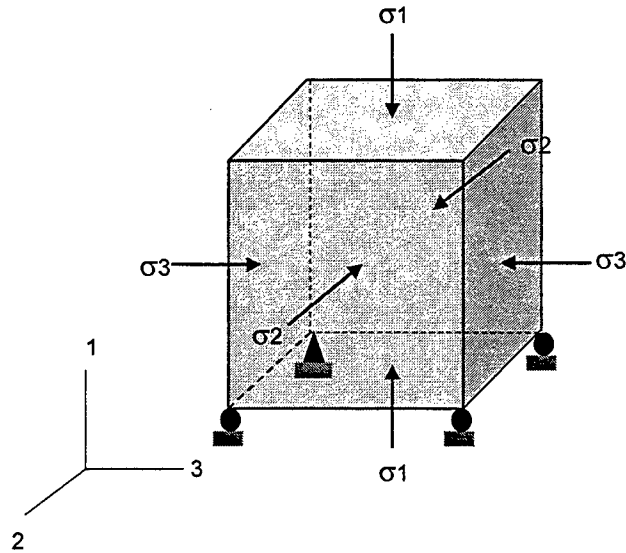


Figure I.1. 3D element under triaxial compression loading

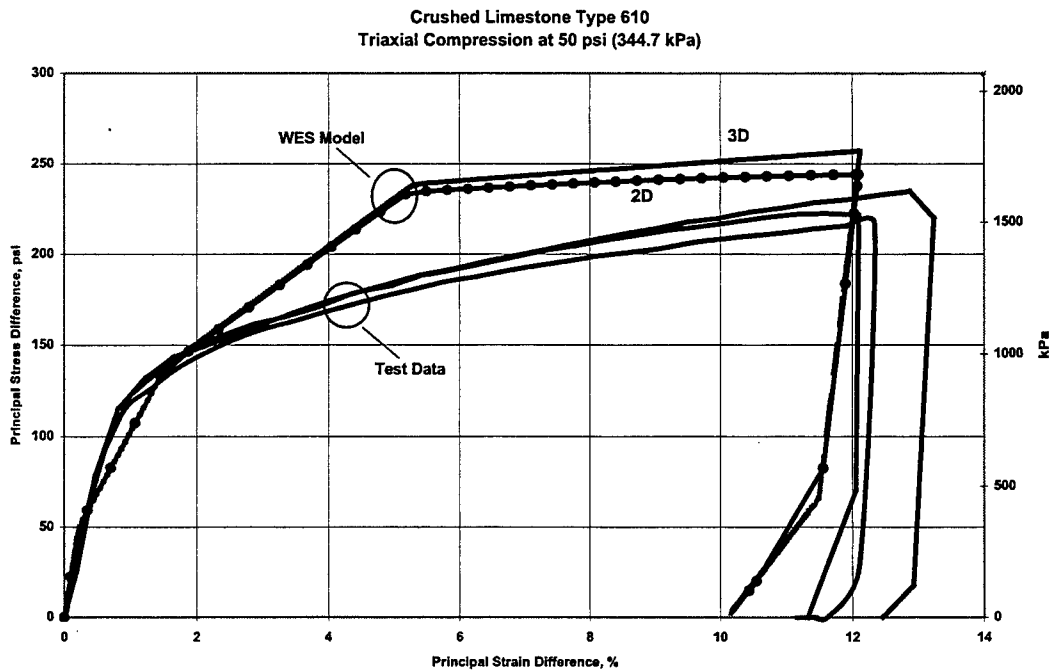


Figure I.2. Laboratory test results and FEM predictions for a 50 psi triaxial compression test

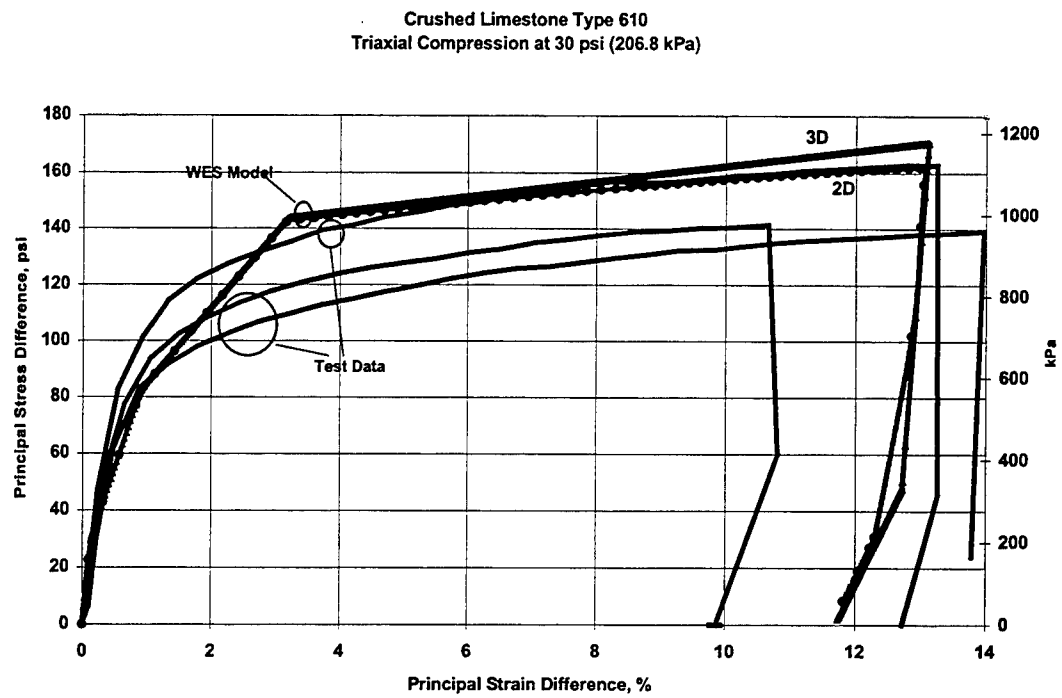


Figure I.3. Laboratory test results and FEM predictions for a 30 psi triaxial compression test

# REPORT DOCUMENTATION PAGE

Form Approved  
OMB No. 0704-0188

Public reporting burden for this collection of information is estimated to average 1 hour per response, including the time for reviewing instructions, searching existing data sources, gathering and maintaining the data needed, and completing and reviewing this collection of information. Send comments regarding this burden estimate or any other aspect of this collection of information, including suggestions for reducing this burden to Department of Defense, Washington Headquarters Services, Directorate for Information Operations and Reports (0704-0188), 1215 Jefferson Davis Highway, Suite 1204, Arlington, VA 22202-4302. Respondents should be aware that notwithstanding any other provision of law, no person shall be subject to any penalty for failing to comply with a collection of information if it does not display a currently valid OMB control number. **PLEASE DO NOT RETURN YOUR FORM TO THE ABOVE ADDRESS.**

**1. REPORT DATE (DD-MM-YYYY)**

May 2000

**2. REPORT TYPE**

Final report

**3. DATES COVERED (From - To)****4. TITLE AND SUBTITLE**

Response of Granular Layers in Flexible Pavements Subjected to Aircraft Loadings

**5a. CONTRACT NUMBER****5b. GRANT NUMBER****5c. PROGRAM ELEMENT NUMBER****6. AUTHOR(S)**

Donald Mark Smith

**5d. PROJECT NUMBER****5e. TASK NUMBER****5f. WORK UNIT NUMBER****7. PERFORMING ORGANIZATION NAME(S) AND ADDRESS(ES)**

U.S. Army Engineer Research and Development Center  
Geotechnical Laboratory  
3909 Halls Ferry Road  
Vicksburg, MS 39180-6199

**8. PERFORMING ORGANIZATION REPORT NUMBER**

ERDC/GL TR-00-3

**9. SPONSORING / MONITORING AGENCY NAME(S) AND ADDRESS(ES)**

U. S. Army Corps of Engineers  
Washington, DC 20314-1000

**10. SPONSOR/MONITOR'S ACRONYM(S)****11. SPONSOR/MONITOR'S REPORT NUMBER(S)****12. DISTRIBUTION / AVAILABILITY STATEMENT**

Approved for public release, distribution unlimited.

**13. SUPPLEMENTARY NOTES****14. ABSTRACT**

Airfield pavement design is a complex blend of relatively simple linear elastic theory, fatigue concepts, correlations with small-scale and full-scale and full-scale tests, and pragmatic adjustments to reflect observations of in-service pavements. The granular base and subbase have always posed the most difficult analytical problem in traditional pavement design methodologies. For this reason, the granular layers have never been treated explicitly in design as have the asphalt concrete (AC) layer and subgrade layer, which have used predictive models for cracking in the AC and rutting in the subgrade as a function of linear-elastic strain and material properties. Instead, these granular layers were carefully specified in terms of gradation, plasticity, and in-situ density to minimize deformation under traffic.

However, today's designers are being asked to predict pavement performance under a variety of nonstandard conditions. This is a far more complex task than simply providing safe thickness and specifications for the material. To deal with this new challenge, the design community must have material models that predict cumulative deformations under repetitive aircraft loads. In order to apply these material models, mechanical response data are required to calibrate the necessary model parameters.

(continued)

**15. SUBJECT TERMS**

Airfield pavements, Base course, Constitutive model, Cyclic loads, Finite element method, Granular material, Pavement analysis, Pavement model, Plasticity, Triaxial test

**16. SECURITY CLASSIFICATION OF:**

a. REPORT

b. ABSTRACT

c. THIS PAGE

UNCLASSIFIED

UNCLASSIFIED

UNCLASSIFIED

**17. LIMITATION OF ABSTRACT****18. NUMBER OF PAGES**

266

**19a. NAME OF RESPONSIBLE PERSON****19b. TELEPHONE NUMBER (include area code)**

#### **14. ABSTRACT (Concluded)**

The parameters used to define strength, failure, and deformation properties must be defined for any material to be modeled. This report describes the constitutive model requirements, laboratory tests, and analysis used in developing a response model for an unbound granular base course typical of an airfield pavement.